Nonlinearity in photonic crystal fibres

Xiong, Chunle

Award date:
2008

Awarding institution:
University of Bath

NONLINEARITY IN PHOTONIC CRYSTAL FIBRES

Chunle Xiong

A thesis submitted for the degree of
Doctor of Philosophy
University of Bath
Department of physics

July 15, 2008

Abstract

This thesis introduces the linear and nonlinear properties of photonic crystal fibre (PCF), describes the fabrication and characterisation of different PCFs, and demonstrates their applications to supercontinuum (SC) generation and single-photon sources. The linear properties of PCF include endlessly single-mode transmission, highly controllable dispersion and birefringence. These unique properties have made PCFs the best media to demonstrate all kinds of nonlinear effects such as self-phase modulation (SPM), cross-phase modulation (XPM), Raman effects, four-wave mixing and modulation instability (FWM and MI), and soliton effects. The combination of these nonlinear effects has led to impressive spectral broadening known as SC generation in PCFs. The intrinsic correlation of signal and idler photons from FWM has brought PCF to the application of single-photon generation.

Four projects about SC generation were demonstrated. The first was visible continuum generation in a monolithic PCF device, which gave a compact, bright (-20 dBm/nm), flat and single-mode visible continuum source extending to short wavelength at 400 nm. The second was polarised SC generation in a highly birefringent PCF. A well linearly polarised continuum source spanning 450-1750 nm was achieved with >99% power kept in a single linear polarisation. This polarised continuum source was then applied to tuneable visible/UV generation in a BIBO crystal. The third was residual pump peak removal for SC generation in PCFs. The fourth was to design an all-fibre dual-wavelength pumping for spectrally localised continuum generation.

Two projects about photon pair generation using FWM were then demonstrated. One was an all-fibre photon pair source designed in the telecom band for quantum communication. This source achieved >50% heralding efficiency which is the highest in fibre photon pair sources reported so far. Another one was to design birefringent PCFs for naturally narrow band photon pair generation in the Si SPAD high detection efficiency range. 0.122 nm bandwidth signal photons at 596.8 nm were generated through cross polarisation phase matched FWM in a weakly birefringent PCF pumped by a picosecond Ti:Sapphire laser at 705 nm in the normal dispersion regime.

ACKNOWLEDGEMENTS

There are lots of people I should thank for their help and support both in my Ph.D study and in the three years of my overseas life in the UK.

First of all, I would like to give great thanks to my supervisor Dr. William Wadsworth. Most of the knowledge about PCF and nonlinearity comes from him directly. He taught me many experiment skills and data analysis methods to guarantee that the research results and conclusions are scientific and reliable. He did not only support me to do research but also made me clear what research work would be like and what attitude I should have for scientific research. The discussion with him really made me achieve a lot.

Thanks must go to Professor Philip Russell, who provided me this chance to study in the Centre for Photonics and Photonic Materials (CPPM) at Bath.

To Dr. Dmitry Skryabin for supporting me to successfully apply Overseas Research Studentship (ORS).

To Professor Jonathan Knight and Tim Birks. The discussion with them made me learn a lot about fibre modes and nonlinearity.

To Alan George and Steve Renshaw, two fibre fabrication experts, who provided me with many ideas and assistances in fibre fabrication.

To Agata Witkowska, who spent lots of time on the visible SC generation device fabrication.

To Francois Couny who taught me and helped me to splice PCFs and conventional fibres.

To Alex McMillan who did photon pair generation experiments with me and gave me many useful suggestions, and helped me to read this thesis.

To Jim Stone for giving me lots of help during my Ph.D study and providing me with the preform to fabricate the weakly birefringent PCFs.

To Professor David Bird and Dr. Greg Pearce for their powerful codes which enabled me to easily carry out fibre dispersion calculations.

To Dr. Weimin Sun for helping me to prepare the preform for the weakly birefringent PCF fabrication.

To Bob Draper who taught me and helped me to make different holders for my experiments.

To Mathew Burnett for providing me the information about scanning near-field optical microscopy (SNOM).

To Alexey Yulin and Andrey Gorbach for discussion about soliton effects in SC generation during my writing.

To Matthew Welch for helping me to read this thesis and making it more readable.

To Feng Luan, Wei Ding, Aimin Wang, Ke Lai, Yingying Wang, Jing Hou, Xiaoze Gong, Lei Yao, Zilun Chen and Limin Xiao, my Chinese friends in this group, for being so supportive during my Ph.D study. Without you, the work would have become difficult and life would be boring.

At last but not the least, I would give great thanks to all other group members who gave me many useful suggestions during my study.

Finally, I would like to thank my wife, Ying Ai, my sister and my parents. Even though they could not accompany me for the last 36 months, the support from them has always inspirited me to finish my Ph.D as soon as possible.

Contents

List of Figures

List of Tables

Chapter 1

Introduction

The basic phenomenon responsible for guiding light in optical fibres—total internal reflection—is known from the nineteenth century, but the development of optical fibres was long after the discovery of this phenomenon. In the 1920s, uncladded glass fibres were first fabricated [1]. It was not until the 1950s that a cladding layer was used to improve the fibre characteristics [2][3]. During the 1960s, glass fibres, mainly used for image transmission, were still extremely lossy (loss $>$ 1000 dB/km) by modern standards [4]. In 1970, losses of silica fibres were reduced to below 20 dB/km [5]. Further progress in fabrication technology resulted by 1979 in a loss of only 0.2 dB/km in the 1.55 μm wavelength region [6], a loss level limited mainly by the fundamental processes of Rayleigh scattering and infrared absorption of silica.

The early history of optical fibre development showed that it was mainly the fibre losses that limited its applications. The availability of low-loss silica fibres led not only to a revolution in the field of optical fibre communications [7] but also to the advent of the new field of nonlinear fibre optics [8]. The demonstration of nonlinear phenomena in optical fibres needs not only low-loss fibres but also high intensity light sources. In 1960 the first working laser was made by T. H. Maiman [9]. This invention rapidly stimulated the development of laser sources, which fuelled the research on nonlinear fibre optics. During the two decades of the 1970s and 1980s, a wide variety of new nonlinear effects were found or demonstrated in optical fibres. Stimulated Raman scattering (SRS) and stimulated Brillouin scattering (SBS) processes in optical fibres were studied as early as 1972 [10]-[12]. Then other nonlinear phenomena such as optically induced birefringence [13], parametric four-wave mixing (FWM) [14]-[16] and self-phase

modulation (SPM) [17] were found in the following several years. Optical solitons, arising as a result of an interplay between the dispersive and nonlinear effects, were predicted theoretically in 1973 [18] and observed experimentally in 1980 [19]. Modulation instability (MI), now known as the time domain description of FWM, was presented in 1980 [20] and experimentally demonstrated in 1985 [21]. Cross-phase modulation (XPM), a nonlinear interaction between different wavelengths copropagating inside an optical fibre, was experimentally measured in 1984 [22].

Starting in 1996, new types of fibres, known as photonic crystal fibres (PCFs), were developed [23]-[34]. Holey fibres or microstructured fibres are also used as the name of such fibres in some papers and books. In this thesis, PCFs will be always used to denote such fibres to distinguish them from conventional fibres. The original idea of PCFs was to trap light in a hollow fibre core by means of two-dimensional (2-D) photonic band gap (PBG) formed by a "photonic crystal" of microscopic air capillaries running along the entire length of a glass fibre; however the first attempt to fabricate such fibres in 1995 did not lead to observation of PBG guidance because of relatively small air holes [31][34]. A simple change of the air core to a solid core resulted in the birth of the first working PCF in 1996 [23]. However this PCF did not guide light by PBG. It behaved somewhat like a conventional fibre because the "average" refractive index was lower outside the core; but it had an exciting property that the core did not ever seem to become multimode, no matter how short the wavelength of the light [24]. The success of this fibre rapidly stimulated a series of new discoveries including the real hollow core PCFs (HC-PCFs) [28] and even all solid PBG fibres [33]. The discussion about these two particular PCFs is beyond the interest of this thesis. I will focus on the investigation of PCFs with solid silica core surrounded by the periodic air-silica structure, which are similar to the first working PCF mentioned above. The special structure of such PCFs brings more degrees of freedom to fibre design. Besides the single-mode property, another striking property of such PCFs is the highly controllable dispersion [26][29], which plays a critical role in many nonlinear processes. These breakthroughs led quickly to the demonstration of supercontinuum (SC) generation which is the combined effects of SPM, XPM, SRS, FWM/MI and solitons [35]-[45]. Benefitting from the novel dispersion and nonlinear properties of PCFs, soliton delivery and pulse compression in both uniform and tapered PCFs [46]-[48] have been demonstrated at different wavelengths, some of which were previously impossible in conventional

fibres.

It is clear that the invention of PCFs has brought prosperity and perspectives to the research of nonlinear fibre optics. New technologies are enabling both new insights into nonlinear physics and the development of new application areas. The study of SC generation not only provides further understanding of the nonlinear effects involved but also leads to versatile applications in spectroscopy, microcopy, optical coherence tomography [49] and optical device characterisation. Some nonlinear phenomena in PCFs are not fundamentally new, but they have been found very useful in some recently developing areas because of their striking features. Discrete FWM in PCFs, for example, can be used to generate high brightness correlated photon pairs for quantum information [50] because of the wide separation between signal, idler and pump wavelengths. Undoubtedly, nonlinear optics in PCFs is a research area with great importance from both scientific and industrial points of view and is expected to have further development in the near future.

This thesis is intended to provide a comprehensive understanding of nonlinear effects involved in SC generation in PCFs and particularly FWM as well as its applications to quantum information. The organization of the material is outlined as follows. Chapter 2 takes a view of the conventional fibre characteristics and then describes the guidance mechanisms as well as the unique properties of PCFs. Fabrication of PCFs is also included in this chapter. The comparison between PCFs and conventional fibres is given over the entire chapter. Chapter 3 focuses on the general introduction of nonlinear phenomena in PCFs, including SPM, XPM, SRS, FWM/MI and solitons. Chapter 4 is devoted to the study of SC generation in PCFs and mainly presents three projects finished during my Ph.D study. The first is compact visible SC generation in a monolithic PCF device, the second is polarised SC generation in a highly birefringent PCF, and the last is residual pump peak removal for SC generation in PCFs. A new idea is also proposed to make an all-fibre dual-wavelength pumping SC source and some preliminary results are shown. Some applications of SC sources are discussed in the end of this chapter. Chapter 5 demonstrates photon pair generation in PCFs pumped at 1064 nm and $\sim$710 nm, respectively. Chapter 6 summarizes this thesis and considers some future work.

Chapter 2

Photonic Crystal Fibres

This chapter is intended to provide an overview of photonic crystal fibre (PCF) characteristics that are important for understanding the nonlinear effects discussed in later chapters. Section 2.1 provides a brief description of the characteristics and fabrication of conventional fibres. Section 2.2 introduces two kinds of PCF guidance mechanisms known as total internal reflection (TIR) and photonic band gap (PBG) guidance. Section 2.3 gives an introduction to the state-of-the-art PCF fabrication from silica glass preforms and the post-processing of PCFs in stock. Section 2.4 discusses several important properties of PCFs: endlessly single-mode (ESM) transmission, widely controllable dispersion, high nonlinearity, and birefringence. Section 2.5 discusses the splicing of PCFs. The comparison between PCFs and conventional fibres will be covered throughout this chapter.

2.1 Conventional Fibres

Knowledge of PCFs is established on the basis of conventional fibre technologies, therefore it is necessary to give a brief discussion about conventional fibres. In its simplest form, a conventional fibre with cylindrical symmetry consists of a central core surrounded by a cladding layer whose refractive index is slightly lower than that of the core. Such fibres are generally referred to as step-index fibres to distinguish them from graded-index fibres in which the refractive index of the core decreases gradually from centre to the core boundary. In this thesis, the term conventional fibres refers to step-index fibres unless noted otherwise. The basic principle responsible for the guiding of light in conventional fibres is well

known as TIR: A ray of light will be totally reflected at the interface between two dielectric media when incident from the medium with higher refractive index at an angle of incidence ϕ greater than a critical value ϕ_c determined by [7]

$$\phi_c = \sin^{-1}(\frac{n_{\rm cl}}{n_{\rm co}}), \tag{2.1}$$

where $n_{\rm co}$ and $n_{\rm cl}$ are the core and cladding layer refractive indices, respectively. A schematic diagram of a conventional fibre structure and TIR is provided in Fig. 2.1. Since such reflections occur throughout the fibre length, all rays with $\phi > \phi_c$ remain confined to the fibre core and propagate along the fibre to the other end. This ray picture is based on geometrical-optics, which is approximate and valid when the core size is much larger than the light wavelength. When the two become comparable, it is necessary to use the more general theory about fibre modes discussed in Section 2.1.1.

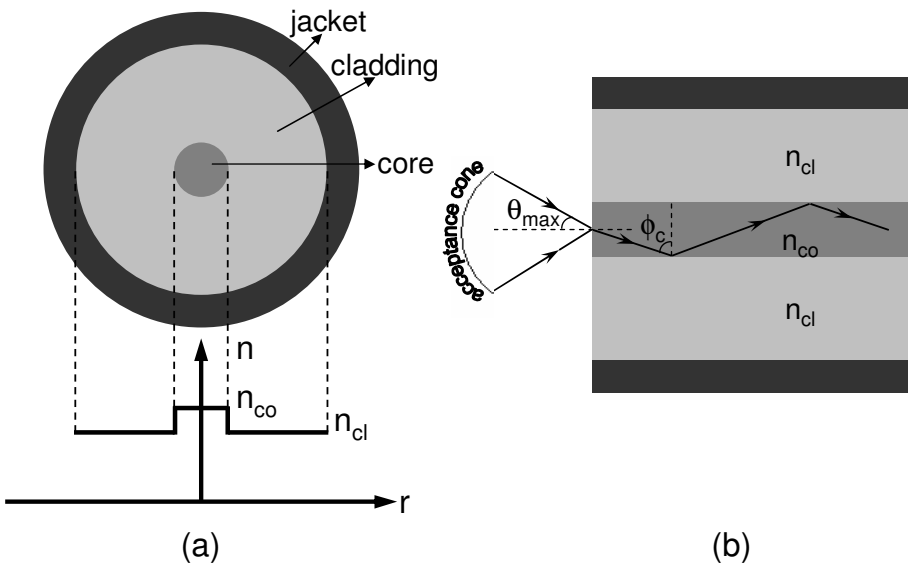

Figure 2.1: (a) Schematic of the cross section and refractive index profile of a conventional fibre; (b) fibre side view and guiding mechanism of TIR. The incident light within the acceptance cone can be guided in the fibre core (also see Section 2.1.2).

2.1.1 Fibre Modes

Like all other electromagnetic phenomena, the complete description of light behavior in optical fibres relies on solutions of Maxwell's equations. The detailed information about this can be found in the book written by G. P. Agrawal [7]. This section will introduce some important conclusions about fibre modes.

Mathematically, fibre modes refer to the solutions $\mathbf{E}(\mathbf{r}, t)$ that satisfy Maxwell's equations and the fibre core-cladding boundary conditions. Physically, a fibre mode refers to the spatial distribution of the electric field $\mathbf{E}(\mathbf{r}, t)$ in the fibre core area; and this spatial field distribution does not change along the propagation. Each fibre mode has a unique propagation constant β_{mn} ($m = 0, 1, ...;\ n = 1, 2, ...$). The corresponding modal field distribution is designated as HE_{mn} or EH_{mn}, depending on whether H_z or E_z dominates. In the special case of $m = 0$, HE_{0n} and EH_{0n} are also denoted by TE_{0n} and TM_{0n}, respectively, since they correspond to transverse-electric ($E_z = 0$) and transverse-magnetic ($H_z = 0$) modes of propagation. A quantity called mode index is defined by $n_{\mathrm{mod}} = \beta/k_0$. k_0 is the vacuum wavevector and $k_0 = 2\pi/\lambda = \omega/c$, where λ is the vacuum wavelength of the optical field oscillating at the frequency ω, c is the speed of light in vacuum. n_{mod} has the physical significance that each fibre mode propagates with an refractive index whose value lies in the range of $n_{\mathrm{co}} > n_{\mathrm{mod}} > n_{\mathrm{cl}}$. A mode ceases to be guided when $n_{\mathrm{mod}} \leq n_{\mathrm{cl}}$. This can be understood by noting that the optical field of guided modes decays exponentially inside the cladding layer but the exponential decay does not occur when $n_{\mathrm{mod}} \leq n_{\mathrm{cl}}$. So far the fibre modes theory draws the same conclusion to geometrical-optics, but this theory is far more than that.

Single-Mode Condition

The number and intensity profiles of the guided modes depend on the light wavelength and the physical parameters of the waveguide. In general a fibre supports more than one mode unless it has a specific design for single-mode transmission. A mode is said to reach cutoff when $n_{\mathrm{mod}} = n_{\mathrm{cl}}$. A parameter that plays an important role in determining the cutoff condition is defined as

$$V = k_0 a (n_{\mathrm{co}}^2 - n_{\mathrm{cl}}^2)^{1/2} = \frac{2\pi a}{\lambda} (n_{\mathrm{co}}^2 - n_{\mathrm{cl}}^2)^{1/2}, \tag{2.2}$$

where a is the core radius, and k_0, n_{co} and n_{cl} have the same definitions as above.

The parameter V is called the normalised frequency ($V \propto \omega$) or simply the V parameter. It is also useful to introduce a normalised propagation constant b as

$$b = \frac{\beta/k_0 - n_{\rm cl}}{n_{\rm co} - n_{\rm cl}} = \frac{n_{\rm mod} - n_{\rm cl}}{n_{\rm co} - n_{\rm cl}}. \tag{2.3}$$

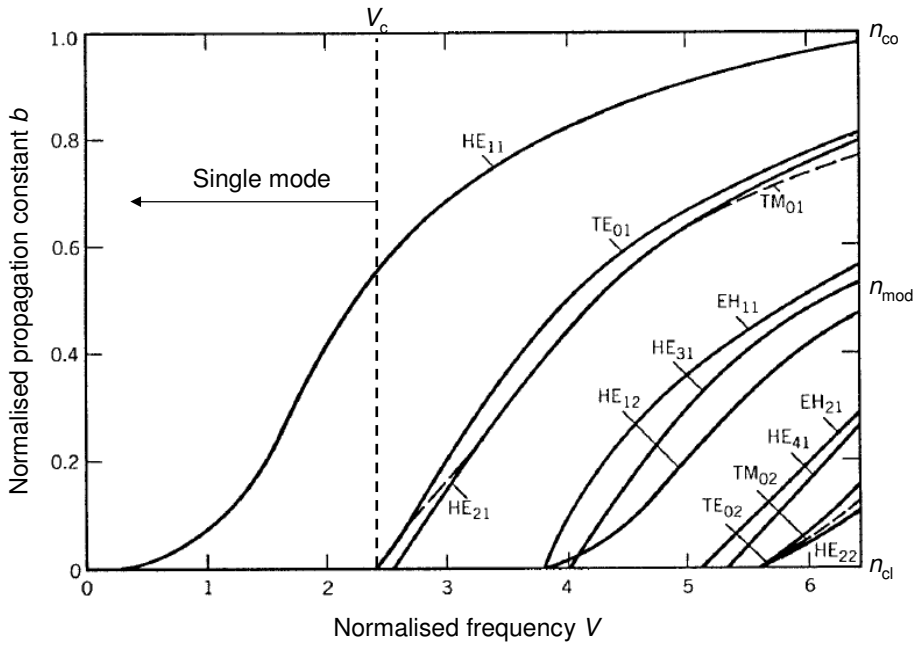

Figure 2.2: Normalised propagation constant b as a function of normalised frequency V for a few low-order fibre modes (Ref. [7] Chapter 2). The right scale shows the mode index $n_{\rm mod}$.

Figure 2.2 shows a plot of b as a function of V for a few low-order fibre modes. As seen in Fig. 2.2, a fibre with a large value of V supports many modes. A rough estimate of the number of modes for such a multimode fibre is given by $V^2/2$ [51]. However, the number of modes decreases rapidly as V is reduced. Particularly when $V < V_c$, all modes except the $\rm HE_{11}$ mode reach cutoff. $\rm HE_{11}$ mode is known as the fundamental mode of a fibre. Such fibres designed to only support the fundamental mode are called single-mode fibres. The single-mode condition $V_c = 2.405$ is given by the smallest value of V for which Bessel function $J_0(V) = 0$ where the $\rm TE_{01}$ and $\rm TM_{01}$ modes reach cutoff (see Fig. 2.2). Or for a given fibre, there is a cutoff wavelength λ_c for single-mode transmission.

According to Eq. (2.2),

$$\lambda_c = \frac{2\pi a}{2.405}(n_{\mathrm{co}}^2 - n_{\mathrm{cl}}^2)^{1/2}. \tag{2.4}$$

Only the wavelengths longer than λ_c have one guided mode in such a fibre; when the operating wavelength is shorter than λ_c, the fibre becomes a multimode fibre.

Fibre Birefringence

In single-mode fibres, the mode field distribution $\mathbf{E}(\mathbf{r}, t)$ corresponding to the HE_{11} mode has three nonzero components E_ρ, E_ϕ, and E_z, or in Cartesian coordinates E_x, E_y, and E_z. Among these, either E_x or E_y dominates [52]. Thus, to a good degree of approximation, the fundamental fibre mode is linearly polarised in either the x or y direction depending on whether E_x or E_y dominates. In this respect, even a single-mode fibre is not truly single mode because it can support two modes of orthogonal polarisations.

In a stress-free fibre with perfectly cylindrical symmetry, the two orthogonally polarised modes of a single-mode fibre are degenerate (i.e. they have the same propagation constant and mode shape). In real fibres, however, limited by the practical fabrication processes, small departures from cylindrical symmetry are unavoidable, such as random fluctuations in the core shape and size along the fibre length. Fibres may also experience nonuniform stresses in practice due to fibre bends or twists. These effects break the mode degeneracy, and the mode propagation constant β will become slightly different for modes polarised in the x and y directions. This is known as modal birefringence of optical fibres. The degree of modal birefringence is defined by [7]

$$B_m = \frac{|\beta_x - \beta_y|}{k_0} = |n_x - n_y|, \tag{2.5}$$

where β_x and β_y are the propagation constants of these two orthogonally polarised modes and n_x and n_y are their modal refractive indices.

In conventional single-mode fibres without birefringence design, birefringence B_m is small and changes randomly along the fibre because of variations in the core shape (elliptical rather than circular) and the anisotropic stress acting on the core. Coupling between the two orthogonal polarisation modes is easy and random. As a result, light launched into the fibre with linear polarisation quickly reaches a state of arbitrary polarisation. Fortunately it is possible to make fibres

for which random fluctuations in the core shape and size and nonuniform stresses are not the governing factor in determining the state of polarisation. A large amount of birefringence is introduced intentionally in these fibres through design modifications so that small random birefringence fluctuations do not affect the light polarisation significantly. In other words, coupling between the two orthogonal polarisation modes can not occur because of the big difference between them. Such fibres are called polarisation-maintaining (PM) fibres or highly birefringent fibres. Typically, $B_m \sim 10^{-4}$ for PM fibres. In PM fibres, the two specific directions corresponding to the two orthogonal polarisation states are referred to as the principal axes. The axis along which β or the mode index is smaller is called the fast axis. The other axis is called the slow axis. Even in PM fibres linearly polarised light remains linearly polarised only when it is initially polarised along one of these principal axes. Otherwise, its polarisation state changes along the fibre length, from linear to elliptical, and then back to linear in a periodic manner over a length called beat length L_B, which is given by

$$L_B = \lambda / B_m. \tag{2.6}$$

This is because of the relative phase change of the two polarisation modes along the fibre, which leads to their coupling in phase and out phase periodically. Figure 2.3 schematically shows such polarisation state change when a linear polarised light is coupled into a PM fibre at 45° with respect to the principal axes.

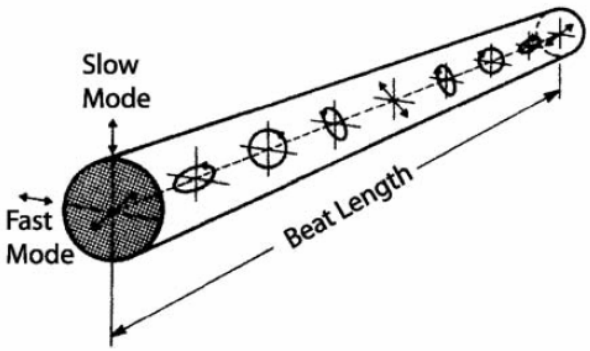

Figure 2.3: Evolution of the polarisation state along a PM fibre over one beat length when the input beam is linearly polarised at 45° from the principal axes (Ref. [7] Chapter 2).

Mode Field Size

Mode field size is one of the most important parameters for the fibre nonlinearity since it determines the optical intensity inside fibres. Although a guided mode is well confined by the core-cladding boundary of an optical fibre, the light energy is still able to penetrate into the cladding layer and the mode field can expand into the cladding. The fraction of the power contained in the core can be expressed as

$$\Gamma = \frac{P_{\text{core}}}{P_{\text{total}}} = \frac{\int_0^a |F|^2 r \mathrm{d}r}{\int_0^\infty |F|^2 r \mathrm{d}r}, \tag{2.7}$$

where F is the modal electric field distribution, and r is the distance from the core centre.

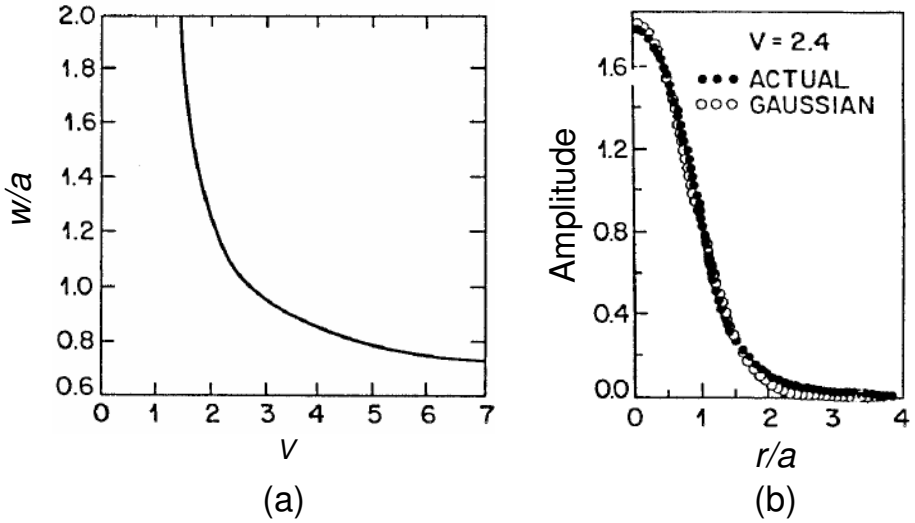

Figure 2.4: (a) Normalised mode field radius w/a as a function of the V parameter obtained by fitting the fundamental fibre mode to a Gaussian distribution; (b) quality of fit for $V = 2.4$ (Ref. [7] Chapter 2).

In practice, it is convenient and reasonable to consider a linearly polarised mode and approximate the mode field distribution by a normalised Gaussian distribution

$$F = \exp(-r^2/w^2), \tag{2.8}$$

where w is the mode field radius (corresponding to the points where the optical intensity drops to $1/e^2$ of the maximum value). It is determined by fitting the exact distribution to the Gaussian function. Figure 2.4 shows the dependence of w/a on the V parameter defined by Eq. (2.2). A comparison of the actual field

distribution with the fitted Gaussian is also shown for $V = 2.4$. The quality of fit is generally quite good for values of V in the neighborhood of 2. The mode field radius w can be determined from Fig. 2.4. Equations (2.7), (2.8) and Fig. 2.4(a) determine the fraction of the mode power contained inside the core for a given value of V. It is easy to find that the percentage of the mode power remaining in the core drops quickly from 75% for $V = 2$ to 20% for $V = 1$. Moreover, the large mode field due to small V makes the fibre more sensitive to fibre bending losses. For these reasons, even though $V/V_c < 1$ must be satisfied for the single-mode operation, V/V_c cannot be too small. The typical V-value is chosen to be close to V_c but not greater than V_c for both single-mode operation, small mode field size, and high power ratio in the core. This is very important for fibre nonlinear effects. It will be seen later that the effective mode area, defined as

$$A_{\text{eff}} = \frac{(\int\int_{-\infty}^{+\infty} |F(x,y)|^2 \mathrm{d}x\mathrm{d}y)^2}{\int\int_{-\infty}^{+\infty} |F(x,y)|^4 \mathrm{d}x\mathrm{d}y}, \tag{2.9}$$

directly affects the fibre nonlinearity (see Section 2.1.6). In Eq. (2.9), $F(x, y)$ is the mode field distribution. If $F(x, y)$ takes the Gaussian form similar to Eq. (2.8)

$$F(x,y) = \exp[-(x^2 + y^2)/w^2], \tag{2.10}$$

A_{eff} can be related to the spot size as $A_{\text{eff}} = \pi w^2$.

2.1.2 Numerical Aperture [7]

An optical fibre will only guide light that enters the fibre within a certain cone, known as the acceptance cone of the fibre. The half-angle of this cone is called the acceptance angle $\theta_{\max}$ (see Fig. 2.1(b)). The numerical aperture (NA) of an optical fibre represents such light-gathering capacity of the fibre. It is defined as

$$\text{NA} = \sin(\theta_{\max}). \tag{2.11}$$

It should be noted that the output light beam from a fibre has the maximum divergence full-angle equal to $2\theta_{\max}$ because of the symmetry of the fibre input and output ends. Therefore the NA of an optical fibre can be directly determined through the measurement of the maximum divergence angle of the output beam from the fibre. The NA can also be calculated from the TIR critical condition (see

Fig. 2.1(b)):

$$\mathrm{NA} = \sin\theta_{\max} = \cos\phi_c = \sqrt{n_{\mathrm{co}}^2 - n_{\mathrm{cl}}^2}. \tag{2.12}$$

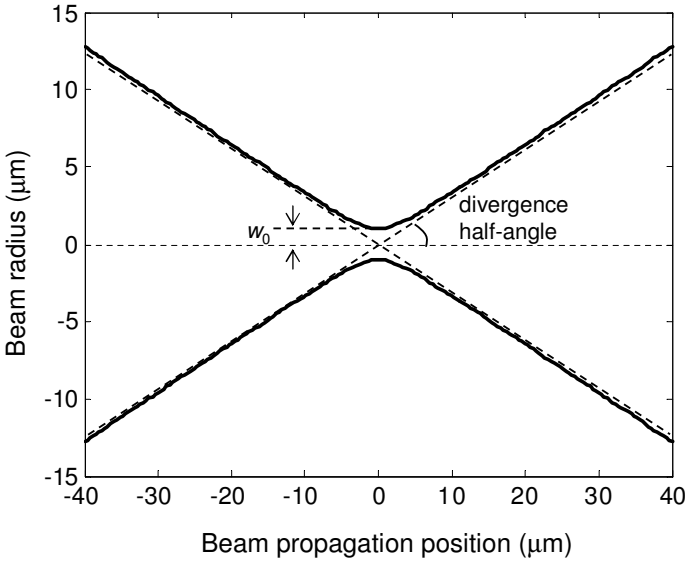

Figure 2.5: The divergence half-angle of a Gaussian beam is defined via the asymptotic variation of the beam radius (solid line) along the beam direction.

Although Eq. (2.12) is simply derived in the ray picture, it has become a common definition of the NA for any type of fibres. It is very convenient to evaluate the NA of conventional fibres from Eq. (2.12) since both n_{co} and n_{cl} have defined values. Manufacturers often quote "NA" for fibres based on this formula. For PCFs, however, n_{cl} is an effective index which is normally unknown and highly dispersive (see Section 2.4.1). To estimate the NA of such fibres, it can be understood as the divergence of the beam, analogous to the diffraction from an aperture. For a diffraction-limited Gaussian beam under the paraxial approximation, the divergence half-angle is

$$\theta_{\max} = \frac{\lambda}{\pi w_0}, \tag{2.13}$$

where λ is the wavelength in the medium and w_0 is the beam radius at the beam waist (see Fig. 2.5). To roughly estimate the NA of such a fibre, w_0 can be thought as the mode field radius which can be further approximated to the fibre

core radius.

2.1.3 Fibre Losses [7]

As mentioned in Chapter 1, fibre losses limited the applications of optical fibres for a long time. Modern techniques have produced low loss conventional fibres for telecommunications. However it is still a considerable concern for PCF design and applications.

If P_0 is the input power of a fibre of length L, the transmitted power P_T is given by

$$P_T = P_0 \, \mathrm{e}^{(-\alpha L)}, \tag{2.14}$$

where α is the attenuation constant, commonly referred to as the fibre loss parameter. It is customary to express the fibre loss in units of dB/km by using the relation

$$\alpha_{\mathrm{dB}} = -\frac{10}{L} \log_{10} \left(\frac{P_T}{P_0} \right) = 4.343\alpha. \tag{2.15}$$

Fibre losses depend on the wavelength of transmitted light. Figure 2.6 shows a typical loss spectrum of a single-mode conventional fibre [7]. The main contributions to fibre losses are material absorption and Rayleigh scattering. Material absorption can be divided into two categories. Intrinsic absorption losses correspond to absorption by fused silica (material used to make fibres) whereas extrinsic absorption is related to losses caused by impurities within silica. Any material absorbs at certain wavelengths corresponding to the electronic and vibrational resonances associated with specific molecules. For silica (SiO_2) molecules, electronic resonances induce the ultraviolet absorption loss in the region of $\lambda < 0.4$ μm, whereas vibrational resonances induce the infrared absorption loss in the region of $\lambda > 7$ μm. Because of the amorphous nature of fused silica, these resonances are in the form of absorption bands whose tails extend into the visible region. Pure silica does not absorb much light in the wavelength window 0.5-2 μm, but a relatively small amount of impurities can lead to significant absorption in this range. Hydroxyl ions in the glass structure are the most important impurity affecting fibre losses. In silica-based glasses, a strong fundamental Si-OH vibration occurs at ~ 2.7 μm and results in a first and second overtone at 1.38 and 0.95 μm, respectively, and a combination overtone at 1.25 μm [53]-[55].

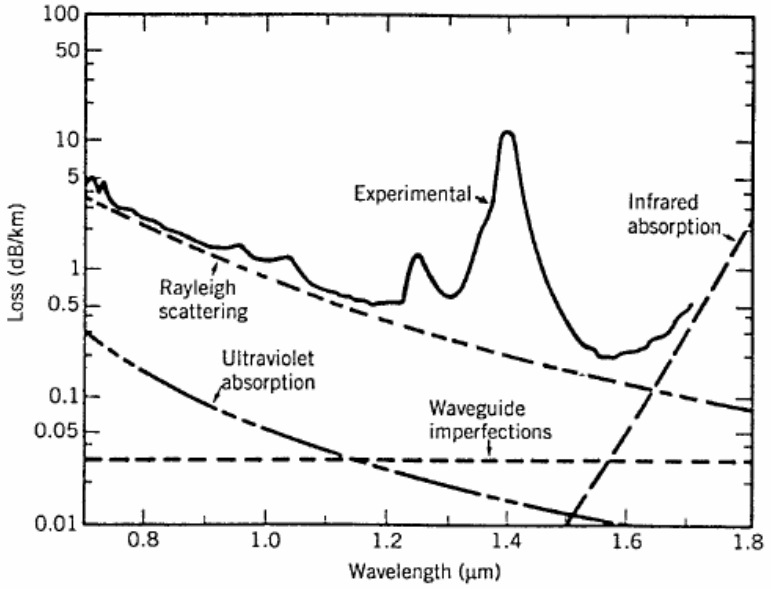

Figure 2.6: A typical loss spectrum of a single-mode conventional fibre. Wavelength dependence of several fundamental loss mechanisms is also shown (Ref. [7] Chapter 2).

Rayleigh scattering is a fundamental loss mechanism arising from local microscopic fluctuations of molecule density. Silica molecules move randomly in the molten state and freeze in place during fibre fabrication. Molecule density fluctuations lead to random fluctuations of the refractive index on a scale smaller than the optical wavelength λ. Light scattering in such a medium is known as Rayleigh scattering. The scattering cross section varies as λ^{-4}. As a result, the loss of silica fibres from Rayleigh scattering can be written as

$$\alpha_R = C/\lambda^4, \tag{2.16}$$

where the constant C is in the range 0.7-0.9 (dB/km)-μm^4, depending on the constituents of the fibre core.

Waveguide imperfections resulting from imperfect cylindrical geometry, index inhomogeneities and fibre bending are other possible contributions to fibre losses.

Intrinsic absorption losses and Rayleigh scattering loss can not be avoided since they are fundamental, but the operation wavelength window can be chosen in the range where the sum of these losses is relatively small. For silica glass

fibres, this window is chosen in the range of 0.5-2 μm. Particularly the telecom wavelength is chosen at 1550 nm where the loss is minimum. Extrinsic absorption losses can be reduced during the fabrication process by purifying the fibre material. For example, in a new kind of fibre known as the dry fibre, the OH ion concentration is reduced to such low levels that the 1.38 μm peak almost disappears [56]. Extra care can also be taken to minimize the losses resulting from waveguide imperfections.

2.1.4 Fibre Fabrication [7]

The optimum material for low-loss fibre in visible and near infrared region is silica glass formed by fusing SiO_2 molecules. The refractive index difference between the core and the cladding in conventional fibres is realised by the use of dopants during the fabrication process. GeO_2 and P_2O_5 can increase the refractive index of pure silica and so are suitable for the core. On the other hand, B_2O_3 and fluorine can be used for the cladding since it decreases the refractive index of silica. The fabrication process of silica glass fibres involves two stages. In the first stage, a modified chemical vapor-deposition (MCVD) method is used to make a cylindrical preform with the desired refractive index profile and the relative core-cladding dimensions. In the second stage, the preform is drawn into a fibre in a fibre drawing tower with a precision-feed mechanism that feeds it into a furnace at a proper speed. Both stages can ensure the uniformity of the core size and the index profile.

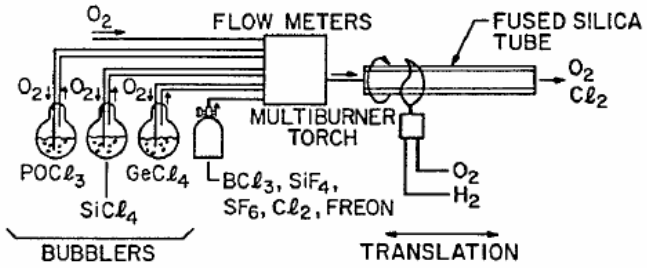

Figure 2.7: Schematic diagram of MCVD process (Ref. [7] Chapter 2).

The MCVD process is based on the high temperature oxidation of reagents inside a rotating tube which is heated by an external heat source. A schematic of the process is depicted in Fig. 2.7 [7][57]. The high purity gas mixture is

injected into a rotating silica tube which is mounted in a glass working lathe and heated by a traversing oxyhydrogen torch in the same direction as gas flow. The reagents react by a homogeneous gas phase reaction at high temperatures to form glassy particles which are subsequently deposited downstream of the hot zone. The heat from the moving torch fuses the material to form a transparent glassy film. Typical deposition temperatures are sufficiently high to sinter the deposited material, but not so high as to cause distortions of the substrate tube. The torch is traversed repeatedly in order to build up, layer by layer, the desired amount of material. As MCVD is practised, a thin cladding layer is first deposited. This serves as a barrier to diffusion of any impurities, such as OH, which could degrade the optical attenuation (see Section 2.1.3). After the cladding is deposited, the core material is laid down according to a programmed chemical delivery rate. The typical chemical reactions occurring in the silica tube are

$$\begin{aligned} SiCl_4 + O_2 &\longrightarrow SiO_2 + 2Cl_2, \\ GeCl_4 + O_2 &\longrightarrow GeO_2 + 2Cl_2, \\ 4POCl_3 + 3O_2 &\longrightarrow 2P_2O_5 + 6Cl_2. \end{aligned}$$

The details of the deposited layers inside the substrate tube are schematically shown in Fig. 2.8. Following deposition, the tube and deposit are collapsed to a solid rod called preform by heating to temperatures sufficient to soften the substrate tube.

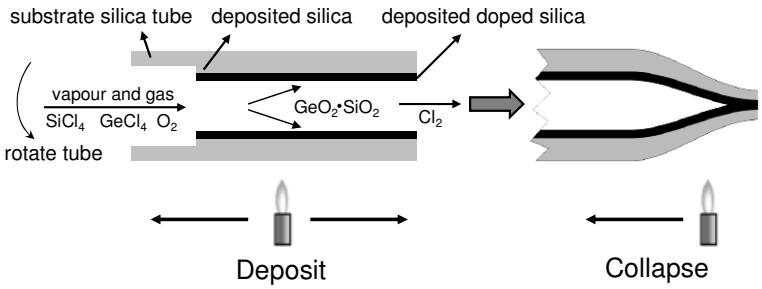

Figure 2.8: Schematic diagram of deposit and collapse procedure in MCVD process.

After the preform is prepared by MCVD, it is then transferred to a fibre drawing tower where it is drawn and coated. The structure of the fibre exactly replicates the preform. Figure 2.9 shows the drawing apparatus schematically.

The preform with a diameter of ϕ_{in} is fed into a furnace in a controlled manner where it is heated to a temperature of about 2000 °C. The melted preform is drawn into a fibre by using a precision-feed mechanism. The feeding speed v_{in} is typically a few mm/min, while the drawing speed v_{out} may range from a few m/min to a few km/min. The fibre diameter ϕ_{out} is determined by

$$\phi_{\text{out}} = \phi_{\text{in}} \sqrt{\frac{v_{\text{in}}}{v_{\text{out}}}}. \tag{2.17}$$

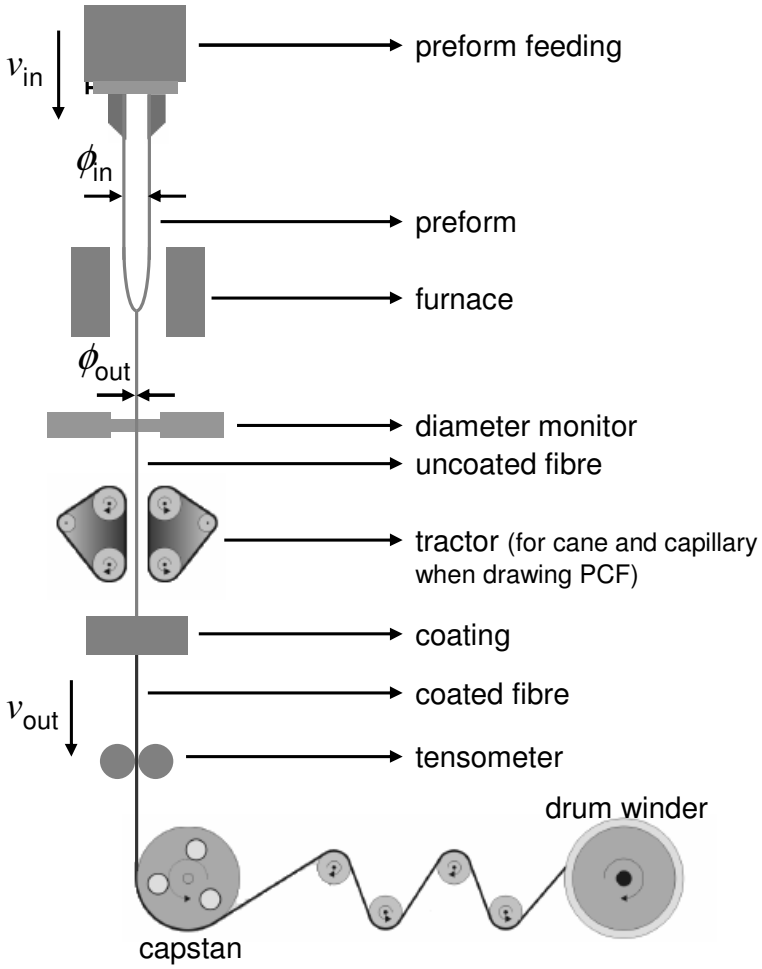

Figure 2.9: Schematic diagram of fibre drawing apparatus.

During the drawing process, the fibre diameter is monitored optically by diffracting light emitted by a laser from the fibre. A change in the diameter

changes the diffraction pattern, which in turn changes the photodiode current. This current change acts as a signal for a servocontrol mechanism that adjusts the winding rate of the fibre. The fibre diameter can be maintained constant with the fluctuation smaller than 0.1% by this technique. A polymer coating is applied to the fibre just after the diameter monitor to improve the durability and preserve the transmission properties of the fibre. The tensile strength of the fibre is also monitored before it is finally wound around a drum. The most common diameter of the commercial conventional fibres is 125 μm before coating and 250 μm after coating.

2.1.5 Fibre Dispersion [8]

Fibre dispersion is one of the most important properties of an optical fibre. In single-mode fibres, fibre dispersion manifests through the frequency dependence of the refractive index $n(\omega)$. This is also referred to as chromatic dispersion. On the fundamental level, the origin of chromatic dispersion is related to the characteristic resonance frequencies at which the medium absorbs the electromagnetic radiation through oscillations of bound electrons. A monochromatic wave propagates in an optical fibre with a speed of $c/n(\omega)$, which is known as the phase velocity v_p. Real optical signals are usually optical pulses, which are composed of a group of frequencies very close to each other around a central frequency ω_0. The envelope of an optical pulse moves at a speed called group velocity

$$v_g = \frac{\mathrm{d}\omega}{\mathrm{d}\beta}|_{\omega=\omega_0}, \tag{2.18}$$

which is also frequency dependent. Thus chromatic dispersion affects the propagation of short optical pulses through group-velocity dispersion (GVD) since different spectral components associated with the pulse travel at different speeds.

Mathematically, the effects of chromatic dispersion are taken into account by expanding the mode propagation constant β in a Taylor series about the center frequency ω_0:

$$\beta(\omega) = n(\omega)\frac{\omega}{c} = \beta_0 + \beta_1 \cdot (\omega - \omega_0) + \frac{1}{2}\beta_2 \cdot (\omega - \omega_0)^2 + \cdots, \tag{2.19}$$

where

$$\beta_m = \left(\frac{\mathrm{d}^m \beta}{\mathrm{d}\omega^m}\right)_{\omega=\omega_0} \qquad (m = 0, 1, 2, \ldots). \tag{2.20}$$

It can be seen that β_1 represents the pulse envelope group velocity by the relation $v_g = 1/\beta_1$ while β_2 (in $\mathrm{ps}^2/\mathrm{km}$) is responsible for GVD. The parameters β_1 and β_2 are related to the refractive index n and its derivatives through the relations

$$\beta_1 = \frac{1}{v_g} = \frac{n_g}{c} = \frac{1}{c}\left(n + \omega\frac{\mathrm{d}n}{\mathrm{d}\omega}\right), \tag{2.21}$$

$$\beta_2 = \frac{1}{c}\left(2\frac{\mathrm{d}n}{\mathrm{d}\omega} + \omega\frac{\mathrm{d}^2 n}{\mathrm{d}\omega^2}\right), \tag{2.22}$$

where n_g is the group index and is related to the refractive index $n(\omega)$ by

$$n_g = n + \omega\frac{\mathrm{d}n}{\mathrm{d}\omega}. \tag{2.23}$$

The dispersion parameter D (in $\mathrm{ps}/(\mathrm{km}\cdot\mathrm{nm})$) is related to β_2 by

$$D = -\frac{2\pi c}{\lambda^2}\beta_2. \tag{2.24}$$

D defined by Eq. (2.24) is a very useful engineering parameter. 1 $\mathrm{ps}/(\mathrm{km}\cdot\mathrm{nm})$ means that a pulse with 1 nm bandwidth will broaden 1 ps after it propagates 1 km.

To determine the dispersion from Eqs. (2.21)-(2.24), one needs to know how the refractive index of a material changes with the frequency, i.e. the form of $n(\omega)$. At the frequencies far from the material resonances, $n(\omega)$ is well approximated by the Sellmeier equation

$$n^2(\omega) = 1 + \sum_{j=1}^{m} \frac{B_j \omega_j^2}{\omega_j^2 - \omega^2}, \tag{2.25}$$

where ω_j is the material resonance frequency and B_j is the strength of jth resonance. The sum in Eq. (2.25) extends over all material resonances that contribute to the frequency range of interest. In the case of optical fibres, the parameters B_j and ω_j are obtained experimentally by fitting the measured dispersion curves [58] to Eq. (2.25) with $m = 3$ and depend on the core constituents. For bulk fused silica, these parameters are found to be [59] $B_1 = 0.6961663$, $B_2 = 0.4079426$,

$B_3 = 0.8974794$, $\lambda_1 = 0.0684043$ μm, $\lambda_2 = 0.1162414$ μm, and $\lambda_3 = 9.896161$ μm, where $\lambda_j = 2\pi c/\omega_j$ and c is the speed of light in vacuum.

Figure 2.10 shows the wavelength dependence of n, n_g and D in the range of 0.5-1.6 μm for fused silica using Eqs. (2.23)-(2.25). The most notable feature is that D vanishes at a wavelength of about 1.27 μm and changes sign for longer wavelengths. This wavelength is referred to as the zero-dispersion wavelength (ZDW) λ_D. The region where $D < 0$ is called normal dispersion regime; and the region where $D > 0$ is called anomalous dispersion regime. However, it is worth mention that the dispersive effects do not disappear completely at $D = 0$. Pulse propagation near this wavelength requires inclusion of the cubic term in Eq. (2.19). The coefficient β_3 appearing in that term is called the third-order dispersion (TOD) parameter. TOD is one of the most important effects resulting in soliton-related nonlinear phenomena.

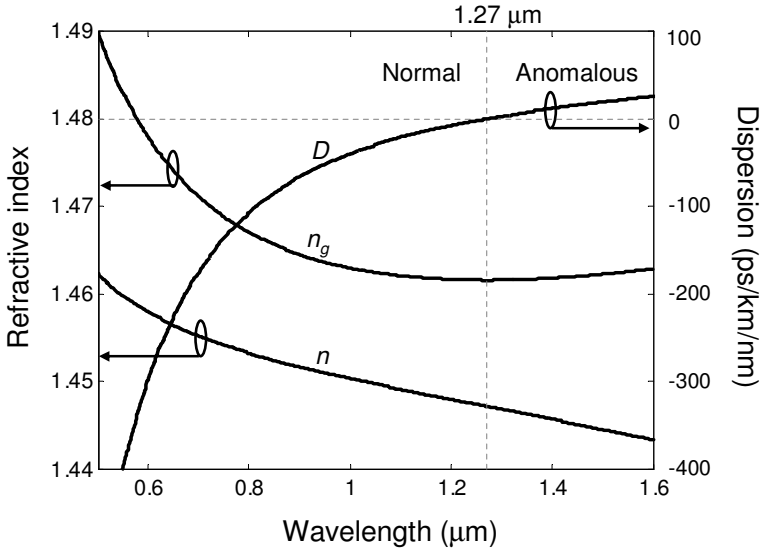

Figure 2.10: Variation of refractive index n, group index n_g and dispersion D with wavelength for fused silica.

It should be stressed that the curves shown in Fig. 2.10 are for pure bulk fused silica. The dispersion of actual glass fibres normally deviates from that shown in this figure for the following two reasons. First, the fibre core may have small amounts of dopants such as GeO_2 and P_2O_5. Equation (2.25) in that case should be used with parameters appropriate to the amount of doping levels. As we will see later in PCFs, this does not exist since they are normally made from

pure silica (see Section 2.2.1). Second, because of dielectric waveguiding, the mode index is slightly lower than the material index of the core. This results in a waveguide contribution that is also wavelength dependent and must be "added" to the material dispersion contribution to obtain the total dispersion. Figure 2.11 shows the measured total dispersion of a conventional single-mode fibre [8]. It can be seen that the main effect of the waveguide contribution is to shift λ_D slightly toward a longer wavelength at about 1.31 μm.

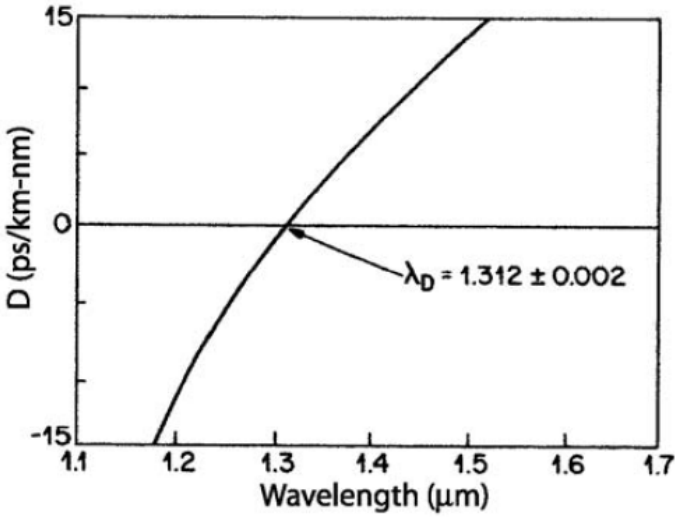

Figure 2.11: Measured variation of dispersion parameter D with wavelength for a conventional single-mode fibre (Ref. [8] Chapter 1).

It is obvious that the waveguide dispersion depends on the waveguide structure. For optical fibres, the structure is mainly determined by fibre-design parameters: the core radius a and the relative core-cladding index difference [7]

$$\Delta = \frac{(n_{\mathrm{co}} - n_{\mathrm{cl}})}{n_{\mathrm{co}}}. \tag{2.26}$$

Both can be controlled during the fabrication process described in Section 2.1.4. This feature can be used to shift the ZDW to the desired wavelength. However, in conventional fibres, a high dopant level will result in some disadvantages. Firstly, a high dopant level means more Si atoms are replaced by Ge atoms. Ge atoms are bigger than Si atoms, so they will deform the glass structure so much that fibres are very easily broken. Figure 2.12 shows how dopants deform the structure of silica glass schematically. Secondly, a high dopant level will induce high

losses [60]. Thirdly, a high dopant level is very likely to make fibres support multimode. Therefore the adjustment ability of dopants to the relative core-cladding index difference is limited. As mentioned in Section 2.1.1, to maintain high power in the fibre core while staying single mode the V value must be close to but not greater than 2.405. This limits the adjustment of the core radius. It can be shown that the waveguide dispersion can only shift ZDW towards longer wavelengths in a conventional single-mode fibre [60]. For more sophisticated dispersion control in conventional fibres, one usually needs to introduce extra degrees of freedom into fibre design, such as extra layers in the cladding. For example, a low loss single-mode fibre with flat dispersion over the 1.28-1.65 μm wavelength range needed four (quadruple-clad) cladding layers [60]. This indicates that dispersion control is limited or complicated in conventional fibres. In later discussion, it will be seen that the dispersion is controllable over a wide range in a easier way in PCFs, which is very important for nonlinear processes such as four-wave mixing or modulation instability (FWM or MI) and supercontinuum (SC) generation (see Chapters 3 and 4).

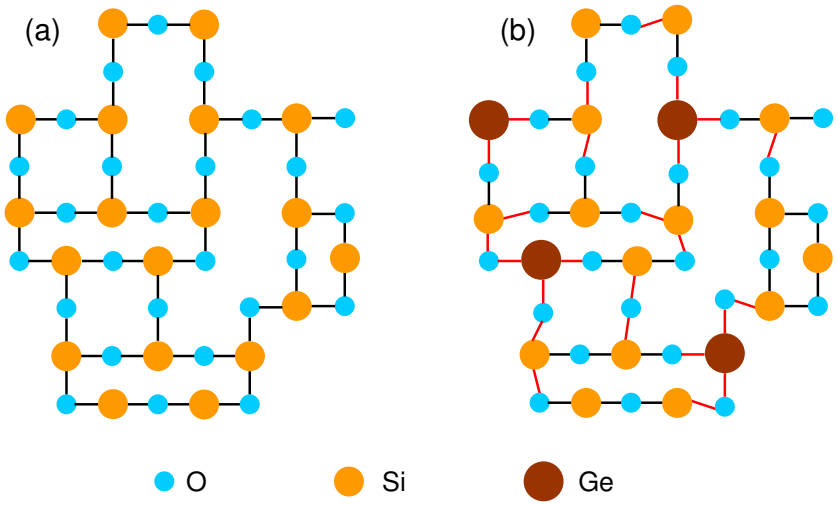

Figure 2.12: Schematic diagram showing the effect of dopants to the structure of silica glass. (a) Original structure of silica glass, (b) structure of silica glass doped with Ge. Red lines shows the bonds affected directly by the dopant. Other bonds may also be affected.

The waveguide dispersion contribution is not only able to shift the dispersion for the fundamental mode, but also able to result in dispersion for the same wave-

length at different modes. This is referred to as intermodal dispersion. In most cases, intermodal dispersion will degrade the performances of fibres. For this reason, most fibres are designed to only support the fundamental mode. However in some particular situations, intermodal dispersion is useful. For example, the third-order harmonic generation in fibres can only be realized by the phase matching between the higher-order mode of the third-order frequency and the fundamental mode of the fundamental frequency [61]-[65].

As mentioned in Section 2.1.1, even a single-mode fibre is not strictly single mode since there are two orthogonal polarisation modes for each mode shape. In birefringent fibres, the propagation constants (i.e. mode indices) of the two polarisation modes are slightly different. If an input pulse excites both polarisation components, the two components travel along the fibre at different speeds because of their different group velocities. This phenomenon is called polarisation mode dispersion (PMD).

Fibre dispersion is extremely important to nonlinear effects in optical fibres. As we will see in Section 3.4, phase matching for efficient FWM in optical fibres is absolutely determined by fibre dispersion. To form solitons, fibres have to be designed to exhibit anomalous dispersion at the wavelength of interest (see Section 3.5). As mentioned above, GVD means that pulses at different wavelengths propagate at different speeds inside a fibre because of a mismatch in their group velocities. This feature leads to a walk-off effect that plays an important role in the nonlinear processes involving two or more optical pulses at different central wavelengths. The nonlinear interaction between two optical pulses ceases to occur when the faster moving pulse completely walks through the slower moving pulse. This feature is governed by the walk-off parameter d_{12} defined as

$$d_{12} = \beta_1(\lambda_1) - \beta_1(\lambda_2) = \frac{1}{v_g(\lambda_1)} - \frac{1}{v_g(\lambda_2)}, \tag{2.27}$$

where λ_1 and λ_2 are the central wavelengths of the two pulses and β_1 at these wavelengths is evaluated using Eq. (2.21). For pulses of width T_0 (defined as where the intensity falls to $1/e^2$ of the maximum), one can define the walk-off length L_W by the relation

$$L_W = T_0/|d_{12}|. \tag{2.28}$$

Figure 2.13 shows the variation of d_{12} with λ_1 for fused silica using Eq. (2.27)

with $\lambda_2 = 0.8$ μm. The negative time scale in Fig. 2.13 means that the pulses at the wavelength range of 0.9-1.6 μm travel faster than the pulse at 0.8 μm. For example, if a pulse at $\lambda_1 = 1.3$ μm copropagates with the pulse at 0.8 μm, it will separate from the shorter-wavelength pulse at a rate of about 20 ps/m. This corresponds to a walk-off length L_W of only 50 cm for $T_0 = 10$ ps. The group-velocity mismatch plays an important role for nonlinear effects such as cross-phase modulation (XPM) and FWM. It will be seen later that the short wavelength edge of SC generation in PCFs is mainly determined by this walk-off effect (see Chapter 4.2).

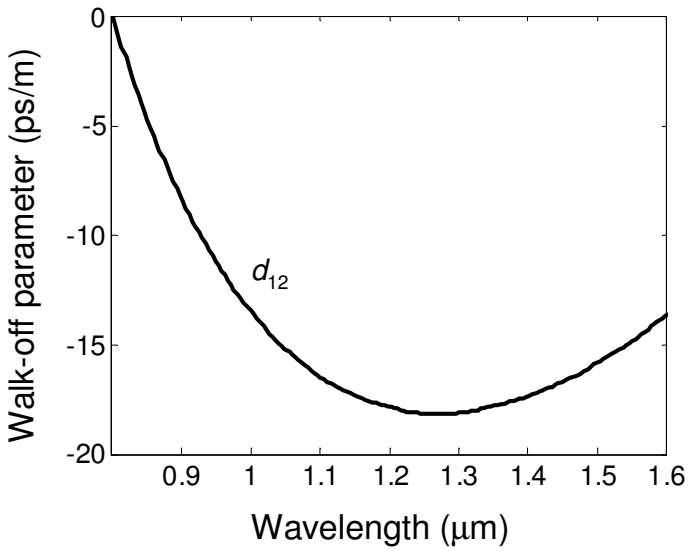

Figure 2.13: Variation of d_{12} with wavelength for fused silica.

2.1.6 Fibre Nonlinearity [8]

Generally speaking, the response of any dielectric to light becomes nonlinear for intense electromagnetic fields, and optical fibres are no exception. The typical fibre material silica has a relatively small nonlinearity, but the fibre geometrical structure and guiding properties, resulting in a very small cross section and a long interaction length, make nonlinear effects in fibres enhanced and very important to many applications. On a fundamental level, the nonlinear response originates from anharmonic motion of bound electrons under the influence of an applied field. In the case of intense fields, the induced polarisation $\mathbf{P}$ from the electric

dipoles is not linearly related to the electric filed **E**, but satisfies the more general relation

$$\mathbf{P} = \varepsilon_0 \left(\chi^{(1)} \cdot \mathbf{E} + \chi^{(2)} : \mathbf{EE} + \chi^{(3)} \vdots \mathbf{EEE} + \cdots \right), \tag{2.29}$$

where ε_0 is the vacuum permittivity and $\chi^{(j)}$ $(j = 1, 2, \cdots)$ is jth order susceptibility. To account for the effect of the polarisation of light, $\chi^{(j)}$ is a tensor of rank $j+1$. The linear susceptibility $\chi^{(1)}$ effects dominate through the reflective index n and the attenuation coefficient α. The second-order susceptibility $\chi^{(2)}$ is responsible for such nonlinear effects as second-harmonic generation and sum-frequency mixing. However, because of the inversion symmetry of silica glass, $\chi^{(2)}$ vanishes for silica fibres. As a result, optical fibres made from silica glass normally do not exhibit second-order nonlinear effects. Therefore the lowest-order nonlinear effects in optical fibres are from the third-order susceptibility $\chi^{(3)}$ which is responsible for nonlinear processes such as third-order harmonic generation, four-wave mixing, and nonlinear refraction. To study nonlinear effects in silica fibres, it is more useful to write Eq. (2.29) as

$$P_i = \varepsilon_0 \left(\sum_{j=1}^{3} \chi_{ij}^{(1)} E_j + \sum_{j=1}^{3} \sum_{k=1}^{3} \sum_{l=1}^{3} \chi_{ijkl}^{(3)} E_j E_k E_l \right), \tag{2.30}$$

where the subscripts $i, j, k, l = 1, 2, 3$ denote the x, y, z components of a vector. In Eq. (2.30), the higher-order terms have been neglected .

As a fourth-rank tensor, $\chi^{(3)}$ is described in terms of $3^4 = 81$ separate elements, which makes the expression of P_i very complicated. Fortunately, for materials possessing a higher degree of spatial symmetry, the number of independent elements is very much reduced. For silica glass, there are only three independent elements. The nonlinear susceptibility $\chi^{(3)}$ can be expressed as [66]

$$\chi_{ijkl}^{(3)} = \chi_{1122}^{(3)} \delta_{ij} \delta_{kl} + \chi_{1212}^{(3)} \delta_{ik} \delta_{jl} + \chi_{1221}^{(3)} \delta_{il} \delta_{jk}, \tag{2.31}$$

where δ_{ij} is the Kronecker delta function defined such that $\delta_{ij} = 1$ when $i = j$ and zero otherwise. More specifically, only E_x and E_y are of interest for silica fibres. Therefore it is useful to write Eq. (2.31) as

$$\chi_{1111}^{(3)} = \chi_{2222}^{(3)} = \chi_{1122}^{(3)} + \chi_{1212}^{(3)} + \chi_{1221}^{(3)}, \tag{2.32}$$

or in x and y subscripts,

$$\chi^{(3)}_{xxxx} = \chi^{(3)}_{yyyy} = \chi^{(3)}_{xxyy} + \chi^{(3)}_{xyxy} + \chi^{(3)}_{xyyx}. \tag{2.33}$$

Using Eqs. (2.30) and (2.33), we can quantitatively study most of the nonlinear effects in silica fibres. A commonly used parameter to value the fibre nonlinearity is the effective nonlinear coefficient [8] defined by

$$\gamma = \frac{2\pi n_2}{\lambda A_{\text{eff}}}, \tag{2.34}$$

where A_{eff} is the effective mode area defined by Eq. (2.9) (see Section 2.1.1), λ is the pump wavelength in free space and n_2 is the nonlinear refractive index which can be derived from Eqs. (2.30) and (2.33). In the scalar approximation, n_2 has the form of

$$n_2 = \frac{3}{8n}\text{Re}(\chi^{(3)}_{xxxx}), \tag{2.35}$$

where n is the refractive index mentioned above. For silica, $n_2 = 2\times10^{-20}$ m^2/W.

2.2 Guidance Mechanisms for Photonic Crystal Fibres

Like conventional fibres, PCFs contain the two-layer structure: a core and a cladding layer surrounding the core (see Fig. 2.14). The difference is that the cladding layer has a structure of two-dimensional photonic crystal (PC) [67]—material that has a periodic modulation of the refractive index on the scale of the optical wavelength. The periodic modulation of the refractive index is realized by embedding inclusions periodically in a background matrix. The core is composed of the same material as the matrix material and can be regarded as a defect in the periodic structure of the cladding. This type of refractive index distribution extends along the entire length of the fibre. If the core (matrix) material has a higher index than the inclusions, light can be guided in the core by a form of total internal reflection (TIR). Such fibres are referred to as TIR PCFs. By contrast, if the refractive index of the core (matrix) material is lower than that of the inclusions in the cladding, guided modes still exist at certain frequencies. These correspond to photonic band gaps formed in the cladding. Such fibres are

referred to as photonic band gap fibres (PBGFs).

2.2.1 Total Internal Reflection Photonic Crystal Fibres

TIR PCFs are also known as index-guiding PCFs. The most typical TIR PCFs have a solid core (often fabricated from pure silica) surrounded by a cladding with a regular periodic array of air holes. These air holes make the effective refractive index of the cladding region lower than pure silica, so light is confined to the solid core area, which has a relatively higher refractive index [23]. A schematic cross section of such a PCF cross is given in Fig. 2.14, where the two parameters which characterize the dimensions of PCFs are the hole-to-hole pitch Λ and the hole diameter d.

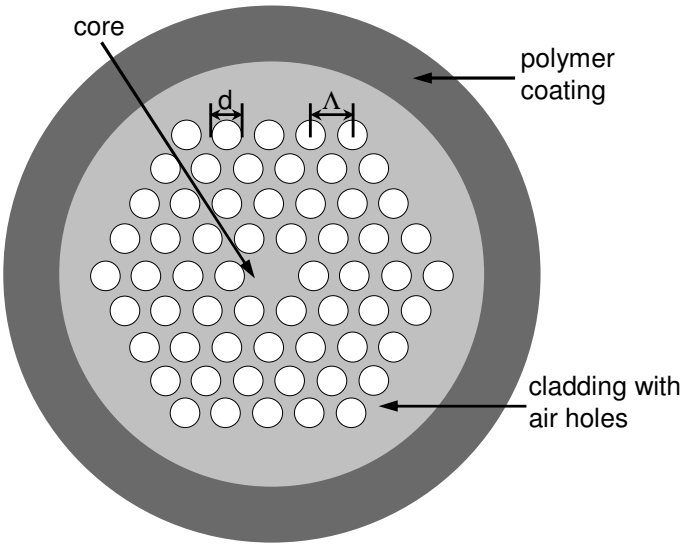

Figure 2.14: Schematic of a PCF cross section. The light grey areas are silica, the white areas are air holes and the dark grey areas are polymer coating. Λ is the hole-to-hole pitch and d is the hole diameter.

From the guidance mechanism point of view, TIR PCFs guide light by TIR, as conventional fibres do. Thus it is convenient to establish an effective refractive index model to analyse the behaviors and characteristics of such PCFs since many concepts can be borrowed directly from conventional fibres. In the effective refractive index model, the effective refractive index of the cladding n_{eff} is defined as the highest modal index of modes propagating in the cladding structure [24]. As an example, this model successfully analysed the endlessly single-mode (ESM)

transmission property of PCFs by simply replacing the core radius a and the cladding index n_{cl} in Eq. (2.2) by the hole to hole pitch Λ and the effective cladding index n_{eff}, respectively [24] (see Section 2.4.1). However, this does not mean that TIR PCFs are just another kind of conventional fibre. As discussed in Section 2.1.5, the only parameters which could be changed for conventional fibres are the core radius and the dopant concentration. Further, neither the core radius nor the dopant concentration can be changed too much. The situation in TIR PCFs, however, is very different. There are three parameters (Strictly only two of them are independent for a regular fibre unless more air holes are omitted), known as hole-to-hole pitch Λ, air hole diameter d and core radius, ready to be controlled. The values of d/Λ and Λ, which are responsible for the air-filling ratio as well as the effective cladding index, can be adjusted over a large range. More degrees of design freedom enable TIR PCFs to exhibit some unique characteristics which are not obtainable in conventional fibres. For example, the cladding structure is highly dispersive and the waveguide dispersion of PCFs can be highly anomalous in the wavelength range shorter than 1.27 μm (see Section 2.4).

2.2.2 Photonic Band Gap Fibres

Photonic band gap fibres (PBGFs) are so called because the cladding with PC structure can exhibit photonic band gaps (PBG) at optical frequencies [67]. Light whose frequency falls into the band gaps would be totally trapped in the core even when the refractive index of the core is lower than that of the cladding. This low-index core ensures that there is no possibility of waveguiding by TIR. The light guiding can only be achieved by the PBG property. The first PBGF was demonstrated in 1998 [27], where an extra hole was introduced to the solid core area to lower the effective index of the core. In PBG guidance mechanism, hollow core guidance becomes possible [28]. Single-mode hollow core waveguides have a multitude of potential applications such as ultrahigh-power transmission, guiding of atoms and particles and gas-based nonlinear optics [31].

PBGFs seem obviously interesting because of the new guidance mechanism, however TIR PCFs also display unique and useful properties. This thesis will focus on TIR PCFs. Thus, in the following discussion of this thesis, the term PCFs refers to silica TIR PCFs unless noted otherwise.

2.3 Fabrication of Photonic Crystal Fibres

This section gives a brief introduction to the fabrication of PCFs in a fibre drawing tower and post-processing of PCFs in stock.

2.3.1 Stacking Preforms and Fibre Drawing

The fabrication of PCFs derives from the fabrication technique of conventional fibres (see Section 2.1.4), but with some differences. A PCF is made by reducing a relatively large, easily produced macro-structure, down to a micro-structure with features comparable in size to the wavelength of light. A "Stack-and-draw" technique is the most commonly utilized technique to fabricate PCFs, schematically illustrated in Fig. 2.15.

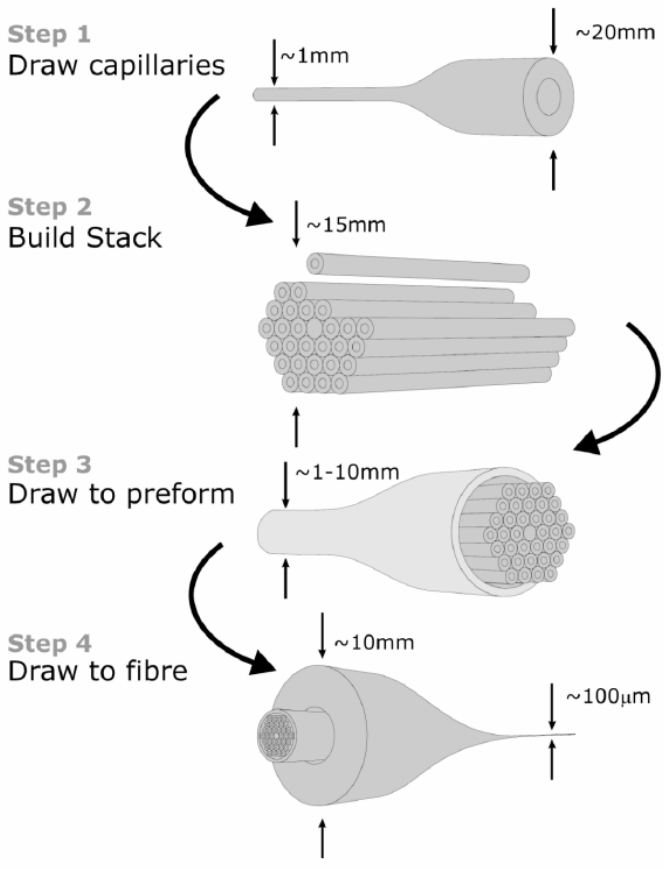

Figure 2.15: Schematic diagram of PCF fabrication process [68].

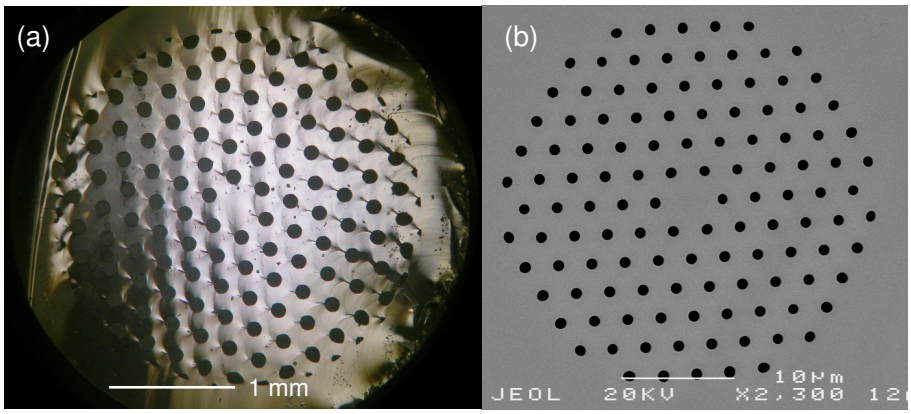

Figure 2.16: (a) Typical microscope photograph for the preform. (b) Typical SEM image for the final PCF drawn from the preform shown in (a).

Four stages are involved in the process. In the first stage, a commercially available silica glass tube and a silica rod with a outer diameter (OD) of about 20 mm are drawn to capillaries or rods with diameter about 1 mm using the drawing tower (Fig. 2.9). The capillaries and rod are cut to suitable lengths. In the second stage, the capillaries and rods are stacked manually in a hexagonal array, normally with one rod placed in the center surrounded by capillaries, forming the core and the two-dimensional PC structured cladding of the final PCF. The nominal OD of the stack is normally about 15 mm depending on the inter diameter (ID) of the selected silica tube in the next stage. In the third stage, such a prepared stack is put into a silica tube with an OD of $\sim$20 mm to hold the stack together. The stack is then fused at one end and brought to the fibre drawing tower to be drawn down to a preform (Fig. 2.16(a)). The preform has an OD of 1-10 mm which should be able to fit the jacket tube in the final stage. During the preform drawing process, a vacuum is applied between the capillaries to collapse the air-space between them. The ambient pressure inside the capillaries protects them from collapse. As the result, the preform is composed of air-holes arranged in a regular hexagonal array and a solid core in the centre. In the fourth stage, a preform is placed into a jacket tube and then drawn down to the final PCF. The size of the holes is controlled through an applied pressure. The core diameter is controlled through the feeding rate and drawing speed (see Section 2.1.4 and Fig. 2.9). In order to make the PCF compatible to most commercial fibre components such as fibre adapters, the OD of the final fibre is normally designed to be 125 μm without coating and 250 μm with coating (Fig. 2.16(b)). The desired

fibre OD, fibre dispersion (i.e. d/Λ and Λ, see Fig. 2.14 and Section 2.4.2) and the layers of cladding holes determine the selection of silica tubes and the size of the capillaries.

2.3.2 Post-Processing: Tapering and Inflation

As mentioned above, PCFs have several degrees of design freedom. The hole-to-hole pitch Λ and d/Λ ratio are the two parameters that can be modified most easily. Not only can the modification be realized during fabrication process described in Section 2.3.1, but also it can be performed on PCFs in stock through post-processing techniques described in this section.

There are two types of post-processing techniques called tapering [69] and inflation [70], both of which are realized on a taper rig (Fig. 2.17). During the processes, the fibre is stretched while a part of it is heated by a small flame. Both the burner stage and elongation stages are operated by motors which are controlled through a computer. To decrease the core size and the air-filling fraction whilst maintaining the air holes open, a taper is normally processed in a fast and cold way, with a cold flame to minimize the rate of hole collapse, and stretching as quickly as possible to minimize the processing time.

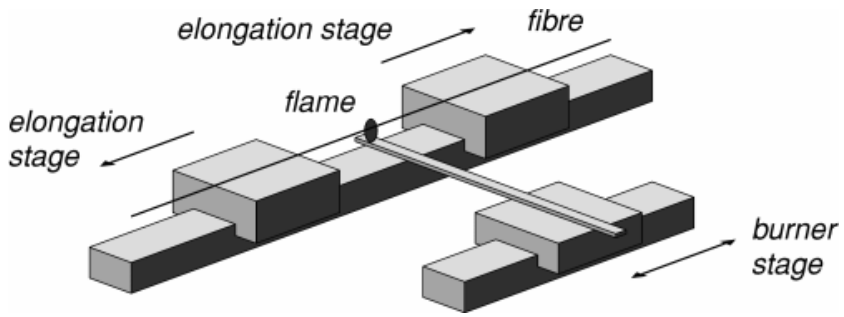

Figure 2.17: Schematic for tapering or inflation of PCF on a taper rig [71].

To increase the air-filling fraction, an inflation process is required to expand the holes. The parameters are actually the opposite of those needed to taper with little hole collapse. In contrast, inflation is normally processed in a slow and hot way, using a hot flame for rapid hole inflation and stretching slowly to increase the processing time. Normally this method would result in significant hole collapse, so a nitrogen pressure should be applied to the holes first. Whether

a hole in fused silica shrinks or expands when the fibre is heated depends only on the pressure difference between the excess air pressure P in the hole and the effective pressure P_{st} due to the surface tension γ_s of the glass

$$P_{\mathrm{st}} = 2\gamma_s/d, \tag{2.36}$$

where d is the hole diameter. If $P > P_{\mathrm{st}}$ then the hole will expand instead of collapsing. Given the commonly-quoted value of $\gamma_s = 0.3$ J/m^2 for silica, Eq. (2.36) is conveniently expressed in terms of pressure in bar and hole diameter in μm:

$$P_{\mathrm{st}}\,(\mathrm{bar}) = 6/d\,(\mu\mathrm{m}). \tag{2.37}$$

So an excess pressure of 6 bar is needed to keep a 1 μm hole in (unstable) equilibrium. Although the viscosity of silica glass does change rapidly with temperature close to the softening point of 1700 °C, the surface tension varies little with temperature. Further, different pressures can control the amount of inflation when the flame temperature and other parameters are kept constant. In practical applications, a tapering process may be needed to taper the inflated fibre down to achieve a desired high nonlinear PCF with the expected dispersion property (see Section 4.3).

In general a structure resulting from the process discussed above is called taper waist which is connected to untreated fibre at the ends by transitions. The insertion loss is a consideration for such structures. It turns out that as long as the adiabaticity condition [72] is satisfied, the loss will be very small. Here this condition is easy to fulfil by making the transition gradual enough. In devices fabricated for my experiment the loss is as low as 0.12 dB at 1550 nm (see Section 4.3).

These powerful post-processing techniques can form PCF taper transitions and waists of almost any shape and size with the waist core diameter down to 200 nm. A typical device is given in Fig. 2.18. The limitation of these techniques is that the produced fibre length is only 15 cm due to the limited length of the taper rig. Nevertheless they provide a convenient and useful method to tailor the dispersion of PCFs in cases where we do not need a long piece of fibre.

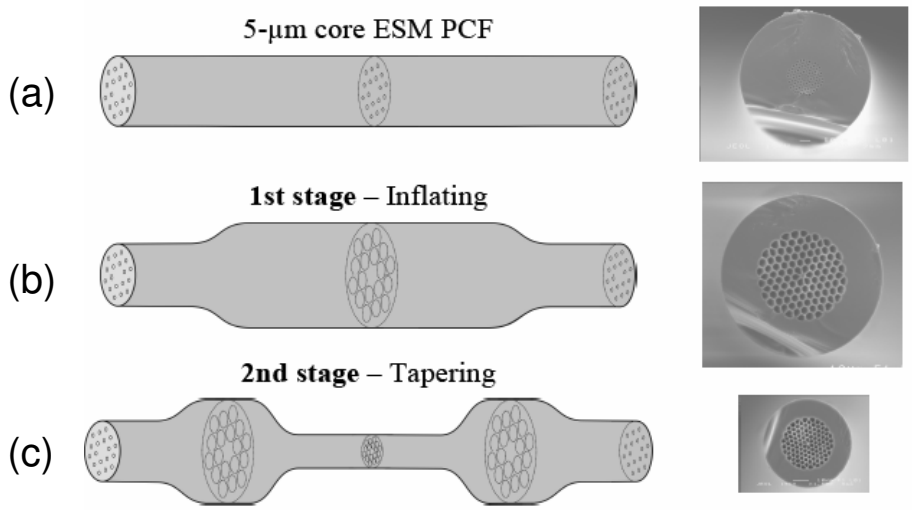

Figure 2.18: Fibre inflation and tapering process to produce a 2 μm core PCF with large air holes, connected at both ends to 5 μm PCF pigtails with small air holes [70]. (a) initial PCF before processing, (b) inflated fibre, (c) taper waist. All SEM images on the right are to the same scale.

2.4 Characteristics of Photonic Crystal Fibres

PCFs have a lot of unique characteristics because of the novel structure. This section will present some important properties which are tightly related to nonlinear effects in PCFs. They are ESM transmission, highly controllable group-velocity dispersion (GVD), high nonlinearity and birefringence.

2.4.1 Endlessly Single-Mode Transmission

One of the most striking features of PCFs is the ESM behavior, which was presented in Ref. [24] as soon as the first PCF was fabricated [23]. Qualitatively, this ESM property can be understood from the effective-index model mentioned in Section 2.2.1. In the regime of the effective-index model, the V parameter in Eq. (2.2) can be rewritten for PCFs:

$$V_{\text{eff}} = \frac{2\pi\Lambda}{\lambda}(n_{\text{co}}^2 - n_{\text{eff}}^2)^{1/2}, \tag{2.38}$$

which determines whether the PCF is single mode or not. In conventional fibres, V defined by Eq. (2.2) will be infinite when $\lambda \to 0$, which results in the multimode transmission at short wavelengths. In PCFs, however, the effective cladding index

n_{eff} is strongly wavelength dependent. At shorter wavelengths, the light becomes more concentrated in the silica region and avoids the holes, which increases the effective cladding index n_{eff}. This dispersion effect in the PC cladding is much stronger than that in the core. It counteracts the decrease of λ in the denominator in Eq. (2.38) and removes the strong dependence of V on wavelength and so extends the single-mode range to short wavelengths. In Fig. 2.19, the solid curves show the variation of V_{eff} with Λ/λ for various relative hole diameters d/λ for TIR PCFs, and the dotted curve indicates the behavior of a conventional fibre with fixed $(n_{\text{co}}^2 - n_{\text{cl}}^2)$. It can be seen that at short wavelengths V tends to be constant in TIR PCFs instead of infinite in conventional fibres. Thus it is possible to keep V less than the second order mode cutoff value V_c for all wavelengths as long as d/Λ is properly designed. Numerical calculations of the propagation constant, second-mode cutoff for PCFs, and also the effective index of the cladding shows that V_c, the V-value at which the second mode is cut off in a PCF, is almost a constant about 4.1 for d/Λ in the range of 0.5-0.65 (see Fig. 2.20). For d/Λ less than about 0.4, the second mode is never guided even at infinite frequency; V is always less than V_c and the PCF is endlessly single-mode [73].

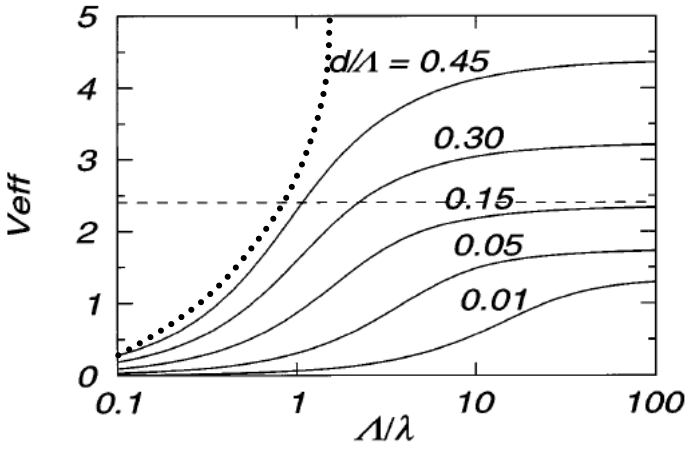

Figure 2.19: Variation of V_{eff} with Λ/λ for various relative hole diameters d/λ. The dashed line marks $V_{\text{eff}} = 2.405$, the cutoff V value for a conventional fibre [24]. The dotted curve schematically indicates the behavior of a conventional fibre with fixed $(n_{\text{co}}^2 - n_{\text{cl}}^2)$.

As we all know, $V_c = 2.405$ for conventional fibres. It is obvious that 4.1, the value of V_c for PCFs is a lot greater than 2.405. Nevertheless, the PCF is after all a very different waveguide to a conventional fibre, and it is not obvious

that a quantitative analogy exists between them. Investigation [73] indicates that $V_c = 4.1$ because the effective core radius of the PCF is simply taken to equal Λ (see Eq. (2.38)). Naive substitution of Λ as PCF core radius into Eq. (2.2) to get Eq. (2.38) can give useful information, but this may neglect the fact that the boundaries of the PCFs core are not well defined. Therefore the core radius of PCFs can be any given fraction of Λ. Study [73] shows that taking the core radius $a = 0.625\Lambda$ can not only make it possible to approximate some modal quantities, such as the propagation constant, through the analogy between PCFs and conventional fibres, but also make $V_c = 2.55$ which is close to 2.405.

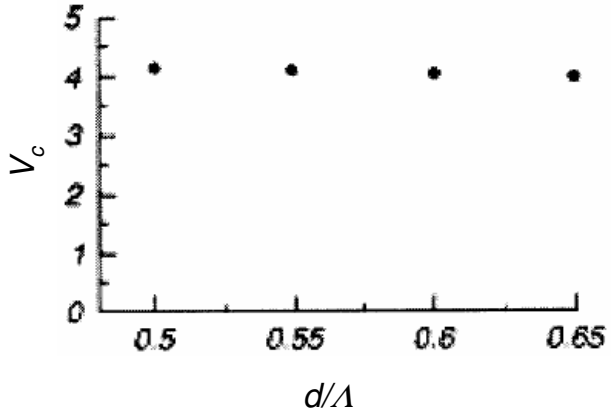

Figure 2.20: A plot of V-value at second mode cutoff versus d/Λ for PCFs [73].

Ideally, PCFs could be designed to guide all wavelengths of light in a single-mode. From the above discussion, it can be seen that larger holes make the fibre likely to be multimode whilst smaller holes make single-mode guidance more likely. However, smaller holes mean the decrease in effective index difference, which makes the fibre more susceptible to bend loss. The bend-loss edge limits the ESM range both at short wavelengths and at long wavelengths. Thus, the ESM PCFs actually have a range of wavelengths for which they guide efficiently (e.g. from 337 to 1550 nm [24]). Although the bend loss limits the single-mode range of PCFs, the remarkably wide single-mode wavelength range is good enough for many applications such as single-mode supercontinuum (SC) generation [43].

2.4.2 Control of Dispersion

Fibre dispersion plays an important role in nonlinear processes whether in conventional fibres or in PCFs. As we discussed in Section 2.1.5, dispersion does not only directly determine the efficiencies of some nonlinear effects through phase-matching condition (FWM, for example), but also determines if the nonlinear interaction between two or more pulses at different wavelengths can occur or not through GVD (XPM and FWM, for example). Therefore it is very important to control fibre dispersion. In single-mode fibres without birefringence, the overall GVD has two contributions known as material dispersion and waveguide dispersion (see Section 2.1.5). Because this thesis mostly considers silica TIR PCFs, material dispersion offers fixed contribution to GVD, the same as in silica conventional fibres. The unusual dispersion properties of PCFs mainly derive from the highly controllable waveguide dispersion. We have discussed a lot about the dispersion control for conventional fibres in Section 2.1.5. The degrees of freedom are found to be limited. For PCFs, however, the control of dispersion is more flexible and easier. By adjusting the size of the hole-to-hole pitch, Λ, and the hole diameter, d, one can control the air-filling ratio easily to change the core-cladding index difference and the core size so that desired dispersion is achieved.

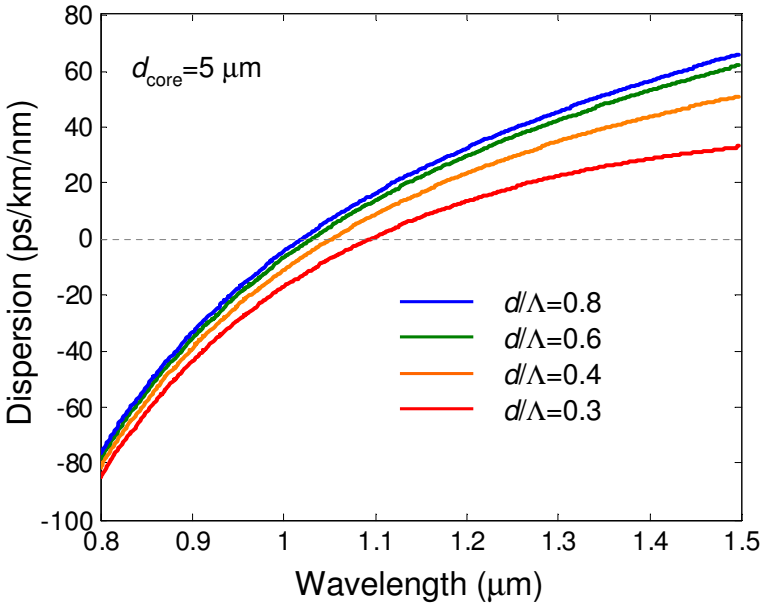

Figure 2.21: Calculated GVD for PCFs with different d/Λ but having a fixed core diameter $d_{\text{core}} = 5$ μm.

To investigate how the GVD of PCFs changes with d/Λ, the GVD curves of the fundamental mode are calculated for PCFs with different d/Λ but having a fixed core diameter d_{core} =5 μm using an empirical relation [74]. The results are plotted in Fig. 2.21. It shows that the zero-dispersion wavelength (ZDW) of a PCF can be shifted to the wavelengths shorter than 1.27 μm, the ZDW of bulk silica. When the holes get bigger, the ZDW is shifted to further shorter wavelengths. However, the ZDW shift is not unlimited and becomes slower with the increasing of d/Λ. This can be understood from the fact that the ZDW shift is due to the large waveguide dispersion contribution to the total GVD. Large air holes increase the core-cladding index step resulting in a large anomalous waveguide dispersion, which can cancel the normal material dispersion at $\lambda < 1.27$ μm or even overcome it to yield anomalous net dispersion there [26]. However, when the holes get big enough (d/Λ =0.95, for example), making the holes further bigger will not bring significant change to the core-cladding index step. Therefore, the waveguide dispersion induced by big holes can not further change the overall GVD. If we want to shift the ZDW of PCFs to even shorter wavelengths, we need to consider another degree of freedom–the fibre core diameter.

To study how the GVD of PCFs varies with the fibre core diameter d_{core}, the GVD curves of the fundamental mode are calculated for PCFs with different core diameters but having a fixed d/Λ and plotted in Fig. 2.22. It can be seen that when d/Λ is fixed, decreasing d_{core} can also shift the ZDW to shorter wavelengths. We can understand this from the discussion about mode size in Section 2.1.1. According to Eq. (2.38), when fibre core becomes smaller whilst core-cladding index difference keeps constant, the V_{eff} will be smaller. As a result, the fibre mode will expand more into the cladding (see Fig. 2.4(a)). This will lead to a large anomalous waveguide dispersion at $\lambda < 1.27$ μm as well. However, when d/Λ is not very big, d/Λ =0.4, for example, as shown in Fig. 2.22(a), simply decreasing d_{core} can not shift the ZDW further once $d_{\text{core}} < 3$ μm. Instead, a second ZDW appears at a longer wavelength. If we want to achieve an even shorter ZDW, we need to increase d/Λ when decreasing d_{core}. Figure 2.22(b) shows that the ZDW can be as short as 680 nm when $d/\Lambda = 0.8$ and d_{core} =1.5 μm. Such PCFs with high d/Λ and small d_{core} are normally referred to as highly nonlinear PCFs which have been widely used for visible SC generation [36][40]. A major concern about such fibres is whether they are single-mode fibres since ESM transmission requires $d/\Lambda \leq 0.4$ (see Section 2.4.1). Theoretically, calculations of modes need

to be conducted to see if such highly nonlinear PCFs support higher-order modes. In practice, the core is so small that higher-order modes are not excited easily. Experimentally, a strictly single-mode PCF with ZDW as short as 700 nm has been achieved [29].

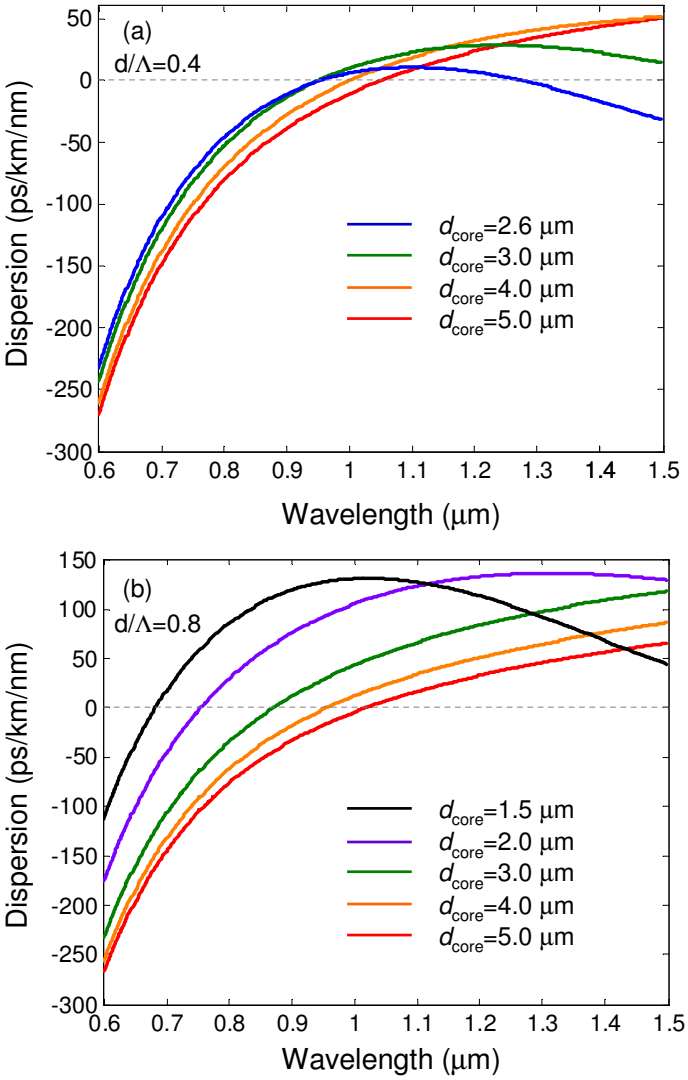

Figure 2.22: Calculated GVD for PCFs with different core diameters but having a fixed d/Λ. (a) $d/\Lambda = 0.4$, (b) $d/\Lambda = 0.8$.

The discussion above shows that the GVD of PCFs is controllable over the wavelength range of 0.6-1.5 μm, which is the most interesting region for silica glass fibres. Both d/Λ and d_{core} are easy to control during fabrication (see Section 2.3) or through the inflation and tapering techniques (see Section 2.3.2). The most

striking feature is that the ZDW is tailorable from 1.04 to 1.10 μm whilst the fibre keeps ESM transmission (see Fig. 2.21 and Fig. 2.22(a)). As high-quality compact microchip lasers and fibre lasers operating at around 1.064 μm are commercially available, SC and wavelength conversion have been demonstrated in such a set of PCFs with the ZDW from 1.04 to 1.10 μm [43]. Figure 2.23 gives the measured GVD curves for several typical PCFs demonstrated in Ref. [43].

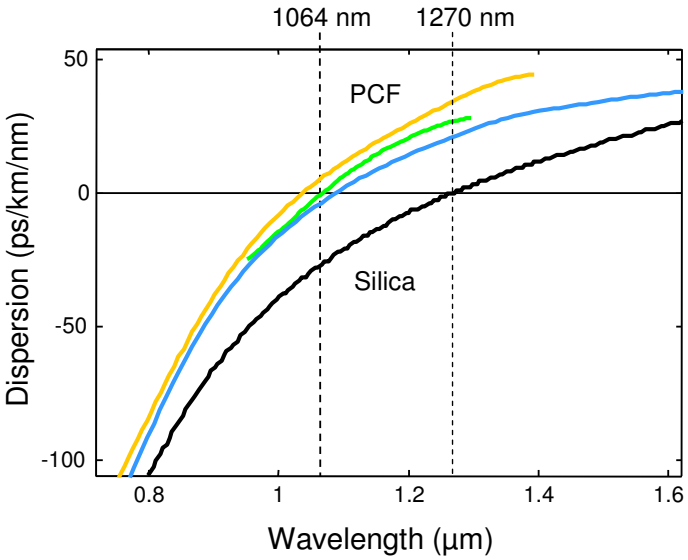

Figure 2.23: Orange, green and blue curves are the measured overall GVD for three different PCFs [43]. Black curve is the GVD for pure silica.

2.4.3 High Nonlinearity

PCFs are widely used for nonlinear processes. Although silica is not an intrinsically highly nonlinear medium, silica-based conventional fibres improve nonlinearity by long interaction lengths and confining the intense light in a small core. A figure of merit for the efficiency of a nonlinear process in bulk media is the product $I_0 L_{\text{eff}}$ where I_0 is the optical intensity and L_{eff} is the effective length of the interaction region [8]. If light is focused to a spot of radius w_0, then $I_0 = P_0/(\pi w_0^2)$, where P_0 is the incident optical power. Clearly, I_0 can be increased by focusing the light tightly to reduce w_0. However, this results in a smaller L_{eff} because the length of the focal region decreases with tight focusing. In bulk media, L_{eff} is determined by the Rayleigh length z_R, which is defined

as the distance along the propagation direction of a beam from the waist to the place where the beam radius is increased by a factor of $\sqrt{2}$ (see Fig. 2.24). For a circular beam, this means that the mode area is doubled at this point. For a Gaussian beam, $z_R = \pi w_0^2/\lambda$, $L_{\text{eff}} = 2z_R = 2\pi w_0^2/\lambda$, where λ is the wavelength in the medium. We can see the product

$$(I_0 L_{\text{eff}})_{\text{bulk}} = \frac{P_0}{\pi w_0^2}\frac{2\pi w_0^2}{\lambda} = \frac{2P_0}{\lambda} \tag{2.39}$$

is independent of the spot size w_0.

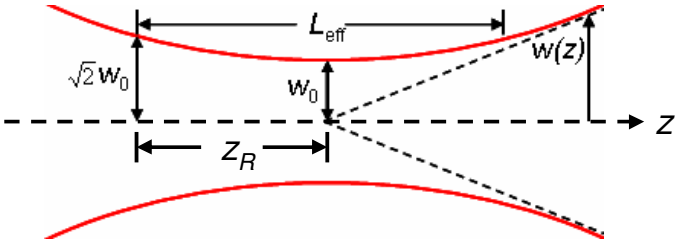

Figure 2.24: Rayleigh length and the effective interaction length in bulk media.

In single-mode fibres, spot size w_0 is determined by the core radius. Furthermore, because of dielectric waveguiding, the same spot size can be maintained over the entire fibre length L. In this case, the interaction length L_{eff} is limited by the fibre loss. According to Eq. (2.1.3), $I(z) = I_0 \exp(-\alpha z)$, where $I_0 = P_0/(\pi w_0^2)$ and P_0 is the optical power coupled into the fibre, the product $I_0 L_{\text{eff}}$ becomes

$$(I_0 L_{\text{eff}})_{\text{fibre}} = \int_0^L I(z)\exp(-\alpha z)\mathrm{d}z = \frac{P_0}{\pi w_0^2 \alpha}[1 - \exp(-\alpha L)]. \tag{2.40}$$

A comparison of Eqs. (2.39) and (2.40) shows that, for sufficiently long fibres, the efficiency of a nonlinear process in optical fibres can be improved by a factor

$$\frac{(I_0 L_{\text{eff}})_{\text{fibre}}}{(I_0 L_{\text{eff}})_{\text{bulk}}} = \frac{\lambda}{2\pi w_0^2 \alpha}, \tag{2.41}$$

where $\alpha L \gg 1$ was assumed. For the conventional fibre SMF-28, w_0 =5 μm, at the wavelength about 1.55 μm, α_{dB} =0.2 dB/km (α =4.6×10^{-5} m^{-1}), the enhancement factor can approach 10^8. As optical fibres, PCFs also have high nonlinearity. The high nonlinear PCFs with small core ($d_{\text{core}} \leq$2 μm) and large

core-cladding index contrast can further increase the nonlinear efficiency [75]. It is also possible to use nonlinear materials for which nonlinearity is larger than silica. Optical fibres made with with lead silicate glasses [76] or chalcogenide and other nonsilica materials [77] have been demonstrated. The nonlinearity of these material is one or two orders of magnitude higher, but the material dispersion is far away from the wavelength range of interest. For example, bulk chalcogenide glasses have a ZWD at about 5 μm. For SC generation in such fibres pumped at 1.55 μm, the fibre needs to be tapered down to less than 1 μm which is nontrivial [78]. According to Eq. (2.41), the relatively high loss in nonsilica fibres may also counteract the advantage of their higher nonlinearity. However, for silica PCFs even without design for high nonlinearity (where d_{core} is typically 5 μm), the unique dispersion properties of PCFs still make them the best candidate for nonlinear processes such as SC generation and FWM [43].

2.4.4 Birefringence

Fibre birefringence is usually introduced intentionally through making fibres with asymmetrical structures. In conventional fibres, one scheme breaks the symmetry by making the fibre core elliptical in shape [79]. In an alternative scheme, the asymmetry is achieved by incorporating materials with different thermal expansion close to the core, which generate stress when the fibre cools down in the drawing process. "Panda" and "bow-tie" fibres (Fig. 2.25(a)) achieved birefringence with $B_m \sim 10^{-4}$ (see Eq. (2.5)) in this way [8].

In PCFs birefringence is much easier to introduce because of the "stack and draw" fabrication process (see Section 2.3). Since a small core fibre exhibits large birefringence even with only a slightly elliptical core, the easiest way to achieve birefringence is to make a small core PCF [80]. Birefringence then results from small unintentional asymmetry in a symmetrical design, however, the strength of the birefringence is then uncontrollable. The asymmetry may also be introduced into the fibre during stacking process by careful positioning of capillaries with the same external diameter but different wall thicknesses, leading to different airhole sizes in the cladding of the final fibre and twofold rotational symmetry (Fig. 2.25(b)) [30]. Similarly to Ref. [30], the asymmetrical structure can also be made through enlarging [81] or reducing the size of two holes around the core (Fig. 2.25(c)(d)). All of these designs are quite straight forward and very

useful in practical applications.

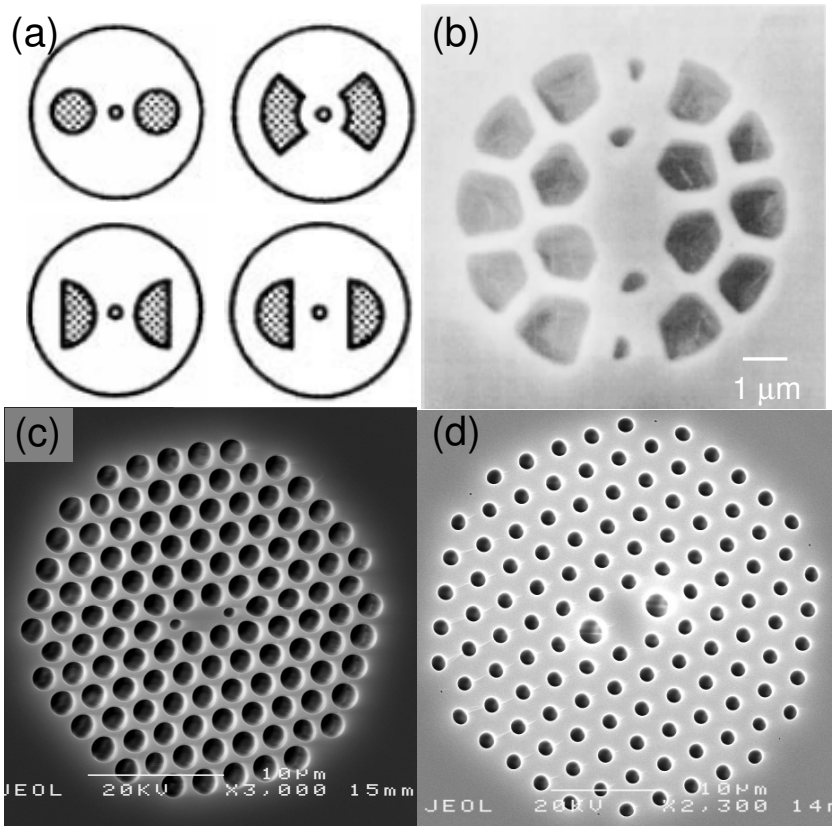

Figure 2.25: Different polarisation maintaining fibres. (a) "Panda" and "bow-tie" fibres [8]. (b) PCF with four smaller holes induced birefringence [30]. (c) PCF with two smaller holes induced birefringence (see Section 5.3.1). (d) PCF with two bigger holes induced biregringence (see Section 4.4).

To make a birefringent PCF for nonlinear experiments, the most important parameters we need to consider are fibre GVD, the strength of the birefringence and the fibre mode shape (which determines the coupling efficiency of the fibre with laser sources or other optical devices). Making the asymmetry bigger can induce huge birefringence, but bigger asymmetry can make the mode further away from a good circular shape. So there is a trade-off between birefringence and fibre mode shape. To achieve a desired fibre GVD profile, obviously the structures like Fig. 2.25(c) or (d) are the best choice. In these structures, one can use differential pressure to control the size of the two specific holes and the other cladding holes respectively. The decision to make the two holes smaller or

bigger depends on how big the other cladding holes are. If the other cladding holes are already very big (d/λ =0.8 for example), there is no way to make two holes even bigger to introduce enough birefringence, so the two holes need to be made smaller (Fig. 2.25(c)). On the contrary, if the other cladding holes are already relatively small (d/λ =0.3-0.5 for example), the two holes need to be made bigger (Fig. 2.25(d)). We will see later in Section 4.4 that we can introduce a modal birefringence about $B_m \sim 10^{-4}$ without power coupling penalty. In other words, the fibre GVD, birefringence and mode shape are all under control in PCFs.

2.5 Splicing of Photonic Crystal Fibres

The novel properties of PCFs bring many potential applications. However since many commercial optical components and devices have conventional fibre pigtails, it is necessary to be able to connect PCFs to conventional fibres (see Section 4.5). Sometimes it is also necessary to join two different PCFs together (see Section 4.6). One of the major concerns with respect to the practical applications of PCFs is the question of whether or not a PCF could be spliced to a conventional fibre or another PCF with reasonable loss level.

The standard arc fusion splicer is normally used to splice conventional fibres by fusing the ends of fibres at high temperature. The whole process is completed automatically. In the case of PCFs, however, the same operation on the standard arc fusion splicer will result in significant loss. From a physical point of view, the splicing loss has two main origins: one is the mode field mismatch between the fibres to be spliced; the other is that the air holes in PCFs may completely collapse in the vicinity of the splice joint during the splicing process, which significantly increases the coupling loss by destroying the waveguide structure of the PCF near the joint interface. Actions need to be taken to overcome these two problems.

For PCFs and conventional fibres having similar mode field diameters (MFDs), the key point is avoiding hole collapse to maintain MFD match. Some experiments based on the standard arc fusion splicer have been reported to minimize hole collapse so as to achieve low splicing loss [82][83]. Compared with the conventional fibre splicing technique, the main difference of PCF involved splicing is using an arc of shorter duration and lower power. At 1550nm, a loss level as low as 0.19 dB was achieved by this method [83]. However this approach is not

applicable to the splicing between PCFs and conventional fibres or PCFs with very different MFDs. For example, highly nonlinear PCFs, used in nonlinear research, normally have much smaller MFDs than conventional single-mode fibres. The mode mismatch will be the main splicing loss mechanism since the mode change from one fibre to another is significant and non-adiabatic. To overcome the mode mismatch, one indirect technique is to make the highly nonlinear PCF structure in the PCF with similar MFD to another fibre to be spliced, using the post-processing techniques described in Section 2.3.2. The drawback of this technique is that the length of the highly nonlinear PCF is limited by the taper rig. Alternatively, another direct technique was also developed to enlarge the MFD of PCFs with relatively small MFDs [84]. The technique used a standard arc fusion splicer to partially collapse the holes of the PCF whilst maintaining a good waveguide. This enlarges the MFD at the fibre end. This technique works well for the PCFs with relatively low air-filling ratio ($d/\Lambda \sim 0.5$), where the splicing loss at 1550 nm can be as low as 0.9 dB [84]. However, for the PCFs with high air-filling ratio ($d/\Lambda \sim 0.9$), the splicing loss at 1550 nm can be reduced to 2.5 dB from 8.1 dB butt-coupling loss. The improvement is promising but not enough. Further improvements will be proposed in Chapter 6.

As mentioned above, to maintain mode match and the waveguide structure, some splicing parameters need to be set manually. The manual operation is more or less limited for the standard arc fusion splicer. A filament fusion splicing system (*Vytran, FFS-2000*) is another commercial system with much more flexible manual operation ability. There is a camera inside to monitor the positions of both fibres ready to splice. The associated ffs-2000 program is used to set the splicing parameters (e.g. the fusion temperature and splicing time) and control the fibres in good alignment. Many splicing parameters are controllable in a wide range. With the help of this system, when we tried to splice a 5 μm core PCF to a HP1060 conventional fibre (roughly 5 μm core), the best result was 0.2 dB loss at 1550 nm.

Chapter 3

Nonlinear Effects in Photonic Crystal Fibres

Silica total internal reflection (TIR) PCFs have the same nonlinear refractive index as silica-based conventional fibres and guide light in a similar way to conventional fibres. Thus all of the nonlinear phenomena in conventional fibres will take place in this type of PCF. The difference is that these nonlinear phenomena are more efficient in such PCFs because of their unique dispersion properties (see Section 2.4.2) and sometimes higher nonlinearity in the case of small core PCFs.

This chapter aims to provide a general discussion about the most common nonlinear effects in optical fibres. It is partly based on material from the book by G. P. Agrawal [8]. Section 3.1 briefly introduces the nonlinear Schrödinger equation that governs the propagation of light pulses in optical fibres. Section 3.2 gives an introduction to self-phase modulation (SPM) and cross-phase modulation (XPM) in optical fibres. Section 3.3 discusses stimulated Raman scattering in optical fibres. Section 3.4 explains parametric processes, such as four-wave mixing (FWM) and modulation instability (MI) as well as the importance of phase-matching techniques. Section 3.5 introduces soliton formation. Section 3.6 describes the polarisation effects that occur in nonlinear pulse propagation such as nonlinear birefringence and FWM through cross polarisation phase-matching or polarisation modulation instability (PMI).

3.1 Pulse Propagation in Fibres

Nonlinear effects in optical fibres become significant when the optical intensity is high. Optical pulses can carry high energy in a short duration as such they are able to provide very high peak intensity, the study of most nonlinear effects in optical fibres involves the use of short pulses with widths ranging from ∼10 ns to 10 fs. This section will briefly discuss what determines the evolution of pulses in optical fibres using the nonlinear Schödinger equation.

Before going further through the details, it is useful to rewrite the form of the induced polarisation in Eq. (2.29). After taking $\chi^{(2)} = 0$ for silica fibres and ignoring the higher order terms than $\chi^{(3)}$, the induced polarisation becomes

$$\mathbf{P} = \varepsilon_0 \left(\chi^{(1)} \cdot \mathbf{E} + \chi^{(3)} \vdots \mathbf{EEE} \right) = \mathbf{P}_L + \mathbf{P}_{\mathrm{NL}}, \tag{3.1}$$

where $\mathbf{P}_L$ and $\mathbf{P}_{\mathrm{NL}}$ are the linear and nonlinear polarisations, respectively. According to Maxwell's equations and Eq. (3.1), the wave equation governing propagation of optical pulses in nonlinear dispersive fibres is

$$\nabla^2 \mathbf{E} - \frac{1}{c^2} \frac{\partial^2 \mathbf{E}}{\partial t^2} = \mu_0 \frac{\partial^2 \mathbf{P}_L}{\partial t^2} + \mu_0 \frac{\partial^2 \mathbf{P}_{\mathrm{NL}}}{\partial t^2}, \tag{3.2}$$

where μ_0 is the vacuum permeability.

Equation (3.2) is complex. To solve it, several simplifying assumptions need to be made. Firstly, $\mathbf{P}_{\mathrm{NL}}$ is treated as a small perturbation to $\mathbf{P}_L$ so that the perturbation theory can be used. The mode property discussed in Section 2.1.1 is actually a linear description corresponding to this approximation. Secondly, The optical field is assumed to maintain its polarisation when propagating in fibres so that a scalar approach is valid. This is not true for optical fibres (except for the PM fibre), but the approximation works very well in practice. Thirdly, the optical field is assumed to be quasi-monochromatic, meaning pulse frequency width is smaller than its own frequency. It is valid for pulses as short as 100 fs. Lastly, the material's response to the applied electric field is assumed to be instantaneous. Based on these simplifications, the slowly varying pulse envelope approximation can be adopted here [8]. Using the method of separation of variables, the electric field propagating along z direction and polarised in x direction in Eq. (3.2) can

be written as

$$\mathbf{E}(\mathbf{r},t)=\frac{1}{2}\hat{\mathbf{x}}\{F(x,y)A(z,t)\exp[\mathrm{i}(\beta_0 z-\omega_0 t)]+\text{c.c.}\},\tag{3.3}$$

where $F(x,y)$ is the field distribution in the cross section of the fibre (i.e. fibre mode discussed in Section 2.1.1), $A(z,t)$ is the slowly varying pulse envelope describing the pulse evolution with the propagation distance and time, ω_0 is the central frequency and $\beta_0=\beta(\omega_0)$. Substituting Eq. (3.3) into Eq. (3.2) and using perturbation theory, We can get a equation for $A(z,t)$ with the form

$$\frac{\partial A}{\partial z}+\beta_1\frac{\partial A}{\partial t}+\frac{\mathrm{i}\beta_2}{2}\frac{\partial^2 A}{\partial t^2}+\frac{\alpha}{2}A=\mathrm{i}\gamma|A|^2A,\tag{3.4}$$

where β_1, β_2, α and γ are defined by Eqs. (2.21), (2.22), (2.14) and (2.34) respectively. A moving reference frame, with velocity v_g, is used to solve Eq. (3.4) such that $T=t-z/v_g$. The equation for $A(z,T)$ can take the form of

$$\mathrm{i}\frac{\partial A}{\partial z}=-\frac{\mathrm{i}\alpha}{2}A+\frac{\beta_2}{2}\frac{\partial^2 A}{\partial T^2}-\gamma|A|^2A.\tag{3.5}$$

Fibre losses (α term), group-velocity dispersion (β_2 term) and fibre nonlinearity (γ term) are all included in Eq. (3.5), affecting the propagation properties of pulses in optical fibres. The dispersion terms higher than the second order are neglected. In the special case of $\alpha=0$, Eq. (3.5) is referred to as the nonlinear Schrödinger equation (NLSE), which describes pulse propagation in terms of dispersion and nonlinearity. Either dispersive or nonlinear effects may dominate along the fibre, depending on the initial width T_0 (described as where the optical intensity drops to $1/e^2$ of its peak value), the peak power P_0 of the incident pulse, and the dispersion and nonlinearity of the fibre. To explore how these factors affect pulse propagation, let us introduce a time scale normalised to the input pulse width T_0 as

$$\tau=\frac{T}{T_0}=\frac{t-z/v_g}{T_0}.\tag{3.6}$$

At the same time, we introduce a normalised amplitude U as

$$A(z,\tau)=\sqrt{P_0}\exp(-\alpha z/2)U(z,\tau).\tag{3.7}$$

Combining Eqs. (3.5)–(3.7), $U(z,\tau)$ is found to satisfy

$$\mathrm{i}\frac{\partial U}{\partial z} = \frac{\mathrm{sgn}(\beta_2)}{2L_D}\frac{\partial^2 U}{\partial \tau^2} - \frac{\exp(-\alpha z)}{L_{\mathrm{NL}}}|U|^2 U, \tag{3.8}$$

where $\mathrm{sgn}(\beta_2) = \pm 1$ depending on the sign of the GVD parameter β_2 and

$$L_D = \frac{T_0^2}{|\beta_2|}, \qquad L_{\mathrm{NL}} = \frac{1}{\gamma P_0}. \tag{3.9}$$

L_D and L_{NL} are the dispersion length and nonlinear length, respectively. They provide the length scales over which dispersive or nonlinear effects become important for pulse evolution.

3.2 Self-Phase Modulation and Cross-Phase Modulation

SPM and XPM are typical manifestations of the intensity dependence of the refractive index in $\chi^{(3)}$ nonlinear media. SPM refers to the self-induced phase shift experienced by an optical field during its propagation in optical fibres. If a linear polarised monochromatic electric field

$$\mathbf{E} = \frac{1}{2}\hat{\mathbf{x}}\left[E\exp(\mathrm{i}n(\omega)k_0 z - \mathrm{i}\omega t) + \mathrm{c.c.}\right] \tag{3.10}$$

is applied to a fibre, the intensity dependence of the refractive index resulting from the contribution of $\chi^{(3)}$ becomes [8]

$$\bar{n}(\omega, |E|^2) = n(\omega) + n_2|E|^2, \tag{3.11}$$

where $n(\omega)$ is the linear part as normally used in Eq. (3.10), $|E|^2$ is proportional to the optical intensity I inside the fibre, and n_2 is the nonlinear refractive index related to $\chi^{(3)}$ by Eq. (2.35). The phase of the optical field changes by

$$\phi = \bar{n}k_0 L_{\mathrm{eff}} = (n(\omega) + n_2|E|^2)k_0 L_{\mathrm{eff}}, \tag{3.12}$$

where the effective fibre length after considering the fibre loss is $L_{\mathrm{eff}} = [1 - \exp(-\alpha L)]/\alpha$ (L being fibre length). The intensity-dependent nonlinear phase

shift

$$\phi_{\mathrm{NL}} = n_2 k_0 L_{\mathrm{eff}} |E|^2, \tag{3.13}$$

which results in a frequency shift from the central frequency or a frequency chirp

$$\delta\omega(t) = -\frac{\partial \phi_{\mathrm{NL}}}{\partial t} = -n_2 k_0 L_{\mathrm{eff}} \frac{\partial |E|^2}{\partial t} \propto -n_2 k_0 L_{\mathrm{eff}} \frac{\mathrm{d}I}{\mathrm{d}t}. \tag{3.14}$$

This simplified analysis gives a clear picture about the origin of SPM. The strict analysis can be derived from Eq. (3.8) (Ref. [8] Chapter 2). We write the results here. If $U(0,\tau)$ is the field amplitude at $z = 0$, the nonlinear phase shift is

$$\phi_{\mathrm{NL}} = \gamma P_0 |U(0,\tau)|^2 L_{\mathrm{eff}}. \tag{3.15}$$

The maximum phase shift ϕ_{max} occurs at the pulse center located at $\tau = 0$. With U normalised such that $|U(0,0)| = 1$, it is given by

$$\phi_{\mathrm{max}} = \gamma P_0 L_{\mathrm{eff}}. \tag{3.16}$$

The frequency shift is given by

$$\delta\omega(\tau) = -\frac{\partial \phi_{\mathrm{NL}}}{\partial \tau} = -\gamma P_0 L_{\mathrm{eff}} \frac{\partial}{\partial \tau} |U(0,\tau)|^2. \tag{3.17}$$

For a chirp free Gaussian pulse, the maximum frequency shift is

$$\delta\omega_{\mathrm{max}} = 0.86 \Delta\omega_0 \phi_{\mathrm{max}}, \tag{3.18}$$

where $\Delta\omega_0$ is the initial bandwidth of the pulse. It can be seen that Eqs. (3.13) and (3.14) are equivalent to Eqs. (3.15) and (3.17) if γ is replaced with n_2 and I is taken to be P_0/A_{eff}.

XPM refers to the nonlinear phase shift of an optical field induced by a copropagating field at a different wavelength. The field for this can be expressed as

$$\mathbf{E} = \frac{1}{2}\hat{\mathbf{x}} \left[E_1 \exp(\mathrm{i}n(\omega_1)k_{01}z - \mathrm{i}\omega_1 t) + E_2 \exp(\mathrm{i}n(\omega_2)k_{02}z - \mathrm{i}\omega_2 t) + \mathrm{c.c.} \right]. \tag{3.19}$$

The two copropagating fields incur a nonlinear phase shift similar to Eq. (3.13).

For the field of frequency ω_1 it is given by

$$\phi_{\mathrm{NL}} = n_2 k_{01} L_{\mathrm{eff}} (|E_1|^2 + 2|E_2|^2). \tag{3.20}$$

The two terms on the right-hand side of Eq. (3.20) represent SPM and XPM respectively. The frequency shift takes the similar form to Eq. (3.14). To analytically describe XPM Eq. (3.5) is not enough, since it only describes the evolution of pulses with a monochromatic assumption. However, a set of coupled equations similar to Eq. (3.5) can describe XPM very well [8].

Equation (3.14) indicates that SPM and XPM induced frequency shift increases its magnitude with the propagation distance. In other words, new frequency components are continuously generated as the pulse propagates down the fibre, which means that SPM and XPM broaden the spectrum over its initial width. And the broadening efficiency critically depends on the intensity profile in time domain. The dependence of Eq. 3.18 on $\mathrm{d}I/\mathrm{d}t$) indicates that SPM and XPM are efficient only for short pulses (10 ps or shorter). It should be noted that this discussion about SPM and XPM does not specify if the fibre is a conventional fibre or a PCF, so the discussion is applicable for both. As we will see in Section 4.2, SPM and XPM are important mechanisms for supercontinuum (SC) generation in the ultrashort pulse pumping scheme.

3.3 Stimulated Raman Scattering

Fundamentally, stimulated Raman scattering (SRS) is different from elastic nonlinear effects such as SPM, XPM and FWM, in which no energy is exchanged between the electromagnetic field and the dielectric medium; the fibre plays a passive role. SRS is a nonlinear effects resulting from stimulated inelastic scattering, in which the optical field transfers part of its energy to the nonlinear medium hence the fibre plays an active role.

In any molecular medium, spontaneous Raman scattering can transfer a small fraction of power from one optical field to another field, whose frequency is downshifted by an amount determined by the vibrational modes of the medium. Quantum mechanically a photon of energy $\hbar\omega_p$ is scattered to a lower-energy photon $\hbar\omega_s$ by a molecule. In doing so the molecule makes a transition to a higher vibrational state (see Fig. 3.1). The incident light is acting as a pump and

generating the frequency-shifted radiation, the Stokes wave. For intense pump fields, once the spontaneous Stokes wave is generated, it seeds this process and the nonlinear phenomenon of SRS can occur in which the Stokes wave grows rapidly inside the medium such that most of the pump energy is transferred to it.

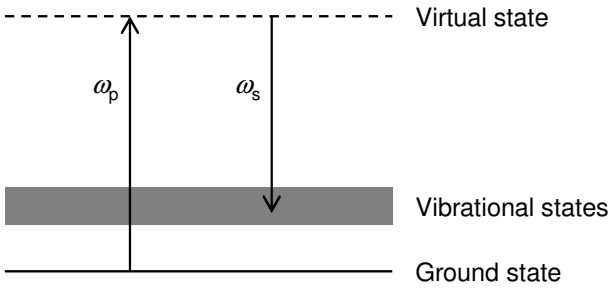

Figure 3.1: Schematic illustration of spontaneous Raman scattering from a quantum-mechanical viewpoint. A photon of reduced energy $\hbar\omega_s$ is created spontaneously, after a pump photon of energy $\hbar\omega_p$ excites the molecule to a virtual state shown by the grey band (Ref. [8] Chapter 8).

On a more fundamental level, SRS is derived from the delayed response property of $\chi^{(3)}$. Equation (3.5) can not be used to describe SRS because an instantaneous response is assumed there. In theory a more general equation, known as the generalized nonlinear Schrödinger equation, should be applied [8].

Under the CW and quasi-CW conditions, the initial growth of the Stokes wave is described by

$$\frac{I_s}{\mathrm{d}z} = g_R I_p I_s, \tag{3.21}$$

where I_s is the Stokes intensity, I_p is the pump intensity. The Raman-gain coefficient $g_R(\Omega)$ (where $\Omega \equiv \omega_p - \omega_s$ that represents the frequency difference between the pump and Stokes waves) is the most important quantity for describing SRS. In optical fibres, g_R usually depends on composition of the fibre core and can vary significantly with the use of different dopants. It also depends on whether the pump and Stokes are copolarised or orthogonally polarised. Figure 3.2 shows g_R for fused silica as a function of the frequency downshift [8], normalised such that $g_R \approx 1 \times 10^{-13}$ at a pump wavelength $\lambda_p = 1$ μm. For other pump wavelengths g_R scales inversely with λ_p. The most significant feature of the Raman gain in silica fibres is that $g_R(\Omega)$ extends over a large frequency range (up to 40 THz) with a broad peak located near 13 THz. This behavior is due to the

noncrystalline nature of silica glass. In amorphous materials such as fused silica, molecular vibrational frequencies spread out into bands that overlap and create a continuum. Therefore in contrast to most molecular media for which the Raman gain occurs at specific well defined frequencies, silica has a Raman gain curve that extends continuously over a broad range of frequencies.

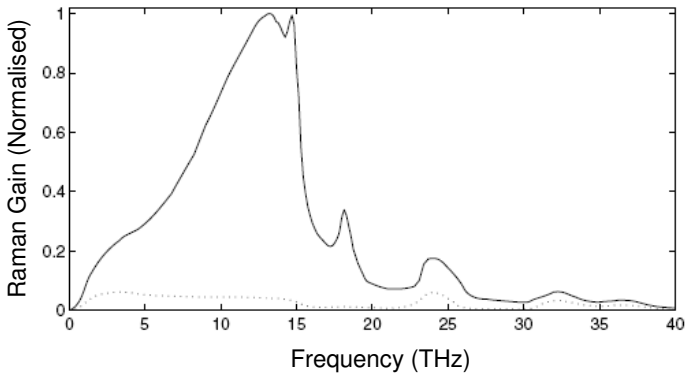

Figure 3.2: Normalised Raman gain for fused silica when pump and Stokes waves are copolarised (solid curve). The dotted curve shows the situation in which the pump and Stokes waves are orthogonally polarised (Ref. [8] Chapter 8).

As we can see, SRS is an intrinsic nonlinear effect taking place in silica and hence in PCFs, SRS exhibits the same Raman-gain spectrum as Fig 3.2. It will be shown later, this broad gain band property is useful for SC generation (see Section 4.2). However, it is also the main origin of noise in single photon experiments (see Chapter 5). SRS is easy to observe because the gain is linearly proportional to the pump light intensity, the threshold pump power is low and no phase-matching is required (see Section 3.4). However, when certain conditions are satisfied so that other nonlinear effects dominate, such as phase matched parametric processes, the Raman effect can be suppressed considerably. In the ultrashort pulse regime, SRS will only occur in the walk-off length range between the pump pulse and Stokes pulse. Since a ultrashort pulse can have a broad bandwidth which spans the Raman-gain bandwidth, the pulse itself can both pump and seed the SRS process. SRS taking place in such a pulse is called intrapulse Raman scattering, which induces soliton self-frequency shift in SC generation (see Section 4.2).

3.4 Parametric Processes

Some nonlinear processes are referred to as parametric processes because they originate from the light-induced modulation of medium parameters, such as the refractive index. This section mainly discusses the parametric processes of FWM and MI. Phase-matching techniques, which are important to FWM and MI, are also included in the discussion.

3.4.1 Four-Wave Mixing and Modulation Instability

Like SPM and XPM, FWM is also a third-order nonlinear effect which can be understood through the third-order polarisation term in Eq. (2.29) given as

$$\mathbf{P}_{\mathrm{NL}} = \varepsilon_0 \chi^{(3)} \vdots \mathbf{EEE}. \tag{3.22}$$

However, as mentioned in Section 3.2, SPM and XPM are only efficient in short pulses. If we now assume a CW or long pulse input so that $\mathrm{d}I/\mathrm{d}t \sim 0$, both SPM and XPM will have negligible contributions. FWM will be the dominant third-order nonlinear effect in this case. If $\mathbf{E}$ in Eq. (3.22) takes the form

$$\mathbf{E} = \frac{1}{2}\hat{\mathbf{x}} \sum_{j=1}^{4} E_j \exp[\mathrm{i}(k_j z - \omega_j t)] + \mathrm{c.c.}, \tag{3.23}$$

$\mathbf{P}_{\mathrm{NL}}$ can be expressed as [8]

$$\mathbf{P}_{\mathrm{NL}} = \frac{1}{2}\hat{\mathbf{x}} \sum_{j=1}^{4} P_j \exp[\mathrm{i}(k_j z - \omega_j t)] + \mathrm{c.c.}, \tag{3.24}$$

where $j = 1 - 4$ indicates four optical waves oscillating at frequencies $\omega_1, \omega_2, \omega_3$ and ω_4, linearly polarised along the same axis x, $k_j = n_j \omega_j / c$ (n_j is the refractive index), the wave vectors which are assumed to be in the same direction z. P_j for $j = 1 - 4$ consists of a large number of terms involving the products of three electric fields. For example, P_4 can be written as

$$\begin{aligned} P_4 &= \frac{3\varepsilon_0}{4}\chi^{(3)}_{xxxx}\{[|E_4|^2 + 2(|E_1|^2 + |E_2|^2 + |E_3|^2)]E_4 \\ &+ 2E_1E_2E_3\exp(\mathrm{i}\theta_+) + 2E_1E_2E_3^*\exp(\mathrm{i}\theta_-) + \cdots\}, \end{aligned} \tag{3.25}$$

where

$$\theta_+ = (k_1 + k_2 + k_3 - k_4)z - (\omega_1 + \omega_2 + \omega_3 - \omega_4)t, \quad (3.26)$$

$$\theta_- = (k_1 + k_2 - k_3 - k_4)z - (\omega_1 + \omega_2 - \omega_3 - \omega_4)t. \quad (3.27)$$

The term proportional to E_4 in Eq. (3.25) is responsible for the SPM and XPM effects discussed in Seciont 3.2. The remaining terms are responsible for FWM. However all of these require phase-matching between E_4 and P_4, which need the relative phase given by θ_+, θ_-, ..., to vanish. This requires both the matching of frequencies as well as wave vectors. From the quantum-mechanical point of view, FWM occurs when photons from one or more waves are annihilated and new photons are created at different frequencies such that net energy and momentum are conserved. The term containing θ_+ in Eq. (3.25) is responsible for the process in which three photons transfer their energy to a single photon. $\omega_1 = \omega_2 = \omega_3$ corresponds to the phenomenon called third-order harmonic generation. In general, such process is not efficient in fibres because it is difficult to satisfy the phase-matching condition. The term containing θ_- in Eq. (3.25) represents the most effective FWM process, in which two photons are destroyed and two new photons are created. The energy conservation and phase-matching conditions are written as

$$\Delta\omega = \omega_3 + \omega_4 - \omega_1 - \omega_2 = 0, \quad (3.28)$$

$$\Delta k = k_3 + k_4 - k_1 - k_2$$

$$= (n_3\omega_3 + n_4\omega_4 - n_1\omega_1 - n_2\omega_2)/c = 0. \quad (3.29)$$

In the partially degenerate case $\omega_1 = \omega_2$, it is relatively easy to satisfy $\Delta k = 0$. A strong pump wave will create two sidebands at symmetrical frequencies from noise. FWM which is talked about most in this thesis is a degenerate case.

Equations (3.28) and (3.29) give a basic description of FWM. In practice we have to take the phase change induced by SPM and XPM into account. Therefore the phase mismatch Δk in Eq. (3.29) should be

$$\kappa = \Delta k + \gamma(P_1 + P_2), \quad (3.30)$$

where γ is the nonlinear coefficient given by Eq. (2.34), P_1 and P_2 are the incident

pump powers at the fibre input for ω_1 and ω_2 respectively. In the degenerate case, $P_1 = P_2 = P$ and Eq. (3.30) becomes

$$\kappa = \Delta k + 2\gamma P. \tag{3.31}$$

The phase-matching condition Eq. (3.29) is now

$$k_1 + k_2 = k_3 + k_4 + 2\gamma P. \tag{3.32}$$

It is worth mentioning that modulation instability (MI), which is sometimes discussed separately, actually is the description of FWM in the time domain. The name 'modulation instability' is still widely used because it was first studied through slightly perturbing a steady state of CW light inside an optical fibre and it was found that such a perturbation can lead to the state become unstable (Ref. [8] Chapter 5). The origin of the instability is that the perturbation with a certain frequency Ω grows exponentially with the propagation distance in the fibre if the carrier frequency ω_0 is in the anomalous dispersion regime. In the frequency domain, two sidebands at $\omega_0 - \Omega$ and $\omega_0 + \Omega$ will be generated. This is exactly the picture of FWM. The requirement of anomalous dispersion is due to the phase-matching requirement in a conventional fibre (see Section 3.4.2). In the time domain, frequency beating between ω_0, $\omega_0 - \Omega$ and $\omega_0 + \Omega$ will occur. The beating plays a role to modulate the intensity of the CW light at a frequency of Ω and transform the CW light into a short pulse train. However, such modulation is only seen when the modulation frequency Ω is low, this corresponding to the case of FWM in the anomalous dispersion regime. That is why most people call FWM in the anomalous dispersion regime MI.

As it can be seen later in Section 4.2, MI is very important to the supercontinuum (SC) generation in the long pulse and CW pumping regime as it is the driver that generates short pulses from long pulses. Soliton-related dynamics are only involved in and hence contribute to SC generation, after short pulses are generated.

3.4.2 Phase-Matching Techniques

From the engineering point of view, it is convenient to write the phase mismatch in Eq. (3.31) in the form

$$\kappa = \Delta\beta + \Delta k_{\mathrm{NL}}, \tag{3.33}$$

where $\Delta\beta$ and Δk_{NL} represent the mismatch as a result of dispersion and from nonlinear effects respectively. Assuming $\omega_3 < \omega_4$, the two pump photons are at same frequency ($\omega_1 = \omega_2$) and in the same fibre mode ($\beta(\omega_1) = \beta(\omega_2)$), the two terms in Eq. (3.33) become

$$\begin{aligned}
\Delta\beta &= \beta(\omega_3) + \beta(\omega_4) - 2\beta(\omega_1) \\
&= \beta(\omega_1 - \Omega) + \beta(\omega_1 + \Omega) - 2\beta(\omega_1) \\
&\approx \beta_2\Omega^2 + \frac{2}{4!}\beta_4\Omega^4 + \frac{2}{6!}\beta_6\Omega^6, \qquad (3.34) \\
\Delta k_{\mathrm{NL}} &= 2\gamma P. \qquad (3.35)
\end{aligned}$$

Here Eq. (3.34) uses the Taylor expansion Eq. (2.19) and includes the terms up to β_6. To achieve phase-matching $\kappa = 0$, all the terms in Eqs. (3.34) and (3.35) are compensating each other. Δk_{NL} is always positive, so techniques have to be adopted to make $\Delta\beta$ negative.

In conventional fibres, if the pump wavelength λ_p is longer than the ZDW λ_D (i.e. in the anomalous dispersion regime) hence $\beta_2 < 0$, phase-matching can be achieved by adjusting the incident power. If $\lambda_p < \lambda_D$ (i.e. in the normal dispersion regime) where $\beta_2 > 0$, phase-matching in single-mode fibres is difficult to achieve, as the waveguide dispersion is so small that β_4, β_6 and higher-order dispersion terms can not counteract the β_2 term. To realize phase-matching in this case, a birefringent phase-matching technique is normally used to obtain two different β terms so as to achieve phase-matching. We will talk about this in Section 3.6.2. Alternatively, a multimode fibre can be used to realize phase-matching through a multimode phase-matching technique. In PCFs, however, single-mode phase-matching can be achieved easily because of their highly controllable dispersion (see Section 2.4.2) in both the normal and anomalous dispersion regimes.

As an example, phase matched FWM wavelengths, calculated from the measured dispersion for a PCF according to Eq. (3.32), are shown in Fig. 3.3 as a function of the pump wavelength offset from λ_D [43]. There are three important regions: (a) $\lambda_p \ll \lambda_D$, (b) $\lambda_p \leq \lambda_D$, (c) $\lambda_p > \lambda_D$.

In case (a) (beyond the left half of Fig. 3.3) there is no phase-matching for FWM. An idealised fibre would show the FWM phase-matching branches which curve back on themselves, giving a limit to the maximum wavelength offset at which FWM can occur.

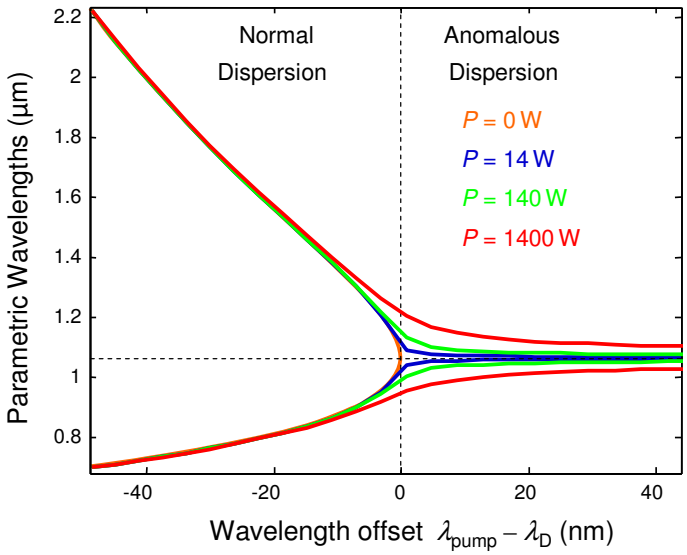

Figure 3.3: Phase-matching curves for the process $2\omega_{\text{pump}} \rightarrow \omega_{\text{signal}} + \omega_{\text{idler}}$, calculated from the measured dispersion curve for a PCF with input powers, $P = 0$ W (orange curve), $P = 14$ W (blue curve), $P = 140$ W (green curve), $P = 1400$ W (red curve) [43].

In case (b) (the left half of Fig. 3.3) phase matching is power-independent with widely separated FWM peaks. Solutions of Eq. (3.32) in this region are present even for zero power (orange curve in Fig. 3.3), but only when higher order dispersion terms are non-zero (even terms only; β_4, β_6, etc., Eq. (3.34)). The gain peaks are relatively narrow, and the central frequencies depend strongly on the higher order dispersion. It can be understood from Eq. (3.34) in the sense that $\beta_2 > 0$ in the normal dispersion region resulting in $\beta_2\Omega^2 > 0$ and $\Delta k_{\text{NL}} > 0$, so β_4 and β_6 have to be involved to cancel these positive terms out. The power-independence is because the contribution of Δk_{NL} is much smaller than $\beta_2\Omega^2$ since Ω is very large in this case. However, when λ_p is very close to λ_D, phase-matching becomes power dependent since β_2 is very small in the vicinity of λ_D.

In case (c) (the right half of Fig. 3.3) shows a strongly power-dependent phase-matching, with the FWM peaks close to the pump wavelength. A non-

zero value of power is required for solution of Eq. (3.32) in this region. This is a well known phenomenon of modulation instability (MI), which only occurs in the anomalous dispersion regime of fibres [8]. The gain peaks are relatively broad, and the central frequencies depend mostly on β_2 and only weakly on higher order dispersion. Here $\beta_2\Omega^2$ is negative and dominates in Eq. (3.34), so the main cancellation to this term comes from the power dependent term Eq. (3.35).

It should be noted that the discussion above is based on the assumption of quasi-CW conditions (i. e. the difference of the group velocities of different wavelengths is neglected). As mentioned in Sections 2.1.5 and 2.4.2, in practice, short or ultrashort pulses are involved to FWM. If the carrier frequencies of the four pulses are widely separated (> 5 THz), the group velocities can be so different that the four pulses walk off. Without a spatial overlap, there is no chance for interaction. As a result, efficient FWM requires not only phase matching but also group-velocity matching. FWM is one of the most important mechanisms for SC generation in PCFs. The extension to very short wavelengths is normally limited by the group-velocity mismatch (see Section 4.2).

3.5 Soliton Effect

A fascinating nonlinear phenomenon in optical fibres is optical solitons, formed as a result of interplay between dispersive and nonlinear effects. The word soliton refers to special kinds of wave packets that can propagate undistorted over long distances. A complete description may be achieved by applying the inverse-scattering method [85] to solve Eq. (3.8). We are more interested in the physical conclusions than the mathematical details, so only a brief description is given here.

Let us recall Eq. (3.8) and write it in a normalised form as

$$\mathrm{i}\frac{\partial U}{\partial \xi} = \frac{\mathrm{sgn}(\beta_2)}{2}\frac{\partial^2 U}{\partial \tau^2} - N^2 \mathrm{e}^{-\alpha\xi L_D}|U|^2 U, \tag{3.36}$$

where ξ represents the normalised distance defined as

$$\xi = \frac{z}{L_D}, \tag{3.37}$$

and the parameter N is introduced by using

$$N^2 = \frac{L_D}{L_{\rm NL}} \equiv \frac{\gamma P_0 T_0^2}{|\beta_2|}. \tag{3.38}$$

The physical significance of N is that it determines which effect dominates; dispersive or nonlinear. Dispersion dominates for $N \ll 1$, while SPM dominates for $N \gg 1$. For values of $N \sim 1$, both SPM and GVD play an equally important role during pulse evolution, and soliton formation occurs in this case if $\beta_2 < 0$. Once the soliton is formed, the pulse will propagate along the fibre without changing either shape or spectrum. This behavior can be understood by noting that the SPM-induced chirp given by Eq. (3.14) has the opposite sign to the dispersion-induced chirp for $\beta_2 < 0$ (Ref. [8] Chapter 3). The two chirp contributions nearly cancel each other along the central portion of the Gaussian pulse when $L_D = L_{\rm NL}$ ($N = 1$). The pulse shape adjusts itself during propagation to make such cancellation as complete as possible. Thus, GVD and SPM cooperate with each other to maintain a chirp-free pulse.

A more detailed investigation shows that N stands for the order of the soliton [8]. $N = 1$ corresponds to a fundamental soliton. If the input pulse has the form of

$$A(0, T) = \sqrt{P_0}\,\mathrm{sech}(T/T_0), \tag{3.39}$$

where the parameter P_0 (the peak power) and $T_0 (= 1.763 T_{\rm FWHM})$ are chosen such that N=1, the pulse will propagate along the fibre in the form of a fundamental soliton. The evolution of fundamental solitons is governed by

$$A(z, T) = \sqrt{P_0}\,\mathrm{sech}(T/T_0)\exp(\mathrm{i}\gamma P_0 z/2), \tag{3.40}$$

which is a strict solution of NLSE (i. e. Eq. (3.5 with $\alpha = 0$)). The most important feature of Eq. (3.40) is that the fundamental soliton propagates along the fibre only with a collective phase change which is frequency independent. The study of perturbation theory indicates that fundamental solitons are very stable. The exact shape of the input pulse used to launch a fundamental ($N = 1$) soliton is not critical. Even if the initial pulse deviates from a 'sech' shape, the combination of GVD and SPM affects the pulse in such a way that it evolves to become a 'sech' pulse. Moreover, solitons can form for values of N in the range $0.5 < N < 1.5$, even with the width and peak power of the input pulse varying

over a wide range (Ref. [8] Chapter 5).

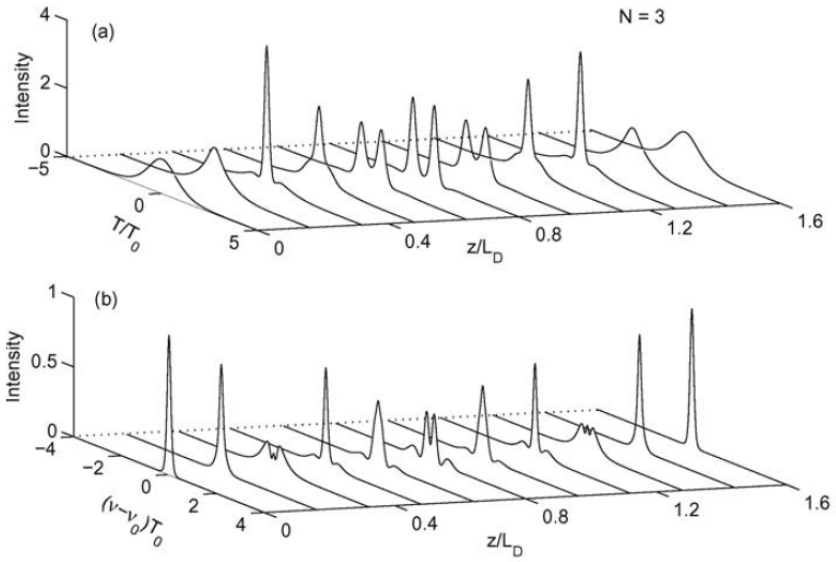

Figure 3.4: (a) Temporal and (b) spectral evolution over one soliton period of the third-order soliton (Ref. [8] Chapter 5).

If N is an integer greater than 1 as a pulse propagates along the fibre, both the shape and spectrum of the pulse will evolve periodically with a period of

$$z_0 = \frac{\pi}{2} L_D. \tag{3.41}$$

These periodically evolving pulses are called Nth-order solitons. As an example, Fig. 3.4 shows the temporal and spectral evolution over one soliton period of the third-order soliton [8]. Similar to a fundamental soliton, the temporal and spectral changes also result from an interplay between the SPM and GVD effects. The difference is that SPM dominates initially to broaden the spectrum but compress the pulse in time, but GVD soon catches up as the pulse becomes narrow, and broadens the pulse; then SPM dominates again. Therefore a periodical evolution occurs. Higher-order solitons are not stable to the perturbation of such effects as third-order dispersion and intrapulse Raman scattering. In practice, a higher-order soliton is split into several fundamental solitons at different wavelengths. This is a very important mechanism for SC generation in PCFs (see Section 4.2).

3.6 Polarisation Effects

All of the discussion about nonlinear phenomena through Sections 3.1 to 3.4 is based on a major assumption that the polarisation state of the light participating in the nonlinear interaction is always the same during propagation inside the optical fibre. Thus the description is a scalar approach (i. e. only the effect of $\chi^{(3)}_{xxxx}$, see Section 2.1.6). This is not really the case in practice. This section introduces effects due to the polarisation on nonlinear phenomena. Two effects, nonlinear birefringence and cross polarisation phase-matching are discussed.

3.6.1 Nonlinear Birefringence

The fibre birefringence mentioned in Section 2.4.4 is a built-in birefringence through the fibre structure. This kind of birefringence is called linear birefringence. When nonlinear effects in optical fibres become important due to a sufficiently intense optical field, nonlinear birefringence can also be induced and is intensity dependent. Nonlinear birefringence is actually a degenerate XPM effect. The XPM discussed in Section 3.2 is the nonlinear interaction between two different wavelengths copropagating in an optical fibre, so it is also called nondegenerate XPM. However nonlinear birefringence takes place between two polarisation modes at the same wavelength. Similar to nondegenerate XPM, the analytical description of nonlinear birefringence uses a set of coupled-mode nonlinear Schrödinger equations. Let us write down the conclusions here (Ref. [8] Chapter 6).

If the light is linearly polarised, the nonlinear contributions to the refractive index are given by

$$\Delta n_x = n_2(|E_x|^2 + \frac{2}{3}|E_y|^2), \qquad \Delta n_y = n_2(|E_y|^2 + \frac{2}{3}|E_x|^2), \tag{3.42}$$

where n_2 is the nonlinear-index coefficient defined in Eq. (2.35). The physical meaning of the two terms on the right-hand side of these equations is quite clear. The first term is responsible for SPM. The second term results in XPM because the nonlinear phase shift acquired by one polarisation component depends on the intensity of the other polarisation component. The presence of this term induces a nonlinear coupling between the field components E_x and E_y. Comparison between Eqs. (3.42) and (3.20) shows that the cross term in the refractive index

change in Eq. (3.42) has a different coefficient '2/3' rather than '2' in Eq. (3.20). This can be understood from the tensor property of $\chi^{(3)}$ (see Section 2.1.6) and the fact that in the scalar case, different wavelengths have an equivalent $\chi^{(3)}_{xxxx}$; however, in the vector case here, each polarisation component only corresponds to $\frac{1}{3}\chi^{(3)}_{xxxx}$ (see Eq. (2.33)).

The total refractive indices are

$$\bar{n}_x = n_x + \Delta n_x, \qquad \bar{n}_y = n_y + \Delta n_y, \tag{3.43}$$

where n_x and n_y are the linear refractive indices. The nonlinear contributions given by Eq. (3.42) play the role of increasing or decreasing the total birefringence. For example, when the input beam is polarised close to the slow axis (the y axis if $n_x < n_y$), nonlinear birefringence adds to the intrinsic linear birefringence, making the fibre more birefringent. By contrast, when the input beam is polarised close to the fast axis, nonlinear effects decrease total birefringence by an amount that depends on the input power. As a result, the fibre becomes less birefringent (see Section 4.4).

3.6.2 Cross Polarisation Phase-Matching

As mentioned in Section 3.4.2, FWM phase-matching in conventional single-mode fibres is usually achieved through birefringent phase-matching. This means FWM can not only occur for four waves with the same polarisation (scalar description in Section (3.4.1)), but can also happen for four waves with orthogonal polarisations, as long as the phase-matching condition is met.

After taking modal birefringence into account, we can rewrite the phase mismatch Eq. (3.33) as

$$\kappa = \delta\beta_D + \delta\beta_B + \Delta k_{\mathrm{NL}}, \tag{3.44}$$

where we factitiously separate $\Delta\beta$ to $\delta\beta_D$ and $\delta\beta_B$ for convenience of discussion. $\delta\beta_D$ is the dispersion induced phase mismatch (without taking modal birefringence into account), which is equivalent to $\Delta\beta$ in scalar case. $\delta\beta_B$ is the modal birefringence induced phase mismatch and can be thought as wavelength independent. $\delta\beta_B$ takes the form of $2(\beta_x - \beta_y)$ or $2(\beta_y - \beta_x)$, depending on if the input light is polarised along y or x axes. Δk_{NL} has the same definition as before but with only minor change on magnitude. In practice, Δk_{NL} can normally

be neglected compared with $\delta\beta_B$. For example, for a fibre with birefringence $\delta n \sim 10^{-5}$, nonlinearity $\gamma \sim 10$ W^{-1}km^{-1}, $\delta\beta_B \sim 200$ m^{-1} and $\Delta k_{\mathrm{NL}} \sim 1$ m^{-1} if the pump peak power is 0.5 kW. Phase-matching through the modal birefringence can also be called cross polarisation phase-matching. Chapter 5 will discuss the application of FWM through cross polarisation phase-matching.

Chapter 4

Supercontinuum Generation in Photonic Crystal Fibres

Spectral broadening and the generation of new frequency components are inherent features of nonlinear optics. The particular process known as supercontinuum (SC) generation occurs when narrow-band incident pulses undergo extreme nonlinear spectral broadening to yield a broadband spectrally continuous output. SC sources have attracted widespread interest because of their broad applications in both fundamental research and technical production such as optical device characterisation, optical coherence tomography (OCT) [49], microscopy [86][87] and spectroscopy [88]. SC generation has been studied extensively to achieve broadband sources since the 1970s [89][90]. PCFs have enabled a burst of new development in SC generation. This chapter introduces some background about SC generation and presents four projects on SC generation in PCFs. Section 4.1 gives an overview of SC generation. Section 4.2 discusses the physical mechanisms leading to SC formation in PCFs. Sections 4.3-4.5 present three projects completed during my Ph.D study. The first is visible continuum generation in a monolithic PCF device. The second is polarised SC generation in a highly birefringent PCF. The third is pump peak removal for ultra-flat SC generation in PCFs. Section 4.6 proposes dual-wavelength pumping SC generation in an all-fibre device and gives some preliminary results achieved so far. All of the SC generation demonstrations are based on a compact microchip laser operating around 1064 nm. Section 4.7 discusses some practical applications of SC sources. Section 4.8 gives a summary for this chapter.

4.1 Overview of Supercontinuum Generation

The development of SC generation may be divided into four generations [41]. The first-generation SC experiments were based on focusing short, intense optical pulses into bulk materials exhibiting a $\chi^{(3)}$ nonlinearity. In those experiments the primary mechanism was self-phase modulation (SPM). Efficient SC generation needs the maximum frequency shift comparable to the frequency of the carrier wave. Equation (3.14) shows that long effective interaction length and tight beam focusing are required to achieve efficient SPM. However, the interaction length is normally limited by diffraction in bulk media (see Section 2.4.3). In that case, ultrashort pulses (10-100 fs) of very high peak power (>10 MW) were needed. The main feature of SC generation in this stage was complexity due to the requirement of the high light intensity.

To overcome the interaction length problem, the second-generation of SC sources was developed based on silica optical fibres. Optical fibres can be made very long to increase the effective interaction length (see Section 2.4.3). This has led to a dramatic reduction in the pump power requirements compared with those for bulk media. In the early fibre experiments, the main mechanisms were cascaded stimulated Raman scattering (SRS) and four-wave mixing (FWM) [91][92]. SPM was relatively limited because the pump pulses were relatively long (10 ps-10 ns) and the power was relatively low. The limitations of SC generation in this stage were the asymmetric spectral broadening characteristics of SRS and the difficulties of phase-matching for efficient FWM (see Section 3.4).

In the third-generation of SC experiments, spectral broadening was still realized in silica fibres, but the requirement of multiwavelength optical source for wavelength-division multiplexing (WDM) transmissions awoke SPM as the primary spectral broadening mechanism. The aim in this stage was to operate the short pulsed SC source at gigahertz repetition rates and obtain a spectrum as flat and symmetric as possible with noise characteristics suitable for optical transmissions [93][94]. In these SC experiments, it was found that the GVD properties of the fibres played an important role [95].

The latest step of SC generation comes with the recent development of PCFs. Not only do PCFs take all advantages of conventional fibres in SC generation, but also the unique characteristics of PCFs such as endlessly single-mode (ESM) transmission, novel dispersion properties and high nonlinearity have brought SC

generation to a brand-new era. The single-mode transmission ensures that the output SC spectra are single-mode at almost all wavelengths, which is useful for many applications. As mentioned in Section 2.4.2, the dispersion of PCFs is tailorable over a wide range. The novel dispersion properties of PCF make single-mode phase-matching (see Section 3.4.2) much easier. Therefore FWM, one of the most important spectrum broadening mechanisms, is much more efficient. Further more, the large waveguide dispersion of PCFs can shift the ZDW of PCFs to shorter wavelengths, which makes the SC spectra extend to the visible region [36][40] since the lasers running at short wavelengths (Ti:sapphire laser, ∼800 nm) are already commercially available. The high nonlinearity of PCFs enables the SC system to be free of high power picosecond or femtosecond lasers, which makes the system more compact [43]. The following sections will focus on the SC generation in PCFs.

4.2 Mechanisms of Supercontinuum Generation in Photonic Crystal Fibres

SC generation in PCFs has been demonstrated very successfully since the first results were obtained in 1999 [35]. However, the understanding of the underlying physical mechanisms is not as easy as the experimental observation. In particular, the wide range of fibre types, pump wavelengths, pulse durations, and pulse energies that have been used in experiments has led to complexity in isolating the relative contributions of processes such as self-phase modulation (SPM), cross-phase modulation (XPM), four-wave mixing and modulation instability (FWM and MI), soliton fission, dispersive wave generation, and Raman scattering. This section will describe the dominant mechanisms in the cases of short and long pump pulses respectively.

4.2.1 SC Generation in the Femtosecond Regime

The first SC experiment in PCFs was demonstrated in 1999 [35], where 100-fs pulses centered at 790 nm were launched into a 75-cm section of a PCF with a calculated ZDW of 767 nm. The spectrum from the fibre output is reprinted in Fig. 4.1. It can be seen that even for such a short fibre, the SC is not only extremely broad, extending from 400 to 1600 nm, it is also flat (on a logarithmic

power scale) over the entire bandwidth.

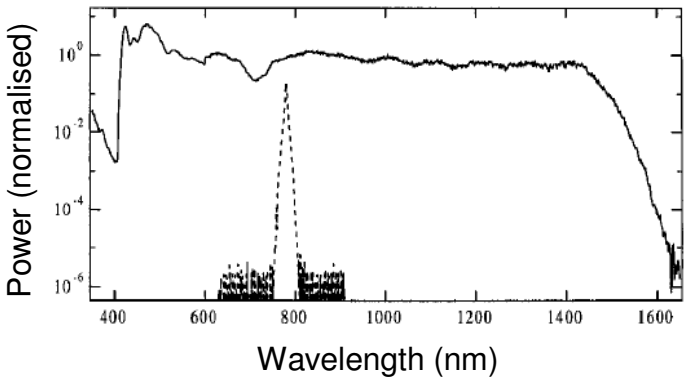

Figure 4.1: SC generated in a 75-cm-long PCF when 100-fs pulses with 0.8 nJ energy were launched close to the ZDW near 767 nm. The dashed curve shows for comparison the spectrum of input pulses [35].

This observation in Fig. 4.1 immediately raised a question: what nonlinear mechanism is responsible for such a massive spectral broadening of a femtosecond pulse? Since then, both theories and experiments about SC generation from ultrashort pulses have been studied extensively. As discussed in Section 3.2, for short pulses, SPM can produce considerable spectral broadening at the fibre output. The maximum spectral broadening factor in Eq. (3.18) is given approximately by the maximum SPM-induced phase shift determined by Eq. (3.15). Indeed, if the pump wavelength is located in the normal dispersion regime and far away from the ZDW, SPM is the dominant effect producing spectral broadening [38][96][97]. Even if the pump wavelength is in the anomalous dispersion regime, but if the fibre length is so short and the pulse is so intense that the dispersion effect is negligible, SPM is still the dominant spectral broadening effect [98]. However, as mentioned in Section 3.5, when the fibre length is comparable with the dispersion length L_D, solitons will be formed as the result of the interplay between the anomalous dispersion and SPM. The presence of solitons results in some new phenomena which can not be explained simply by SPM. For example, according to Eq. (3.18), shorter pulses should be broadened more than longer pulses with the same pulse energy. However, both modelling and experiment [38][39][96] show that the SC spectrum from longer pulses is much broader than that from shorter pulses. This means that soliton dynamics must play a crucial role in SC formation when pumping with femtosecond pulses in the anomalous dispersion

regime.

The soliton picture for SC generation in the femtosecond pumping scheme is now well understood. As mentioned in Section 3.5, when pulse and fibre parameters are chosen such that the soliton order N defined by Eq. (3.38) satisfies $N \geq 2$, higher-order solitons will be formed. For a non-integer value of N, the soliton order $\bar{N}$ is the integer closest to N. When neglecting all higher-order nonlinear and dispersive effects, a higher-order soliton shows periodic spectral and temporal evolution over a soliton period determined by Eq. (3.41) (see Fig. 3.4). However, higher-order effects are always present in optical fibres. In the femtosecond regime, higher-order dispersion and Raman scattering are the two most significant effects that can perturb such ideal periodic evolution and induce pulse breakup through soliton fission [99]. The fission of a higher-order soliton creates $\bar{N}$ fundamental solitons of different widths and peak powers. Their widths and peak powers are related to N as (Ref. [8] Chapter 5).

$$T_k = \frac{T_0}{2N+1-2k}, \qquad P_k = \frac{(2N+1-2k)^2}{N^2} P_0, \tag{4.1}$$

where $k = 1$ to $\bar{N}$. We can see from Eq. (4.1) that half of these solitons from fission have much narrower duration and higher peak power. After the initial fission, each constituent soliton experiences a continuous shift to longer wavelengths from the soliton self-frequency shift because the individual soliton bandwidths overlap the Raman gain (see Fig. 3.2). In the meantime, each soliton simultaneously emits dispersive waves through Cherenkov radiation [100][101] resulting from the higher-order dispersion perturbation. The wavelength of the dispersive waves is determined by a simple phase-matching condition requiring that the dispersive waves propagate at the same phase velocity as the soliton. Recalling that the phase of an optical wave at frequency ω changes as $\phi = \beta(\omega)z - \omega t$, the two phases at a distance z after a delay $t = z/v_g$ are given by [37]

$$\phi(\omega_d) = \beta(\omega_d)z - \omega_d(z/v_g), \tag{4.2}$$

$$\phi(\omega_s) = \beta(\omega_s)z - \omega_s(z/v_g) + \frac{1}{2}\gamma P_s z, \tag{4.3}$$

where ω_d and ω_s are the frequencies of dispersive waves and the soliton, respectively, and v_g is the group velocity of the soliton. The last term in Eq. (4.3) is due to the nonlinear phase shift occurring only for fundamental solitons. Its origin is

related to the phase factor $\exp(\gamma P z/2)$ appearing in Eq. (3.40). We should also notice that this term is only proportional to the peak power of the soliton and does not change with frequency if neglecting the frequency dependence of γ. If we expand $\beta(\omega_d)$ in a Taylor series around ω_s, the two phases are matched when the frequency shift $\Omega_d = \omega_d - \omega_s$ satisfies

$$\sum_{m=2}^{\infty} \frac{\beta_m(\omega_s)}{m!} \Omega_d^m = \frac{1}{2}\gamma P_s. \tag{4.4}$$

Note that P_s is the peak power of the Raman soliton formed after the fission process (and not that of the input pulse). Similarly, the dispersion parameters β_m appearing in Eq. (4.4) are at the soliton central frequency ω_s. As this frequency changes because of a Raman induced frequency shift, the frequency of dispersive waves would also change.

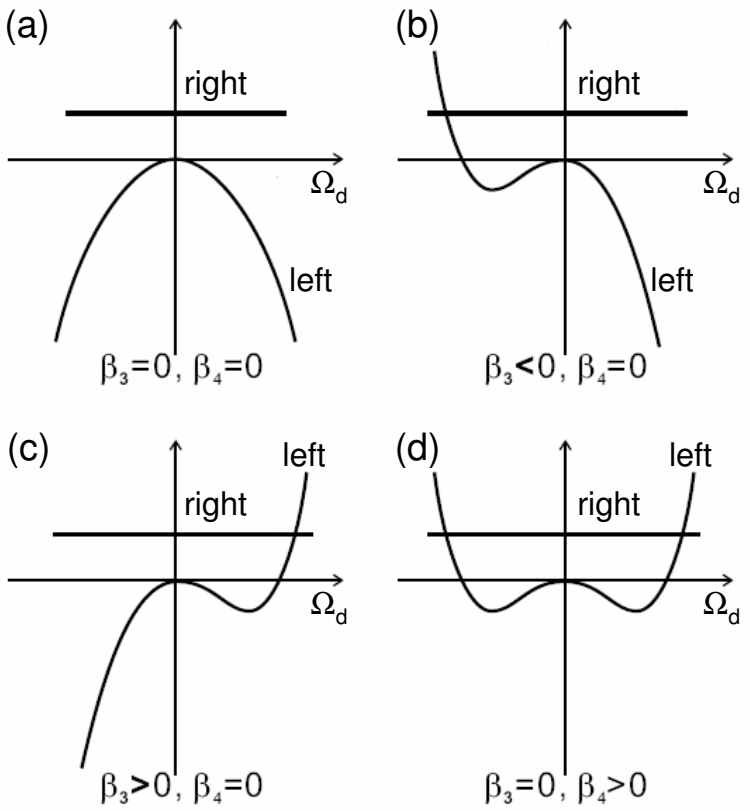

Figure 4.2: Phase-matching plot for soliton induced Cherenkov radiation under different conditions. The straight lines and curved lines represent the right- and left-hand side of Eq. (4.4), respectively [103].

We can see from Eq. (4.4) that no solution for Ω_d exists if the higher-order dispersive terms are neglected and $\beta_2 < 0$. This means that no phase matching occurs for Cherenkov radiation. However, if we include the higher-order dispersion, it is possible to achieve phase matching. We schematically plot the terms on the right- and left-hand side of Eq. (4.4) against Ω_d in Fig. 4.2 to show the phase-matching process under different higher-order dispersion configurations [103]. The crossing point of the straight line and the curved line is the phase-matched point. Figure 4.2(a) shows no crossing point because we neglect the higher-order dispersion. Figure 4.2(b) describes the case that the fibre has two ZDWs and the pump wavelength is closer to the longer ZDW. The dispersive waves are at the red-shifted side. This can suppress the Raman induced frequency shift by spectral recoil, which was observed in 2003 [104]. Figure 4.2(c) is the case that is normally observed [96]-[102], where the dispersive waves are emitted at the blue-shifted side.

At the phase-matching frequency, energy transfer between solitons and dispersive waves is unavoidable. Theoretical analysis [100] shows that the intensity of this radiation is proportional to the intensity of the soliton at the radiation frequency ω_d, so it is the spectral tail of the soliton at ω_d that boosts the radiation [101]. Therefore the gain of the dispersive wave generation is related to Ω_d not only through the phase-matching condition but also through the seeding efficiency of the original soliton spectral tail. The group velocity of the dispersive waves may not necessarily coincide with that of the Raman soliton. However, both theory and experiments reveal that they overlap temporally [105]-[107]. This overlap is related to the phenomenon of soliton trapping. The physical origin of soliton trapping can be understood as the sequential XPM by the Raman shifted soliton pulse. In other words, the Raman soliton traps the dispersive wave and drags it along to the short wavelengths. Since the soliton and the dispersive wave copropagate and overlap temporally, they can also interact in the form of FWM [108]-[111]. This process further flattens and broadens the SC spectrum. As a result the long wavelength edge of the continuum is limited by the high infrared absorption (see Section 2.1.3), whilst the blue edge is limited by the group-velocity mismatch with the longest wavelength solitions.

4.2.2 SC Generation for Longer Pulses: from Picosecond Pulses to CW Regime

After the demonstrations of SC generation in femtosecond regime, one may question whether the pump sources actually have to be as short as femtosecond duration to generate broadband SC. Due to the versatile dispersion properties of PCF, many nonlinear effects can be much more efficient even with lower pump power. Therefore SC generation has been achieved over a wide range of pulse duration from picosecond [40][41] to nanosecond [42][43] and even to CW [44][45][112].

As the pulse is much longer, we can not expect to explain the spectral broadening simply in terms of SPM or soliton fission like the femtosecond case. The dominant mechanisms behind the SC generation when pumping with long pulses have been identified as phase matched FWM/MI, and Raman scattering [40]-[45]. If the pump wavelength is in the vicinity of the ZDW, the spectral broadening will be initialized by phase matched FWM/MI (see Section 3.4). The contribution of Raman effect is relatively low because of the much higher gain of the phase matched processes [43]. However, when the phase-matching condition can not be satisfied, Raman induced broadening will be dominant [43][113][114]. It is easy to tell which process is dominant from the spectral shape since Raman induced broadening is typically asymmetric. We should notice that the Raman effect here is different from the intrapulse Raman scattering as in the femtosecond case since it is manifested by amplification from noise of a 13.2 THz frequency downshifted (Stokes) sideband from the pump. The Raman broading is not considered here as it occurs in any fibre, and cannot generate visible light from single IR lasers.

It should be mentioned that in the time domain, FWM/MI induces a fast modulation of the pump envelope which can subsequently break up (see Section 3.4.1) and evolve into a train of femtosecond solitonlike pulses after sufficient propagation distance. This is different from what mentioned in Section 4.1 because of the fact that the initial FWM/MI is seeded from noise. Nevertheless, the effects of the Raman soliton self-frequency shift and dispersive wave generation (see Section 4.1) are also present for such instability-generated solitons. In contrast to the femtosecond case, solitons play a relatively minor role during the first step of propagation since all of the characteristic lengths L_D and L_{NL} are much longer. In the later stage of SC evolution, soliton-related dynamics

described in Section 4.1 will play an important role and determine the blue edge of the SC spectrum [115].

The complete picture of SC generation pumping with long pulses or CW, with the pump wavelength in the vicinity of the ZDW is as follows. Parametric FWM/MI is mainly responsible for the initial SC formation. As MI breaks up the long pulses or CW into femtosecond pulses, solitons are formed and the soliton-related effects such as dispersive wave generation, soliton trapping and FWM between solitons and dispersive waves are then dominant in the later stage of SC generation.

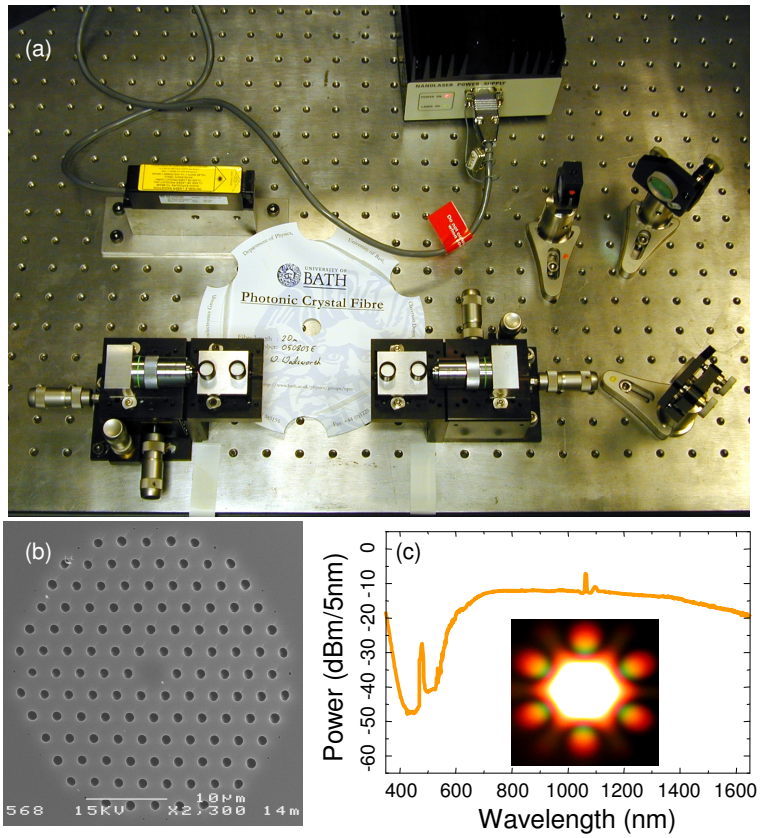

Figure 4.3: (a) Typical experiment setup for SC generation pumping with nanosecond microchip laser at 1064 nm. (b) The scanning electron micrograph (SEM) of the fibre used in the experiment. (c) The SC spectrum and far-field pattern [43].

One of the advantages of using nanosecond pulse lasers is that the SC sources can be made very compact because low cost and compact microchip lasers running at around 1064 nm are readily available. A typical SC source built at Bath

is shown in Fig. 4.3 [43]. We can see that the source is compact, bright, single mode and broadband. However, there are several issues we should raise. Firstly, the continuum is cutoff at 500 nm and can not be extended further to shorter wavelengths in this scheme. Secondly, this source is not perfectly linearly polarised and the power falls to half immediately if we use a polariser to control the polarisation. Thirdly, the residual pump peak is always there. In the following three sections, we will solve each of these separately.

4.3 Visible Supercontinuum Generation

Spatially and spectrally bright visible light generation has attracted much attention because of the potential applications in many visible-based microscopy and spectroscopy systems [86]-[88]. Early experiments to generate visible continuum in PCFs used femtosecond Ti:sapphire lasers ($\sim$ 800 nm) and a small-core PCF [36] or tapered fibres [37] or used picosecond Kr^+ (λ = 647 nm) lasers [40][41]. SC spectra extended from 400 nm across the visible and into the infrared. Femtosecond and picosecond lasers are however relatively complex. A more compact continuum source was demonstrated using a microchip passively Q-switched Nd:YAG laser at 1064 nm and a PCF (see Fig. 4.3) [43], however, the shortest wavelength in such a compact continuum source was typically $>$ 500 nm. This is not sufficiently short in wavelength for many visible-based microscopy and spectroscopy systems [86][88] or for testing of UV hollow core fibres being developed in our group. To produce a compact continuum extending to even shorter wavelengths, visible SC has been demonstrated from a Q-switched 532 nm source in PCFs and tapered fibres with 0.5-0.9 μm core diameter [116], however, the structures are readily damaged by high energy nanosecond pulses. To overcome this problem, several schemes with bigger core fibres were proposed and demonstrated. In 2004, an approach used both 1064 and 532 nm pump pulses combined, to yield a continuum from a 2 μm core PCF [113]. In 2005, two-stage processes were used to generate white-light continua which extended to blue in multiple tapers (ns, Q-switched 1064 nm laser [117]), and also in multiple PCFs (ps, modelocked 1060 nm laser [118]), with sequentially decreasing ZDW. In both cases the first stage was conversion of the infrared pump light to a continuum spanning both sides of the pump wavelength and extending down to the region 700-800 nm. This light was then sent to a second stage PCF or taper, where the ZDW is around

700-800 nm and so the light at 700-800 nm present in the continuum was used as a pump to generate a visible continuum. In early 2006, another technique was developed in our group to draw PCF tapers directly from the fibre drawing tower. These PCF tapers were designed with a continuously-decreasing ZDW along their length. When such a PCF taper was pumped with a nanosecond or picosecond source at 1.064 μm, a supercontinuum spanning from 0.372 μm to beyond 1.75 μm [119] was generated. At that time, this demonstration was thought to be a splicing-free version of the two-stage processes and therefore very compact and convenient. All of these demonstrations, whether the single-stage process or the two-stage processes, indicated that a pump source at short wavelengths and a fibre with ZDW close to the pump wavelength seemed to be absolutely necessary for the generation of a visible continuum extending to blue or UV. Our current improved knowledge points out that the short wavelength edge of a continuum is determined by dispersion induced group-velocity mismatch between the short-wavelength waves and the long-wavelength solitons (see Section 4.2) [107][111]. This implies that the pump wavelength may not necessarily be short for the visible continuum generation. As long as the pump source and the fibre dispersion are suitable for soliton-related SC generation dynamics, it is possible to produce continua covering the blue and UV regions using a single-stage process with an IR laser. Indeed, the most recent experiment in our group shows that a single 1064 nm laser and a uniform PCF can also generate a continuum extending to below 400 nm [115]. In Ref. [115], the fibre was simply designed to fulfill the group-velocity matching between the short-wavelength edge and the long-wavelength solitons. However, the project presented in this section was actually completed at the moment when these new theories were not established, and therefore was still designed in the frame of a short-wavelength pump source and a fibre with ZDW close to the pump wavelength through a novel two-stage process.

Those two-stage methods mentioned above either need to couple light at very different wavelengths into a small core fibre [113], or need to put tapers into D_2O to modify the cladding index of the tapers [117], or need to splice very different PCFs together [118]. All of these processes are tricky. The PCF taper technique demonstrated in Ref. [119] was a great improvement, but this technique was developed almost at the same time as the technique described in this section.

In our technique, a two-stage visible continuum generation pumped by a sim-

ple compact infrared laser was also considered, but with a fundamental difference compared with those mentioned above. The first stage of the process was not continuum generation in a fibre with ZDW $\lambda_D < \lambda_p$ (pump wavelength) [43][117]-[119], but rather FWM in a PCF with $\lambda_D > \lambda_p$ (i.e. pump in the normal dispersion region in Fig. 3.3). It has been previously shown that such fibres can be designed to generate narrow-band radiation at wavelengths widely separated from the pump wavelength with high efficiency [43]. To maximize the power close to the visible region in this first stage, the signal wavelength should be as short as possible, whilst maintaining efficient conversion from pump source. For the experiments described in this section the first fibre was a PCF properly designed to yield intense ∼700 nm pulses which were then fed into a second PCF with ZDW∼ 700 nm which generated SC from this output. As with the technique of [118], two PCFs with very different core sizes are required to extend the continua to short wavelengths, and splicing is not a straightforward low-loss option for coupling. Post-fabrication processing techniques for PCFs (see section 2.3.2) were therefore developed by W. J. Wadsworth, A. Witkowska, S. G. Leon-Saval and T. A. Birks to enable the whole two-stage optical processes to be carried out in a single monolithic fibre device. This has the additional advantage that the final output is not directly from the second, small core, fibre but is coupled back into an output pigtail of the first, 5 μm core diameter, endlessly single-mode fibre which may be easily coupled into an application system. This two-stage process is schematically shown in Fig. 4.4. The absence of a splice in this system ensured low coupling losses at all wavelengths and so maintained a high output brightness.

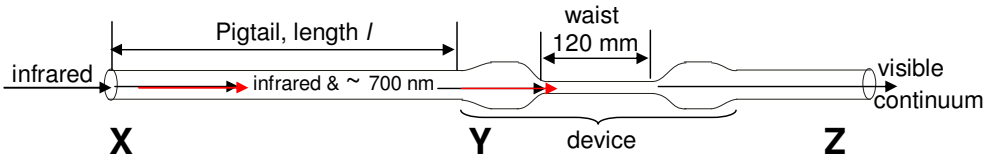

Figure 4.4: Schematic for the two-stage visible generation process. Infrared laser light enters at X and is converted in the pigtail into ∼700 nm by FWM. The ∼700 nm light at Y is then the pump for continuum generation in the inflated and tapered section. The output continuum is measured in the output fibre at Z. Both input and output sections are endlessly single-mode fibre with a relatively large (5 μm diameter) core.

Section 4.3.1 gives the initial results of visible continuum generation from a 1062 nm laser. Based on the analysis to the initial results, some changes were made on the tapered section to enhance the visible generation. Section 4.3.2 presents the improved results of visible continuum generation from a 1064 nm laser.

4.3.1 Visible Continuum Generation from a Microchip 1062 nm Laser

In the experiment the pump laser was a microchip laser running at a wavelength of $\lambda = 1062$ nm and emitting 0.6 ns (FWHM) pulses with 125 mW average power at a 25 kHz repetition rate (*Standa, STA-01*). After passing through a variable attenuator, which was made from a rotating half-wave plate ($\lambda/2$) followed by a polarisation beam splitter (PBS), these pulses were focused into a several meter long PCF structure as depicted in Figs. 4.4 and 4.5. A $\times 30$ anti-reflection coated

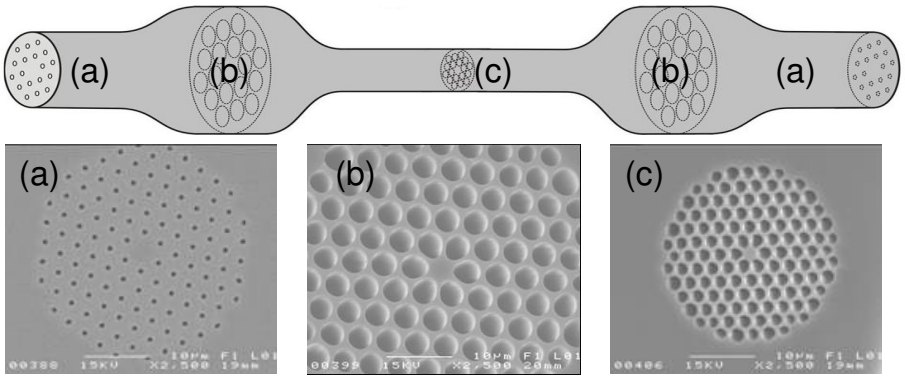

Figure 4.5: Schematic of the inflated and tapered section (top) and scanning electron micrographs (SEMs) for device-C1 (bottom): (a) initial PCF-C before processing, (b) inflated fibre, (c) taper waist. All of the SEMs are to the same scale.

aspheric singlet lens was used to optimize the coupling. The beam exiting from the device was then sent to an optical spectrum analyzer (OSA, *Ando, AO-6315B*) or a thermal power meter. Figure 4.6(a) shows the experimental setup. The fibre used in this experiment was an endlessly single-mode PCF (PCF-C, Λ=3 μm, d/Λ=0.26, d_{core}=5.2 μm, Fig. 4.5(a)). This has a ZDW at about 1103 nm and gives strong FWM gain at 734 nm (Fig. 4.6(b)) by the processes described in Section 3.4. The parametric conversion efficiency in a 5 m long section of this

fibre was determined by measuring the power of the signal and pump beams dispersed by a prism. For 100 mW input power, the total output from the prism was 23 mW, of which 16.5 mW was pump at 1062 nm and 6.2 mW was signal at 734 nm, a conversion of 27%. No radiation was measured at the expected idler wavelength of 1920 nm. It is believed that loss at long wavelengths is the reason for the absence of this wavelength in the output. This fibre with signal wavelength at 734 nm was chosen because the signal wavelength is close to visible region whilst maintaining high conversion efficiency from pump.

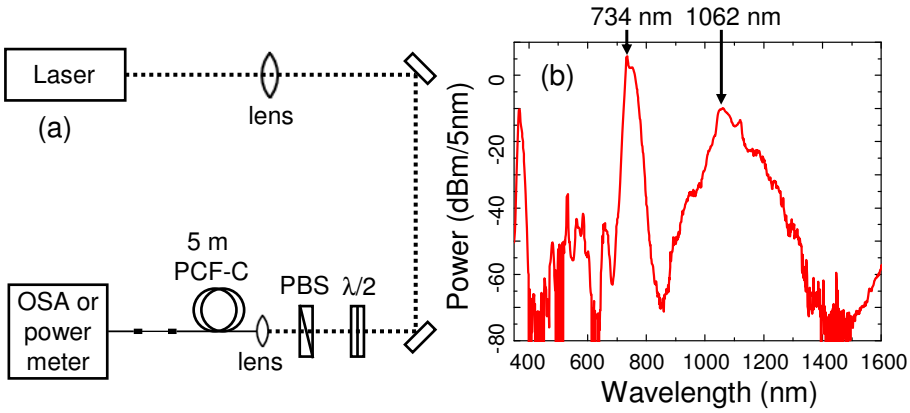

Figure 4.6: (a) Experimental Setup for the two-stage visible generation process. (b) Spectrum from a 5 m long section of bare PCF-C. Note that peaks in the region 350-550 nm in (b) are artefacts of the spectrometer used.

In previous studies it has been well established [36]-[41][70][116] that small-core PCFs are ideal for SC generation from pulsed sources at wavelengths from 600 to 800 nm. To take advantage of SC generation in PCFs pumped by the light converted from PCF-C at 734 nm, the light from PCF-C needs to be coupled into a structure with a small core and high air-filling fraction to achieve a ZDW at ∼700 nm. Bearing these ideas in mind, it was estimated that using the inflation and tapering processes described in Section 2.3.2 to make a high air-filling fraction (>0.9) and about 2.2 μm core device inside PCF-C could be ideal for visible continuum generation. Following my specifications, A. Witkowska made a device (device-C1) for me in the end section of PCF-C with very low loss. At first pressure was applied to the air holes in a length of PCF-C with dry nitrogen at 7-10 bar. The fibre was then heated and stretched in a flame. The pressure makes the holes expand (Fig. 4.5(b)), whilst the stretching reduces the trans-

verse dimensions of the fibre. The result, shown in Fig. 4.5(c), was that the core diameter was reduced from 5.2 μm to 2.2 μm, whilst the air-filling fraction was increased. Thus the fibre in the waist region of the inflated section was equivalent to a bulk small-core PCF, with a ZDW at around 700 nm. All transitions were made gradual so that the insertion loss of the entire device was 0.68 dB at 1550 nm. The waist length was 120 mm (Fig. 4.4).

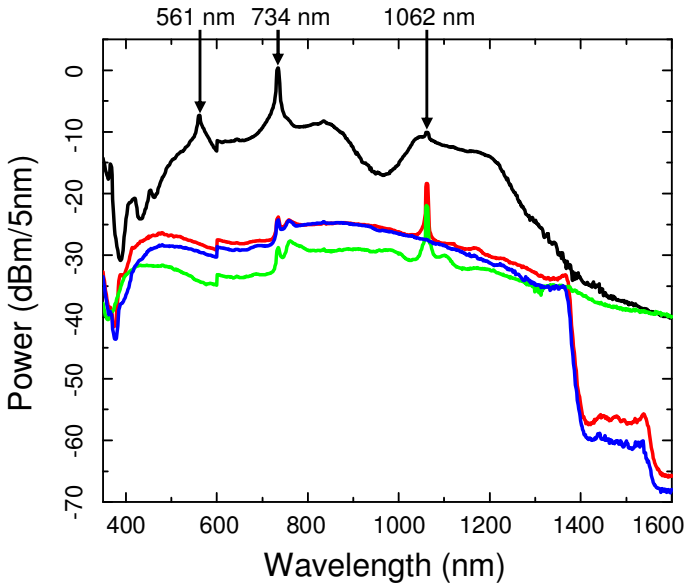

Figure 4.7: Output spectra for the two-stage visible continuum generation processes. Black trace is from device-C1, red trace is from PCF-C + 2.0 μm core diameter PCF, blue trace is from PCF-C + 2.0 μm core diameter PCF with long wavelength reflection dichroic mirror (λ_{pass} $\leq$950 nm) between them, and green trace is from PCF-C + 1.6 μm core diameter PCF.

The final spectrum with up to 40 mW output power from the device-C1 is shown in Fig. 4.7(black trace). With the variable attenuator technique, the continuum development with the launched power was also investigated. The output power spectrum for the device with $l = 5$ m is illustrated in Fig. 4.8(a), where the x-axis is the output average power, the y-axis is wavelength and the color indicates the power level for each wavelength component in the continuum spectra. It can be seen that the spectrum is not a flat continuum in the visible region but a broadened strong peak at 561 nm. It was believed that this 561 nm peak came from the unexpected phase-matching of the FWM process $2\omega_{734} - \omega_{1062} = \omega_{561}$ due to the unsuitable ZDW resulted from the incorrect dimensions

of the device. Similar to Fig. 3.3, the phase-matching curve for this device is given schematically in Fig. 4.9, which indicates that the ZDW of this device is longer than the pump wavelength. The strong 1062 nm pump source acts as a seed to drive the generation of 561 nm. To examine this idea, the tapered section was cut down from the 5 m pigtail and the output light from 5 m PCF C was sent into the tapered section by free-space coupling with a long wavelength reflection dichroic mirror between them. The output power spectrum is plotted in Fig. 4.8(b), from which it can be seen that both of the peaks at 1062 nm and 561 nm are quite weak compared with those in Fig. 4.8(a). As the mirror reflected most of the light at 1062 nm, the seed for the phase-matched FWM did not exist anymore and the generation efficiency of 561 nm was much lower.

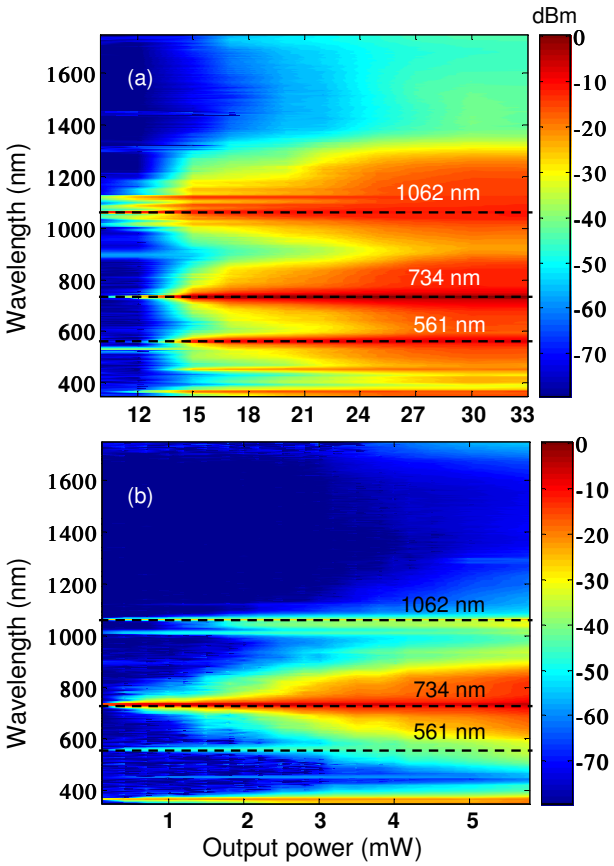

Figure 4.8: Output power spectra for (a) device-C1, (b) free space coupling of PCF-C + tapered section cut down from the pigtail, and with long wavelength reflection dichroic mirror between them.

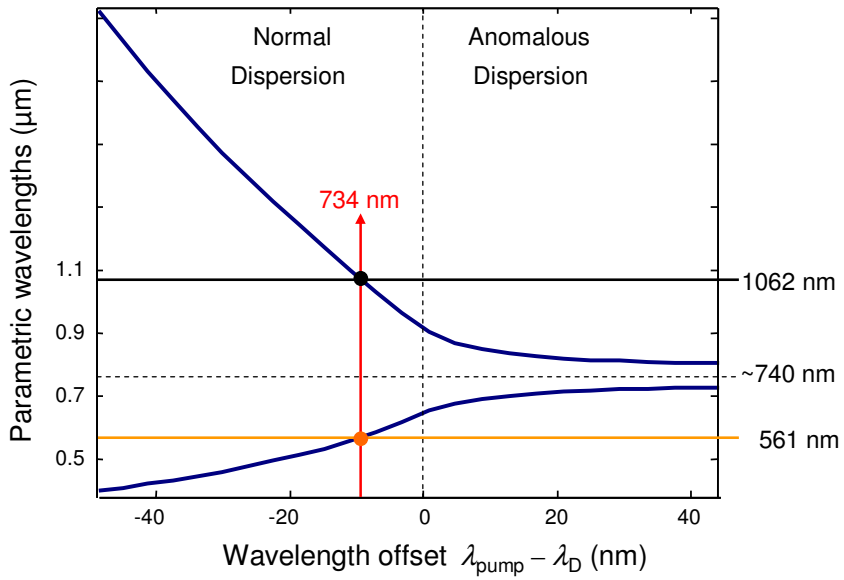

Figure 4.9: Schematic of phase-matching for the FWM process $2\omega_{734} = \omega_{561} + \omega_{1062}$.

In order to find the correct dimension of the device to achieve suitable ZDW for efficient visible continuum generation, output light from PCF-C was coupled using free-space optics to high air-filling fraction PCFs with different core diameters. The output spectra are plotted in Fig. 4.7, which shows that both 2.0 μm and 1.6 μm core PCFs are good candidates for efficient visible continuum generation in this kind of two stage process. This is because the smaller core PCF exhibits shorter ZDW, resulting in $\lambda_0 < 734$ nm in Fig. 4.9 to generate continuum instead of a single peak. The power was much lower than that of device-C1 because the free-space coupling efficiency between two very different PCFs was low. This demonstrated the value of the monolithic inflated and tapered device. By inserting a long wavelength reflection dichroic mirror between PCF-C and the 2.0 μm core PCF, it was found that the spectrum broadening beyond 1062 nm was not the contribution of Raman induced frequency shift from the pump. This can be seen from the fact that the difference between the red trace and blue trace in Fig. 4.7 is only the 1062 nm peak.

4.3.2 Enhanced Visible Continuum Generation from a Microchip 1064 nm Laser

Based on the demonstration and discussion in Section 4.3.1, it is believed that enhanced visible continuum generation from a compact infrared source is possible if the monolithic PCF device is well designed. This section demonstrates the bright single-mode visible continuum generation in the scheme described in Section 4.3.1, with some changes made to the system.

In this experiment, the idea was identical to the one depicted in Fig. 4.4 and the setup was the same to Fig. 4.6. The infrared pump source was changed to a Nd:YAG Q-switched microchip laser running at wavelength λ=1064 nm and emitting 0.6 ns (FWHM) pulses with 65 mW average power at a 7.2 kHz repetition rate (*Teem Photonics, NP-10820*). The average power is lower but the repetition rate is much lower, so the peak power is higher than the 1062 nm laser. The PCF used here was still PCF-C. Pumped by the 1064 nm laser, this fibre gave a strong FWM gain at 742 nm instead of 734 nm, allowing $>$ 35% conversion of the 1064 nm pump light over a 3 m long fibre. Compared with 27% conversion in Section 4.3.1, this was higher due to the higher peak power of the 1064 nm laser. The idler wavelength, calculated to be at 1880 nm, is out of the measurement range of the spectrometer and so still could not be observed.

Figure 4.7 indicates that smaller core PCFs (2.0 μm and 1.6 μm) are efficient for visible continuum in this kind of two stage process. One of the reasons for the unsuccessful results in Section 4.3.1 was believed to be the larger core diameter device waist (2.2 μm) exhibiting longer ZDW, which resulted in FWM in the normal dispersion regime (Fig. 4.9). Here the same inflation and taper techniques as in Section 4.3.1 were used but the parameters were changed to reduced the size of the device (device-C2) waist. The result, shown in Fig. 4.10 (middle row (c)), was that the core diameter was reduced from 5.2 μm to 1.7 μm. Then the fibre in the waist region of the inflated section satisfied λ_D $<$742 nm. The insertion loss of the entire device was just 0.12 dB at 1550 nm, which was significantly lower than previous 0.68 dB. The waist length was still 120 mm (Fig. 4.4).

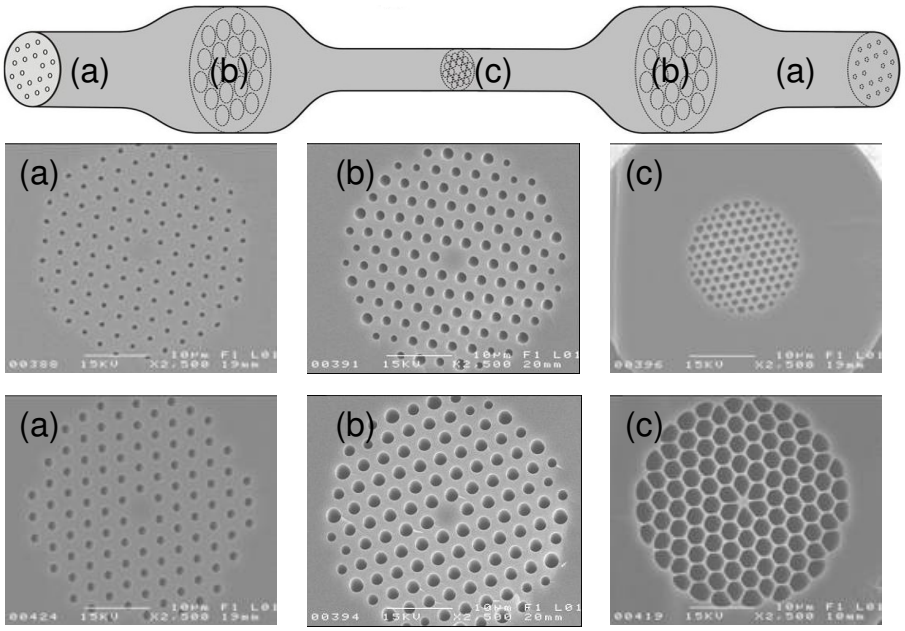

Figure 4.10: Schematic of the inflated and tapered section (top row) and scanning electron micrographs (SEMs) for device-C2 (middle row) and device-D (bottom row): (a) initial PCF-C or PCF-D before processing, (b) inflated fibre, (c) taper waist. All of the SEMs are to the same scale.

In a similar experiment to Section 4.3.1 the continuum development with the launched power was also studied using the variable attenuator technique. The evolution of the spectra with respect to output power and input pigtail length (l, Fig. 4.4) was measured by cutting back the fibre at the input end. The spectra for the device with $l = 7, 5, 3$ and 2 m are illustrated in Fig. 4.11. In order to compare the different pigtail lengths on an equal footing, The results for each length need to be presented for the same coupled input power. To achieve this, in these experiments the same technique was used to couple the pump laser into the input pigtail for each device and the alignment was carefully adjusted to achieve maximum output power, thus the highest output power attained with each different input pigtail length would correspond to the same maximum coupled pump power. So by setting the minimum of the x-axis to zero and the maximum to the measured maximum output power in each case it should be guaranteed that the scale of all graphs is the same in terms of coupled input power. From the spectra, it can be seen that 3 m long pigtail is the optimum one for maximum visible continuum intensity, although the difference between 5 m, 3 m and 2 m is not great. The presence of an optimum pigtail length can be understood from

the fact that the longer the pigtail is, the higher conversion efficiency is achieved from 1064 nm pump source to 742 nm, but also the stronger Raman effect occurs to decrease the peak power at 742 nm.

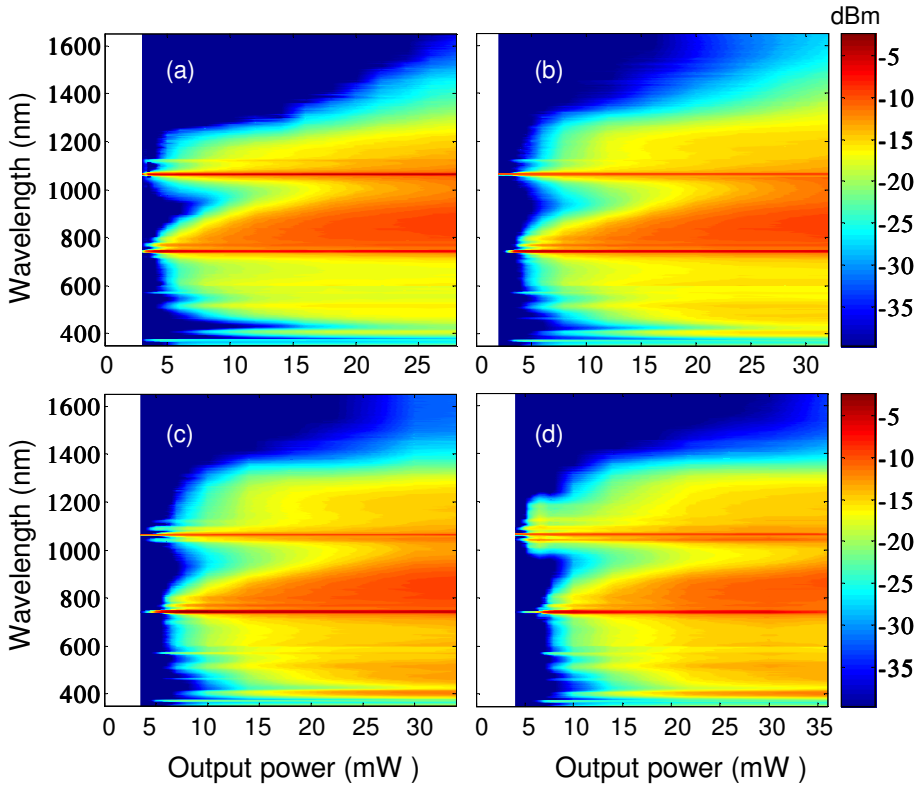

Figure 4.11: Output power spectra (point Z of Fig. 4.4) for (a) 7 m, (b) 5 m, (c) 3 m, (d) 2 m PCF-C with inflated and tapered section inside (device-C2). False-color intensity scales in dBm/5nm are the same for all plots.

The spectrum from the optimum pigtail length of 3 m is given in Fig. 4.12 (blue traces). The spectrum after 3 m of un-modified fibre is shown in Fig. 4.12(a), which demonstrates the spectrum incident on the inflated and tapered section at point Y in Fig. 4.4. The final output spectrum with 30 mW of average output power at point Z of Fig. 4.4 is shown in Fig. 4.12(b) (blue trace). It is obvious that SC generation taking place in the device fills almost the whole visible region and the gap between 742 nm and 1064 nm as well. In principle, this process is very similar to that reported in Ref. [43]. The difference is the shorter pump wavelength, shorter fibre ZDW, lower pump power and shorter length of fibre. It is the high nonlinearity resulting from the much smaller core size that overcomes

the lower pump power and shorter fibre length and delivers good performance in visible SC generation. Raman effect also acts on 742 nm and 1064 nm pump wavelengths in the inflated and tapered section, which makes additional contribution to the gap filling between the two peaks and the long wavelength extension to 1350 nm.

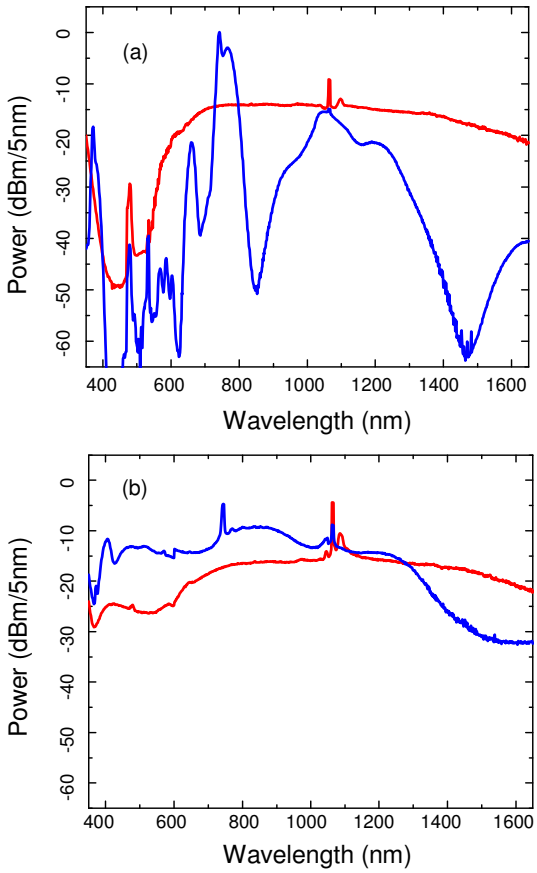

Figure 4.12: Spectra from (a) 3 m bare PCF-C (blue) and PCF-D (red), equivalent to point Y on Fig. 4.4, with average output power 37 mW, (b) device-C2 (blue) and device-D (red), point Z on Fig. 4.4, with average output power 30 mW. Note that peaks of blue curve between 350-550 nm in (a) are artefacts of the spectrometer used.

In comparison with Ref. [118], this device yields an intense peak at 742 nm instead of a continuum in the first stage, which means much more pump power could be provided to the second stage to enhance the visible continuum generation. With a single FWM process, the maximum conversion to the signal wavelength is governed by the partition of the energy of two pump photons at

1064 nm into a signal photon at 742 nm and an idler photon at 1880 nm. This gives a limit on the efficiency of conversion to 742 nm of 72% (half of this quantum limit, 35% conversion efficiency was achieved in this experiment). When the first stage is continuum generation, the pump light is spread out over a broad spectral range. Neglecting Raman contributions, half of the total energy will be at wavelengths shorter than the initial pump. Even if it is assumed that the energy of this short-wavelength portion is evenly distributed between 700 nm and 1064 nm, only about 30% will lie in the useful range, 700-800 nm, for the second stage of continuum generation. This is just 15% of the total pump power.

To illustrate the difference between a continuum and a FWM peak in the first stage, a new device (device-D), was made with the same fabrication parameters as device-C2 but in a different PCF (PCF-D, Λ=3.2 μm, d/Λ=0.43, d_{core}=4.9 μm, Fig. 4.10 (bottom row (a)). It can be seen that PCF-D is similar to PCF-C but has larger air holes, so its ZDW is at 1040 nm which is shorter than that of PCF-C. A 3 m length of PCF D can generate a continuum spanning from 600 to beyond 1700 nm when pumped by the same 1064 nm microchip laser. After interacting with the inflated section, the continuum extends to the visible region, but the power level is much lower than that of the device in PCF-C (device-C2) because of lower pump power at 700-800 nm. The spectra for 3 m length of bare PCF-D and device-D are plotted in Fig. 4.12 (red traces), which have the same average power level as PCF-C and device-C2 (Fig. 4.12, blue traces). From the spectra, it can be seen that device-D converted more power to long wavelengths (1300-1600 nm) than device-C2, and device-C2 gave much more brightness in the visible. In order to see the continuum evolution clearly, the output power spectrum of device-D is also plotted and put together with that of device-C2 in Fig. 4.13. Not only does Fig. 4.13(b) indicate much lower power level in the visible range and higher power level in the infrared region, but also it shows the rapid extension of the spectrum of device-D into the visible as soon as the continuum extends to wavelengths close to the ZDW of the inflated section. The contrast with Fig. 4.13(a) is striking, with the direct FWM from 1064 nm to 742 nm occurring efficiently at low power and providing high pump intensity for the visible SC generation. It should be noted that the performance of devices with SC first then ZDW $\sim$700 nm (like device-D) can be improved by increasing the pump power, or the length of the second stage as in Ref. [118] where meter-length fibres were used. The efficiency of our technique is shown by the excellent performance of device-C2, with a short

length and at low power.

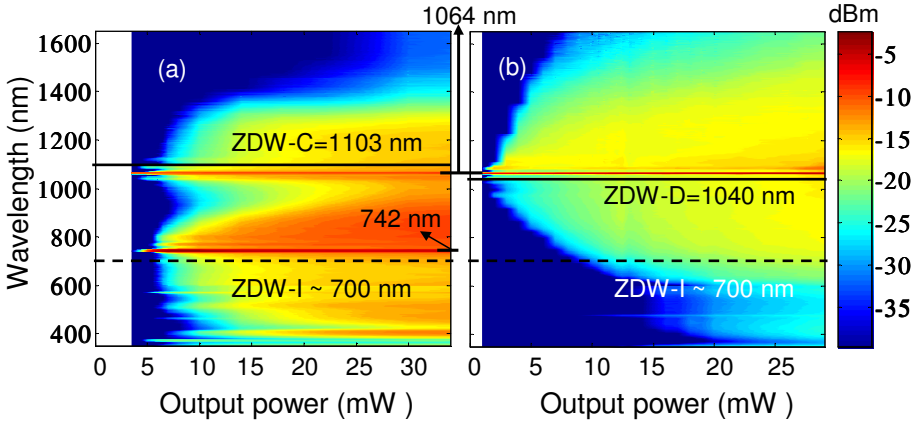

Figure 4.13: Output power spectra for $l = 3$ m for (a) device-C2, (b) device-D. False-color intensity scales in dBm/5nm are the same for both plots. Black solid lines are the ZDW of initial fibres (ZDW-C, ZDW-D) and black dashed lines are the ZDW of inflated sections (ZDW-I).

In summary, this section has presented a compact system which can give a bright single-mode visible light source (∼-20 dBm/nm) with a compact and low-cost microchip laser and a single fibre device. The device is convenient to fabricate and both of the ends are 5 μm core PCFs which are compatible with conventional fibre optical components and offer good coupling efficiency in practical applications. Enhanced visible continuum brightness will widen potential applications in biomedical imaging and visible-based microscopy and spectroscopy systems (see Section 4.7.2). The work described in this section has been published on Optics Express (C. Xiong, A. Witkowska, S. G. Leon-Saval, T. A. Birks and W. J. Wadsworth, vol. **14**, pp. 6188, 2006).

4.4 Polarised Supercontinuum Generation

In Section 4.3, I focused on extending the continuum to blue. Most of the researchers investigating SC have also paid attention to extending the spectrum to short wavelengths [116]-[119]. The continuum generated is generally not linearly polarised, as the fibre core is large (5 μm) and circular, whereas many applications require polarised SC output from a birefringent fibre (see Section 4.7.3). This is readily achieved for PCFs pumped at around 800 nm, where the small

cores required to achieve the necessary dispersion at the pump wavelength acquire large birefringence for very little ellipticity [80][120][121] (see Section 2.4.4). For operation at 1064 nm birefringence can be introduced through the application of stress rods whilst maintaining a circular mode. However, stress is not stable at high temperature and may be annealed out. Here I present a highly birefringent PCF based on simple form birefringence [30][122] introduced to the endlessly single-mode (ESM) PCF fabrication technique [43]. As described in Section 2.4.4, birefringence is simply introduced during fibre drawing process and offers very flexible control. A potential disadvantage of using form birefringence is that the mode is slightly elliptical which causes loss when coupling to circular core fibres or circular laser beams, however it is shown that this loss is small. Using this homemade highly birefringent PCF, a flat, linearly polarised, single-mode and broadband SC was generated.

4.4.1 Highly Birefringent PCF Fabrication

The birefringent PCFs were fabricated using a solid core PCF preform with uniform air hole diameters. This eliminates the need for a special stack with capillaries of different wall thickness [30]. During the final fabrication stage of drawing the preform to fibre (see Section 2.3.1), differential pressure was applied to enlarge two specific holes alongside the core to induce birefringence. Figure 4.14(a) schematically shows how to make two specific holes bigger. Figure 4.14(b) gives the SEMs of PCF-A at different scales. The measured d_2/d_1 ratio is 1.7, hole to hole pitch Λ=3.09 μm and hole-pitch ratio d_1/Λ=0.45. The two big holes make the core area slightly elliptical: the long axis to short axis length ratio is 1.25. It is the asymmetry that induces the birefringence. The calculated polarisation beat length at 1064 nm is 8.6 mm (see Eq. (2.3)) [123].

Unfortunately asymmetry of the core can also reduce the coupling efficiency to the circular pump laser mode or to other circular fibres. To check this the butt-coupling efficiency between this fibre and a standard symmetrical PCF was measured. The measured power penalty at 1550 nm was less than 6% (0.25 dB). The loss of PCF-A was also measured by the cut-back technique using the continuum source described in Fig. 4.3 (see Section 4.7.1). The loss spectrum is plotted in Fig. 4.15, which reproduces the shape of the loss spectrum of conventional fibres (see Fig. 2.6). It can be seen that the fibre attenuation at 1064 nm is about

10 dB/km.

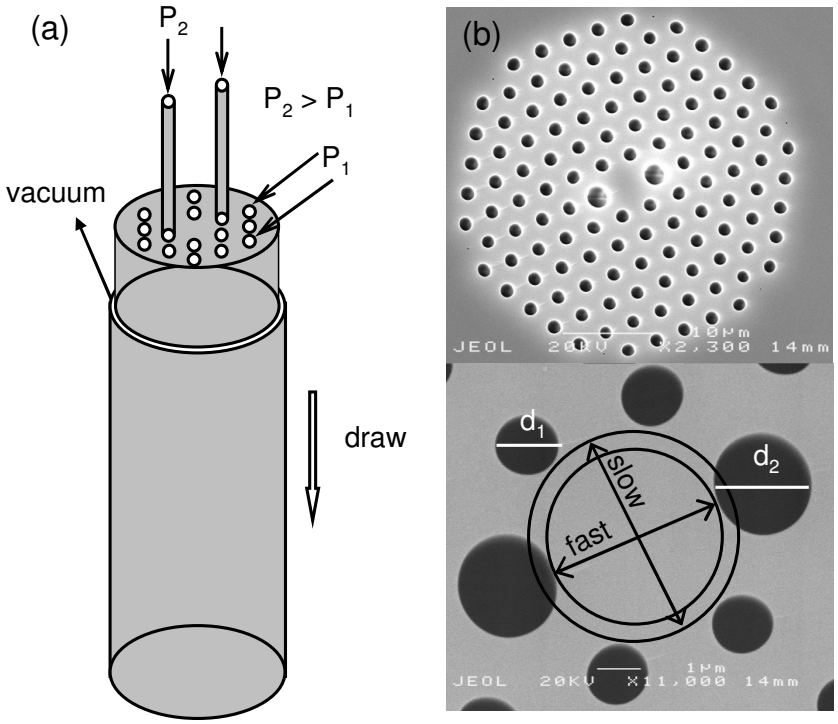

Figure 4.14: (a) Schematic of highly birefringent PCFs fabrication. (b) SEMs of PCF-A at different scales.

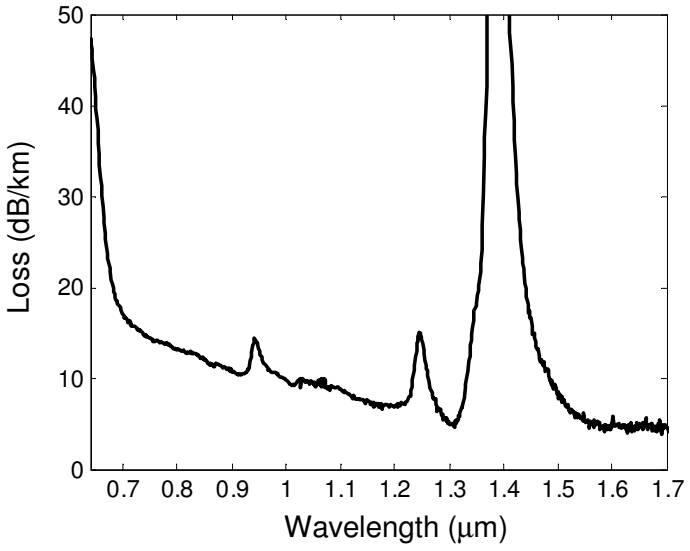

Figure 4.15: Measured loss spectrum for PCF-A.

4.4.2 Polarised Continuum Generation

In the SC experiment, the pump laser was a Nd:YAG Q-switched microchip laser (*Teem Photonics, NP-10820*) running at a wavelength of λ=1064 nm and emitting 0.6 ns (FWHM) pulses with 15 kW peak power at a repetition rate of 7.2 kHz. A polariser was used to purify the input polarisation and a rotating zero-order half-wave plate was put between the polariser and the fibre input end to adjust the input polarisation. A $\times$40 anti-reflection coated aspheric singlet lens was used to optimize the coupling. The experimental setup is illustrated in Fig. 4.16(a). The input coupling efficiency was as high as 60%.

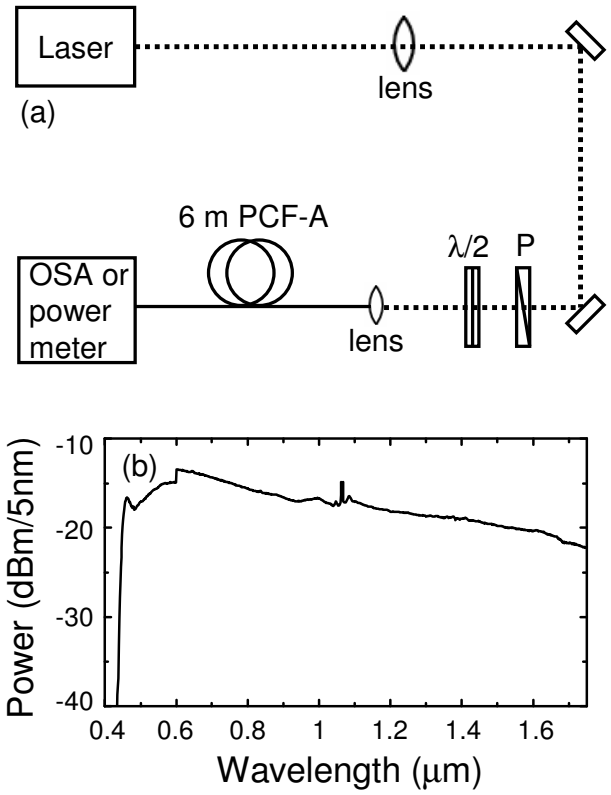

Figure 4.16: (a) Setup for polarised SC generation. P, polariser; $\lambda/2$, half-wave plate. (b) The spectrum measured from the output of (a). The average power is 30 mW. The input polarisation was along the slow axis. The step at 600 nm is an artefact of the spectrometer used. The resolution of the spectrometer was 5 nm.

Figure 4.16(b) shows the SC spectrum with an average power of 30 mW from a 6 m length of PCF-A when the input polarisation was along the slow axis of

the fibre. It can be seen that the short wavelength edge is as short as 450 nm and the spectrum is flat over the whole bandwidth from 450 to 1750 nm except for the residual pump peak. It should be noted that this has a shorter wavelength edge in the blue than Ref. [43] (see Fig. 4.3), although not as short as the results shown in Section 4.3.

In this study, the most important parameter is the polarisation purity of the continuum source. Therefore the polarisation of the output continuum was checked by a broadband birefringent crystal polariser. The polarisation extinction ratio (PER) is defined as the power ratio P_s/P_f or P_f/P_s, where P_s and P_f are the measured power when the output polariser's axis is set along the slow and fast axes of the fibre, respectively. The output PER was $P_s/P_f = 110$ and $P_f/P_s = 40$ when the input polarisation was along the slow and fast axes (99% and 97.5% power kept in a single polarisation). This is much higher than the PER (less than 2) of a SC produced by a PCF without birefringence and means the output light is well linearly polarised for all the spectral components. The difference between the slow and fast axes derives from the intensity-induced nonlinear birefringence (see Section 3.6.1). According to Eqs. (3.42) and (3.43), when the input polarisation is along the slow axis, the nonlinear birefringence enhances the linear birefringence; on the contrary, when the input polarisation is along the fast axis, the nonlinear birefringence can result in the total cancellation of the linear birefringence [120][121].

The effect of input polarisation on the spectrum of the SC generated was also checked. Figure 4.17(a) shows the spectra for different input polarisations with the same pump power. The spectra are similar except that the spectrum extends to shorter wavelengths when the input polarisation is along the fast axis. This small difference is because of the slightly different dispersion properties of the two polarisation modes. To understand this, the calculated group index for the two polarisation modes are plotted in Fig. 4.17 [123]. According the mechanism of SC generation described in Section 4.2.2, the extension to short wavelengths at the SC blue edge is determined by the group-velocity matching between short wavelength pulses and infrared wavelength pulses. Group-velocity matching requires they have the same group index. Pulses at very short wavelengths move more slowly than those at infrared wavelength since the group index is higher at very short wavelengths. It can be seen from Fig. 4.17 that the fast mode has a higher group index in the infrared region than the slow mode. This means that the infrared

wavelength pulses are matched to shorter wavelength pulses. As a result, the SC spectrum is extended further to short wavelengths. At 45° the spectrum is narrower because the power in both polarisation modes is only half of that in either pure slow or pure fast mode.

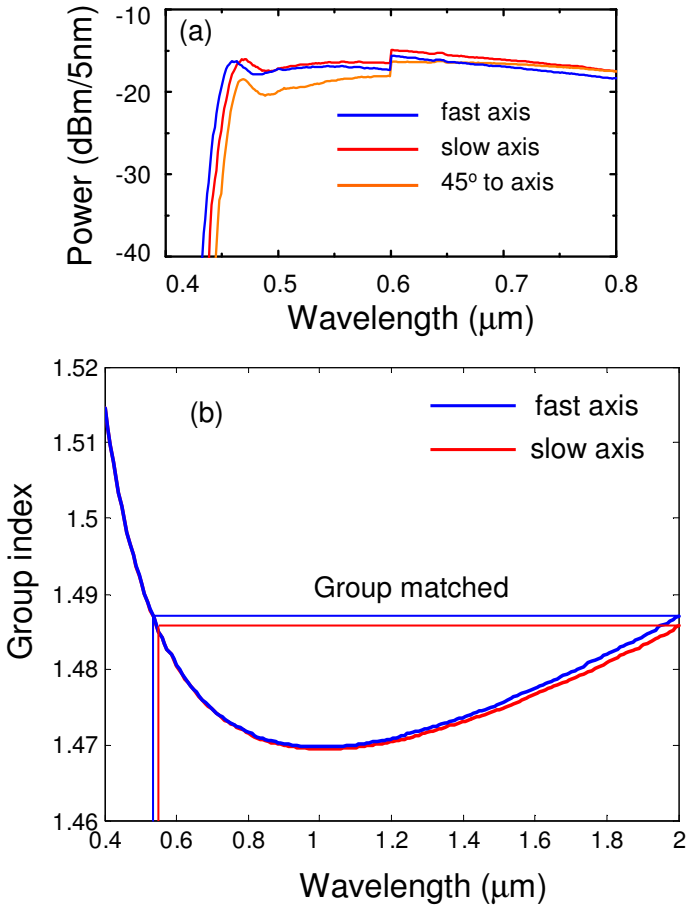

Figure 4.17: (a) Effect of input polarisation on the spectrum of the SC generated. The step at 600 nm is an artefact of the spectrometer used. The resolution of the spectrometer was 5 nm. (b) Calculated group index for the two polarisation modes [123].

In summary, a simple way to fabricate highly birefringent PCFs has been demonstrated. Using such a birefringent PCF, I made a compact continuum source with more than 99% of power in a single linear polarisation, whilst the modal asymmetry was sufficiently low that it yielded less than 6% (0.25 dB) measured power coupling penalty with a symmetrical PCF. The continuum spectrum was flat over the entire bandwidth from 450 to 1750 nm. The work described

in this section has been published as one part of a paper appeared in Optics Express (C. Xiong and W. J. Wadsworth, vol. **16**, pp. 2438, 2008).

4.5 Ultra-Flat Supercontinuum Generation

As mentioned in Section 4.2 and as seen in all SC sources, there is always a residual pump peak in the spectrum. Whilst the actual power remaining at the pump wavelength is small, it is concentrated in a narrow spectral line. This can cause artefacts in spectral measurements (see Section 4.7.1), placing high demands on stray light elimination and on the dynamic range of the detectors. This section demonstrates a method for removal of the residual pump in the nanosecond pulse pumping regime, without leaving an equally problematic spectral trough. It was first reported that the residual pump peak could be removed by using a fibre Bragg grating (FBG) followed by nonlinear flattening of the resulting spectral hole in another PCF. This method also flattens the modulation instability (MI) peaks around the pump peak. The pump power in a SC spectrum before removal was measured to be <10%.

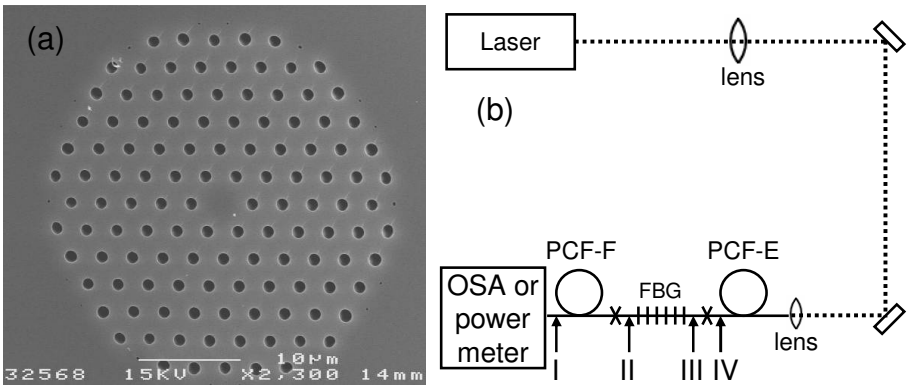

Figure 4.18: (a) The SEM for PCF-E, (b) diagram for experimental setup.

A similar continuum system to Fig. 4.3 was used in the experiment. The pump source was a 1064 nm microchip laser (7.2 kHz repetition rate, 0.6 ns pulse duration, *Teem Photonics, NP-10820*). The different fibres investigated here are labelled PCF-E and PCF-F (pitch, Λ=2.97 and 3.08 μm; hole-pitch ratio d/Λ=0.39 and 0.43; ZDW, λ_D = 1065 and 1050 nm respectively). Figure 4.18(a) shows an SEM image of PCF-E. SC spectra for a single piece of 20 m PCF-E or

15 m PCF-F are given in Fig. 4.19(a) (red and green traces), from which it can be seen that the spectra are very similar except that the MI peaks are slightly different, because of the different ZDW.

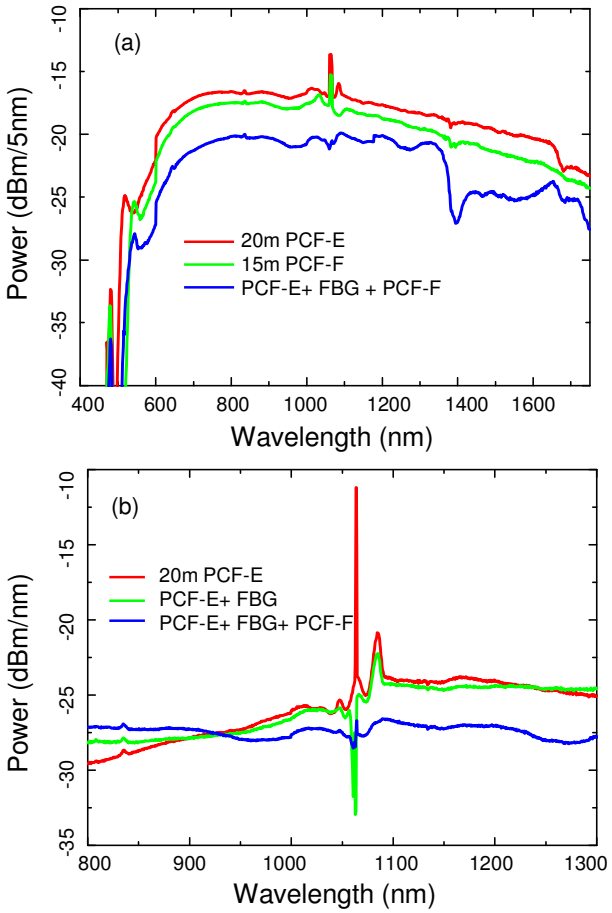

Figure 4.19: SC spectra for PCF-E, PCF-F, PCF-E+FBG+PCF-F. (a) 5 nm resolution and (b) 1 nm resolution.

In order to flatten the spectrum, at first a broad SC spectrum was generated from a single piece of 20 m PCF-E (point IV on Fig. 4.18(b)); then using the *Vytran* splicer (see Section 2.5), a FBG (central wavelength 1064 nm, bandwidth 1 nm, reflectivity 99%, 1060 nm single-mode step-index fibre as the pigtail), which operates as a filter to block the pump component in the SC spectrum and let other wavelengths pass, was spliced to PCF-E. As the mode diameters in the FBG pigtail fibre, PCF-E and PCF-F are similar, the modes of PCF-E and PCF-F both match reasonably well to the 1060 nm single-mode step-index

fibre and splice losses of 1.2 dB at 980 nm were achieved for each splice. By comparing the SC power after the FBG (Fig. 4.19(b), green trace, 6.07 mW, point II on Fig. 4.18(b)) with the power after the splice but with the FBG cut-back (Fig. 4.19(b), red trace, 6.64 mW, point III on Fig. 4.18(b)), it was found that less than 10% of the pump light remained unconverted in the SC process. The spectrum after the FBG then had no pump peak, but instead had a strong dip at the pump wavelength, and it still had strong MI peaks. However the brightness of the SC was such that the continuum itself may undergo nonlinear conversion. Therefore another different piece of PCF, PCF-F, was spliced at the output end of the FBG to make up the valley at pump wavelength. Figure 4.18(b) gives the experimental diagram. The MI peaks were also reduced as MI was not supported at the same frequencies in PCF-F as it was in PCF-E, as indicated in Fig. 4.19(a) (red and green traces). This can be understood from Fig. 3.3 in the sense that different pump wavelength offset from ZDW generates different MI peaks. Finally a very flat SC spectrum was achieved and plotted in Fig. 4.19(a) and (b) (both blue). It is clear that with a FBG and two different pieces of PCFs in the train,the residual pump peak can be efficiently removed and also the MI peaks can be flattened to make the SC spectrum much flatter. There is a step in the spectrum close to 1400 nm, which is because no great care was taken to remove OH during our fibre fabrication process and the total fibre length used was relatively long.

With the configuration of Fig. 4.18(b), the time stability of the final SC was also checked. The output spectra were measured every 30 minutes. The first measurement was regarded as the reference point. Figure 4.20 plots the power offset related to the reference point spectra. Figure 4.20 indicates that this SC generation system has very good time stability in a broad band from 550 to 1750 nm.

The above results are good, but there are two things that could be improved. One is the small fluctuation around the pump wavelength, as shown in Fig. 4.19 (both blue). The other is the relatively small output average power (only 4 mW). It is thought to be the problem of the performance of FBG, the coupling efficiency and the high splicing losses. In order to improve the system, a brand-new FBG (central wavelength 1064 nm, bandwidth 1 nm, reflectivity 99%, 1060 nm single-mode step-index fiber as the pigtail) was carefully spliced to the fibres to replace the old one and a $\times 30$ anti-reflection coated aspheric singlet lens

is used to optimize the coupling. The total splicing loss was reduced to 2.0 dB at 635 nm. The experiment setup was exactly the same to Fig. 4.18(b).

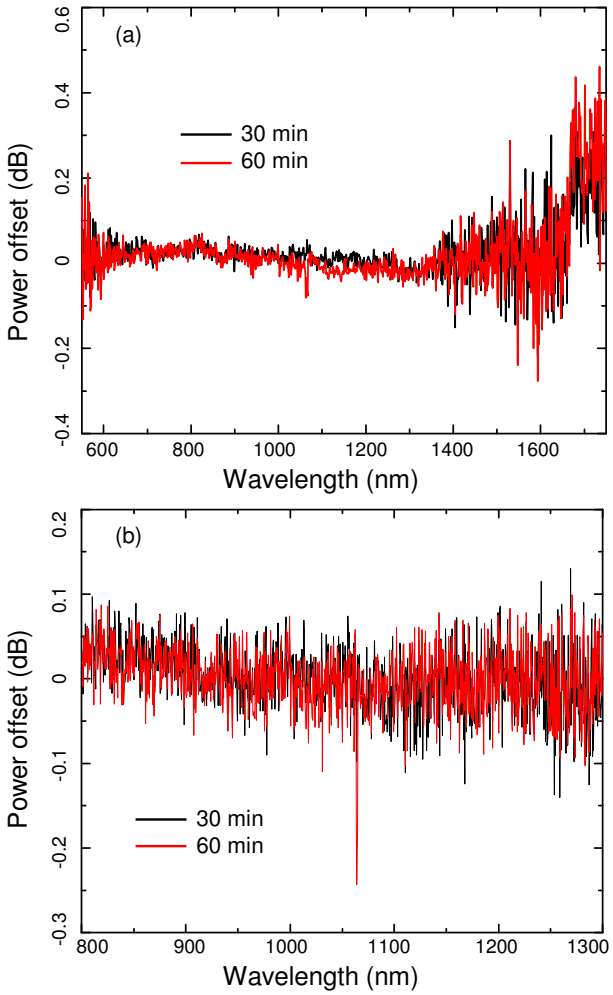

Figure 4.20: Time stability for ultra-flattened SC generation. (a) Low resolution 5 nm, (b) high resolution 1 nm.

The output average power was increased significantly (12 mW) compared with previous 4 mW. Unfortunately, the pump peak was still strong in the spectrum from point I in Fig. 4.18(b) at room temperature (Fig. 4.21(a), black trace). It was believed that this was because of a small deviation of the FBG central wavelength. To check this the transmission spectrum of the FBG was measured by the use of a low power SC source from 1047 nm pump laser. The transmission spectra of the FBG at different temperatures are shown in Fig. 4.21(b). It can be seen that the central wavelength of the FBG is 1063.5 nm at room tem-

perature (Fig. 4.21(b)-black trace). In order to shift the central wavelength to longer, the FBG was heated up to 96 °C to make the period expand. The central wavelength of the FBG at 96 °C is 1064 nm (Fig. 4.21(b), green trace), which is suitable for this experiment. The spectrum in this case is plotted in Fig. 4.21(a), red trace. The green trace in Fig. 4.21(a) is plotted by deducting the red trace from the black trace. The power difference at the pump wavelength is about 7 dB, which means that heating the FBG can shift the central wavelength to longer wavelength efficiently. There was still pump peak due to the insufficient reflection of FBG used. The output spectrum with this lower residual pump peak had a average power of 11 mW.

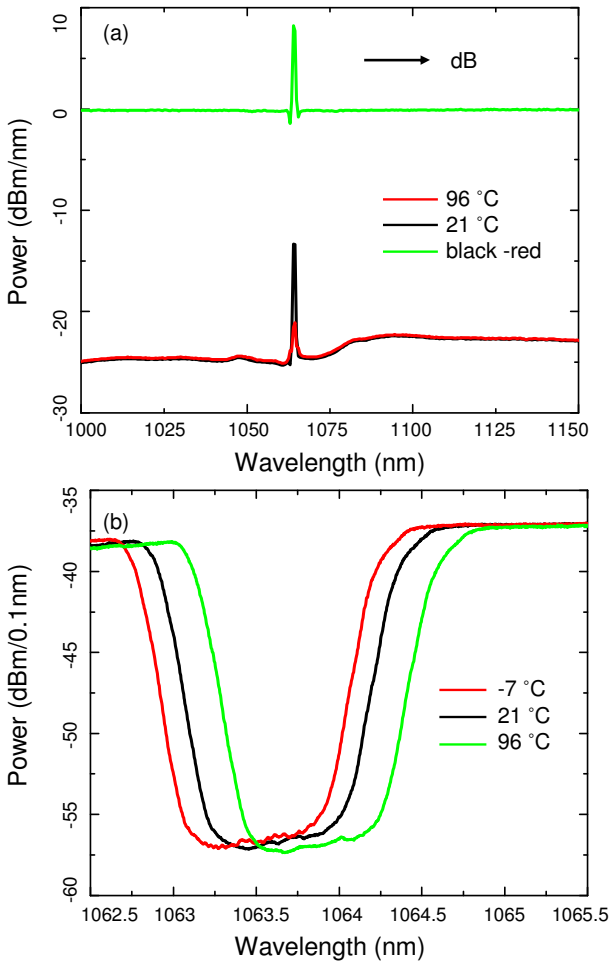

Figure 4.21: Flat SC generation when using the new FBG. (a) Flat SC spectra at room temperature and 96 °C, (b) transmitted spectra of 1047 nm pumped SC for the new FBG at different temperatures.

From the above two experiments, it is easy to draw the conclusion that by the combination of different PCFs and a FBG with high reflectivity and accurate central wavelength, one should be able to achieve ultra-flat SC spectrum with high brightness and good time stability. It should be stressed that this work was completed in 2005 and was presented at a conference (C. Xiong, S. G. Leon-Saval, F. Couny and W. J. Wadsworth, CLEO, paper **CWO4**, 2006). With the development of technique, there may be many possibilities to improve on the results shown above. For example, up to 10 nm bandwidth and 99.9% reflectivity FBGs are commercially available, which means that the central wavelength mismatch in the 1 nm bandwidth FBGs is not a problem any more. Further more, the splicing loss has been reduced to as low as 0.2 dB at 1550 nm very easily in other experiments of mine. And also in later experiments, it was found that the PCFs did not necessarily need to be very long to generate a broad continuum (5-6 m rather than 15-20 m). Short PCFs may mean that the continuum does not suffer from the high loss at around 1400 nm (see Fig. 4.19(a)). With all of these improvements this ultra-flat SC source will be much better and prove very useful to applications such as optical device loss measurement and fibre dispersion measurement.

4.6 Supercontinuum Generation pumped by Dual-wavelength in an All-fibre Device

To generate a broadband continuum in PCFs efficiently, we need to take full advantage of such nonlinear effects as soliton-related effects, phase-matched FWM/MI, XPM and Raman effects. It seems to be common sense that pumping in the vicinity of the fibre ZDW is the most efficient way to achieve this (see Section 4.2). In the long pulse pumping regime, when the pump wavelength λ_p is far away from the ZDW λ_D (i.e. $|\lambda_p - \lambda_D| = 100 - 200$ nm), either in the normal dispersion regime or in the anomalous dispersion regime, the cascaded Raman effect will dominate the spectral broadening because phase matching required for other processes is not easy to achieve [43][112]. The obvious disadvantage of a Raman continuum is that the spectra can not be extended to short wavelengths. Even if phase matching is achieved easily when $\lambda_p - \lambda_D \sim -40$ nm (i.e. normal dispersion), the phase-matched parametric FWM will yield two distinct peaks instead

of a continuum [43]. Therefore it is impossible to get a blue-shifted continuum if using a single-wavelength pump source with large normal dispersion. However, it has been found that pumping in the large normal dispersion regime can also produce a blue-shifted continuum if another pump source with anomalous dispersion [113][114] is provided simultaneously.

In previous dual-wavelength pumping SC generation experiments [113][114], the authors used a second-order nonlinear crystal to double the frequency of a passively Q-switched microchip nanosecond laser operating at an infrared wavelength (1064 nm or 946 nm). 15-35% energy was converted from the infrared wavelength to the second harmonic wave. Then both the residual fundamental wave and the second harmonic wave were coupled into a section of PCF several meter long with the ZDW in between (and far away from) the two pump wavelengths. The experimental setup is schematically shown in Fig. 4.22. The chromatic aberration of the coupling lens and the implementation of a small longitudinal displacement of the fibre allow a variation of the visible/IR power ratio coupled into the fibre core. When a filter was used so that only one pump wave (at either visible or IR wavelength) was fed into the fibre, only the Raman induced continuum was observed [113]. When both waves with a suitable power ratio $P_\omega/P_{2\omega}$ were coupled into the fibre, not only was the Raman effect induced continuum observed on the IR pump, but also the spectrum around the visible pump wavelength was completely modified to yield a smooth and symmetrical continuum. It is obvious that the existence of the IR pump suppresses the Raman effect of the visible pump.

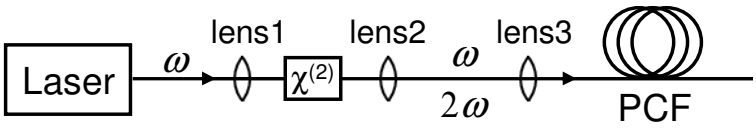

Figure 4.22: Schematic of the setup for the dual-wavelength pumping SC experiment.

The physical mechanism responsible for such continuum generation can in fact be understood in the context of the long pulse pumping regime discussed in Section 4.2.2. As the IR pump is in the anomalous dispersion regime, after a short distance of propagation in the fibre, the IR pump spectrum develops typical MI side-bands from noises. In the time domain MI results in a modulation

of the pulse envelope (see Section 3.4.1). This modulation effectively breaks up the original long pump pulse into multiple ultra-short pulses with widths on the order of tens of femtoseconds. Since the dispersion is anomalous at the IR pump wavelength, these pulses evolve into solitons. The spectra of the solitons overlap with the Raman gain bandwidth and therefore the pulses experience the soliton self-frequency shift. This results in the expansion of the IR continuum solely towards longer wavelengths. In the mean time, the copropagating visible wave can interact with the IR waves through XPM. As the visible wave is in the normal dispersion regime and the IR waves are in the anomalous dispersion regime, they can either be group-velocity matched or become group-velocity matched through Raman induced frequency shift. Further more, the solitons formed in the IR region have high peak power. Consequently, the nonlinear phase-shift imposed by the multiple solitons onto the visible wave through XPM is large. XPM-induced MI can occur on the visible wave even it is in the normal dispersion regime [8]. Similar to the MI of a single beam, in the time domain, this XPM-induced MI breaks up the long pulse to short sub-pulses; in the frequency domain, new frequencies are generated and the spectrum is broadened. The sub-pulses in the visible region can further interact with the IR solitons through soliton trapping and FWM as long as their group velocities are matched (see Section 4.2.1). The IR soliton self-frequency shift is limited by the IR absorption, which gives the red edge of continuum on the IR side. When the visible side is continuously extended to short wavelengths, the blue waves can not catch up the IR waves any more since they have higher group index. The group mismatch determines the blue edge of the continuum on the visible side. All of these phenomena have been predicted in theory [114] and observed in experiments [113][114].

The dual-wavelength pumping scheme for SC generation not only clearly demonstrates the nonlinear effects involved in SC formation, but also provides a way to generate a flat, spectral locally broadening continuum which may be useful for some applications. The combination of an IR microchip laser and a frequency doubling crystal is a good idea to provide a dual-wavelength pump source. The advantages are that the second harmonic can be rather short and the power ratio $P_\omega/P_{2\omega}$ input to the fibre can be easily controlled. However the disadvantages are also obvious. Firstly, using frequency doubling crystals normally induces spatial walk-off between the fundamental and second-order harmonics [124]. Such walk-off makes it very difficult to couple them both into an optical fibre. Secondly, even

if there is no spatial walk-off between the two waves, it is still tricky to couple the two waves at such different wavelengths into a fibre using one lens because of the lens dispersion. Thirdly, the short wavelength in the dual-wavelength system is fixed unless the IR laser is changed as in Ref. [114]. If a fibre rather than a crystal can be used to generate the short wavelength, it is also possible to obtain a dual-wavelength fibre source. According to the discussion in Section 3.4.1 and the demonstration in Section 4.3, this can be achieved through FWM in the normal dispersion regime in a PCF. By changing the dispersion of the PCF, the short wavelength peak can be easily tuned from 686 to 975 nm [43] with reasonably good conversion efficiency. If the output beam from this fibre is then coupled to a second PCF with right dispersion, an all-fibre dual-wavelength pumping system is achieved to yield continuum.

Normally the second PCF is very different from the first PCF because of the different dispersion requirements. There are three methods to realize the coupling between two such PCFs. One is the post-processing technique used in Section 4.3. The visible continuum generation system in Section 4.3 is actually a kind of dual-wavelength pumping system. However, in Section 4.3.2, the two pump wavelengths were both in the anomalous dispersion regime, so the spectral broadening mechanism is totally different from that considered here. In Fig. 4.7, the comparison of blue and red curves shows that the IR pump wavelength has nearly no contribution to the visible broadening in the second PCF. In Section 4.3.1, although the short wavelength pump was in the normal dispersion regime, no continuum but only strong FWM seeded by the residual IR pump was observed. There are two reasons for this. First, the length of the taper rig limits the length of the tapered structure to 12 cm. It is obviously not long enough for soliton-related effects that are the most important to the SC generation reported in Ref. [114]. Second, the 734 nm peak is much closer to the ZDW than 1062 nm, therefore the 734 nm pulse moves faster than the 1062 nm pulse. However, since solion effects are negligible, the nanosecond pulses will not suffer from the pulse walk-off in such a short fibre. The XPM induced spectral broadening is also negligible in this long pulse pumping case. Thus, only strong FWM shown by the black curve in Fig. 4.7 was observed. The length limit of the taper rig makes post-processing technique unsuitable for this all-fibre dual-wavelength pumping scheme. The second method is the free-space coupling as shown in Fig. 4.22. It has been mentioned that the lens dispersion is a problem in this case. A third

method, splicing the two PCFs together, can solve this problem. Although splicing two very different PCFs is tricky, a splicing technique has been developed very successfully to reduce the splicing loss to as low as 2.5 dB [84]. A further improvement of such splice will be proposed in Chapter 6. The splicing loss should be able to be reduced to lower than 1 dB.

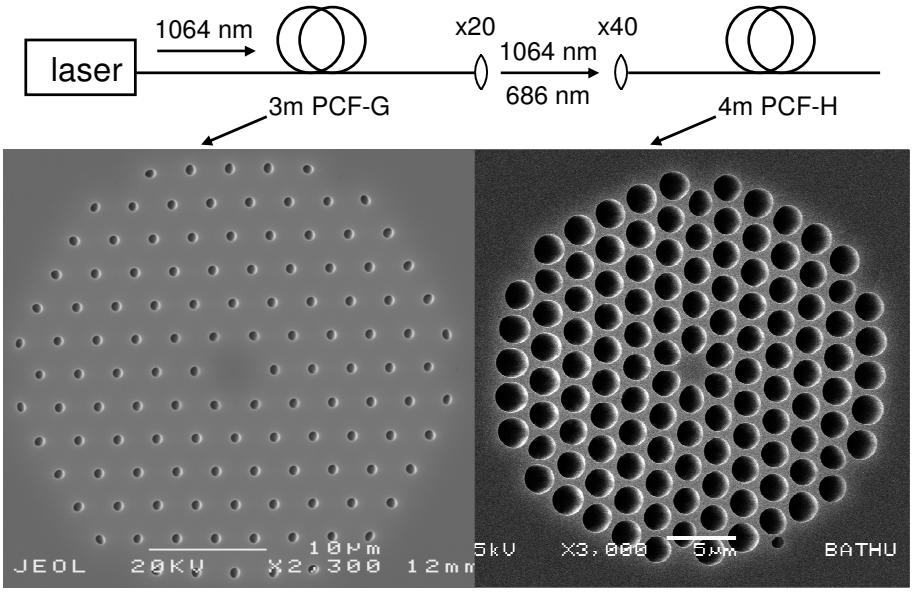

Figure 4.23: Schematic of the experimental setup for SC generation pumped by dual-wavelength in an all-fibre system and the SEMs of the two PCFs used.

To have a look at the performance of this all-fibre dual-wavelength pumping scheme, a quick experiment was demonstrated using free-space coupling. The two PCFs used in the experiment are shown in Fig. 4.23. PCF-G has a pitch Λ=3.2 μm, a hole-pitch ratio d/Λ=0.28 and a core diameter about 5.5 μm. The calculation indicates that the ZDW of PCF-G is about 1117 nm [74]. PCF-H has a pitch Λ=2.4 μm, a hole-pitch ratio d/Λ=0.8 and a core diameter about 2.3 μm. The calculated ZDW of PCF-H is about 800 nm [123]. The pump source was a 1064 nm microchip laser (7.2 kHz repetition rate, 0.6 ns pulse duration, *Teem Photonics, NP-10820*). As the pump wavelength is in the normal dispersion regime of PCF-G, FWM occurred with the signal wavelength at 686 nm. Figure 4.24 shows the spectrum from a 3-meter length PCF-G pumped by the 1064 nm laser. The idler wavelength is calculated to be 2369 nm which exceeds the upper limit of the spectrometer used. The average output power from PCF-G

was 42 mW. The conversion efficiency from pump to 686 nm was measured to be about 30%. The length of PCF-G was chose to be 3 meters for the trade-off between the best FWM efficiency and the least Raman generation from 686 nm.

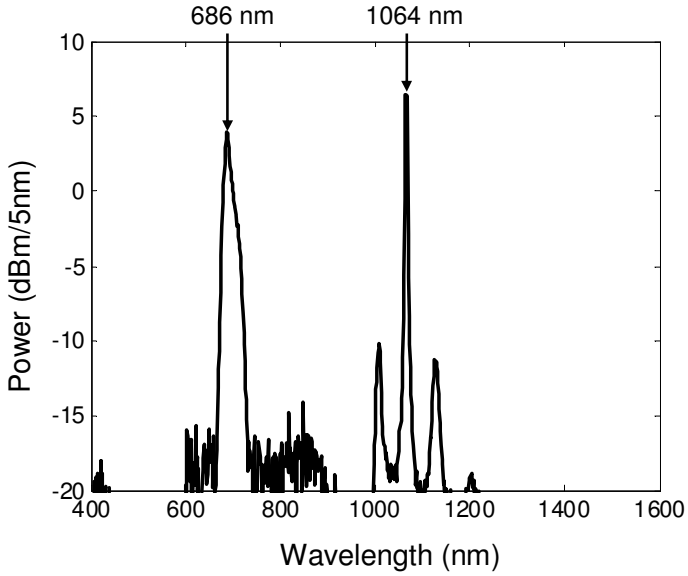

Figure 4.24: FWM spectrum from a 3 m PCF-G pumped by the 1064 nm microchip laser. The average power is 42 mW. The resolution of the spectrometer is 5 nm.

As can be seen in Fig. 4.23, the two PCFs are very different. Therefore one $\times 20$ and one $\times 40$ IR anti-reflection coated aspheric singlet lenses were used to couple the PCF-G output into PCF-H. To investigate the contribution of the two pump wavelengths to the SC formation, two filters were used to allow total filtering of the visible or IR waves at the launching end of PCF-H. One was a long wavelength passing filter which only let wavelengths longer than 715 nm pass through. Another one was a dichroic mirror which reflects light with wavelengths between 1047 nm and 1270 nm. Their transmission spectra were measured using a SC source depicted in Fig. 4.3. The spectra are shown in Fig. 4.25. It can be seen that they can isolate one wavelength and transmit another wavelength very well. At first the coupling was optimized to yield maximum continuum bandwidth on the short wavelength side. With the help of these two filters, the spectra were then measured with single-wavelength pump and dual-wavelength pump, respectively. The spectra are plotted in Fig. 4.26. It can be seen from Fig. 4.26 that only dual-wavelength pumping can result in an efficient broadening

on the visible wavelength side (blue curve). The comparison of the blue and red curves shows that the IR pump is important to the visible continuum generation. When the IR pump was blocked, there was no visible continuum at all except the Raman shift of 686 nm (red curve). The comparison of the blue and black curves tells us that the visible pump is also important to the visible continuum generation. When 686 nm was blocked, its Raman peak was transmitted because the blue edge of the filter is 715 nm. It was this small amount visible light that helped the generation of continuum between 400 to 600 nm (black curve). The presence of the 686 nm pump increased the continuum level by 20 dB (blue curve).

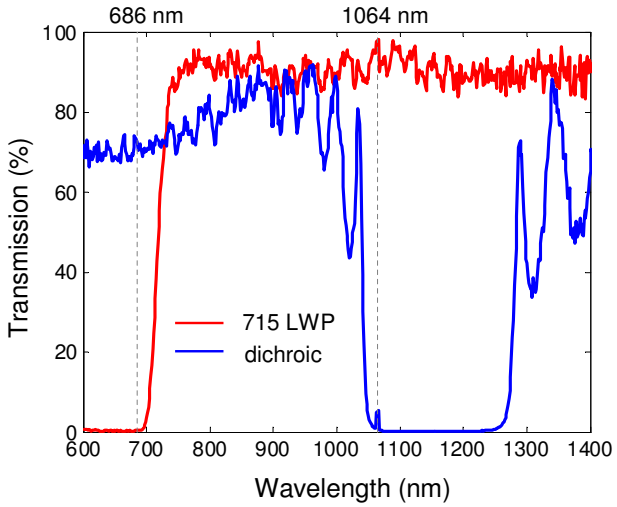

Figure 4.25: Transmission spectra for the 715 nm long wavelength passing filter and 1047-1270 nm reflection dichroic mirror.

The continuum formation observed in Fig. 4.26 was as expected. Unfortunately, the power level of the visible continuum was not very high. There are two reasons for this. First, the power measurement showed that the average output power was only 6.62 mW for dual-wavelength pump while the input power was 37 mW. The average output power was only 0.75 mW for 686 nm pump and only 5.46 mW for 1064 nm pump. It is obvious that the IR anti-reflection coating of the lenses used in the experiment affected the coupling of 686 nm. The dispersion of the lenses also led to the huge difference of coupling efficiency between 686 nm and 1064 nm. It is the free-space setup that makes the overall coupling efficiency low. Second, it can be seen from Fig. 4.26 that the Raman shift at 686 nm for

the single 686 nm pump and dual-wavelength pump is almost the same (blue and red curve). This means that even with dual-wavelength pump, the Raman shift is not efficiently suppressed as described previously. To understand this, the calculated group index for PCF-H is plotted it in Fig. 4.27. It can be seen that there is a big difference between the group indices of 686 nm and 1064 nm. Their group mismatch makes the contribution of the 686 nm pump to the continuum inefficient. It is believed that the 686 nm pump contributes to the continuum formation through the spectral tail at the short wavelength.

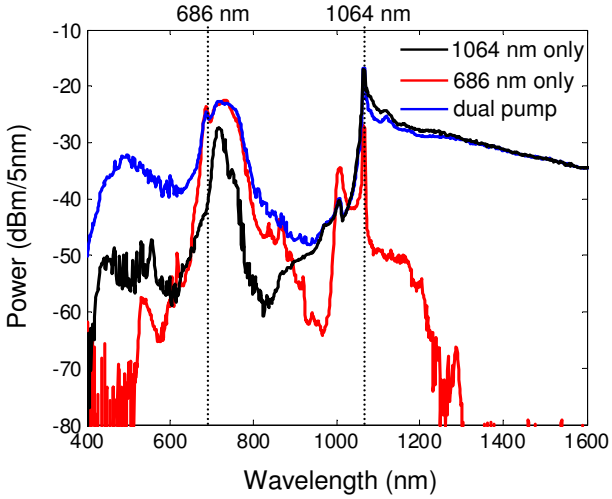

Figure 4.26: Spectra from PCF-H pumped by 1064 nm only (5.46 mW), 686 nm only (0.75 mW) and dual wavelength (6.62 mW).

The results shown here are just preliminary. There are two improvements which can be made in the future. First, the coupling efficiency can be improved by developing a novel splicing technique. Second, a new PCF with the right dispersion can be designed to make the two pump wavelengths group matched. With these developments, a real all-fibre dual-wavelength pumping SC generation system will be implemented.

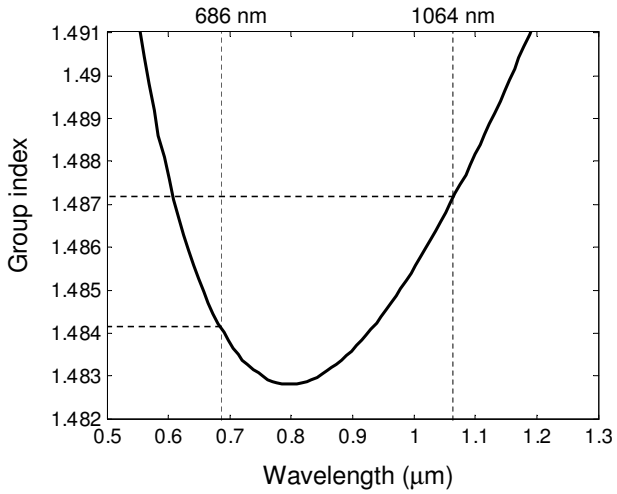

Figure 4.27: Calculated group index for PCF-H [123].

4.7 Applications of Continuum Sources

Supercontinuum (SC) sources in PCFs have many potential applications in both research and industry. This section introduces some of the applications of SC, especially visible continuum and polarised continuum.

4.7.1 Optical Device Characterisation

Before the invention of SC sources in PCFs, it was difficult to find a broadband source to test the optical properties of optical devices. Since the advent of the compact SC source built from a piece of PCF and a microchip laser (see Fig. 4.3), the SC source has been widely used for optical device characterisation, such as optical device transmission measurement and dispersion measurement.

Transmission Measurement

It can be seen that SC sources built like Fig. 4.3 have very good spectral flatness and are single mode at all wavelengths. The good mode shape makes it very convenient to couple the beam into other devices for measurement. The flat spectrum make such a SC source the best candidate for transmission measurement of optical devices. The most common transmission measurements in our lab are the transmission band measurement of photonic band gap fibres (PBGFs), filters and dichroic mirrors (see Fig. 4.25) and transmission loss spectrum measurement for home-made PCFs (see Fig. 4.15).

As an example, Fig. 4.28 shows a schematic diagram for the loss measurement of a PCF using a SC source by cut-back technique. First a spectrum is taken at the output end (O2 point in Fig. 4.28) of several hundred meters of the fibre. Then the fibre is cut down to 10-20 meters and another spectrum is taken at the output end (O1 point in Fig. 4.28) of this short piece of fibre. The difference between these two spectra is the loss induced by the cut fibre. The fibre loss is normally quoted in dB/km. The loss of PCFs made from pure silica is relatively low in the wavelength range of interest. To guarantee the measurement accuracy, extra care needs to be taken in the measurement. First, since the fibre to be measured is a nonlinear medium, an attenuator needs to used to decrease the SC power to guarantee a passive measurement. The attenuator should normally have an equivalent response over the entire bandwidth. Second, the total fibre length should be long enough to induce a loss which is higher than the fluctuation of the spectrometer and the SC source. Several hundred meters are usually needed. When the fibre is cut back, at least 10-20 meters fibre needs to be left to remove the influence of cladding modes. Third, the input end of the fibre needs to be fixed. A typical loss spectrum of a silica glass PCF has a very similar shape as Fig. 2.6 (see Fig. 4.15).

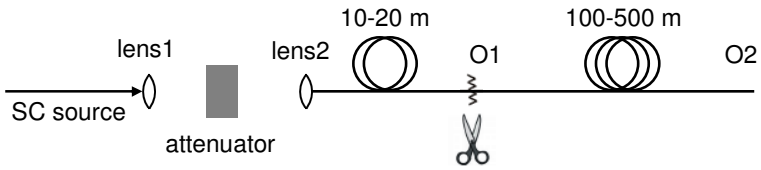

Figure 4.28: Diagram for the loss measurement of a PCF using a SC source by the cut-back technique.

Compared with previous light sources used in transmission measurement, the advantages of SC sources made from PCFs are obvious. For example, the white light bulb has a broader bandwidth but still has no blue and little green light. The light bulb also has a very low power, making the scanning of the specometer very slow. Other sources like super light-emitting diodes (SLED) or amplified spontaneous emission (ASE) sources are bright but typically narrow band (no visible at all). SC sources made from PCFs, however, are both bright and broadband.

Dispersion Measurement

Another important application of SC sources is to measure the group-velocity dispersion (GVD) of optical fibres. An interferometric method was demonstrated to measure the GVD of a single-mode fibre in 1981 [125]. This method has a very high time resolution (1 ps), so only a short fibre (<1 m) is needed as the sample under test. It is very convenient in practical measurements provided that a wavelength tuneable laser source is available. The SC source made from a PCF is exactly the tuneable source we want. Figure 4.29 shows a schematic diagram of the experiment setup, which employs a Mach-Zehnder interferometer. One arm contains the fibre under test. The other arm, named reference arm, has dispersion compensation lenses and a mirror pairs mounted on a computer controlled linear translation stage. The position of the translation stage should make the translation range cover the point at which the two arms have the same delay. The polariser is used to remove the influence of different polarisation components on the visibility of the interference fringe. The tuneable narrow bandwidth source is obtained by passing the SC source through a bandpass filter or a monochromator. The interference signal is collected by an endlessly single-mode PCF and sent to a detector with fast response. The detector is connected to the same computer which controls the moving mirrors.

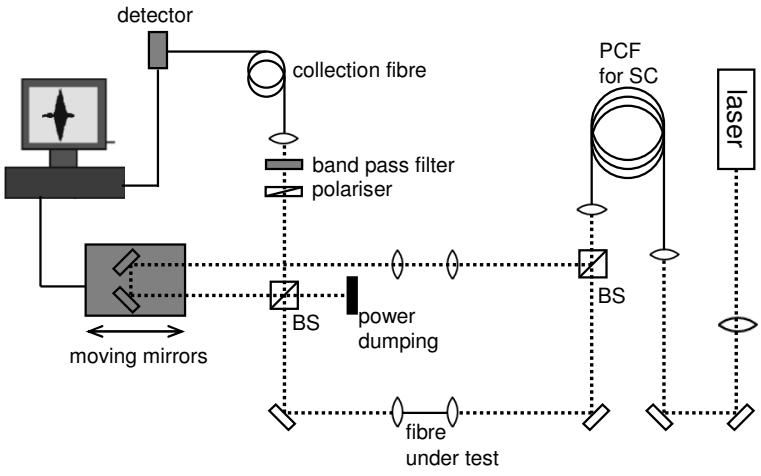

Figure 4.29: Diagram for the group-velocity dispersion measurement of a PCF using the interferometric method.

At a particular wavelength, by scanning the translation mirrors the interference fringe can be recorded. The fringe is peaked at a mirror position x that

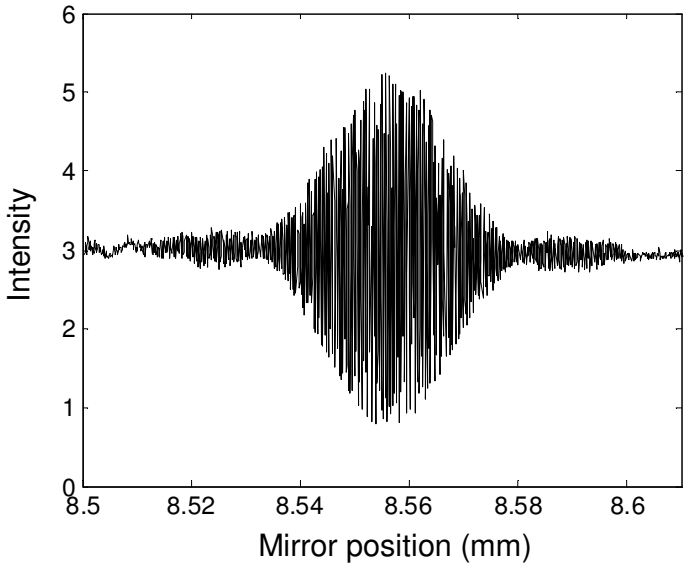

Figure 4.30: The measured interference fringe at 700 nm for a 38 mm piece of PCF using the configuration in Fig. 4.29.

makes the delay of the two arms equal at this wavelength. As an example, Fig. 4.30 gives the interference fringe at 700 nm for a 38 mm piece of PCF using the configuration in Fig. 4.29. When the bandpass filter is changed to change the wavelength detected, the position where the interference fringe peak occurs will change because the delay of different wavelengths in the fibre is different due to GVD. Therefore a set of data can be obtained, showing the variation of x with λ. According to the original definition of GVD [7],

$$D = \frac{(\Delta\tau)}{(\lambda_1 - \lambda_2) \cdot L}, \tag{4.5}$$

where $\Delta\tau$ is the delay difference between λ_1 and λ_2, L is the fibre length. In the dispersion measurement described here, $\Delta\tau = 2(x_1 - x_2)/c$. c is the light speed in vacuum and x_i corresponds to the mirror position where the peak of the interference fringe occurs for λ_i (i=1, 2). If lots of data are measured so that $\Delta\tau$ and $\Delta\lambda = \lambda_1 - \lambda_2$ are small, Eq. (4.5) can be written as the form of derivatives

$$D = \frac{1}{L}\frac{\mathrm{d}\tau}{\mathrm{d}\lambda} = \frac{2}{cL}\frac{\mathrm{d}x}{\mathrm{d}\lambda}. \tag{4.6}$$

Once the data about the variation of x with λ are obtained through the interference fringe measurement, the data can then be fitted to a funtion $x(\lambda)$. After

taking the first-order derivative of $x(\lambda)$, Eq.(4.6) can be used to calculate the GVD curve in the wavelength range measured. The dispersion curves shown in Fig. 2.23 were measured using this method.

The SC source makes it possible to measure the dispersion of a fibre in the entire bandwidth of the continuum. The only problem is that the fringe can normally not be measured in the vicinity of the SC pump wavelength because of the coherence of the residual pump peak mentioned in Section 4.5. However, the demonstration of the pump peak removal in that section may solve this problem in case where the information around the SC pump wavelength is wanted.

4.7.2 Visible Continuum Generation for Microscopy

Scanning near-field optical microscopy (SNOM) is a type of microscopy where a sub-wavelength light source is used as a scanning probe [126]. The probe is used to scan over a surface at a height above the surface of a few nanometers. Normally a small aperture on the end of a tapered and aluminum-coated optical fibre is used as the probe. By illuminating a sample with the near-field of a small light source, one can construct optical images with high resolution. Because the images are constructed through the collection of reflected or transmitted spectra using a silicon CCD or by eye, a visible source is required.

One of my colleagues was working on surface plasmons. He needed to take microscopy images of structures which were designed to generate surface plasmon. An image of the surface was obtained by mechanically moving the probe to scan the sample point by point, and recording the spectra after the probe-surface interaction as a function of position. As the surface was constructed with a periodically arranged metal array in a background, the spectral response was different at the points with metal or without metal. The surface pattern was therefore imaged by the spectral information recorded. Since the background and the metal have different spectral response to the probe light, a broadband source is required rather than a laser source working at a fixed wavelength. For an infinitely small gold particle in air, plasmon frequency corresponds to a wavelength of 490 nm. In reality spectra are red shifted to 500-600 nm. To excite such surface plasmons efficiently, a bright single-mode broadband visible source is needed. My visible continuum source demonstrated in Section 4.3.2 has been used for this experiment.

4.7.3 Tuneable Visible/UV Generation from Polarized Continuum Sources

One of the potential applications of the polarised SC source demonstrated in Section 4.4 is tuneable visible or UV generation by nonlinear frequency upconversion in nonlinear crystals. BIBO [127][128] is an attractive nonlinear material for frequency conversion in the visible and UV as it combines the advantages of both high UV transparency and enhanced nonlinearity: the optical transmission of BIBO extends from 2500 nm in the infrared down to 280 nm in the UV. Figure 4.31 schematically shows the frequency upconversion in BIBO. It can be seen that three photons are involved in the nonlinear interaction through the second-order nonlinearity $\chi^{(2)}$. It is well known that the nonlinear process does not take place efficiently unless the energy conservation and phase-matching conditions are satisfied [66]. It is convenient to only consider collinear phase matching. The energy conservation and collinear phase-matching conditions are written as

$$\omega_1 + \omega_2 = \omega_3, \tag{4.7}$$

$$n(\omega_1)\omega_1 + n(\omega_2)\omega_2 = n(\omega_3)\omega_3, \tag{4.8}$$

where $n(\omega_i)$ is the refractive index at ω_i $(i = 1, 2, 3)$. The process described by Fig. 4.31 and Eqs. (4.7) and (4.8) is known as the sum-frequency mixing (SFM). The special case of $\omega_1 = \omega_2$ is normally referred to as second-harmonic generation (SHG), where solution of Eqs. (4.7) and (4.8) requires $n(\omega_1) = n(2\omega_1)$. This is usually impossible because of the material dispersion. Indeed, the phase-matching condition for either SFM or SHG is usually achieved through the birefringent phase-matching. This means that these nonlinear effects are polarisation dependent. Using a linearly polarised source will enhance the nonlinear efficiency considerably.

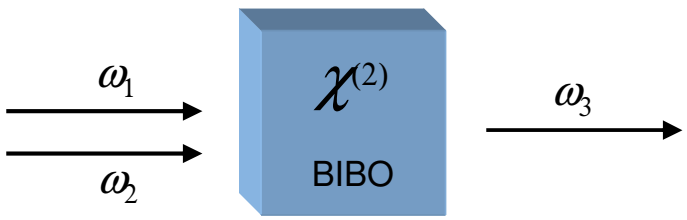

Figure 4.31: The diagram of frequency upconversion in BIBO.

As a biaxial crystal, BIBO offers versatile phase-matching properties. Since the introduction of BIBO, a number of frequency conversion experiments have been performed, including SHG of continuous-wave (CW) radiation at 1.06 μm [129], single-pass SHG of a pulsed laser at 1.06 μm [130], Q-switched SHG at 1.06 μm [131], frequency doubling of a CW Nd:YAG laser [132], tuneable single-pass SHG of a mode-locked Ti:sapphire laser [133]-[135], CW or Q-switched intra-cavity SHG at 1.34 μm [136], tuneable intra-cavity SHG of a CW Ti:sapphire laser [137], and optical parametric oscillators (OPOs) [138][139]. All of these experiments directly used a high power laser as the pump source. To achieve tuneability, a complex tuneable laser system such as Ti:sapphire laser is normally needed [133]-[135][137][139]. The presence of a polarised SC source makes compact tuneable visible/UV generation possible. Unlike the single pump wavelength source in previous frequency conversion experiments, the pump source here is a continuum source, so SFM becomes possible and the large residual peak at the SC pump wavelength may enhance the process (see Section 4.5).

As an application of the polarised SC source, visible/UV output has been demonstrated using SFM and SHG in BIBO. For a particular nonlinear crystal and pump power, the main factors limiting the conversion efficiency are the acceptance angle and acceptance bandwidth of the crystal and the effective nonlinear interaction length. Both acceptance angle and bandwidth are determined by the crystal length and the effective nonlinear interaction length is determined by the crystal length and the Rayleigh length of the pump beam (see Eq. (2.24) and Fig. 2.5). Either a longer crystal and less focused pump beam or shorter crystal and tighter focused pump beam may give optimum efficiency. However, in many applications, the generated beam needs to be coupled back into fibres, which requires good beam quality. A beam which is too tightly focused will yield a big divergence angle which will make both measurement and collection difficult. A relatively long crystal and a weakly focused pump beam are therefore preferred. Here a 5 mm long BIBO crystal was chosen for the experiment. In order to make full use of the crystal, the optimum Rayleigh length of the focused beam should be 2.5 mm, which corresponds to a 20 μm beam waist diameter at a wavelength of $\sim$1 μm. Thus a $\times$4 lens or lens combination should be chosen to focus the beam coming from the $\sim$5 μm core diameter fibre. In practice, different lenses or lens combinations with various magnifications were tested and $\times$4 lens combination showed the best performance.

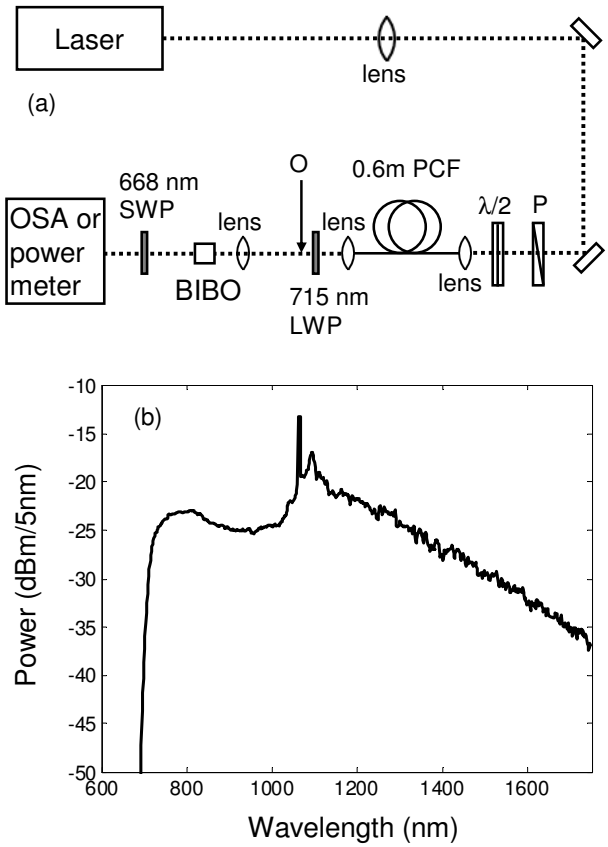

Figure 4.32: (a) Setup for SFM and SHG experiment. P, polarizer; $\lambda/2$, half-wave plate; 715 nm LWP, long wave pass filter, cut-off wavelength 715 nm; 668 nm SWP, short wave pass filter, cut-off wavelength 668 nm. (b) The output spectrum measured at point O in (a) from a 0.6 m length of PCF-A, collected using a multimode collection fibre. The resolution of the spectrometer was 5 nm.

The experimental configuration for nonlinear conversion is shown in Fig. 4.32(a). The continuum source setup was the same as the polarised SC generation setup in Fig. 4.16, except that a shorter piece of fibre (0.6 m) was used because maximum power rather than bandwidth was desired in the wavelength range of 750-1000 nm. The pump polarisation was set along the slow axis of fibre because of the higher output polarisation extinction ratio (PER). The spectrum taken at point O in Fig. 4.32(a) is plotted in Fig. 4.32(b). By use of the continuum source, a tuneable visible/UV source could be achieved through simply rotating the crystal to the critical phase-matching angle. To take the advantage of the high nonlinearity of BIBO, the most interesting plane for nonlinear optical interactions is

yz ($\phi = 90°$), which offers the highest effective nonlinearity, with a maximum effective nonlinear coefficient $d_{\text{eff}} \sim 3.4$ pm/V. Type-I (e+e$\longrightarrow$o) phase-matching is available for SFM and SHG in this plane for angles $90° < \theta < 180°$ [128][133]. The crystal was cut for type-I phase-matching in the yz plane at an internal angle close to $\theta = 155°$ at normal incidence, and the facets were anti-reflection coated for 850 nm and 425 nm. All experiments were performed at room temperature. A wavelength tuning range from 400 to 525 nm was achieved and the tuning range was limited by the crystal aperture at larger angles.

Table 4.1: Comparison of powers between the upconverted wavelengths from BIBO and the short wavelengths in the broad continuum source.

Powers for specific wavelengths in the continuum generated from a 0.6 m length of fibre A and corresponding upconverted wavelengths generated from BIBO						
λ (nm)	800	850	900	950	1000	1050
P (μW)	136	144	140	140	218	460
$\lambda/2$ (nm)	400	425	450	475	500	525
P (μW)	12	27	66	120	166	190
Powers for short wavelengths in the continuum generated from a 6 m length of fibre A						
λ (nm)	400	450	488	500	530	550
P (μW)	0	11	20	24	40	45

In order to determine the nonlinear processes involved the powers were measured for some specific wavelengths in the continuum generated from a 0.6 m length of PCF-A using 10 nm bandwidth interference bandpass filters (about 45%-50% transmission). The measured powers are shown in table 4.1 together with the measured powers for upconverted wavelengths corresponding to the second harmonics. It is noticed that the powers at fundamental wavelengths from 800 nm to 950 nm are quite similar, but the powers at upconverted wavelengths differ by a large amount. Moreover, the power at 475 nm is 120 μW which would correspond to 40% SHG conversion efficiency from 950 nm (taking the filter transmission efficiency at 950 nm into account). This would be a remarkable efficiency for such a low pump power. To understand this, the spectra for two typical wavelengths, 425 nm and 475 nm, were plotted in Fig. 4.33(a) and the SFM tuning phase-matching (type-I) curves were calculated (Fig. 4.33(b)) by the use of Sellmeier equations for BIBO [128]. From Fig. 4.33(b) it can be seen that by changing the crystal orientation 475 nm output can be generated by many

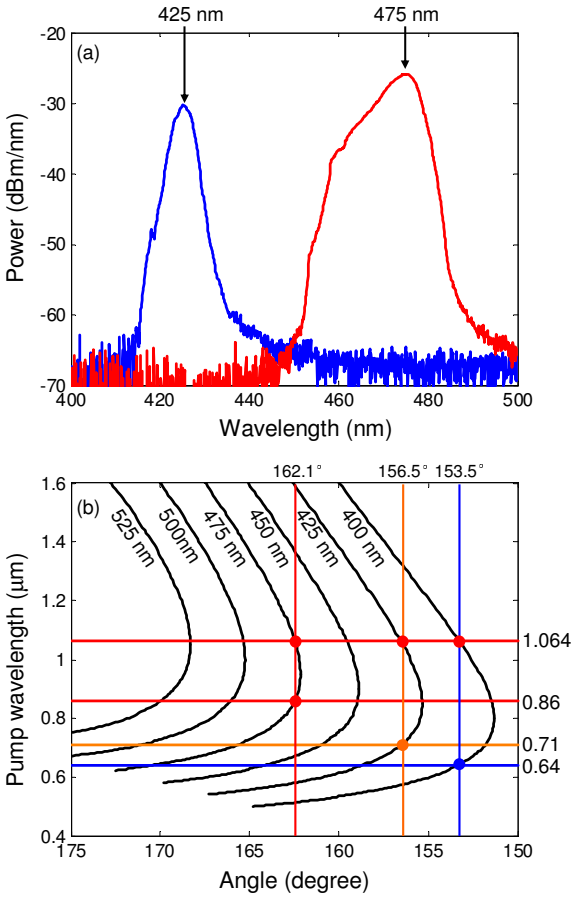

Figure 4.33: (a) Spectra at 425 and 475 nm generated in BIBO pumped by the continuum source from a 0.6 m length of PCF-A. The resolution of the spectrometer was 1 nm. (b) SFM tuning phase-matching curves in the yz plane of BIBO for different output wavelengths (marked beside each curve).

different SFM processes as well as by SHG of 950 nm. In particular at an angle of about 162.1° (vertical red line), SFM 1064 nm + 860 nm $\longrightarrow$ 475 nm will occur. This will be an efficient process as the residual pump intensity at 1064 nm is very strong and the 860 nm component is included in the continuum, and can explain the high output power at 475 nm. The residual pump power in a similar continuum (but 15 m of PCF-E) has been previously measured to be around 10% of the total output power (see Section 4.5). Whilst this is a small fraction of the total power, it is concentrated in a narrow spectral range and is far stronger than any of the infrared powers measured in table 4.1. If the crystal is supposed to be placed at 162.1°, strong 475 nm output should be seen, but Fig. 4.33(b) also shows that other blue/visible wavelengths generated from other SFM/SHG

processes at this angle should also be seen: a wavelength slightly longer than 475 nm will be produced by SHG of a wavelength longer than 950 nm; many wavelengths shorter than 475 nm will be produced by SFM of one photon with a wavelength longer than 1064 nm and one shorter than 860 nm. As the input was a continuum spectrum all these processes would occur. Thus not only was a spectrum with a peak at 475 nm observed, but also a broad tail to shorter wavelengths (see Fig. 4.33(a)) would be seen. There is a short wavelength limit to the tail as it can be seen from Fig. 4.33(b) that to generate 450 nm at an angle of 162.1° requires pump wavelengths less than 710 nm, which are not available in the continuum after the 715 nm long-pass filter. The same type of spectrum was observed when generating visible wavelengths from 500 nm to 450 nm.

Compared with the spectrum at 475 nm, the spectrum at 425 nm is symmetrical (see Fig. 4.33(a)). It can be seen from the phase-matching curve in Fig. 4.33(b) that at 156.5° (vertical orange line), SFM 1064 nm + 710 nm $\longrightarrow$ 425 nm can take place. This will be weaker than the SFM process considered above generating 475 nm using 1064 nm, as the intensity at 710 nm in the continuum is low. There is now no tail to shorter wavelengths as that would require wavelengths shorter than 710 nm for SFM.

To generate 400 nm there is no SFM possible using the residual pump at 1064 nm, so this must be achieved by SHG of the 800 nm component of the continuum, with consequently very low observed output power.

From this discussion it can be seen that the nonlinear process contributing to frequency upconversion here is mainly SFM rather than SHG. Since the pump power is not very high the generated components have very low power, but the powers are still higher compared with what can be generated directly from SC (table 4.1). Also the use of continuum source brings some new features such as compact, convenient tuning. With the development of high power picosecond fibre lasers, there is a clear possibility for generating more power in the blue/UV.

As discussed above, visible/UV generation based on a continuum source is tuneable but the power is low. Another way to get a pump source for frequency upconversion is to fabricate a different PCF yielding distinct FWM peaks instead of a broad continuum [43]. Here the fibre which was using is labelled as PCF-B. PCF-B was made in the same way as PCF-A, except that the pressure applied in the holes was slightly different so that d_1/Λ=0.29, Λ=2.95 μm and d_2/d_1=1.8 (see Fig. 4.14). The pump source, at 1064 nm, is now in the normal dispersion regime

of PCF-B, so a FWM process will take place [43], in this case generating a signal wave at 834 nm and an idler at 1478 nm.

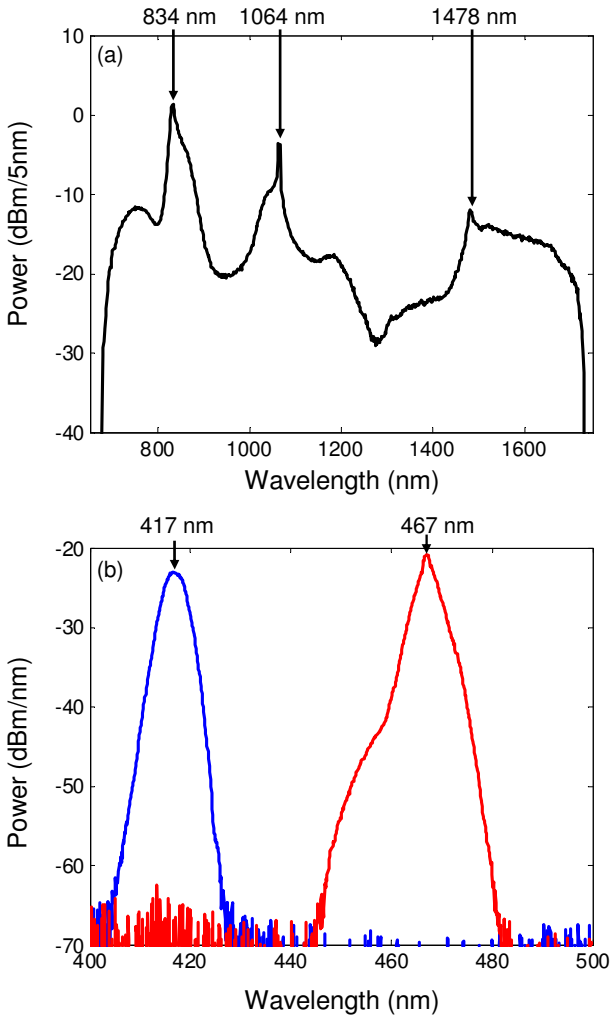

Figure 4.34: (a) FWM spectrum from a 1.2 m length of PCF-B with an average power of 38 mW. The resolution of the spectrometer was 5 nm. (b) SHG and SFM spectra in BIBO pumped by the FWM output from a 1.2 m length of PCF-B. The resolution of the spectrometer was 1 nm.

The conversion from the pump to the signal at 834 nm can be very efficient, leading to sufficient power at 834 nm to allow Raman conversion from this wavelength as it propagates further down the fibre. An optimum fibre length of 1.2 m was chosen in order to balance the FWM efficiency and Raman effect. Like PCF-A, PCF-B is a highly birefringent fibre. The PER was 245 and 60 when the pump polarisation was set along the slow and fast axes respectively, which corresponds

to 99.6% and 98.4% of power kept in a single polarisation. Again for efficient nonlinear upconversion, the pump polarisation was set along the slow axis. The FWM spectrum is illustrated in Fig. 4.34(a). A signal at 834 nm and an idler at 1478 nm were generated. The power at 834 nm was measured to be 14 mW, which was 37% of the total output power, 38 mW. A $\times 4$ lens combination was used to focus the beam into a 5 mm BIBO crystal and the crystal was rotated for phase matching. Bright visible output was achieved at two different angles. The spectra are plotted in Fig. 4.34(b). The power measurements showed that the powers at 417 nm and 467 nm were 0.53 mW and 0.76 mW respectively. 417 nm comes from SHG of 834 nm and 467 nm comes from SFM between 834 nm and 1064 nm. The SHG efficiency was about 3.8%, which was comparable with previous results at similar pump power level [133]. Also the spectra are symmetric because there is no additional contribution from other wavelengths. For the existing fibre and pump laser, the FWM peak is fixed. But for different fibres with slightly different dispersion properties, the FWM peaks vary. For example, if the ZDW of the PCF is shifted 1 nm which is equivalent to the shift of the pump wavelength $\Delta\lambda_p$=1 nm, the shift of signal wavelength will be $\Delta\lambda_s$=6-12 nm. Therefore the shift of the second harmonics wavelength will be $\Delta\lambda_{2\omega}$=3-6 nm. As discussed in Section 2.4.2, the ZDW of the PCF is actually very easy to change over tens of nanometers. From this point of view, the SHG will be tuneable by use of different PCFs in the first stage. PCFs with FWM peaks at around 700 nm have been fabricated in our group previously, which means the short wavelength can be tuned to as short as 350 nm in this way. The operation is more complex, but the system is still compact and much higher power output than the continuum case can be achieved.

According to Figs. 4.33(a) and 4.34(b), the short wavelengths are generated with no pedestal, down to the level of -35 to -45 dB. This is very useful in some applications such as fluorescence microscopy, where generated fluorescence has longer wavelength but is very weak. The clean spectrum with high extinction ratio makes it easier to distinguish the fluorescence from any background at the same wavelength emitted by the pump. This source is therefore potentially more useful than simply a filtered continuum as a tuneable pump for such applications.

For many applications, it is necessary to couple the generated short wavelength light to a single mode fibre. It is therefore necessary to measure the coupling efficiency of the free space beam to a piece of ESM PCF. It was found

that a power of 66 μW at 417 nm could be coupled into a 3 m length of ESM PCF. The efficiency was 12.5%, which is not high because the beam is not round due to the spatial walk-off between the fundamental beam and SHG beam in the crystal [124][140]. If a walk-off compensation technique using multiple crystals [124][140] could be applied in this experiment, both the upconversion efficiency and the free space-fibre coupling efficiency would be enhanced.

The work described in this subsection has been published as one part of a paper appeared in Optics Express (C. Xiong and W. J. Wadsworth, vol. **16**, pp. 2438, 2008).

4.8 Conclusion

In this chapter I have introduced the development history of supercontinuum (SC) generation. It shows that the most recent development of SC generation has been based on PCFs. Therefore I discussed the mechanisms of SC generation in PCFs. It has been found that the pulse duration determines the dominant spectral broadening mechanisms. In the femtosecond pulse pumping regime, soliton-related effects, such as soliton fission, Raman induced intra-pulse soliton self-frequency shift, Cherenkov radiation and soliton trapping through XPM and FWM predominates the spectral broadening. In the long pulse or CW pumping scheme, it is the phase matched parametric FWM/MI processes that initialize the continuum generation. Soliton-related dynamics comes into effect in the later stage because of the generation of MI-induced solitons.

Following the introduction of the background of SC generation, several projects on compact SC generation from a 1064 nm microchip laser have been presented in this chapter. They are enhanced visible continuum generation in a monolithic PCF device, polarised SC generation in a highly birefringent PCF, pump peak removal for ultra-flat SC generation and SC generation pumped by dual-wavelength in an all-fibre device. Finally, I introduced some applications of SC sources to transmission measurement, dispersion measurement and microscopy. In particular, I demonstrated the application of the polarised continuum to tuneable visible/UV generation.

Chapter 5

Photon Pair Generation in Photonic Crystal Fibres

Quantum mechanics, discovered and formalized during the last century, has helped us reveal the nature of numerous physical phenomena which can not be understood in the frame of classic physics. Its success in application to lasers and semiconductors is well known. The most peculiar characteristics of quantum mechanics, the existence of indivisible quanta and of entangled systems, have enabled the development of quantum information processing which includes quantum communication [141][142] and quantum computation [143][144]. Compared with classic communications, quantum communication systems have much higher security and have attracted much interest from physicists and information engineers. For commercial applications quantum communication faces several important technological challenges: single-photon sources, quantum channels, single-photon detection, quantum random-number generators and quantum repeaters [145]. Each of these challenges corresponds to different functions in a quantum communication system. Single-photon sources provide the information carriers. Quantum channels connect the single-photon sources and detectors. The quantum random-number generators are used to produce a truly random key. The quantum repeaters can extend the information transmission distance. The realization of quantum computation relies on the implementation of quantum logic gate, which also needs the development of single-photon sources and single-photon detection.

As an interdisciplinary subject, the details of quantum information process-

ing are very much beyond the context of this thesis. This chapter will focus on one of those important technological challenges: single-photon sources. Section 5.1 gives an introduction to the development of single-photon sources. Section 5.2 demonstrates the design and fabrication of an all-fibre entangled photon pair source suitable for fibre quantum communication using heralded single photons (810-1550 nm pairs), using a modelocked Yb fibre laser pump source. Section 5.3 presents PCF-based photon pair sources for efficient generation and detection of correlated photon pairs in the visible ∼500-700 nm and near-infrared region ∼700-900 nm, using a Ti:sapphire laser pump source. Such a source would be suitable for free-space heralded single-photon quantum communication and multiphoton quantum gate. Section 5.4 summarizes this chapter.

5.1 Introduction

Optical quantum information processing is based on the use of single-photon Fock states. In the development of single-photon sources, several popular techniques have been proposed and demonstrated. The most straight forward one was the faint laser pulses emitted from standard semiconductor lasers and calibrated attenuators [146]. Such sources guarantee the single-photon state through making the pulses so weak that most pulses are empty and only one photon exists in the remaining pulses. The idea is simple, but the obvious drawback is that the empty pulses decrease the bit rate. Although the gigahertz modulation rates available with telecommunication lasers may compensate for it, the requirement of keeping the detector active for all pulses including the empty pulses can result in an increase of dark counts with the laser's modulation rate.

Another way to create single-photon states is the generation of photon pairs and the use of one photon as a signal to indicate the arrival of the other one [147]. In contrast to the faint laser sources, the second detector must be activated only whenever the first one has detected a photon, and not whenever a pump pulse has been emitted, therefore solving the problem of empty pulses. In various demonstrations, the photon pairs are generated by spontaneous parametric downconversion in a $\chi^{(2)}$ nonlinear crystal [142][147]-[152]. In this process, the inverse of the well-known sum-frequency mixing (SFM, see Section 4.7.3), one photon spontaneously splits into two daughter photons–traditionally called signal and idler photons–conserving total energy and momentum. Like SFM, this

process is only efficient when phase matching is achieved. Indeed, this parametric downconversion process shares the same phase-matching condition as SFM (see Section 4.7.3). Phase matching can be achieved by exploiting the birefringence of a nonlinear crystal. Such phase matching allows one to choose the wavelength and determines the bandwidth of the downconverted photons (see Fig. 4.33(b)). Nonlinear crystals have high nonlinearity, and can thus be efficient sources of photon pairs with only short interaction lengths. However, in any experiment involving photon pairs, the observed count rate depends not only on the rate of generation but more importantly on the square of the total collection efficiency of the photons. This includes the coupling efficiency of the pairs through the experiment in a single spatial mode, the transmission of any spectral filters, and the detection efficiency. It is clear that efficient creation of photon pairs is only a small part of a high count-rate system. We also require efficient interfacing to single-mode fibre, natural narrow bandwidths (to reduce the need for inefficient filtering) and photon wavelengths at the peaks of detection efficiency of common detectors. Therefore a major problem of bulk nonlinear crystal photon pair sources for quantum optical experiments is the generally low spatial beam quality. This limits the efficient coupling of the photons generated into single-mode fibre, which is used for many experiments. Poor coupling efficiency dramatically reduces the rate of detected pair correlations by the square of the coupling efficiency [152]. Recently waveguide photon pair sources have been attempted both in fibres using a poling induced $\chi^{(2)}$ [153] and in periodically poled waveguides of lithium niobate [154]. The $\chi^{(2)}$ fibre source showed a rather low efficiency due to the low nonlinearity. The periodically poled waveguides are extremely efficient sources for generating long wavelength photon pairs but again it is difficult to transform the waveguide mode into one suitable for launching efficiently into single-mode fibres. Most recently there has been much work worldwide aiming to improve the spatial mode of waveguide photon pair sources [155]-[157].

Since the bulk photon pair sources lead to the coupling problem with single-mode fibres, an obvious solution is to generate photon pairs in the optical fibre itself. Compared with bulk nonlinear materials, optical fibres made from fused silica use the $\chi^{(3)}$ nonlinearity to generate photons directly in the fibre fundamental mode. As mentioned in Section 2.4.3, despite the low intrinsic nonlinearity of fused silica, nonlinear optics in optical fibres is possible because of the long interaction length available. Section 3.4 tells us that using $\chi^{(3)}$ the photon pairs

are produced by four-wave mixing (FWM). Phase matching is provided by the chromatic dispersion of the fibre mode. Previous attempts at photon pair generation in optical fibres [158]-[162] have concentrated on the phase matching which occurs in fibres with anomalous dispersion (usually referred to as modulation instability, MI, see Section 3.4.1). Since single-photon sources are pumped at low power, Raman effect is stronger than FWM because Raman gain is pump power independent while FWM gain is low at low pump power. Thus many photon pairs were generated, but there was also a very high level of background in the idler channel from spontaneous Raman scattering because of the broad Raman gain spectrum (see Fig. 3.2).

A significant breakthrough was recent application of phase matching in the normal dispersion regime of PCFs for photon pair generation [163]-[167]. As discussed in Section 3.4.1, in this case the parametric wavelengths lie far from the pump wavelength, and in particular the idler wavelength is far from the main Raman band. This makes it very attractive to build photon pair sources in PCFs. The criteria of a high-quality photon pair source is how bright the source is and how pure the single-photon state is. "Bright" means high coincidence count rate of the photon pairs. "Pure" means narrowband, polarised, single spatial mode and high coincidence/accidental ratio. Undoubtedly PCF is an excellent candidate for this application. As can be seen, the endlessly single-mode PCFs can guarantee photons at a single fundamental mode. The flexibility of dispersion and birefringence control of PCFs can make the photons naturally narrowband, polarised and located in the wavelength range desired for different applications. Pumping in the normal dispersion regime can make the main noise contribution from the Raman effect much less. These advantages will be demonstrated in the following sections.

5.2 Fibre Photon Pair Sources Pumped with 1064 nm Fibre Laser

One of the most important reasons to build a single-photon source is for quantum communication through the well established modern telecommunication systems. As mentioned in Section 5.1, the aim is to make full use of the potential of FWM in PCFs to build high-quality fibre photon pair sources. When the photon

pairs are generated in a PCF through phase matched degenerate FWM, the photon used for quantum experiments is normally called a heralded photon and the photon used for indicating the presence of the heralded photon is called a heralding photon. To take advantage of the low fibre loss in the telecom band, the heralded photon wavelength should ideally be at 1550 nm. On the other hand the complementary photons need to be passively and efficiently detected for the heralding purpose. The requirement of a high bit rate means that the ideal pump source is a pulsed laser with a high repetition rate. The pump laser pulses should also be time-bandwidth limited because the FWM gain bandwidth in the normal dispersion regime is quite narrow (see Section 3.4.1). After taking all of these into account, an amplified modelocked fibre laser delivering up to 100 mW average power at 1064 nm in close to transform limited 5 ps pulses at 80 MHz pulse repetition rate (*Fianium Femtomaster1060-0.1*) should be a suitable pump source. Indeed, the phase-matching condition is therefore chosen to produce 810-1550 nm photon pairs. Silicon detectors have very good detection efficiency at ∼800 nm. According to the discussion about dispersion control and FWM in PCFs in Sections 2.4.2 and 3.4.1, an endlessly single-mode PCF is very easy to design for such a specific phase-matching condition. In this section, I will demonstrate an all-fibre photon pair source based on all of these ideas.

5.2.1 Free-Space Demonstration

A heralded single-photon source made from the degenerate FWM in a PCF is a complex system including filtering of pump photons and their Raman photons or other possible noise, generation, separation and detection of heralding and heralded photons. Therefore it is a good idea to demonstrate a free-space setup to identify the wavelengths of the generated photon pair and check the performance of such a source before integrating an all-fibre system.

Figure 5.1 shows the experimental setup with free-space wavelength filtering schematically. As mentioned above, the pump laser was an amplified modelocked fibre laser delivering up to 100 mW average power at 1064 nm in close to transform limited 5 ps pulses at 80 MHz pulse repetition rate (*Fianium Femtomaster1060-0.1*). An optical isolator was used to protect the laser from optical feedback. A prism (P1, Fig. 5.1) separated the required 1064 nm laser output from any residual fluorescent light that may be at the same wavelength as the proposed

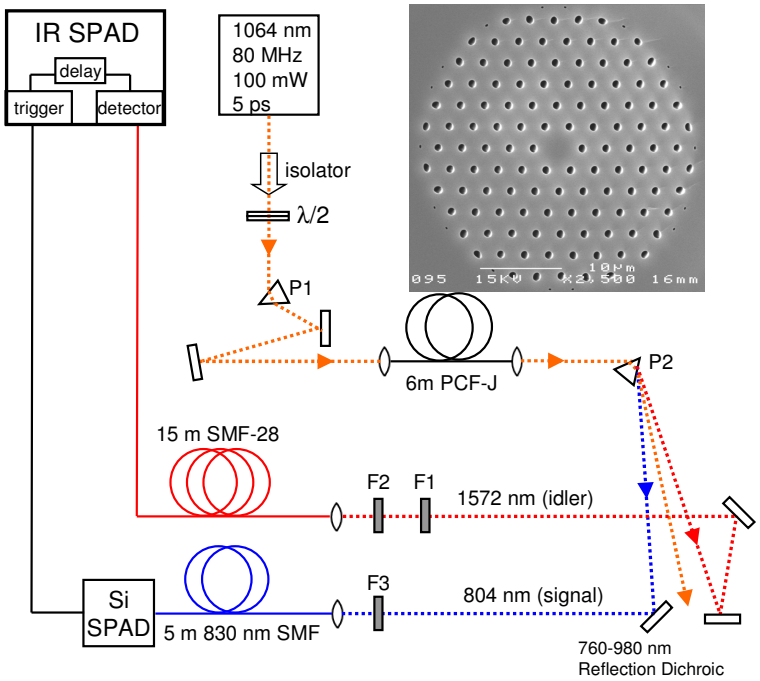

Figure 5.1: Schematic of the heralded single-photon source setup with free-space filtering and the SEM of PCF-J used. P1, P2: prism; F1: 100 nm broad bandpass filter centred at 1550 nm; F2: 1220 nm long wavelength passing filter; F3: 10 nm bandpass filter centred at 800 nm.

single photons. After these free-space optics, the pump power before entering the PCF was 60-70% of the output power from the laser. The pump light was then coupled into a 6 m length of PCF (labelled as PCF-J) shown in Fig. 5.1. This PCF has a hole-to-hole pitch, Λ=2.93 μm, and a hole-pitch ratio, d/Λ=0.33, which was designed to give phase matching for FWM generating 810 nm and 1550 nm photons if pumped at 1064 nm. Up to half of the pump power could be coupled into the fibre using an IR anti-reflection coated aspheric singlet lens. Another prism (P2, Fig. 5.1) was inserted in the collimated output from the PCF. This separated the pump, signal and idler wavelengths. The final wavelength filtering was provided by bulk dichroic mirrors and interference filters to eliminate residual 1064 nm light present in both arms. The heralding photons (signal arm) were collected with a 5 m length of single-mode fibre (SMF, λ_{cutoff}=830 nm) and detected with a *Perkin Elmer* silicon single-photon avalanche detector (SPAD, *SPCM-AQR*). The heralding signals were then used to trigger the gate of an *ID Quantique* InGaAs SPAD (*ID200*) with a variable delay. A 15 m length of single-mode fibre (SMF-28) in the idler arm overcame the signal arm delay within the

silicon SPAD, 5 m SMF, cable, and the triggering circuit of the InGaAs SPAD. The silicon SPAD was operated ungated and had a detection efficiency of 55% at 800-810 nm. The gate width of the InGaAs SPAD was 2.5 ns, the detection efficiency is not well characterised at the bias used, but is less than 30%. By scanning the delay of the gate coincidences between the detection of signal and idler photons from the same pump pulse could be observed.

Maximum filtering of noise and efficient detection of heralding and heralded photons are the most important considerations in the single-photon source experiment. As mentioned in Section 3.4.1 and shown in Fig. 3.3, the FWM in the normal dispersion regime has very narrowband gain and the slope of the phase-matching curve is large. Even if the pump wavelength is slightly different from 1064 nm, the signal and idler wavelengths may change a lot. Thus it is very important to identify the pump, signal and idler wavelengths before choosing suitable filters for both arms.

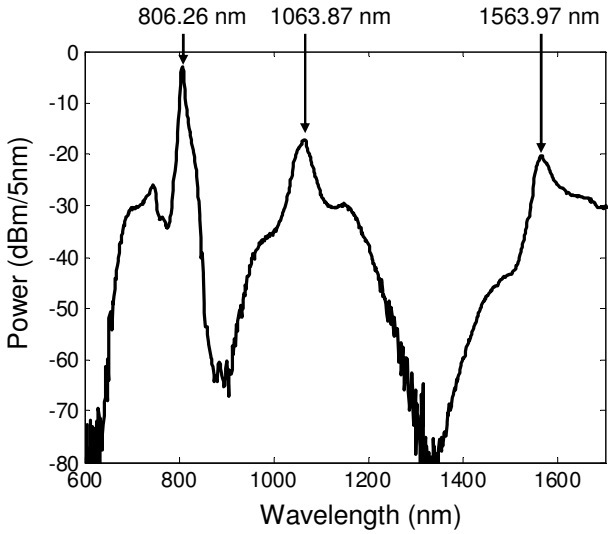

Figure 5.2: Measured spectrum of FWM in PCF-J pumped with a nanosecond microchip laser used in Chapter 4.

As the picosecond laser used for the single-photon experiment has a maximum average power 100 mW, the peak power is too low to generate FWM photons detectable by a normal optical spectral analyzer (OSA). The SPADs can detect signal at single-photon level but can not tell the wavelength. Two methods were demonstrated to identify the signal and idler wavelengths and then they were

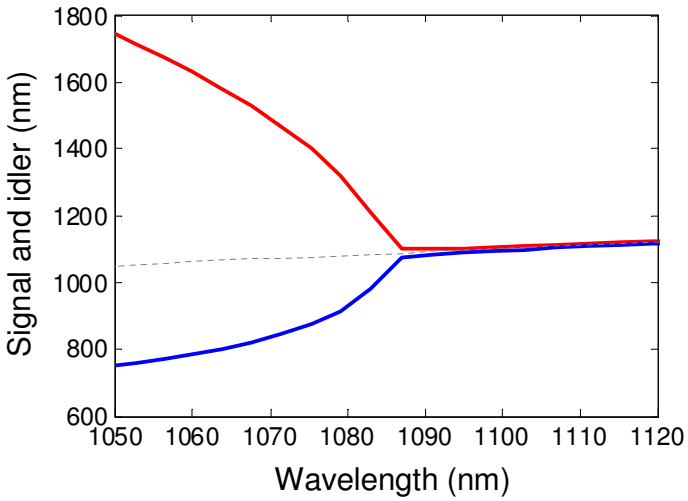

Figure 5.3: Calculated phase-matching curve for PCF-K which emits the same FWM peaks as PCF-J when pumped by the same microchip laser.

compared with each other to see if they were consistent. An obvious way to identify the signal and idler wavelengths is to use another laser operating at the same wavelength but with higher peak power to pump the same fibre and measure the FWM spectrum with a normal OSA. The nanosecond microchip laser running at 1064 nm used in previous experiments (see Chapter 4) seems to be the good candidate. The ns microchip laser was coupled into PCF-J and the output of PCF-J was sent to an OSA (*Ando, AO-6315B*) to measure the spectrum. As shown in Fig. 5.2, the pump, signal and idler wavelengths are at 1063.87, 806.26 and 1563.97 nm, respectively. It should be noted that these wavelengths were identified at high resolution and not at the 5 nm resolution shown in Fig. 5.2, so these results should be reliable. It can be seen that the nanosecond laser is not exactly working at 1064 nm. It was also found that the picosecond laser was not exactly running at 1064 nm but at 1063.2 nm instead. So it is difficult to tell what the FWM wavelengths are when pumping with the picosecond laser simply by this measurement. Fortunately it is well known that the FWM peaks are determined by the phase-matching condition (see Section 3.4.1). If the dispersion of the fibre is measured and then used to calculate the phase-matching curve like Fig. 3.3, the FWM peaks may be confirmed. However a small measurement error in the dispersion measurement and a small calculation error in the phase-matching calculation may also induce a shift of several nanometers at the FWM signal and idler wavelengths, but it is believed that the slope of the

phase-matching curve should not change in the vicinity of 1064 nm. Therefore I could measure the dispersion for PCF-J and then calculate the phase-matching curve. However measuring the dispersion for a fibre might take a few days, so for simplicity I simply took the measured dispersion data of another fibre, PCF-K, which emits the same FWM peaks as PCF-J when pumped by the same microchip laser and calculated the phase-matching curves. As shown in Fig. 5.3, the slopes of the curves at around 1064 nm for the signal (blue) and idler (red) band is 5 and 13.5 respectively. Then the signal and idler wavelengths were estimated to be 803 nm and 1573 nm respectively when pumping with the 1063.2 nm picosecond laser. It can be seen that this is an indirect method since this method did not measure the signal and idler wavelength directly using the picosecond laser.

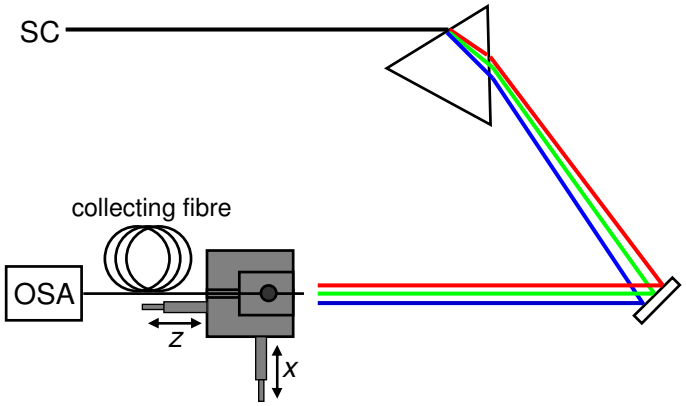

Figure 5.4: Schematical diagram of wavelength calibration using a SC source and a translation stage. Further detail is given in Fig. 5.1

In another method, the signal and idler wavelengths were measured when PCF-J was directly pumped by the picosecond laser. As the SPADs do not have the function of a spectrometer, the wavelengths need to be calibrated for the photons collected by the single-mode fibres in both arms using a supercontinuum (SC) source. When a SC source is injected into PCF-J and collimated on the prism, photons at different wavelengths will be refracted to different directions. After being reflected by the mirrors, the photons at slightly different wavelengths will be selected by the collecting fibre through adjusting the x vernier of the xyz translation stage (see Fig. 5.4). An OSA (*Ando, AO-6315B*) was used to measure the wavelengths corresponding to each reading of the x vernier. Using these data the wavelengths were fitted to the readings linearly (linear fitting is reasonable

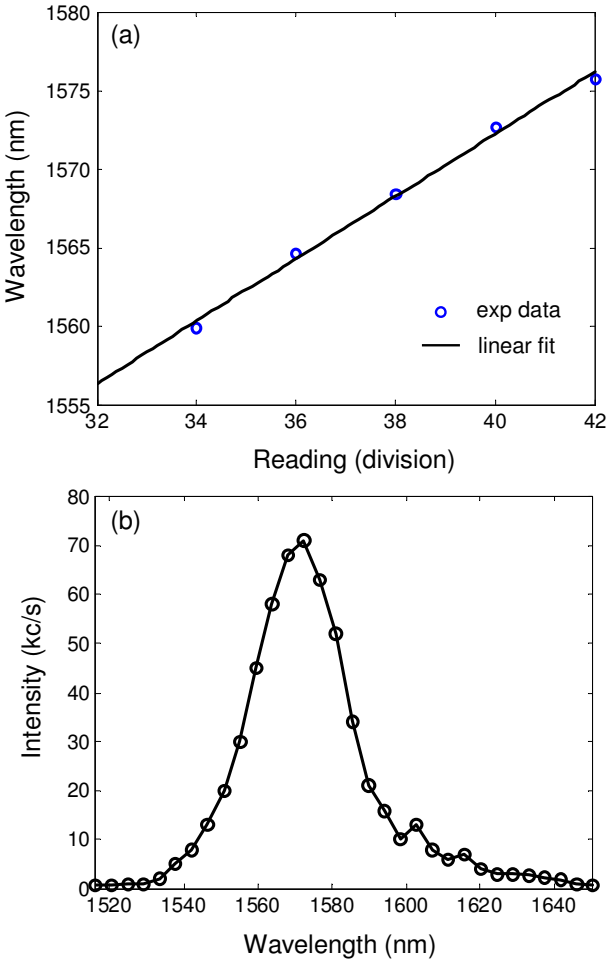

Figure 5.5: (a) Wavelength calibration for the idler arm. (b) Wavelength measurement using the SPAD and the calibration results shown in (a).

when these wavelengths are very close to each other). Figures 5.5(a) and 5.6(a) give the fitted calibration curves for each arm respectively. In the meantime, the SC source was also used to pre-align both arms of the full photon pair generation system shown in Fig. 5.1. The careful pre-alignment guaranteed that the low power parametric fluorescence was able to be detected efficiently in the following experiments. Then the pump source was changed back to the picosecond laser and the photon intensity was measured for each arm using the SPADs (SPADs give photon counts in kilo-counts per second (kc/s) which are equivalent to intensity). To remove the influence of noise, filters need to be inserted in each arm. Since some information about the wavelengths had been obtained from the indirect measurement, a 1220 nm long wavelength passing (LWP) filter was used

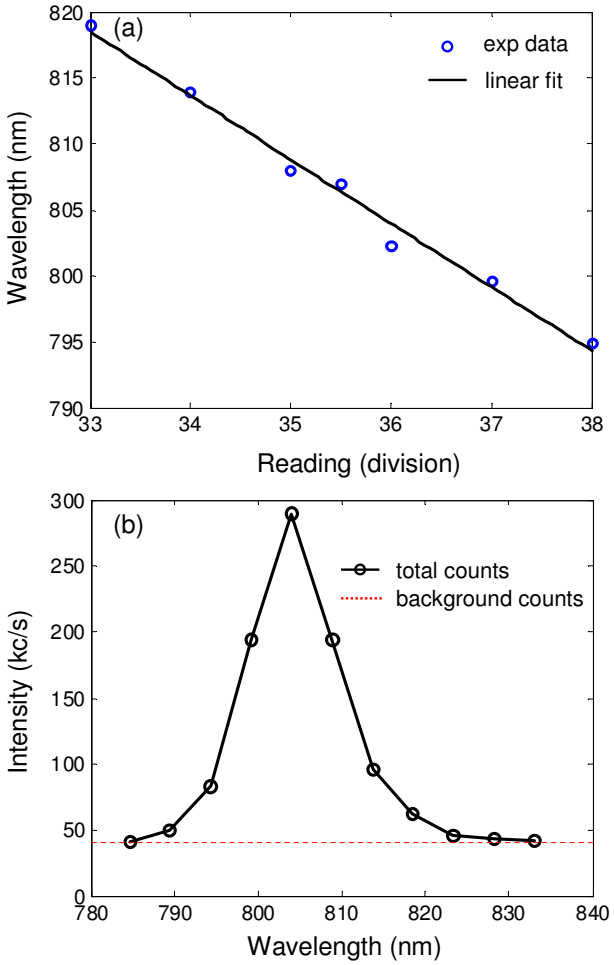

Figure 5.6: (a) Wavelength calibration for the signal arm. (b) Wavelength measurement using the SPAD and the calibration results shown in (a).

in the idler arm and a 10 nm bandpass filter centred at 800 nm was used in the signal arm. A dichroic mirror with the reflection band at 760-980 nm was also used in the signal arm for further filtering of 1064 nm pump photons. When the photon counts of the idler arm were measured, the trigger for the detector was set to 1 MHz internal trigger. The photon counts of the signal arm was given directly by connecting the output of the Si SPAD to the input of a counter integrated in the InGaAs SPAD. An intensity peak was found for each arm when the x vernier of the translation stage was adjusted. Using the calibration curves, the wavelength information for each arm was obtained as shown in Figs. 5.5(b) and 5.6(b). As the Si SPAD was sensitive to the visible light, the background counts in the signal arm were much higher than those in the idler arm (the 40 kc/s

background count came from the lamp). From Figs. 5.5(b) and 5.6(b) the signal and idler wavelengths were found to be 804 nm and 1572 nm respectively, which agreed with the results from the indirect method very well. A slight shift in the wavelengths of the parametric peaks may result from the different pump peak powers of the picosecond and nanosecond lasers (see Fig. 3.3) [163]. It should be noted that the purpose of this wavelength identification experiment was for choosing suitable filters in each arm, but filters have actually been used in this experiment. We should be clear that this was not self-contradictory. Firstly, we already had some information about the wavelengths from the indirect measurement. Secondly, the filter used in the idler arm was a broadband filter, so the intensity peak at 1572 nm should be a real peak and not an effect of the filter. Once the idler wavelength was confirmed, the signal wavelength could be estimated to be at about 803 nm through the energy conservation condition in FWM. Lastly, the same experiment for the signal arm was also performed without the bandpass filter. It was found that the peak at 804 nm was still there but with massive counts which are believed to come from the residual pump photons. Thus the 804 nm peak was also a real peak and not an effect of the 10 nm bandpass filter.

Both methods may bring errors into the wavelength identification. For the indirect method, as mentioned previously, a small measurement error in the dispersion measurement and a small calculation error in the phase-matching calculation may induce a shift of several nanometers of the FWM signal and idler wavelengths. For the direct method, turning the x vernier forwards and backwards may also induce errors since the thread of the screw may not come back to exactly the same position even if the reading is the same. However, both methods are nearly independent and give almost the same results, so these results were reliable and the following experiments were all based on these measurements. It can also be seen later that this wavelength identification was accurate enough for the single-photon coincidence measurements (see the following results in this section and Section 5.2.2).

Once the wavelength information was obtained for the signal and idler photons, suitable filters could be chosen for the single-photon measurements. In the photon pair coincidence experiments, the same filters were used in the signal arm as for the wavelength identification experiment described above. In the idler arm, besides the 1220 nm LWP filter, one more filter, a 100 nm bandwidth band-

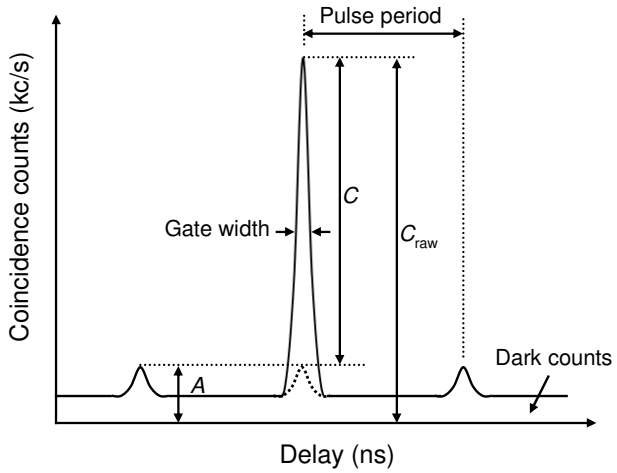

Figure 5.7: A schematic diagram showing the coincident photon detection peak. The central large peak corresponds to signal and idler photons belonging to the same pulse. The time between two peaks reflects the pump laser repetition rate. The small satellite peaks stand for uncorrelated events, i. e. signal and idler coming from subsequent pulses, whether they are actual pairs of photons or background photons. The width of the peaks corresponds to the gate width of the InGaAs SPAD.

pass filter centred at 1550 nm, was also used to further isolate the Raman noise. Using the signal at 804 nm as the trigger of the InGaAs SPAD, the 1572 nm photons could be detected if the photons arrived the detector at the same time as the detector was triggered. The signal and idle photons from the same pair travelled in different channels and experienced different delay, therefore an adjustable electronic delay was introduced to the idler arm so that coincidence could be observed by scanning the delay over the delay difference of the two arms. Figure 5.7 schematically shows the idler arm count rate variation with the delay. If the delay is properly set such that the 1572 nm photon arrives the detector at the same time as the detector is triggered by the 804 nm photon from the same pair, a coincidence event could be recorded. This possibility is determined by the detection efficiency of the detector. Such a photon pair must be generated in the same pulse, so all of the coincidence events recorded by this method correspond to photon pair generation in different individual pulses. However, in practical experiments, the detected count rates in the idler arm may be the dark count rates, Raman noise or a 1572 nm photon from different pairs. All of these count rates are called accidental rates (A). Therefore the central large peak in Fig. 5.7 corresponds to the raw coincidence rates (C_{raw}) made up of the real coincidence

rates (C) of pair photons and those accidental rates. The width of the peak is determined by the gate width of the detector (i. e. the active duration of the detector). To find the real coincidence rates, it is necessary to find the accidental rates. It is impossible to extract the accidental rates directly from the central large peak. However, we can directly measure the accidental rates by changing the delay so that the signal and idler photons come from adjacent pulses. Since these two photons come from different pulses, all of the count rates are the contribution of accidental rates. The small satellite peaks in Fig. 5.7 stand for these uncorrelated events. The time between two peaks reflects the pump laser repetition rate.

Table 5.1: Photon count rates at different pump powers in the free-space filtering experiment.

Input power at 1064 nm (mW)	10.5	19.2	21.5	53
Heralding trigger rates (kc/s)	40	N/A	N/A	N/A
Raw coincidence rates C_{raw} (kc/s)	0.5	1.7	2.2	15
Accidental rates A (kc/s)	0.02	0.13	0.2	6
Coincidence rates $C = C_{\text{raw}} - A$ (kc/s)	0.48	1.57	2.0	9
Coincidence/accidental ratio (C/A)	24	12	10	1.5

In the coincidence measurement experiment as shown by Fig. 5.1, the count rates in the 1572 nm arm were measured at two delay points between the trigger and the detection gate when pumping at different powers. The results are tabulated in table 5.1. The raw coincidence rates were measured at a delay of 11.4 ns and the accidental rates were measured at a delay of 23.6 ns. The time interval between these two delays is 12.2 ns which indicates a $\sim$80 MHz pump laser repetition rate. It can be seen that higher pump power gives a higher coincidence rate, but also induces a high accidental rate. The coincidence/accidental (C/A) ratio changed from 24 to only 1.5 when the pump power was increased from 10.5 mW to 53 mW. A low C/A means that there is a large amount of noise and accidental counts from pairs of pairs. Simply increasing the pump power can not improve C/A, meanwhile it can be seen from table 5.1 that a low pump power results in a low coincidence rate which is not useful. However the low coincidence rate does not necessarily mean the photon generation rate is low. As mentioned previously, the low collection efficiency is most probably the reason

for a low coincidence rate. For example, when the pump power was 10.5 mW, the triggering rate was 40 kcs/s, but the coincidence rate was only 0.48 kcs/s. We can determine the lumped efficiency of collection and detection of the 1572 nm photons by the ratio of the coincidences to the heralding triggers as 1.2%. After taking the detection efficiency (∼30% at high bias as set in the experiment) into account, the heralding efficiency was only 4%.

The results from the free-space demonstration are not perfect, but they show the potential of such photon pair sources. Since the problem here is the loss induced by the bulk optics, there is a great deal to be gained in simplicity and coupling efficiency by using fibre components spliced into an all-fibre system.

5.2.2 All-Fibre Demonstration

As shown in last section, the single-photon state was guaranteed through the wavelength separation and filtering using bulk components such as prism and bandpass filters. Unfortunately these bulk components may induce significant losses and decrease the photon collection efficiencies considerably. For example, when the output beam of the PCF was collimated on the prism, one wavelength might be collimated but another one might not be collimated due to the dispersion of the lens. The reflection on the incident surface of the prism was also inevitable. The transmission efficiency of the 10 nm bandpass filter is typically less than 50%. In order to improve the coupling efficiency, an all-fibre system was demonstrated in this section. The experiments described in this subsection were performed by A. McMillan and me.

To build an all-fibre photon pair source, the most important thing is to find the fibre counterparts of the bulk components used to separate, filter and transmit the photons efficiently. If a 15 mW average pump power is coupled into the fibre, there will be about 10^9 pump photons in each pulse. To guarantee the single-photon state, we need much less than one signal/idler photon per pulse. This means that the pump photons need to be isolated at least with an efficiency of 90 dB.

At first we set up a partially fibre-components filtering experiment as shown in Fig. 5.8. There were several differences compared with Fig. 5.1. Firstly, a 2 m length of PCF from the same fibre spool as PCF-J but emitting 810 and 1550 nm FWM peaks was used. This PCF is labelled as PCF-L. We did not

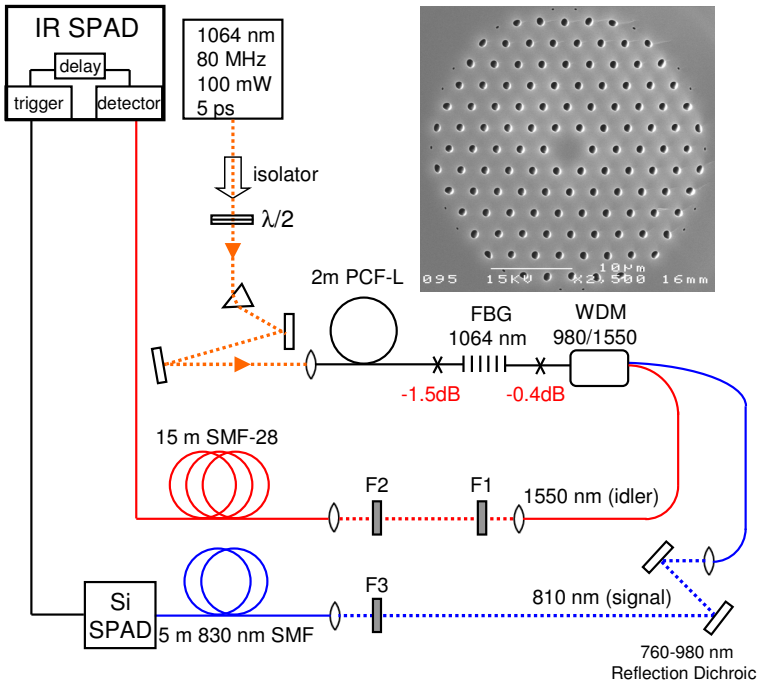

Figure 5.8: Schematic of the heralded single-photon source setup with partially fibre-components filtering. F1: 100 nm broad bandpass filter centred at 1550 nm; F2: 1220 nm long wavelength passing filter; F3: 10 nm bandpass filter centred at 810 nm.

use exactly the same piece of fibre, PCF-J, because the fibre device used in the following experiments had already been made with PCF-L before we started the free-space experiment described above, and there were no more sections of fibre PCF-L available. Secondly, instead of using a prism at the output of PCF-L, we spliced the output of PCF-L to a fibre Bragg grating (FBG, 99% reflectivity at 1064 nm, ∼1 nm bandwidth) to provide initial rejection of the input pump light. A standard 980/1550 fused fibre coupler (WDM) was then spliced to the FBG output to separate the generated 810 nm and 1550 nm photons. The combination of the FBG and WDM provided 35-40 dB isolation of the pump photons. However, the two splices induced 1.9 dB loss at 1550 nm which was not great. The final wavelength filtering used bulk optics in a very similar way to the free-space setup, except that a 10 nm bandpass filter with the central wavelength at 810 nm was used in the signal arm since the signal wavelength was 810 nm. The collection fibres, detection and measurement were also very similar to the free-space demonstration. The only difference was that we scanned the delay gate from 0 ns to 20 ns rather than just measuring two delay points.

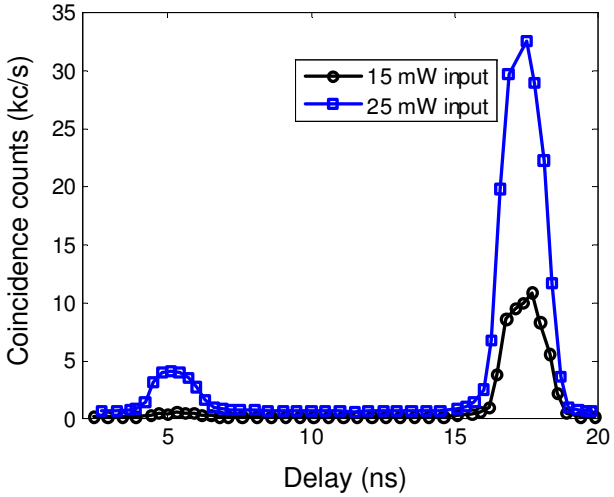

Figure 5.9: 1550 nm SPAD count rate as a function of delay between the trigger and the detection gate, showing the coincidence peak for photons from the same laser pulse at 17 ns, and accidental coincidences from adjacent pulses at 5 ns.

Table 5.2: Photon count rates at different pump powers in the partial fibre-components filtering experiment.

Input power at 1064 nm (mW)	15	25	70
Heralding trigger rates N_s (kc/s)	310	850	1400
Raw coincidence rates C_{raw} (kc/s)	10.8	32.6	80
Accidental rates A (kc/s)	0.55	4.1	40
Coincidence rates $C = C_{\text{raw}} - A$ (kc/s)	10.25	28.5	40
Coincidence/accidental ratio (C/A)	19	7	1
Lumped efficiency, 1550 nm arm (C/N_s)	3.3%	3.4%	2.9%
Heralding efficiency	11%	11.3%	9.7%

Figure 5.9 shows the observed coincidences between detection of signal and idler photons from the same pulse at 17 ns and accidental coincidences between signal photons in one pulse and idler photons or noise in the previous pulse at 5 ns. Table 5.2 shows the photon count rates for different pump power levels. A detected net heralded single photon rate of 10.25 kc/s is achieved at just 15 mW pump power with low accidental counts. The heralding rate is then 310 kc/s. We can determine the lumped efficiency of collection and detection of the 1550 nm

photons as about 3.3%. After taking the detection efficiency (∼30% at high bias as set in the experiment) into account, the heralding efficiency was 11%. The C/A ratio was as high as 19 when the pump power was only 15 mW. It is obvious that compared with the free-space filtering experiment, this partially fibre-components filtering system was much more efficient. At a lower pump power (15 mW compared with 19.2 mW), much higher coincidence rate (10.25 kc/s compared with 1.7 kc/s) and higher C/A ratio (19 compared with 12) were achieved.

The partial fibre-components filtering experiments have shown the advantages of all-fibre configuration for photon pair generation. However, the heralding efficiency was still very low due to the coupling losses. We can estimate the losses for the idler arm according to the setup shown in Fig. 5.8. The splicing loss is 1.9 dB and the WDM loss is about 0.5 dB. In a separate experiment the fibre-to-fibre coupling loss (including lenses) was measured to be 3 dB. The two filters' losses are not less than 4 dB. The total loss is about 9.4 dB in the idler arm, which means the coupling efficiency was only about 11.5%. The loss in the signal arm is similar to that of the idler arm. We shall see later that an all-fibre coupling in the idler arm can reduce the loss significantly. We can also estimate the idler coupling efficiency from the measured triggering rates N_s, raw coincidence rates C_{raw} and accidental rates A by referring to the following equations [163]:

$$N_i = \eta_i \eta_o r + B_i, \tag{5.1}$$

$$N_s = \eta_s \eta_o^{'} r + B_s, \tag{5.2}$$

$$C_{\text{raw}} = \eta_i \eta_s \eta_o \eta_o^{'} r + A, \tag{5.3}$$

where N_i is the count rate for idler arm which actually can not be measured unless there is a triggering source synchronized with the pump laser, r is the rate of photon pair generation in PCF-L, η_i, η_s are idler and signal detector efficiencies, η_o, $\eta_o^{'}$ are the efficiencies of coupling light from PCF-L to the collection fibres (including filter and WDM losses) and B_i, B_s are lumped background and dark count rates in the detectors. The raw coincidence rate is made up of real coincidence rate C and accidental coincidences A. The FBG, WDM, dichroic mirror and bandpass filter provide spectral filtering, so by adjusting the collection fibre launch slightly we could tune the frequency of collected light away from the photon pairs and saw immediately the B_s was small and could be neglected (similar to Fig. 5.6, but when the lamp was switched off, B_s=0.3 kc/s).

Thus according to Eq. (5.3), we can calculate

$$\eta_i \eta_o = \frac{C_{\text{raw}} - A}{N_s}. \tag{5.4}$$

When the pump power was 15 mW, as shown in table 5.2, C_{raw}=10.8 kc/s, A=0.55 kc/s and N_s=310 kc/s. If η_i is taken as 30%, the coupling efficiency η_o=11% which agrees with above estimated efficiency 11.5% very well. As we do not have sufficient information, we can not estimate the photon pair generation rate in the PCF. We can not estimate the background counts in the idler arm (B_i) either because we do not have the information of N_i.

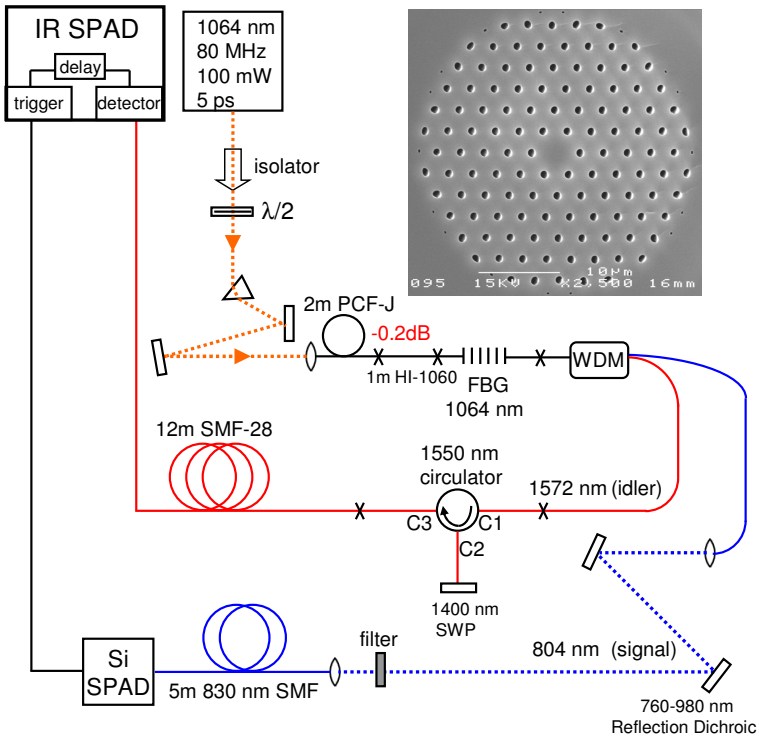

Figure 5.10: Schematic of the heralded single-photon source setup with all-fibre filtering in the idler arm.

In order to further improve the performance of the fibre photon pair source, we considered an all-fibre spectral filtering system in the idler arm (see Fig.5.10) and also tried to reduce the splicing loss of PCF-to-FBG-to-WDM. The walk-off length between the pump photons, signal and idler photons in PCF-J was calculated to be 30 cm for 5 ps pulses, so we changed the PCF to 2 m length of

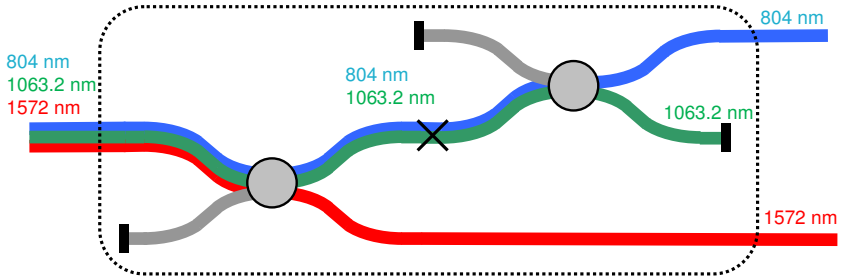

Figure 5.11: The diagram of the WDM used for separation of pump, signal and idler photons.

PCF-J allowing for future cut-back to check the optimum length. Referring to the specification of the new FBG (bought from *AOS*), the pigtail of the FBG is HI-1060 single-mode fibre (SMF), the insertion loss at 804 nm and 1572 nm is less than 0.1 dB, the central wavelength is 1063.8 nm and the reflectivity is not less than 99.9% (30 dB) in 2.04 nm bandwidth. The pump wavelength falls into the high reflection band of the FBG, which is good for pump photons isolation. The core diameter of the FBG pigtail is very similar to that of PCF-J, therefore their mode fields should match very well and low loss splicing should be possible. Indeed, by using the *Vytran* splicer and carefully setting the splicing parameters, we achieved a splicing loss as low as 0.2 dB at 1550 nm when we spliced PCF-J to a piece of bare HI-1060 SMF. It should be noted that we did not splice PCF-J directly to the FBG pigtail because the pigtail is short (2 m) and we needed to practise the splicing lots of times to find the optimum splicing parameters. Once we found the optimum parameters, it was trivial to splice the same HI-1060 SMFs together with negligible loss. Then we spliced the output end of the FBG to a customized WDM (bought from *Gooch & Housego*) to separate pump, signal and idler photons using a standard arc splicer (*Fujikura FSM-40PM*). A diagram shows the configuration of the WDM in Fig. 5.11. It can be seen that a WDM is first used to separate 1572 nm photons from the pump and signal photons, and then another WDM is spliced to one output port of the first WDM to separate 1063.2 nm and 804 nm photons. The pump photons are terminated inside the box, so one output port of this combined WDM is the signal and another port is the idler. The specified insertion loss is 0.05 dB at 1572 nm and 0.6 dB at 804 nm. Isolation of pump photons is about 25 dB in both ports. The idler output port of the WDM was then spliced to a circulator input port C1 and the circulator output port C3 was spliced to a 12 m length of SMF-28. As all of these

pigtails are SMF-28, the splicing was easy and low loss. The circulator provides a 40 dB isolation from C1 to C3 at 1572 nm but unspecified at 1063.2 nm, and induces 0.4 dB loss at 1572 nm. The signal arm was the same as in the partial fibre-components filtering experiment setup except that the filter needed to be tilted to shift the central wavelength to 804 nm.

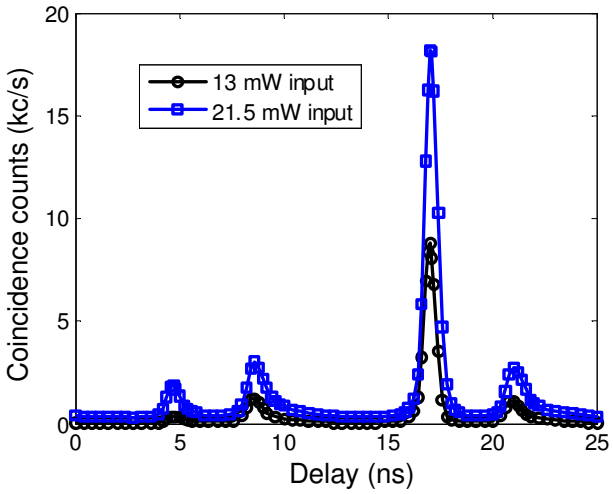

Figure 5.12: 1572 nm SPAD count rate as a function of delay between the trigger and the detection gate, showing the coincidence peak for photons from the same laser pulse at 17 ns, and accidental coincidences from adjacent pulses at 5 ns. The satellite peaks at 9 ns and 21 ns are believed to come from the direct passing of photons from the circulator port C1 to C3.

To make the photon pair coincidence measurements, we used a short wavelength passing (SWP, reflect wavelength>1400 nm) filter at the circulator output port C2 to reflect 1572 nm photons. Since the total coupling loss may be very low, we set the bias of the IR SPAD to the value which is well calibrated to have a detection efficiency of 10%. Similar to the above coincidence measurements, we scanned the delay gate from 0 ns to 25 ns to detect the coincidence peak and accidental rate. Figure 5.12 shows the observed raw coincidences between detection of 804 and 1572 nm photons from the same pulse at 17 ns and accidental coincidences between 804 nm photons in one pulse and 1572 nm photons or noise in the previous pulse at 5 ns. The two additional satellite peaks at 9 ns and 21 ns are believed to come from the direct passing of residual pump photons from the circulator port C1 to C3. This can be understood from the facts that they were still visible even if the 1400 nm SWP filter was removed from port C2

and the relative position to the main peaks moved when a length of fibre was cleaved from port C2. This will not affect the performance of this photon pair source since these peaks do not overlap with the coincidence peak, but we should be able to remove these peaks by splicing another FBG between the WDM and port C1. Table 5.3 shows the photon count rates for different pump power levels. A detected net heralded single photon rate of 8.41 kc/s was achieved at just 13 mW pump power with low accidental counts. The heralding rate was then 160 kc/s. We can determine the lumped efficiency of collection and detection of the 1572 nm photons as about 5.3%. After taking the detection efficiency (∼10% as set in the experiment) into account, the heralding efficiency was 53%. The C/A ratio was as high as 22 when the pump power was only 13 mW. It is obvious that compared with the free-space and partial fibre-components filtering experiments, this all-fibre filtering setup in the idler arm was much more efficient. The coincidence rate was lower than that of partial fibre-components filtering setup because the triggering rate was lower and the detection efficiency was 10% not 30%. We are still investigating why the triggering rate was lower since the signal arm was almost the same as in the partial fibre-components filtering experiment. One possible reason is that the generation rate of photon pairs in PCF-J was different from that in PCF-L. Another possible reason is the signal wavelength was 804 nm but we titled a 10 nm bandpass filter centred at 810 nm to change the central wavelength to 804 nm, which may reduce the transmission efficiency.

Table 5.3: Photon count rates at different pump powers in the all-fibre filtering experiment.

Input power at 1064 nm (mW)	13	21.5
Heralding trigger rates N_s (kc/s)	160	370
Raw coincidence rates C_{raw} (kc/s)	8.8	18.2
Accidental rates A (kc/s)	0.39	1.86
Coincidence rates $C = C_{\text{raw}} - A$ (kc/s)	8.41	16.34
Coincidence/accidental ratio (C/A)	22	9
Lumped efficiency, 1572 nm arm (C/N_s)	5.3%	4.4%
Heralding efficiency	53%	44%

It can be seen that the heralding efficiency in this all-fibre experiment was 53% which was much higher than any other fibre photon pair sources. We believe

this impressive improvement benefits from the low loss fibre components and splices. When we connected the fibre components one by one through splicing, we measured the loss (including the splicing loss and insertion loss) for the idler arm using a 1550 nm CW laser diode (*Thorlabs, S1FC1550*). The loss measurement experimental setup is shown in Fig. 5.13. The measurement showed that the total loss at 1550 nm in the idler arm was only 1.7 dB (67.6% efficiency) which was much lower than 9.4 dB (11.5% efficiency) in the partial fibre-components filtering experiment. The efficiency 67.6% estimated from the loss measurement is higher than 53% calculated from the coincidence measurement. The possible reason is that the loss at 1572 nm is higher than the measured loss at 1550 nm.

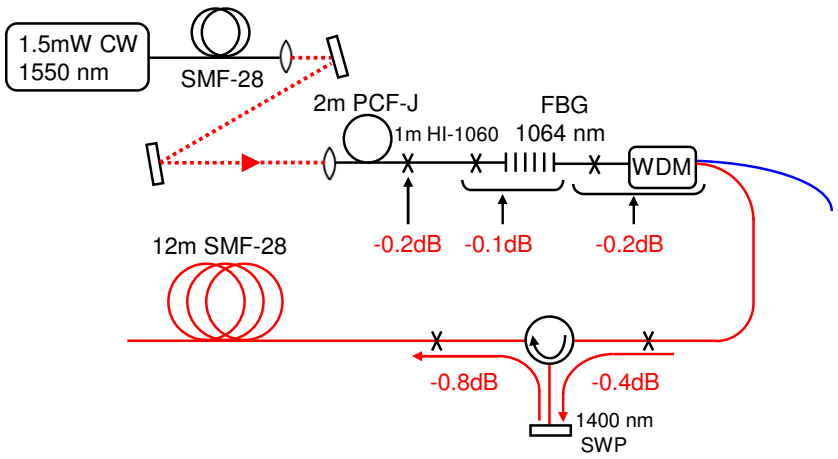

Figure 5.13: Schematic of the experimental setup for measuring the loss in the idler arm.

The work described in this section was presented at CLEO2008 (C. Xiong, A. R. McMillan, O. Alibart, J. Fulconis, J. G. Rarity and W. J. Wadsworth, CLEO, paper **QF12**, 2008).

5.3 Fibre Photon Pair Sources Pumped with ~710 nm Ti:Sapphire Laser

In Section 5.2, fibre photon pair sources were demonstrated to generate single photons in the telecom band using a modelocked 1064 nm fibre laser. It can be seen that the lumped efficiency is mainly limited by the low detection efficiency

of the InGaAs SPAD when the idler photons have very low transmission loss. In the case of short transmission distance or benchtop demonstration of quantum logic gates, the single photons should not necessarily be in the telecom band since the detection efficiency is more important than the transmission loss. As can be seen in the experiments above, the Si SPAD has much higher detection efficiency than the InGaAs SPAD. To make full use of the high detection efficiency of the Si SPAD, the ideal case is that both signal and idler photons are detected by Si SPADs. This means that a different laser and fibre are required to generate FWM peaks in the wavelength region where the Si SPAD provides high detection efficiencies. Our collaborators in Prof. Rarity's group at University of Bristol have successfully demonstrated high brightness fibre photon pair sources using a PCF with a zero-dispersion wavelength (ZDW) λ_D=715 nm and a modelocked picosecond Ti:Sapphire pump laser [164][165]. The FWM signal (587 nm) and idler (897 nm) peaks are both detected by the Si SPAD with high efficiencies.

Before the photon pair source can be used in quantum experiments or applications, the source needs to be filtered to very narrow bandwidth (0.28 nm in Ref. [166][167]) to further guarantee the purity of single-photon states. The narrowband filters significantly reduce the lumped efficiency of detection, which reduces count rates and makes the experiment take a long time. For any spectrally filtered source of photon pairs, the trade off between purity and count rate imposes a limit on the production rate of heralded photons and, in the situation where both arms are filtered, also the heralding efficiency. As shown in Section 5.2, simply reducing the filter bandwidth and increasing the pump power does not solve this problem. As one pumps harder, the background contribution from simultaneous generation of multiple pairs increases. If the purity is low then the fidelity of any operation will be poor. This has limited the multiphoton experiments to four-photon effects [166][167]. To achieve significant count rates whilst guaranteeing purity, the ideal case is that the photon pair source is naturally narrow band. It has recently been theoretically suggested that naturally narrow band phase matching can be achieved when the PCF is birefringent and the pair photons are created in orthogonal polarisation to the pump [168][169]. In this section, I shall describe the fabrication of a range of weakly birefringent PCFs designed for such phase matching and compare modelled phase matching curves to measured pair photon wavelengths. I shall also show the FWM bandwidth in a preliminary experiment done by M. Halder using one of these PCFs.

5.3.1 Fabrication and Modelling of Weakly Birefringent PCFs

It has been demonstrated in Section 4.4 that highly birefringent PCFs can be fabricated through enlarging two holes alongside the core area. It has also been mentioned in Section 2.4.4 that birefringence can also be introduced by making two holes smaller (Fig. 2.25(c)). The PCF described in this section needs to be designed to generate FWM peaks when pumped in the normal dispersion regime by a ∼710 nm laser. The desired ZDW of the PCF should be about 780-800 nm, which means that the core is small and the air holes are big (see Section 2.4.2). In the case of big cladding air holes, birefringence needs to be introduced by making two holes smaller because making the big holes even larger is difficult. A

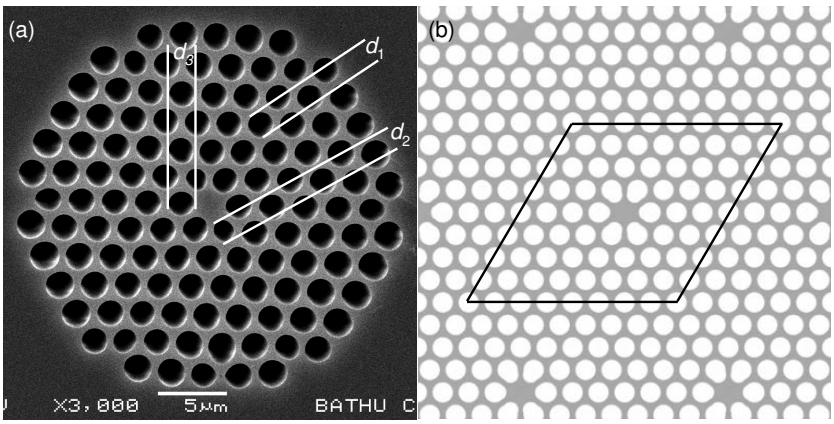

Figure 5.14: (a) The SEM of PCF-M. (b) The structure used for modelling of PCF-M [123]. The area surrounded by the diamond is the region of calculation.

preliminary calculation performed by our collaborators shows that weak rather than high birefringence is required because the highly birefringent PCF will shift the suitable pump wavelength to very short wavelength which is not in the tunable range of their laser. Using the same method as shown in Fig. 4.14 except that the pressure in the two specific holes are lower than that in other cladding holes, a set of weakly birefringent PCFs were fabricated. Their dispersion profiles were similar, but they had slightly different birefringence due to the different size of the two specific holes. As an example, the SEM of PCF-M, is shown in Fig. 5.14(a). Table 5.4 gives the parameters of PCF-M, PCF-N and PCF-O. In table 5.4, Λ is the hole to hole pitch. d_1 is the size of the cladding holes not in the first ring, d_2

is the size of the two smaller holes in the first ring and d_3 is the size of the other four holes in the first ring, as indicated in Fig. 5.14(a). d_3 is different from d_1 because the holes around core area are easier to deform and the whole fibre has been slightly inflated.

Table 5.4: The parameters of PCF-M, PCF-N and PCF-O.

Fibre No.	Λ (μm)	d_1/Λ	d_2/Λ	d_3/Λ	short axis (μm)	long axis (μm)
PCF-M	2.30	0.71	0.78	0.83	2.18	2.53
PCF-N	3.20	0.91	0.91	0.99	2.72	2.38
PCF-O	3.19	0.98	0.95	0.99	2.50	2.38

Using plane-wave method and the code developed by G. Pearce [123], the dispersion curves were calculated for PCF-M, PCF-N and PCF-O. Figure 5.14(b) shows the structure used for the modelling. The structure in Fig. 5.14(b) was reproduced from the SEM of PCF-M. The grey area is silica and the white area is air holes. It should be noted that in Fig. 5.14(b) only the central area surrounded by the diamond is the region of calculation. This area is called a supercell in the theory model. The exponential decay of electric fields in the cladding region ensures that the interaction between adjacent areas (introduced by the periodicity of the supercell lattice) is negligible. The calculation gave two propagation constants for fundamental modes of each PCF. This means that these PCFs are birefringent PCFs. To calculate the copolarisation and cross polarisation phase-matching curves using the modal parameters, let's recall the phase-mismatch equation

$$\kappa = \Delta\beta + \Delta k_{\mathrm{NL}}. \tag{5.5}$$

When the signal and idler have the same polarisation as the pump, the calculation is the same as in the scalar case discussed in Section 3.4.2, i. e. $\Delta\beta$ is the phase mismatch induced by dispersion and $\Delta k_{\mathrm{NL}} = 2\gamma P$ is the phase mismatch induced by nonlinearity. When the signal and idler are polarised orthogonally to the pump, $\Delta k_{\mathrm{NL}} = 2\gamma P/3$ if γ takes the same form as in the scalar case; and $\Delta\beta$ includes two contributions: phase mismatch $\delta\beta_D$ induced by dispersion and phase mismatch $\delta\beta_B$ induced by modal birefringence (see Section 3.6.2). The total phase mismatch becomes

$$\kappa = \delta\beta_D + \delta\beta_B + \Delta k_{\mathrm{NL}}. \tag{5.6}$$

According to Eqs. (5.5), (5.6) and energy conservation, both copolarisation and cross polarisation phase-matching curves can be calculated. Figure 5.15 shows the phase-matching curves calculated for PCF-M. In Fig. 5.15, ss→ss and ff→ff mean that both the FWM signal and idler are in the same slow/fast polarisation mode as the pump; ss→ff and ff→ss mean that both the FWM signal and idler photons are in the polarisation orthogonal to the pump. As discussed in Section 3.6.2, in cross polarisation cases Δk_{NL} is negligible compared with $\delta\beta_B$. Comparison between ff→ss and ff→ff or ss→ss shows that for the process of ff→ss, $\delta\beta_B$ looks like nonlinear contribution due to a high pump power in the scalar cases.

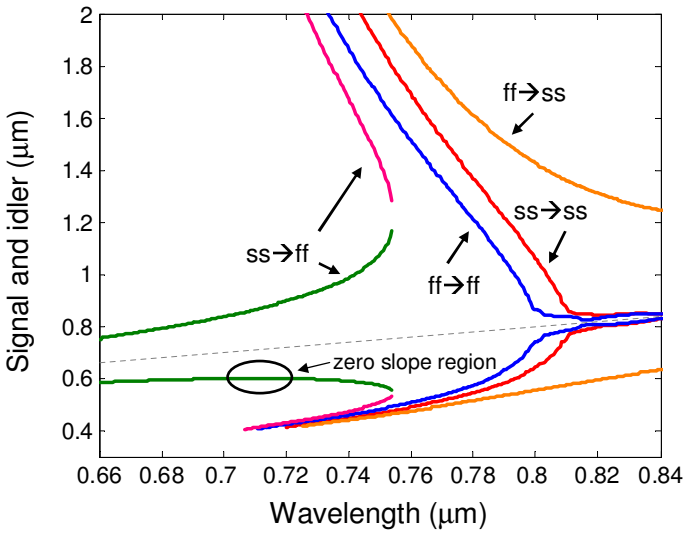

Figure 5.15: Calculated copolarisation and cross polarisation phase matching curves for PCF-M.

To be naturally spectrally narrow, the phase matched signal or idler wavelength should be insensitive to the pump wavelength, which is only possible if the phase-matching curve has a very small slope. It can be seen from Fig. 5.15 that all of these phase-matching curves have a region which may be suitable for such an application. For the copolarisation case, whether ss→ss or ff→ff, the phase-matching curve in the anomalous dispersion regime has a slope close to 1. However, as mentioned in Section 5.1, the idler wavelength is in the Raman gain band and suffers from the Raman noise. For the case of ff→ss, the curve slope is also close to 1 in the anomalous dispersion regime and the idler is further from the Raman gain band, but the copolarisation phase matching has higher

gain in this region and will compete with the cross polarisation phase matching. For the case of ss→ff, however, the situation indicated by the green curves is different. Phase matching only occurs in the normal dispersion regime and is the only efficient process in its phase-matching area. The most important feature is that the phase-matching curve has a slope of nearly zero in the signal band at a particular pump wavelength (710 nm).

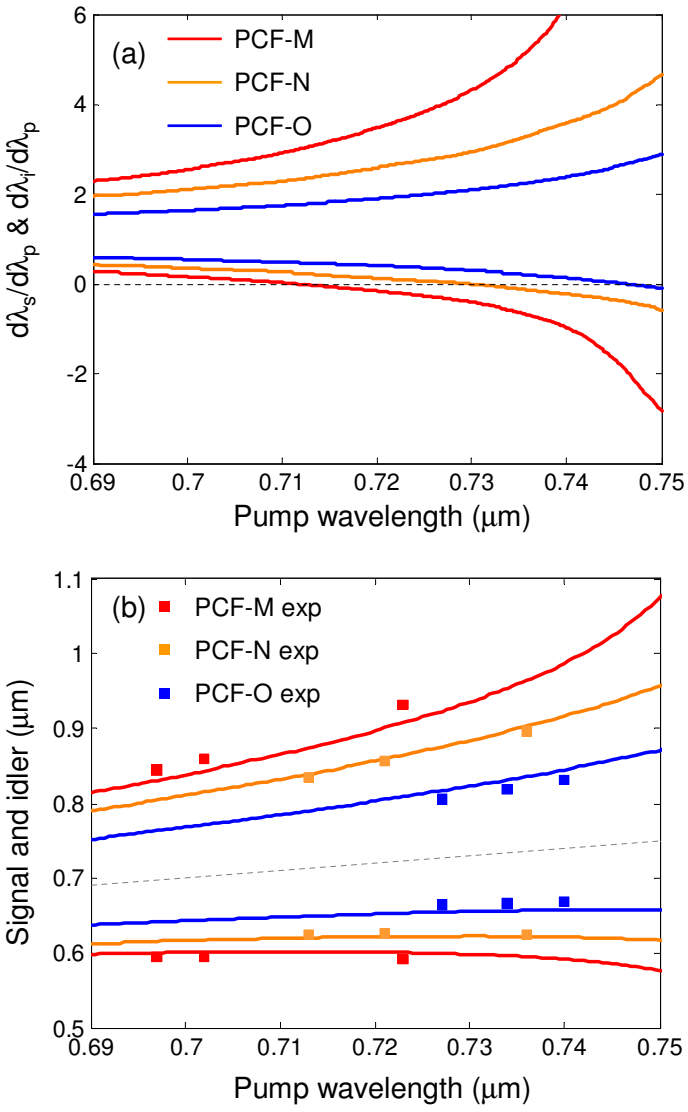

Figure 5.16: (a) Slope of the phase-matching curves in the case of ss→ff for PCF-M, PCF-N and PCF-O. (b) Comparison of experimental FWM peaks and the calculated FWM wavelengths for PCF-M, PCF-N and PCF-O.

To find out which pump wavelength corresponds to the zero slope point in

the phase-matching curves, the slope of the phase-matching curves like the green curve in Fig. 5.15 is plotted in Fig. 5.16(a) for PCF-M, PCF-N and PCF-O. It can be seen that all of these PCFs exhibit a zero slope pump wavelength in the cross polarisation phase-matching curves. Even if the pump wavelength is not exactly at the zero slope wavelength, the slope is very close to zero, which makes the insensitivity of the signal wavelength to the pump wavelength possible. Using these PCFs, M. Halder did a set of FWM experiments pumped by a picosecond Ti:sapphire laser tuneable from 690 nm to 750 nm. The experimental results are plotted with the calculated phase-matching curves together in Fig. 5.16(b). It can be seen that the experimental results agree with the calculations very well for all of these three PCFs.

5.3.2 Naturally Narrow Band Photon Pair Source

All the PCFs described in Section 5.3.1 can be used to make naturally narrow band photon pair sources. In order to optimize the source, the idler wavelength should be as far as possible from the Raman gain band. It can be seen from Fig. 5.16(b) that PCF-M seems to be the best one. The difference between other two PCFs and PCF-M is that PCF-M has highest birefringence and PCF-O has the lowest birefringence. So it is the strength of birefringence that determines how far the idler wavelength is from the pump and the Raman gain band. However, as indicated by Fig. 5.16(a), when the birefringence gets higher, the zero slope pump wavelength will be shifted to shorter wavelength. If the birefringence is too high, the suitable pump wavelength will be not in the tuneable range of the laser. So there is an interplay between avoiding the Raman noise and obtaining naturally narrow bandwidth. PCF-M has been proved to be the optimum one in our experiment.

M. Halder took a 102 cm piece of PCF-M to measure the FWM signal and idler bandwidth as well as their wavelengths. The pump laser was operating at 705 nm. The spectra for both signal and idler are shown in Fig. 5.17. The signal wavelength is centred at 596.8 nm and the full width at half maximum (FWHM) is only 0.122 nm which is extremely narrow. The idler wavelength is centred at 865.2 nm and FWHM is several nanometers. Although the Raman noise is clearly seen in the idler band, a polariser with high transmission can be used to remove the noise since most of the Raman photons have the same polarisation as

the pump photons (see Fig. 3.2). The idler photons can be used as the heralding photons rather than heralded photons in quantum experiments since they are not naturally narrow band. The signal photon is naturally narrow band and can be used as the heralded photons without the need of extremely narrow band filters. Another advantage of this source is that the photons are linearly polarised since they are generated in a birefringent PCF. PCF-M has been incorporated in quantum experiments and we are expecting good performance.

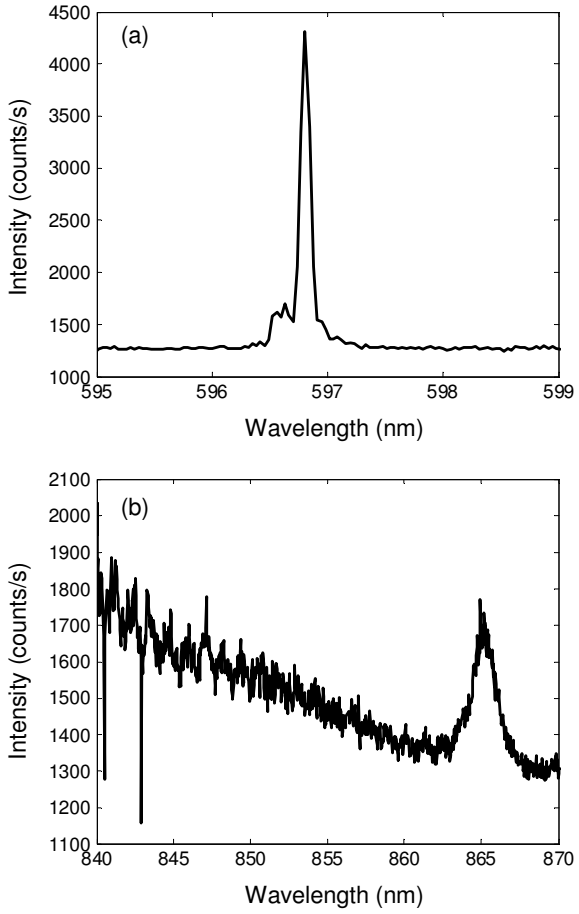

Figure 5.17: (a) The spectrum of FWM signal in PCF-M pumped by a 705 nm laser. (b) The spectrum of FWM idler in PCF-M pumped by a 705 nm laser.

The work described in this section has been accepted as an oral presentation at the 3rd International Conference on Quantum Information (J. Fulconis, A. Clark, M. Halder, J. L. O'Brien, J. G. Rarity; C. Xiong, W. J. Wadsworth, ICQI, paper **QWB5**, 2008).

5.4 Conclusion

In this chapter I have given a short review of single-photon sources. As one of the most important elements in the quantum information system, researchers have paid great attention and interest into designing high-quality single-photon sources by both bulk optics and optical fibres. It turns out that fibre photon pair sources based on the $\chi^{(3)}$ nonlinear FWM in PCFs have great potential to be developed for practical applications. The endlessly single-mode PCFs can guarantee photons in a single fundamental mode. The flexibility of dispersion and birefringence control of PCFs can make the photons naturally narrowband, polarised and located in the wavelength range desired for different applications. Pumping in the normal dispersion regime can greatly reduce the main noise contribution from the Raman effect. With the development of splicing technique, the PCF source has been connected to conventional fibre components with very low loss. All of these advantages have enabled PCFs to be used to make photon pair sources for different applications.

One of the most important current applications of photon pair sources is in long-distance quantum communication systems compatible with the modern telecom system. Therefore I have demonstrated an all-fibre photon pair source using a PCF designed for emitting photons in the telecom band. This source has exhibited the highest brightness compared with other sources working in the same wavelength band. Work is still going on for further improvement.

Another possible application is the short-distance free-space quantum communication and quantum logic gates. In this case the single photons need not necessarily be in the telecom band, and it is better if they are in the wavelength range where high detection efficiency detectors are available. The Si SPAD provides a high detection efficiency in the wavelength range from 550 nm to 900 nm. Thanks to the flexible dispersion and birefringence control of PCFs and the availability of ∼710 nm lasers, I have fabricated weakly birefringent PCFs suitable for making naturally narrow band photon pair sources. Both modelling and experimental results show that extremely narrow band photons can be generated in such a weakly birefringent PCF. This has immediately eliminated the need of narrow band filters in most quantum experiments and will provide a much brighter source for multiphoton experiments and demonstrations.

Chapter 6

Summary and Future Work

6.1 Summary

In this thesis I have introduced the linear and nonlinear properties of PCF, described the fabrication and characterisation of different PCFs, and demonstrated their applications to supercontinuum (SC) generation and single-photon sources. The linear properties of PCF include endlessly single-mode transmission, highly controllable dispersion and birefringence. These unique properties have made PCFs the best media to demonstrate all kinds of nonlinear effects such as self-phase modulation (SPM), cross-phase modulation (XPM), Raman effects, four-wave mixing and modulation instability (FWM and MI), and soliton effects. The combined effect of these nonlinear effects has led to impressive spectral broadening known as SC generation in PCFs. The intrinsic correlation of the FWM signal and idler photons makes PCF ideal for use in the application of single-photon generation. In this section, I summarize the research work described in this thesis.

Visible Supercontinuum Generation

In this project, I designed and A. Witkowska made an inflated and tapered device in an endlessly single-mode PCF, PCF-C, for two-stage visible SC generation. In the first stage, as the pump wavelength is a nanosecond microchip laser running at 1064 nm which is in the normal dispersion regime of PCF-C (zero-dispersion wavelength, ZDW, λ_D=1103 nm), the original PCF-C emitted an intense FWM peak at 742 nm with an efficiency of 35%. The light at 742 nm then entered the inflated and tapered device through a splicing-free tapering transition with low

loss to become the pump source in the second stage. As the device has large air holes and a small core, it is equivalent to a piece of highly nonlinear PCF with λ_D ~700 nm. When the device was pumped by the 742 nm light in the anomalous dispersion regime, a flat, bright and single-mode visible continuum was achieved. The short wavelength edge was 400 nm and the power level was -20 dBm/nm. Compared with other two-stage visible SC systems, this device is convenient to fabricate and both of the ends are 5 μm core PCFs which are compatible with conventional optical components and offer good coupling efficiency in practical applications.

Polarised Supercontinuum Generation and its Appication

In this project, I designed and fabricated a set of highly birefringent PCFs using a solid core PCF preform with uniform air hole diameters. The birefringence was induced through applying differential pressure to enlarge two specific air holes alongside the core area during the final fabrication stage of drawing the preform to fibre. This eliminates the need for a special stack with capillaries of different wall thickness. Both dispersion and birefringence were easy to control. A highly birefringent (beat length 8.6 mm at 1064 nm) PCF, PCF-A, was achieved. PCF-A has low transmission loss (10 dB/km at 1064 nm), low coupling loss with symmetrical PCFs and lasers and the right dispersion for SC generation when pumped at 1064 nm. When 6 m length of PCF-A was pumped by a nanosecond microchip 1064 nm laser, a flat continuum spanning 450-1750 nm was generated. The polarisation purity of this continuum was high. More than 99% power was kept in a single linear polarisation.

I then demonstrated a particular application of this polarised continuum generated from 0.6 m length of PCF-A: tuneable visible/UV generation in a nonlinear crystal BIBO. It was found that sum-frequency mixing (SFM) was more efficient than second harmonic generation (SHG) due to the relatively strong residual power at the pump wavelength and the existence of different wavelengths in the continuum. By simply rotating the crystal to different phase-matching angles, the upconverted wavelength was tuneable from 400 to 525 nm, limited by the crystal aperture at larger angles. The resulting spectra were very clean. As a comparison, I also demonstrated polarised FWM in another highly birefringent PCF, PCF-B, whose ZDW was at a longer wavelength than PCF-A so that the 1064 nm pump wavelength was in the normal dispersion regime. The FWM

process generated a distinct and intense signal peak at 834 nm. Using SFM between 834 nm and 1064 nm, and SHG of 834 nm, bright and clean blue light were generated at 467 nm and 417 nm, respectively.

Ultra-flat Supercontinuum Generation

In this project, I demonstrated a method to remove the residual pump peak of SC in the nanosecond pulse pumping regime, without leaving an equally problematic spectral trough. It was first reported that the residual pump peak of SC generated from a PCF could be removed by using a fibre Bragg grating (FBG) followed by nonlinear flattening of the resulting spectral hole in another PCF. This method also flattens the modulation instability (MI) peaks around the pump peak. The pump power in a SC spectrum before removal was measured to be <10%.

Supercontinuum Generation with a Dual-wavelength Pump in an All-fibre Device

In this project, I proposed a dual-wavelength pumping scheme for SC generation in an all-fibre device and demonstrated its performance in a preliminary experiment. In previous dual-wavelength pumping experiments, the dual-wavelength pump source was achieved through frequency doubling an IR pump wavelength in a $\chi^{(2)}$ nonlinear crystal. In my preliminary experiment, the dual-wavelength pump source was achieved by FWM in the first piece of PCF, PCF-G, when pumped by a 1064 nm nanosecond microchip laser. The FWM process in PCF-G emitted an intense peak at 686 nm. Then the residual pump and the 686 nm photons were fed into another piece of PCF, PCF-H, which was designed to make the 686 nm and 1064 nm photons travel at the same group velocity. The nonlinear interaction between the two pump wavelengths led to spectral broadening around 686 nm. The flexibility of dispersion control of both PCFs in this scheme enables a spectrally localised continuum to be generated around the wavelength of interest. The aim is to splice the two PCFs together with low loss at both pump wavelengths.

Fibre Photon Pair Sources Pumped with 1064 nm Fibre Laser

In this project, I demonstrated a fibre photon pair source pumped with a 1064 nm picosecond fibre laser. The wavelengths of the pair photons were supposed to be in the telecom band so that this source was applicable to quantum communication

in the modern telecom systems. The aim of this project was to build an all-fibre photon pair source with high brightness and high purity. Before the all-fibre demonstration, I identified the wavelengths of the pair photons to be 804 nm and 1572 nm in a free-space experiment and also observed the coincidence, but with low count rate. The partial fibre-components photon pair source showed a much higher coincidence count rate and lower noise than the free-space case, but the heralding efficiency of single photons was still quite low due to the total loss of 9.2 dB. Then an all-fibre photon pair source was demonstrated with only 1.7 dB loss in the heralded photon arm. A heralding efficiency of >50% was achieved, which is high compared with other fibre photon pair sources. Further progress is still going on.

Naturally Narrow Band Fibre Photon Pair Source

In this project, I designed and fabricated weakly birefringent PCFs for naturally narrow band photon pair generation pumped by a picosecond Ti:sapphire laser source. The modelling showed that the naturally narrow band photon generation could be achieved through cross polarisation phase matching FWM in the normal dispersion regime of a weakly birefringent PCF. Using the PCFs I made, our collaborators in the group of Prof. Rarity at University of Bristol have been able to measure the FWM peaks at different pump wavelengths. The experimental results agreed with the modelling very well. They also measured the FWM signal and idler spectra for one of the PCFs, PCF-M. Indeed, the spectrum of the signal showed that the bandwidth was only 0.122 nm without the use of any narrow band filters. This source will eliminate the need of extremely narrow band filters, which normally induce high transmission loss in the single-photon experiments. Another advantage of this source is that both signal and idler wavelengths are in the high detection efficiency range of Si SPAD. The lumped efficiency may be increased significantly so that 6- or even 8-photon experiments become possible.

6.2 Future Work

Based on what I have done and the results describe in this thesis, some important improvements or new research probabilities are discussed in this section.

Supercontinuum Generation with a Dual-wavelength Pump in an All-fibre Device

In Section 4.6, the idea of a dual-wavelength pumping scheme was proposed for SC generation in an all-fibre device. Only a preliminary experiment using free-space optics was demonstrated there. However, even the preliminary experiment showed good results of SC generation as expected. Further improvements should be possible to achieve a real all-fibre device. First, as indicated in Section 4.6, the SC generation mechanism in this dual-wavelength pumping scheme is mainly soliton trapping, and FWM between dispersive waves and IR solitons in the second PCF. These nonlinear interactions require group velocity matching of dispersive waves and IR solitons. Therefore designing a PCF with the right dispersion for the group matching is essential to this experiment and should not be difficult. Second, the coupling efficiency between two different PCFs is also very important. As mentioned in Section 2.5, low splicing loss is possible for two different PCFs. However, the best record for such splicing in literature is 2.5 dB [84]. The main limit of the technique described in Ref. [84] is that the mode field matching is achieved through hole collapse in an uncontrollable way. However our group members have shown that the hole collapse can be controlled [170]. By blocking the holes that are intended to be collapsed, pressurizing other cladding holes and then heating the fibre, we can collapse any holes we want. The mode field diameter in the highly nonlinear PCF used for SC generation in our case can be enlarged through collapsing the first ring or even the second ring holes in this way. When the holes are collapsed, the loss will be low because the tapering rig can make an adiabatic transition. A splicing loss of less than 3 dB at 1550 nm was achieved in a very preliminary experiment. It is believed that the splicing loss can be reduced to less than 1 dB. Then a real all-fibre device can be used to realize a dual-wavelength pumping scheme for SC generation. By the selection of the first piece of PCF, we can actually control the spectral location of the continuum.

Fibre Photon Pair Sources in the Telecom Band

In Section 5.2, a photon pair source was demonstrated looking towards an all-fibre setup for operation in the telecom band, and showed very good performance. However there are still many possibilities to improve it further. Firstly, it can be seen that the idler photons used as heralded photons were not exactly at

1550 nm but at 1572 nm. We should be able to make a set of new PCFs that generate this wavelength so that all of the common fibre components, such as the WDM and circulator, are immediately available and provide the lowest loss. Secondly, the quantum experiments using photon pair sources need polarisation control. The source described in Section 5.2 did not consider polarisation yet. When we fabricate a fibre to make the FWM process generate 1550 nm, we can also introduce birefringence as demonstrated in Section 4.4. Thirdly, the aim of this project is to make an all-fibre photon pair source. As can be seen in Fig. 5.10, the experimental setup was not a completely all-fibre setup. There were still free-space coupling between the pump laser and PCF-J, and free-space filtering and coupling in the signal arm. We can integrate a combination of a FBG and a circulator acting as an isolator and a filter into the laser source and splice the fibre pigtail to PCF-J to remove the bulk optics in the input end. For the filtering in the signal arm, we can use a circulator, designed for the signal wavelength, in a similar way to the idler arm. Lastly, we need to splice a FBG to the circulator port C2 to filter the photons in both arms to narrow bandwidth for quantum interference experiments. Figure 6.1 gives the all-fibre photon pair source experimental configuration.

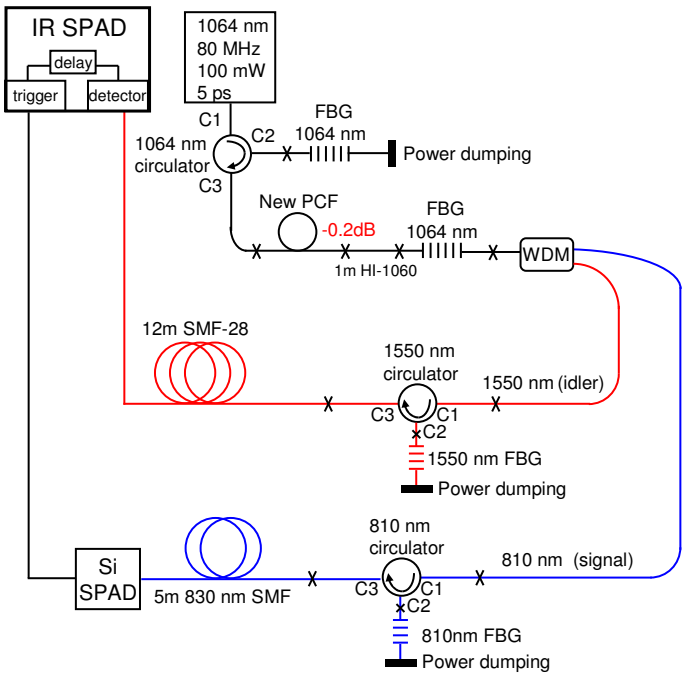

Figure 6.1: A completely all-fibre setup for photon pair source.

References

[1] J. L. Baird, British Patent **285**, 738 (1928).

[2] A. C. S. van Heel, "A New Method of transporting Optical Images without Aberrations," *Nature* **137**, 39 (1954).

[3] H. H. Hopkins and N. S. Kapany, "A Flexible Fibrescope, using Static Scanning," *Nature* **173**, 39 (1954).

[4] N. S. Kapany, *Fiber Optics: Principles and Applications* (Academic, 1967).

[5] F. P. Kapron, D. B. Keck, and R. D. Maurer, "Radiation Losses in Glass Optical Waveguides," *Appl. Phys. Lett.* **17**, 423 (1970).

[6] T. Miya, Y. Terunuma, T. Hosaka, and T. Miyashita, "Ultimate Low-Loss Single-Mode Fibre at 1.55 μm," *Electron. Lett.* **15**, 106 (1979).

[7] G. P. Agrawal, *Fiber-Optic Communication Systems*, 3rd ed. (Wiley, 2002).

[8] G. P. Agrawal, *Nonlinear Fiber Optics*, 4th ed. (Academic, 2007).

[9] T. H. Maiman, "Stimulated Optical Radiation in Ruby," *Nature* **187**, 493 (1960).

[10] R. H. Stolen, E. P. Ippen, and A. R. Tynes, "Raman Oscillation in Glass Optical Waveguide," *Appl. Phys. Lett.* **20**, 62 (1972).

[11] E. P. Ippen and R. H. Stolen, "Stimulated Brillouin scattering in optical fibers," *Appl. Phys. Lett.* **21**, 539 (1972).

[12] R. G. Smith, "Optical Power Handling Capacity of Low Loss Optical Fibers as Determined by Stimulated Raman and Brillouin Scattering," *Appl. Opt.* **11**, 2489 (1972).

[13] R. H. Stolen and A. Ashkin, "Optical Kerr effect in glass waveguide," *Appl. Phys. Lett.* **22**, 294 (1973).

[14] R. H. Stolen, J. E. Bjorkholm, and A. Ashkin, "Phase-matched three-wave mixing in silica fiber optical waveguides," *Appl. Phys. Lett.* **24**, 308 (1974).

[15] K. O. Hill, D. C. Johnson, B. S. Kawaski, and R. I. MacDonald, "cw three-wave mixing in single-mode optical fibers," *J. Appl. Phys.* **49**, 5098 (1974).

[16] R. H. Stolen, "Phase-Matched-Stimulated Four-Photon Mixing in Silica-Fiber Waveguides," *IEEE J. Quantum Electron.* **11**, 100 (1975).

[17] R. H. Stolen and C. Lin, "Self-phase-modulation in silica optical fibers," *Phys. Rev. A* **17**, 1448 (1978).

[18] A. Hasegawa and F. Tappert, "Transmission of stationary nonlinear optical pulses in dispersive dielectric fibers .I. Anomalous dispersion," *Appl. Phys. Lett.* **23**, 142 (1973).

[19] L. F. Mollenauer, R. H. Stolen, and J. P. Gordon, "Experimental Observation of Picosecond Pulse Marrowing and Solitons in Optical Fibers," *Phys. Rev. Lett.* **45**, 1095 (1980).

[20] A. Hasegawa and W. F. Brinkman, "Tunable Coherent IR and FIR Sources Utilizing Modulational Instability," *IEEE J. Quantum Electron.* **16**, 694 (1980).

[21] K. Tai, A. Hasegawa and A. Tomita, "Observation of Modulational Instability in Optical Fibers," *Phy. Rev. Lett.* **56**, 135 (1986).

[22] A. R. Chraplyvy and J. Stone, "Measurement of Crossphase Modulation in Coherent Wavelength-Division Multiplexing Using Injection Lasers," *Electron. Lett.* **20**, 996 (1984).

[23] J. C. Knight, T. A. Birks, P. St. J. Russell and D. M. Adkin, "All-silica single-mode optical fiber with photonic crystal cladding," *Opt. Lett.* **21**, 1547 (1996); J. C. Knight, T. A. Birks, P. St. J. Russell and D. M. Adkin, "All-silica single-mode optical fiber with photonic crystal cladding: errata," *Opt. Lett.* **22**, 484 (1997).

[24] T. A. Birks, J. C. Knight and P. St. J. Russell, "Endlessly single-mode photonic crystal fiber," *Opt. Lett.* **22**, 961 (1997).

[25] J. C. Knight, T. A. Birks, R. F. Cregan, P. St. J. Russell and J. -P. de Sandro, "Large mode area photonic crystal fibre, " *Electron. Lett.* **34**, 1347 (1998).

[26] D. Mogilevtsev, T. A. Birks, and P. St.J. Russell, "Group-velocity dispersion in photonic crystal fibers," *Opt. Lett.* **23**, 1662, (1998).

[27] J. C. Knight, J. Broeng, T. A. Birks and P. St. J. Russell, "Photonic Band Gap Guidance in Optical Fibers," *Science* **282**, 1476(1998).

[28] R. F. Cregan, B. J. Mangan, J. C. Knight, T. A. Birks, P. St.J. Russell, P. J. Roberts, and D. C. Allan, "Single-mode photonic band gap guidance of light in air," *Science* **285**, 1537 (1999).

[29] J. C. Knight, J. Arriaga, T. A. Birks, A. Ortigosa-Blanch, W. J. Wadsworth, and P. St.J. Russell, "Anomalous dispersion in photonic crystal fibers," *IEEE Photon. Technol. Lett.* **12**, 807 (2000).

[30] A. Ortigosa-Blanch, J. C. Knight, W. J. Wadsworth, J. Arriaga, B. J. Mangan, T. A. Birks, and P. St.J. Russell, "Highly birefringent photonic crystal fibers," *Opt. Lett.* **25**, 1325 (2000).

[31] P. St. J. Russell, "Photonic Crystal Fibers," *Science* **299**, 358 (2003).

[32] J. C. Knight, "Photonic crystal fibres," *Nature* **424**, 847 (2003).

[33] F. Luan, A. K. George, T. D. Hedley, G. J. Pearce, D. M. Bird, J. C. Knight, and P. St. J. Russell, "All-solid photonic bandgap fiber," *Opt. Lett.* **29**, 2369 (2004).

[34] P. St. J. Russell, "Photonic-Crystal Fibers," *J. Lightwave Technol.* **24**, 4729 (2006).

[35] J. K. Ranka, R. S. Windeler and A. J. Stentz, "Visible continuum generation in air-silica microstructure optical fibers with anomalous dispersion at 800nm," *Lasers and Electro-Optics, 1999. CLEO '99. Summaries of Papers Presented at the Conference on* paper **CPD8**, (1999).

[36] J. K. Ranka, R. S. Windeler and A. J. Stentz, "Visible continuum generation in air-silica microstructure optical fibers with anomalous dispersion at 800nm," *Opt. Lett.* **25**, 25 (2000).

[37] T. A. Birks, W. J. Wadsworth and P. St. J. Russell, "Supercontinuum generation in tapered fibers," *Opt. Lett.* **25**, 1415 (2000).

[38] A. V. Husakou and J. Herrmann, "Supercontinuum Generation of Higher-Order Solitons by Fission in Photonic Crystal Fibers," *Phys. Rev. Lett.* **87**, 203901 (2001).

[39] J. Herrmann, U. Griebner, N. Zhavoronkov, A. Husakou, D. Nickel, J. C. Knight, W. J. Wadsworth, P. J. Russell, and G. Korn, "Experimental Evidence for Supercontinuum Generation by Fission of Higher-Order Solitons in Photonic Fibers," *Phys. Rev. Lett.* **88**, 173901 (2002).

[40] S. Coen, A. H. L. Chau, R. Leonhardt and J. D. Harvey, J. C. Knight, W. J. Wadsworth and P. St. J. Russell, "White-light supercontinuum generation with 60-ps pump pulses in a photonic crystal fiber," *Opt. Lett.* **26**, 1356 (2001).

[41] S. Coen, A. H. L. Chau, R. Leonhardt and J. D. Harvey, J. C. Knight, W. J. Wadsworth and P. St. J. Russell, "Supercontinuum generation by stimulated Raman scattering and parametric four-wave mixing in a photonic crystal fiber," *J. Opt. Soc. Am. B* **19**, 753 (2002).

[42] P. A. Champert, S. V. Popov, and J. R. Taylor, "Generation of multiwatt, broadband continua in holey fibers," *Opt. Lett.* **27**, 122 (2002).

[43] W. J. Wadsworth, N. Joly, J. C. Knight, T. A. Birks, F. Biancalana and P. St. J. Russell, "Supercontinuum and four-wave mixing with Q-switched pulses in endlessly single-mode photonic crystal fibres," *Opt. Express* **12**, 299 (2004).

[44] A. V. Avdokhin, S. V. Popov, and J. R. Taylor, "Continuous-wave, high-power, Raman continuum generation in holey fibers," *Opt. Lett.* **28**, 1353 (2003).

[45] J. C. Travers, R. E. Kennedy, S. V. Popov, and J. R. Taylor, H. Sabert and B. Mangan, "Extended continuous-wave supercontinuum generation in a low-water-loss holey fiber," *Opt. Lett.* **30**, 1938 (2005).

[46] W. J. Wadsworth, J. C. Knight, A. Ortigosa-Blanch, J. Arriaga, E. Silvestre and P. St. J. Russell, "Soliton effects in photonic crystal fibres at 850nm," *Electron. Lett.* **36**, 53 (2000).

[47] M. L. V. Tse, P. Horak, J. H. V. Price, F. Poletti, F. He, and D. J. Richardson, "Pulse compression at 1.06 μm in dispersion-decreasing holey fibers," *Opt. Lett.* **31**, 3504 (2006).

[48] J. C. Travers, J. M. Stone, A. B. Rulkov, B. A. Cumberland, A. K. George, S. V. Popov, J. C. Knight and J. R. Taylor, "Optical pulse compression in dispersion decreasing photonic crystal fiber," *Opt. Express* **15**, 13203 (2007).

[49] S. Bourquin, A. D. Aguirre, I. Hartl, P. Hsiung, T. H. Ko and J. G. Fujimoto, T. A. Birks, W. J. Wadsworth, U. Bünting and D. Kopf, "Ultrahigh resolution real time OCT imaging using a compact femtosecond Nd:Glass laser and nonlinear fiber," *Opt. Express* **11**, 3290 (2003).

[50] J. G. Rarity, J. Fulconis, J. Duligall, W. J. Wadsworth and P. St. J. Russell, "Photonic Crystal fiber source of correlated photon pairs," *Opt. Express* **13**, 534 (2005).

[51] J. Gower, *Optical Communication Systems*, 2nd ed. (Prentice Hall, London, 1993).

[52] K. Okamoto, *Fundamentals of Optical Waveguides*, 2nd ed. (Academic, 2006).

[53] D. B. Keck, R. D. Maurer, and P. C. Schultz, "On the ultimate lower limit of attenuation in glass optical waveguides," *Appl. Phys. Lett.* **22**, 307 (1973).

[54] P. Kaiser, "Spectral losses of unclad fibers made from high grade vitreous silica," *Appl. Phys. Lett.* **23**, 45 (1973).

[55] O. Humbach, H. Fabian, U. Grzesik, U. Haken and W. Heitmann, "Analysis of OH absorption bands in synthetic silica," *J. Non-Crystalline Solid* **203**, 19 (1996).

[56] G. A. Thomas, B. L. Shraiman, P. F. Glodis, and M. J. Stephan, "Towards the clarity limit in optical fibre," *Nature* **404**, 262 (2000).

[57] S. R. Nagel, J. B. Macchesney, and K. L. Walker, "An Overview of the Modified Chemical Vapor Deposition (MCVD) Process and Performance," *IEEE J. Quantum Electron.* **18**, 459 (1982).

[58] L. G. Cohen, "Comparison of Single-Mode Fiber Dispersion Measurement Techniques," *IEEE J. Lightwave Technol.* **3**, 958 (1985).

[59] I. H. Malitson, "Interspecimen Comparison of the Refractive Index of Fused Silica," *J. Opt. Soc. Am.* **55**, 1205 (1965).

[60] B. J. Ainslie and C. R. Day, "A Review of Single-Mode Fibers with Modified Dispersion Characteristics," *IEEE J. Lightwave Technol.* **4**, 967 (1986).

[61] F. G. Omenetto and A. J. Taylor, M. D. Moores, J. Arriaga, J. C. Knight, W. J. Wadsworth, and P. St. J. Russell, "Simultaneous generation of spectrally distinct third harmonics in a photonic crystal fiber," *Opt. Lett.* **26**, 1158 (2001).

[62] F. G. Omenetto, A. Efimov, A. J. Taylor and J. C. Knight, W. J. Wadsworth, P. St. J. Russell, "Polarization dependent harmonic generation in microstructured fibers," *Opt. Express* **11**, 61 (2003).

[63] A. Efimov, A. J. Taylor, F. G. Omenetto, J. C. Knight, W. J. Wadsworth, P. St. J. Russell, "Phase-matched third harmonic generation in microstructured fibers," *Opt. Express* **11**, 2567 (2003).

[64] V. Grubsky, A. Savchenko, "Glass micro-fibers for efficient third harmonic generation," *Opt. Express* **13**, 6798 (2005).

[65] V. Grubsky, J. Feinberg, "Phase-matched third-harmonic UV generation using low-order modes in a glass micro-fiber," *Opt. Commun.* **274**, 447 (2007).

[66] R. W. Boyd, *Nonlinear Optics*, 2nd ed. (Academic Press, San Diego, 2003).

[67] J. D. Joannopoulos, R. D. Meade and J. N. Winn, *Photonic Crystals*, (Princeton University Press, 1995).

[68] W. H. Reeves, *Photonic crystal fibre : the ultra-flattened dispersion regime*, Ph.D. thesis (University of Bath, 2003).

[69] T. A. Birks and Y. W. Li, "The Shape of Fiber Tapers," *IEEE J. Lightwave Technol.* **10**, 432 (1992).

[70] W. J. Wadsworth, A. Witkowska, S. G. Leon-Saval and T. A. Birks, "Hole inflation and tapering of stock photonic crystal fibers," *Opt. Express* **13**, 6541 (2005).

[71] Group resources in the Centre of Photonics and Photonic Material at University of Bath.

[72] J. D. Love, "Spot Size, Adiabaticity and Diffraction in Tapered Fibres," *IEEE Electron. Lett.* **23**, 993 (1987).

[73] T. A. Birks, D. Mogilevtsev, J. C. Knight, P. St. J. Russell, J. Broeng, P. J. Roberts, J. A. West, D. C. Allen, J. C. Fajardo, "The analogy between photonic crystal fibres and step index fibres," *Proceedings of the Optical Fiber Communication Conference* (OFC, San Diego, California), paper **FG4** (1999).

[74] K. Saitoh and M. Koshiba, "Empirical relations for simple design of photonic crystal fibers," *Opt. Express* **13**, 267 (2005).

[75] V. Finazzi, T. M. Monro and D. J. Richardson, "The Role of Confinement Loss in Highly Nonlinear Silica Holey Fibers," *IEEE Photon. Technol. Lett.* **15**, 1246 (2003).

[76] M. A. Newhouse, D. L. Weidman, and D. W. Hall, "Enhanced-nonlinearity single-mode lead silicate optical fiber," *Opt. Lett.* **15**, 1185 (1990).

[77] X. Feng, A. K. Mairaj, D. W. Hewak, and T. M. Monro, "Nonsilica Glasses for Holey Fibers," *IEEE J. Lightwave Technol.* **23**, 2046 (2005).

[78] D. -I. Yeom, E. C. Mägi, M. R. E. Lamont, M. A. F. Roelens, L. Fu, and B. J. Eggleton, "Low-threshold supercontinuum generation in highly nonlinear chalcogenide nanowires," *Opt. Lett.* **33**, 660 (2008).

[79] R. B. Dyott, *Elliptical Fiber Waveguides* (Artec House, Boston, 1995).

[80] M. Lehtonen, G. Genty, and H. Ludvigsen, M. Kaivola, "Supercontinuum generation in a highly birefringent microstructured fiber," *Appl. Phys.Lett.* **82**, 2197 (2003).

[81] K. Suzuki, H. Kubota, S. Kawanishi, M. Tanaka and M. Fujita, "Optical properties of a low-loss polarization-maintaining photonic crystal fiber," *Opt. Express* **9**, 676 (2001).

[82] B. Bourliaguet, C. Paré, F. Émond, A. Croteau, A. Proulx, and R. Vallée, "Microstructured fiber splicing," *Opt. Express* **11**, 3412 (2003).

[83] L. Xiao, M. S. Demokan, W. Jin, Y. Wang, and C. Zhao, "Fusion Splicing Photonic Crystal Fibers and Conventional Single-Mode Fibers: Microhole Collapse Effect," *IEEE J. Lightwave Technol.* **25**, 3563 (2007).

[84] L. Xiao, W. Jin, and M. S. Demokan, "Fusion splicing small-core photonic crystal fibers and single-mode fibers by repeated arc discharges," *Opt. Lett.* **32**, 115 (2007).

[85] M. J. Ablowitz and P. A. Clarkson, *Solitons, Nonlinear Evolution Equations, and Inverse Scattering* (Cambridge University Press, New York, 1991).

[86] K. Shi, P. Li, S. Yin, and Z. Liu, "Chromatic confocal microscopy using supercontinuum light," *Opt. Express* **12**, 2096 (2004).

[87] G. McConnell, "Confocal laser scanning fluorescence microscopy with a visible continuum source," *Opt. Express* **12**, 2844 (2004).

[88] P. Li, K. Shi, and Z. Liu, "Optical scattering spectroscopy by using tightly focused supercontinuum," *Opt. Express* **13**, 9039 (2005).

[89] R. R. Alfano and S. L. Shapiro, "Emission in the region 4000 to 7000 Å via four-photon coupling in glass," *Phys. Rev. Lett.* **24**, 584 (1970).

[90] R. R. Alfano and S. L. Shapiro, "Observation of self-phase modulation and small-scale filaments in crystals and glasses," *Phys. Rev. Lett.* **24**, 592(1970).

[91] C. Lin and R. H. Stolen, "New nanosecond continuum for excited-state spectroscopy," *Appl. Phys. Lett.* **28**, 216 (1976).

[92] P. L. Baldeck and R. R. Alfano, "Intensity effects on the stimulated four photon spectra generated by picosecond pulses in optical fibers," *IEEE J. Lightwave Technol.* **5**, 1712 (1987).

[93] T. Morioka, K. Mori, and M. Saruwatari, "More than 100-wavelength-channel picosecond optical pulse generation from single laser source using supercontinuum in optical fibers," *Electron. Lett.* **29**, 862 (1993).

[94] T. Morioka, S. Kawanishi, K. Mori, and M. Saruwatari, "Nearly penalty-free, <4 ps supercontinuum Gbit/s pulse generation over 1535-1560 nm," *Electron. Lett.* **30**, 790 (1994).

[95] K. Mori, H. Takara, S. Kawanishi, M. Saruwatari, and T. Morioka, "Flatly broadened supercontinuum spectrum generated in a dispersion decreasing fibre with convex dispersion profile," *Electron. Lett.* **33**, 1806 (1997).

[96] J. M. Dudley, G. Genty and S. Coen, "Supercontinuum generation in photonic crystal fiber," *Rev. Mod. Phys.* **78**, 1135 (2006).

[97] G. Humbert, W. J. Wadsworth, S. G. Leon-Saval, J. C. Knight, T. A. Birks, P. St. J. Russell, M. J. Lederer, D. Kopf, "Supercontinuum generation system for optical coherence tomography based on tapered photonic crystal fibre," *Opt. Express* **14**, 1596 (2006).

[98] F. G. Omenetto and N. A. Wolchover, M. R. Wehner, M. Ross, A. Efimov, and A. J. Taylor, V. V. R. K. Kumar, A. K. George, and J. C. Knight, N. Y. Joly, and P. St. J. Russell, "Spectrally smooth supercontinuum from 350 nm to 3 μm in sub-centimeter lengths of soft-glass photonic crystal fibers," *Opt. Express* **14**, 4928 (2006).

[99] Y. Kodama and A. Hasegawa, "Nonlinear Pulse Propagation in a Monomode Dielectric Guide," *IEEE J. Quantum Electron.* **23**, 510 (1987).

[100] N. Akhmediev and M. Karlsson, "Cherenkov radiation emitted by solitons in optical fibers," *Phys. Rev. A* **51**, 2602 (1995).

[101] I. Cristiani, R. Tediosi, L. Tartara and V. Degiorgio, "Dispersive wave generation by solitons in microstructured optical fibers," *Opt. Express* **12**, 124 (2004).

[102] D. R. Austin, C. M. de Sterke, B. J. Eggleton, T. G. Brown, "Dispersive wave blue-shift in supercontinuum generation," *Opt. Express* **14**, 11997 (2006).

[103] F. Luan, *Linear and nonlinear properties of photonic band-gap fibres*, Ph.D. thesis (University of Bath, 2005).

[104] D. V. Skryabin, F. Luan, J. C. Knight, P. St. J. Russell, "Soliton Self-frequency Shift Cancellation in Photonic Crystal Fibers," *Science* **301**, 1705 (2003).

[105] N. Nishizawa and T. Goto, "Pulse trapping by ultrashort soliton pulses in optical fibers across zero-dispersion wavelength," *Opt. Lett.* **27**, 152 (2002).

[106] N. Nishizawa and T. Goto, "Characteristics of pulse trapping by use of ultrashort soliton pulses in optical fibers across the zero-dispersion wavelength," *Opt. Express* **10**, 1151 (2002).

[107] A. V. Gorbach and D. V. Skryabin, "Light trapping in gravity-like potentials and expansion of supercontinuum spectra in photonic-crystal fibres," *Nature Photonics* **1**, 653 (2007).

[108] A. V. Yulin, D. V. Skryabin, and P. St. J. Russell, "Four-wave mixing of linear waves and solitons in fibers with higher-order dispersion," *Opt. Lett.* **29**, 2411 (2004).

[109] D. V. Skryabin and A. V. Yulin, "Theory of generation of new frequencies by mixing of solitons and dispersive waves in optical fibers," *Phys. Rev. E* **72**, 016619 (2005).

[110] A. Efimov, A.V. Yulin, D.V. Skryabin, J. C. Knight, N. Joly, F. G. Omenetto, A. J. Taylor, and P. Russell, "Interaction of an Optical Soliton with a DispersiveWave," *Phys. Rev. Lett.* **95**, 213902 (2005).

[111] A. V. Gorbach, D. V. Skryabin, J. M. Stone, J. C. Knight, "Four-wave mixing of solitons with radiation and quasi-nondispersive wave packets at the short-wavelength edge of a supercontinuum," *Opt. Express* **14**, 9854 (2006).

[112] B. A. Cumberland, J. C. Travers, S. V. Popov, and J. R. Taylor, "29 W High power CW supercontinuum source," *Opt. Express* **16**, 5954 (2008).

[113] P. A. Champert, V. Couderc, P. Leproux, S. Février, V. Tombelaine, L. Labonté, P. Roy, C. Froehly, and P. Nérin, "White-light supercontinuum generation in normally dispersive optical fiber using original multiwavelength pumping system," *Opt. Express* **12**, 4366 (2004).

[114] E. Räikkönen, G. Genty, O. Kimmelma, and M. Kaivola, "Supercontinuum generation by nanosecond dual-wavelength pumping in microstructured optical fibers," *Opt. Express* **14**, 7914 (2006).

[115] J. M. Stone and J. C. Knight, "Visibly "white" light generation in uniform photonic crystal fiber using a microchip laser," *Opt. Express* **16**, 2670 (2008).

[116] S. G. Leon-Saval, T.A. Birks, W.J. Wadsworth, P.St.J. Russell and M.W. Mason, "Supercontinuum generation in submicron fibre waveguides," *Opt. Express* **12**, 2864 (2004).

[117] C.M.B. Cordeiro, W.J. Wadsworth, T.A. Birks and P.St.J. Russell, "Engineering the dispersion of tapered fibers for supercontinuum generation with a 1064 nm pump laser," *Opt. Lett.* **30**, 1980 (2005).

[118] J. C. Travers, S. V. Popov and J. R. Taylor, "Extended blue supercontinuum generation in cascaded holey fibers," *Opt. Lett.* **30**, 3132 (2005).

[119] A. Kudlinski, A. K. George and J. C. Knight, J. C. Travers, A. B. Rulkov, S. V. Popov, and J. R. Taylor, "Zero-dispersion wavelength decreasing photonic crystal fibers for ultraviolet-extended supercontinuum generation," *Opt. Express* **14**, 5715 (2006).

[120] Z. Zhu and T. Brown, "Polarization properties of supercontinuum spectra generated in birefringent photonic crystal fibres," *J. Opt. Soc. Am. B* **21**, 249 (2004).

[121] Z. Zhu and T. Brown, "Experimental studies of polarization properties of supercontinua generated in a birefringent photonic crystal fibre," *Opt. Express* **12**, 791 (2004).

[122] K. Suzuki, H. Kubota, S. Kawanishi, M. Tanaka and M. Fujita, "Optical properties of a low-loss polarization-maintaining photonic crystal fibre," *Opt. Express* **9**, 676 (2001).

[123] G. J. Pearce, *Plane-wave methods for modelling photonic crystal fibre*, Ph.D. thesis (University of Bath, 2006).

[124] A. V. Smith, D. J. Armstrong, and W. J. Alford, "Increased acceptance bandwidths in optical frequency conversion by use of multiple walk-off-compensating nonlinear crystals," *J. Opt. Soc. Am. B* **15**, 122 (1998).

[125] M. Tateda, N. Shibata and S. Seikai, "Interferometric method for chromatic dispersion measurement in a single-mode optical fiber," *IEEE J. Quantum Electron.* **17**, 404 (1981).

[126] L. Novotny, D. W. Pohl and B. Hecht, "Scanning near-field optical probe with ultrasmall spot size," *Opt. Lett.* **20**, 970 (1995).

[127] H. Hellwig, J. Liebertz, and L. Bohaty, "Exceptional large nonlinear optical coefficients in the monoclinic bismuth borate BiB_3O_6 (BIBO)," *Solid State Commun.* **109**, 249 (1999).

[128] H. Hellwig, J. Liebertz, and L. Bohaty, "Linear optical properties of the monoclinic bismuth borate BiB_3O_6," *J. Appl. Phys.* **88**, 240 (2000).

[129] C. Du, Z. Wang, J. Liu, X. Xu, B. Teng, K. Fu, J. Wang, Y. Liu, and Z. Shao, "Efficient intracavity second-harmonic generation at 1.06 μm in a BiB_3O_6 (BIBO) crystal," *Appl. Phys. B* **73**, 215 (2001).

[130] Z. Wang, B. Teng, K. Fu, X. Xu, R. Song, C. Du, H. Jiang, J. Wang, and Z. Shao, "Efficient second-harmonic generation of pulsed laser radiation in BiB_3O_6 (BIBO) crystal with different phase matching directions," *Opt. Commun.* **202**, 217 (2002).

[131] C. Du, B. Teng, Z. Wang, J. Liu, X. Xu, G. Xu, K. Fu, J. Wang, Y. Liu, and Z. Shao, "Actively Q-switched intracavity second-harmonic generation of 1.06 μm in BiB_3O_6 crystal," *Opt. Laser Technol.* **34**, 343 (2002).

[132] C. Czeranowsky, E. Heumann, and G. Huber, "All-solid-state continuous-wave frequency-doubled Nd:YAG BiBO laser with 2.8-W output power at 473 nm," *Opt. Lett.* **28**, 432 (2003).

[133] M. Ghotbi and M. Ebrahim-Zadeh, A. Majchrowski and E. Michalski, and I. V. Kityk, "High-average-power femtosecond pulse generation in the blue using BiB_3O_6," *Opt. Lett.* **29**, 2530 (2004).

[134] M. Ghotbi and M. Ebrahim-Zadeh, "Optical second harmonic generation properties of BiB_3O_6," *Opt. Express* **12**, 6002 (2004).

[135] M. Ghotbi and M. Ebrahim-Zadeh, "990 mW average power, 52% efficient, high-repetition-rate picosecond-pulse generation in the blue with BiB_3O_6," *Opt. Lett.* **30**, 3395 (2005).

[136] C. Du, S. Ruan, and Y. Yu, "High-power intracavity second-harmonic generation of 1.34 μm in BiB_3O_6 crystal," *Opt. Express* **13**, 8591 (2005).

[137] M. Thorhauge, J. L. Mortensen, P. Tidemand-Lichtenberg and P. Buchhave, "Tuneable intra-cavity SHG of CW Ti:Sapphire lasers around 785 nm and 810 nm in BiBO-crystals," *Opt. Express* **14**, 2283 (2006).

[138] M. Ghotbi, A. Esteban-Martin, and M. Ebrahim-Zadeh, "BiB_3O_6 femtosecond optical parametric oscillator," *Opt. Lett.* **31**, 3128 (2006).

[139] Z. Sun, M. Ghotbi, and M. Ebrahim-Zadeh, "Widely tuneable picosecond optical parametric generation and amplification in BiB_3O_6," *Opt. Express* **15**, 4139 (2007).

[140] R. J. Gehr, M. W. Kimmel, and A. V. Smith, "Simultaneous spatial and temporal walk-off compensation in frequency-doubling femtosecond pulses in $\beta - BaB_2O_4$," *Opt. Lett.* **23**, 1298 (1998).

[141] A. K. Akert, "Quantum Cryptography Based on Bell's Therorem," *Phys. Rev. Lett.* **67**, 661 (1991).

[142] D. Bouwmeester, J. -W. Pan, M. Daniell, H. Weinfurter, and A. Zeilinger, "Experimental Quantum Teleportation," *Nature* **390**, 575 (1997).

[143] E. Knill, R. Laflamme, G. J. Milburn, "A scheme for efficient quantum computation with linear optics," *Nature* **409**, 46 (2001).

[144] J. L. O'Brien, "Optical Quantum Computing," *Science* **318**, 1567 (2007).

[145] N. Gisin, G. Ribordy, W. Tittel, and H. Zbinden, "Quantum cryptography," *Rev. Mod. Phys.* **74**, 145 (2002).

[146] C. H. Bennett, F. Bessette, G. Brassard, L. Salvail, and J. Smolin, 1992, "Experimental quantum cryptography," *J. Cryptology* **5**, 3 (1992).

[147] C. K. Hong, and L. Mandel, "Experimental realization of a localized one-photon state," *Phys. Rev. Lett.* **56**, 58 (1986).

[148] C. K. Hong, Z. Y. Ou and L. Mandel, "Measurement of subpicosencond time intervals between two photons by interference," *Phys. Rev. Lett.* **59**, 2044 (1987).

[149] J. G. Rarity and P. R. Tapster, "Experimental Violation of Bell's Inequality Based on Phase and Momentum," *Phys. Rev. Lett.* **64**, 2495 (1990).

[150] A. K. Ekert, J. G. Rarity, P. R. Tapster and G. M. Palma, "Practical Quantum Cryptography Based on Two-Photon Interferometry," *Phys. Rev. Lett.* **69**, 1293 (1992).

[151] P. G. Kwiat, K. Mattle, H. Weinfurter and A. Zeilinger, "New High-Intensity Source of Polarization-Entangled Photon Pairs," *Phys. Rev. Lett.* **75**, 4337 (1995).

[152] C. Kurtsiefer, M. Oberparleiter, and H. Weinfurter, "High Efficiency entangled pair collection in type II parametric fluorescence," *Phys. Rev. Lett.* **85**, 290 (2000).

[153] G. Bonfrate, V. Pruneiri, P. Kazanski, P. R. Tapster and J. G.Rarity, "Parametric fluorescence in periodically poled silica fibres," *Appl. Phys. Lett.* **75**, 2356 (1999).

[154] S. Tanzilli, H. de Riedmatten, W. Tittel, H. Zbinden, P. Baldi, M. de Micheli, D. B. Ostrowski, N. Gisin, "Highly efficient photon-pair source using periodically poled lithium niobate waveguide," *Electron. Lett.* **37**, 26 (2001).

[155] S. Fasel, O. Alibart, S. Tanzilli, P. Baldi, A. Beveratos, N. Gisin and H. Zbinden, "High-quality asynchronous heralded single-photon source at telecom wavelength," *New J. Phys.* **6**, 163 (2004).

[156] O. Alibart, D. B. Ostrowsky, P. Baldi, and S. Tanzilli, "High-performance guided-wave asynchronous heralded single-photon source," *Opt. Lett.* **30**, 1539 (2005).

[157] D. Ljunggren and M. Tengner, "Optimal focusing for maximal collection of entangled narrow-band photon pairs into single-mode fibers," *Phys. Rev. A* **72**, 062301 (2005).

[158] J. E. Sharping, M. Fiorentino, and P. Kumar, "Observation of twin-beam-type quantum correlation in optical fiber," *Opt. Lett.* **26**, 367 (2000).

[159] M. Fiorentino, P. L. Voss, J. E. Sharping, P. Kumar, "All-fibre photon pair source for quantum communications," *IEEE Photon. Tech. Lett.* **14**, 983 (2002).

[160] J. E. Sharping, J. Chen, X. Li, P. Kumar, "Quantum Correlated twin photons from microstructured fibre," *Opt. Express* **12**, 3086 (2004).

[161] X. Li, J. Chen, P. Voss, J. E. Sharping, and P. Kumar, "All-fiber photon-pair source for quantum communications: Improved generation of correlated photons," *Opt. Express* **12**, 3737 (2004).

[162] X. Li, P. L. Voss, J. E. Sharping, and P. Kumar, "Optical-Fiber Source of Polarization-Entangled Photons in the 1550 nm Telecom Band," *Phys. Rev. Lett.* **94**, 053601 (2005).

[163] J. G. Rarity, J. Fulconis, J. Duligall, W. J. Wadsworth and P. St. J. Russell, "Photonic Crystal fiber source of correlated photon pairs," *Opt. Express* **13**, 534 (2005).

[164] J. Fulconis, O. Alibart, W. J. Wadsworth, P. St. J. Russell and J. G. Rarity, "High brightness single mode source of correlated photon pairs using a photonic crystal fiber," *Opt. Express* **13**, 7572 (2005).

[165] O. Alibart, J. Fulconis, S. G. Murdoch, G. K. L. Wong, W. J. Wadsworth and J. G. Rarity, "Photon pair generation using four-wave mixing in a microstructured fibre: theory versus experiment," *New J. Phys.* **8**, 67 (2006).

[166] J. Fulconis, O. Alibart, J. L. O'Brien, W. J. Wadsworth, and J. G. Rarity, "Nonclassical Interference and Entanglement Generation Using a Photonic Crystal Fiber Pair Photon Source," *Phys. Rev. Lett.* **99**, 120501 (2007).

[167] J. Fulconis, O. Alibart, W. J. Wadsworth and J. G. Rarity, "Quantum interference with photon pairs using two micro-structured fibres," *New J. Phys.* **9**, 276 (2007).

[168] Q. Lin, F. Yaman, and G. P. Agrawal, "Photon-pair generation by four-wave mixing in optical fibers," *Opt. Lett.* **31**, 1286 (2006).

[169] K. Garay-Palmett, H. J. McGuinness, O. Cohen, J. S. Lundeen, R. Rangel-Rojo, A. B. U'Ren, M. G. Raymer, C. J. McKinstrie, S. Radic, and I. A. Walmsley, "Photon pair-state preparation with tailored spectral properties by spontaneous four-wave mixing in photonic-crystal fiber," *Opt. Express* **15**, 14870 (2007).

[170] A. Witkowska, K. Lai, S. G. Leon-Saval, W. J. Wadsworth, and T. A. Birks, "All-fiber anamorphic core-shape transitions," *Opt. Lett.* **31**, 2672 (2006).

Appendix I: Fibre Table

There are lots of PCFs used in my experiments and they are labelled in an arbitrary way in this thesis. These PCFs actually have different labels on the shelves in our lab. To avoid confusion, I put the fibre labels in this thesis and their corresponding labels in stock of our lab here. For any further inquiry, please contact my supervisor Dr. William Wadsworth.

Label in thesis	PCF-A	PCF-B	PCF-C	PCF-D	PCF-E
Label in stock	240507F	240507B	310703F	Blaze	050803C
Label in thesis	PCF-F	PCF-G	PCF-H	PCF-J	PCF-K
Label in stock	050803A	310703B	290108C	310703E	141106A
Label in thesis	PCF-L	PCF-M	PCF-N	PCF-O	
Label in stock	310703E'	290108A	290108E	290108F	

Appendix II: Publication List

Journal Papers

[1] **C. Xiong** and W.J. Wadsworth, "Polarized supercontinuum in birefringent photonic crystal fibre pumped at 1064 nm and application to tuneable visible/UV generation," *Opt. Express* **16**, 2438 (2008).

[2] K. Cook, **C. Xiong** and W.J. Wadsworth, "Enhanced four-wave mixing and parametric oscillation in photonic crystal fibre," *J. Opt. A: Pure Appl. Opt.* **9**, 1095 (2007).

[3] **C. Xiong**, A. Witkowska, S.G. Leon-Saval, T.A. Birks and W.J. Wadsworth, "Enhanced visible continuum generation from a microchip 1064nm laser," *Opt. Express* **14**, 6188 (2006).

Conference Presentations

[1] J. Fulconis, A. Clark, M. Halder, J. L. O'Brien, J.G. Rarity; **C. Xiong**, W. J. Wadsworth, "Quantum information processing with optical fibres," *3rd International Conference on Quantum Information (ICQI) Topical Meeting 2008 (Boston, Massachusetts, USA)*, paper **QWB5**.

[2] **C. Xiong**, A.R. McMillan, O. Alibart, J. Fulconis, J.G. Rarity and W.J. Wadsworth, "All-Fibre Source of Heralded Single Photons at 1550nm," *CLEOS/QELS and Photonic Applications Systems Technologies 2008 Technical Digest (Optical Society of America, Washington, DC, 2008)*, paper **QFI2**.

[3] **C. Xiong** and W.J. Wadsworth, "Polarized Supercontinuum from a 1064 nm Microchip Laser and Application to Tunable Visible/UV Generation in BIBO," *CLEOS/QELS and Photonic Applications Systems Technologies 2008 Technical Digest (Optical Society of America, Washington, DC, 2008)*, paper **CFC7**.

[4] **C. Xiong** and W.J. Wadsworth, "Polarized Supercontinuum Generation in a Birefringent Photonic Crystal Fibre pumped by a 1064 nm Microchip Laser," *the 20th Annual Lasers and Electro Optics Society (LEOS) Meeting 2007*, paper **ThQ2**.

[5] K. Cook, **C. Xiong** and W.J. Wadsworth, "Enhanced Four-Wave Mixing in Photonic Crystal Fibre: Towards an All-Fibre Based OPO," *the 20th Annual Lasers and Electro Optics Society (LEOS) Meeting 2007*, paper **ThQ3**.

[6] **C. Xiong**, S. G. Leon-Saval, F. Couny and W. J. Wadsworth, "Residual Pump Peak Removal for Ultra-Flattened Supercontinuum Generation by Photonic Crystal Fibres," *CLEO/QELS and Photonic Applications Systems Technologies 2006 Technical Digest (Optical Society of America, Washington, DC, 2006)*, paper **CWO4**.

[7] **C. Xiong**, A. Witkowska, T.A. Birks and W.J. Wadsworth, "Visible Continuum Generation from a Microchip 1062 nm Laser Source," *CLEOS/QELS and Photonic Applications Systems Technologies 2006 Technical Digest (Optical Society of America, Washington, DC, 2006)*, paper **CTuA6**.

Appendix III: Copy of Published Journal Papers

Following below is a copy of the work published during my Ph.D. study in peer reviewed journals. The reproduction of these documents has been allowed under the copyright agreements made with the Optical Society of America (OSA) and Institute of Physics (IOP).

Enhanced visible continuum generation from a microchip 1064nm laser

C. Xiong, A. Witkowska, S. G. Leon-Saval, T. A. Birks and W. J. Wadsworth

Centre for Photonics and Photonic Materials, Department of Physics, University of Bath, Bath, BA2 7AY, UK
w.j.wadsworth@bath.ac.uk

Abstract: We demonstrate a cascaded nonlinear process using pump conversion to 742 nm by four-wave mixing in the normal dispersion regime then continuum generation by modulation instability to generate bright single-mode visible continuum with an average power up to -20 dBm/nm, from a compact 1064 nm infrared source in a monolithic single-mode photonic crystal fibre with a tapered section in one end.

OCIS codes: (190.4370) Nonlinear optics, fibres; (060.2380) Fibre Optic Sources and Detectors.

References and links

1. J. K. Ranka, R. S. Windeler and A. J. Stentz: "Visible continuum generation in air–silica microstructure optical fibers with anomalous dispersion at 800 nm," Opt. Lett. **25**, 25-27 (2000).
2. T. A. Birks, W. J. Wadsworth, and P. St. J. Russell, "Supercontinuum generation in tapered fibers," Opt. Lett. **25**, 1415-1417 (2000).
3. S. Coen, A. H. L. Chau, R. Leonhardt, J. D. Harvey, J. C. Knight, W. J. Wadsworth, and P. St. J. Russell, "Supercontinuum generation by stimulated Raman scattering and parametric four-wave mixing in a photonic crystal fiber," J. Opt. Soc. Am. B **19**, 753-764 (2002).
4. W. J. Wadsworth, N. Joly, J. C. Knight, T. A. Birks, F. Biancalana, P. St. J. Russell, "Supercontinuum and four-wave mixing with Q-switched pulses in endlessly single-mode photonic crystal fibres," Opt. Express **12**, 299-309 (2004).
5. S. G. Leon-Saval, T. A. Birks, W. J. Wadsworth, P. St. J. Russell and M. W. Mason, "Supercontinuum generation in submicron fibre waveguides," Opt. Express **12**, 2864 -2869 (2004).
6. P. A. Champert, V. Couderc, P. Leproux, S. Février, V. Tombelaine, L. Labonté, P. Roy, C. Froehly, and P. Nérin, "White-light supercontinuum generation in normally dispersive optical fiber using original multi-wavelength pumping system," Opt. Express **12**, 4366-4371 (2004).
7. C. M. B. Cordeiro, W. J. Wadsworth, T. A. Birks and P. St. J. Russell, "Engineering the dispersion of tapered fibres for supercontinuum generation with a 1064 nm pump laser," Opt. Lett. **30**, 1980-1982 (2005).
8. J. C. Travers, S. V. Popov and J. R. Taylor, "Extended blue supercontinuum generation in cascaded holey fibers", Opt. Lett. **30**, 3132-3134 (2005).
9. W. J. Wadsworth, A. Witkowska, S. G. Leon-Saval and T. A. Birks, "Hole inflation and tapering of stock photonic crystal fibres," Opt. Express **13**, 6541-6549, (2005).

1. Introduction

Spatially and spectrally bright visible light generation has attracted much attention because of the potential applications in many visible-based microscopy and spectroscopy systems. Supercontinuum (SC) generation in optical fibres is a useful technique for generating broad-band single-mode light, however it is difficult to achieve short wavelengths unless the zero-dispersion-wavelength (ZDW) of fibres is shifted to visible region and a suitable pump source is found to meet the requirements of phase matching. In photonic crystal fibre (PCF) one can design a fibre with a ZDW at wavelengths from 500 nm upwards by adjusting the geometrical parameters (hole to hole pitch, Λ, and hole diameter to pitch ratio, d/Λ). Early experiments to generate visible continuum in optical fibres used femtosecond Ti:sapphire lasers ($\lambda \sim 800$ nm) and small-core PCF [1] or tapered fibres [2] or used picosecond Kr^+ ($\lambda = 647$ nm) lasers [3]. SC spectra extended from 400 nm across the visible and into the infrared. Femtosecond and picosecond lasers are however relatively complex, and we demonstrated a more compact continuum source using a microchip passively Q-switched Nd:YAG laser at 1064 nm and a PCF [4]. With a single nonlinear fibre the shortest wavelengths in a continuum are rarely

#70590 - $15.00 USD Received 3 May 2006; revised 9 June 2006; accepted 9 June 2006

shorter than half the input pump wavelength. Technologically simple systems employing various Nd^{3+} lasers are therefore confined to continuum spectra at >500 nm. This is not sufficiently short in wavelength for many visible-based microscopy and spectroscopy systems. Frequency doubled Nd^{3+} lasers offer intense pump light in the centre of the visible, and would seem ideal candidates for visible SC generation. Unfortunately the fibre core diameter required to give ZDW close to 532 nm is < 1 μm, and whilst we have demonstrated visible SC from a Q-switched 532 nm source in PCFs and tapered fibres with 0.5-0.9 μm core diameter [5], the structures are readily damaged by high energy ns pulses. An alternative approach has been to use both 1064 and 532 nm pump pulses combined, to yield continuum from a 2 μm core PCF [6]. Most recently a white-light continuum which extends to blue pumped by a single 1064 nm source, has been achieved first in multiple tapers(ns, Q-switched 1064 nm laser [7]), and also in multiple PCFs(ps, modelocked 1060 nm laser [8]), with sequentially decreasing ZDW. In both cases the first stage is conversion of the infrared pump light to a continuum spanning both sides of the pump wavelength and extending down to the region 700-800 nm. This light is then sent to a second stage PCF or taper, where the ZDW is around 700 or 800 nm and so the light at 700-800 nm present in the continuum is used as a pump to generate a visible continuum.

Here we also demonstrate bright single-mode visible continuum generation pumped by a simple compact 1064 nm Nd:YAG microchip laser in a two step process, but with a fundamental difference. The first step of the process is not *continuum generation* in a fibre with ZDW < 1064 nm [4,7,8], but rather *four-wave mixing* in a PCF with ZDW > 1064 nm. We have previously shown that such fibres can be designed to generate narrow-band radiation at wavelengths widely separated from the pump wavelength with high efficiency [4]. The narrow band pulses generated in this way are shown to be efficient for subsequent visible continuum generation. To maximize the power close to visible region in stage one the signal wavelength should be as short as possible, whilst maintaining efficient conversion from 1064 nm pump source. For the experiments described in this paper we have chosen for the first fibre a PCF properly designed to yield intense 742 nm pulses which are then fed into a second PCF with ZDW~700 nm which generates supercontinuum from this output. As with the technique of [8], two PCFs with very different core sizes are required to extend the continua to short wavelengths, and splicing is not a straightforward low-loss option for coupling. We have recently developed post-fabrication processing techniques [9] which enable the whole two-stage optical process to be carried out in a single monolithic fibre device. This has the additional advantage that the final output is not directly from the second, small core, fibre but is coupled back into an output pigtail of the first, 5 μm core diameter, endlessly single mode fibre which may be easily coupled into an application system. Our two-stage process is schematically shown in Fig. 1. The absence of a splice in this system ensures low coupling losses (<0.12 dB) and so maintains a high output brightness.

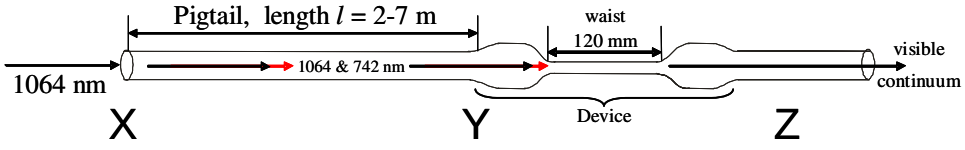

Fig. 1. Schematic for the two-stage visible generation process. 1064 nm laser light enters at X and is converted in the pigtail into 742 nm by four-wave mixing. The 742 nm light at Y is then the pump for continuum generation in the inflated and tapered section. The output continuum is measured in the output fibre at Z. Both input and output sections are endlessly single-mode fibre with a relatively large (5 μm diameter) core.

2. Experiment

In the experiment, the pump laser is a Nd:YAG Q-switched microchip laser running at wavelength λ = 1064 nm and emitting 0.6 ns (FWHM) pulses with 15 kW peak power at a 7.2 kHz repetition rate (*Teem Photonics*, NP-10820). After passing through a variable

#70590 - $15.00 USD Received 3 May 2006; revised 9 June 2006; accepted 9 June 2006

attenuator, which is made from a rotating half-wave plate followed by a polarizing beam splitter, these pulses are focused into a several meter long PCF structure as depicted in Fig. 1 and Fig. 2. A ×30 anti-reflection coated aspheric singlet lens is used to optimize the coupling. Up to 40 mW of power could be coupled into the fibre. The beam exiting in the device is then sent to an optical spectrum analyzer (OSA) or a power meter.

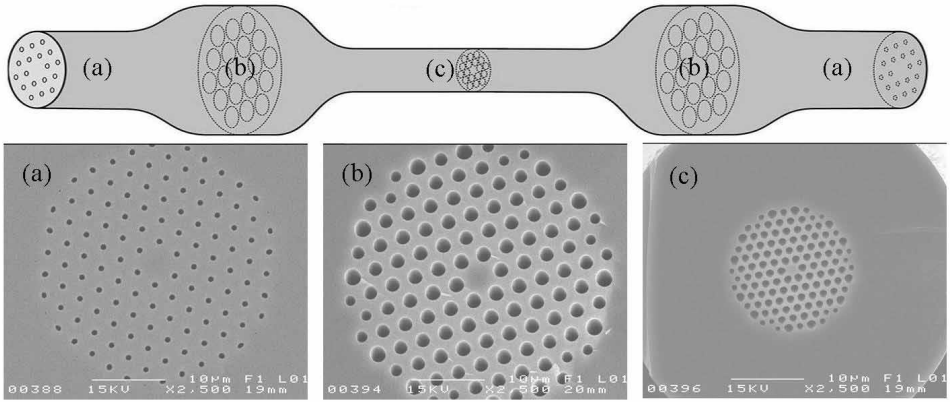

Fig. 2. Schematic of the inflated and tapered section (top) and scanning electron micrographs (SEMs) for device-A (bottom): (a) initial PCF-A before processing, (b) inflated fibre, (c) taper waist. All of the SEM images are to the same scale.

The fibre used in our experiment is an endlessly single mode PCF, PCF-A, with a core diameter close to 5 μm and small holes [Fig. 2(a)]. This has a ZDW at about 1103 nm and gives strong FWM gain at 742 nm by the processes described in [4], allowing >35 % conversion of the 1064 nm pump light over a 3 m long fibre (Fig. 4(a)-blue trace). The idler wavelength, calculated to be at 1880 nm, is out of the measurement range of the spectrometer and so could not be observed. This fibre with signal wavelength at 742 nm was chosen for the signal wavelength being close to visible region whilst maintaining high conversion efficiency from pump.

In previous studies it has been well established that small-core PCF is ideal for SC generation from pulsed sources at wavelengths from 600 to 800 nm [1,2,3,9]. To take advantage of SC generation in PCF pumped by our wavelength converted output from PCF-A at 742 nm, we need to couple light from PCF-A into a structure with a small core and high air-filling fraction to achieve a ZDW at ~700 nm. We fabricated a device with very similar properties to a standard small-core PCF in the end section of PCF-A with very low loss in a tapering process recently developed by us [9]. At first pressure is applied to the air holes in a length of PCF-A with dry nitrogen at 7-10 bar. The fibre is then heated and stretched in a flame. The pressure makes the holes expand [Fig. 2(b)], whilst the stretching reduces the transverse dimensions of the fibre. The result, shown in Fig. 2(c), is that the core diameter is reduced from 5 μm to 1.7 μm, whilst the air-filling fraction is increased. Thus the fibre in the waist region of the inflated section is equivalent to a bulk small-core PCF, with a ZDW at around 700 nm. All transitions are made gradual so that the insertion loss of the entire device is just 0.12 dB at 1550 nm. The waist length is 120 mm (Fig. 1).

With the variable attenuator technique, we can study the continuum development as the launched power is increased. We measured the evolution of the spectra with respect to output power and input pigtail length (l, Fig. 1) by cutting back the fibre at the input end. The spectra for the device with $l = 7$, 5, 3 and 2 m are illustrated in Fig. 3, where the x-axis is the output average power, the y-axis is wavelength and the colour indicates the power level for each wavelength component in the continuum spectra. In order to compare the different pigtail lengths on an equal footing, we need to present the results for each length for the same coupled input power. To achieve this, in these experiments we used the same technique to couple the pump laser into the input pigtail for each device and adjusted the alignment for

#70590 - $15.00 USD Received 3 May 2006; revised 9 June 2006; accepted 9 June 2006

maximum output power, thus the highest output power attained with each different input pigtail length will correspond to the same maximum coupled pump power. So by setting the minimum of the x-axis to zero and the maximum to the measured maximum output power in each case we should be able to ensure that the scale of all graphs is the same in terms of coupled input power. From the spectra, we can see that 3 m long pigtail is the optimum one for maximum visible continuum intensity, although the difference between 5 m, 3 m and 2 m is not great. The presence of an optimum pigtail length can be understood from the fact that the longer the pigtail is, the higher conversion efficiency from 1064 nm pump source to 742 nm but also the stronger Raman effect decreasing the peak power of 742 nm.

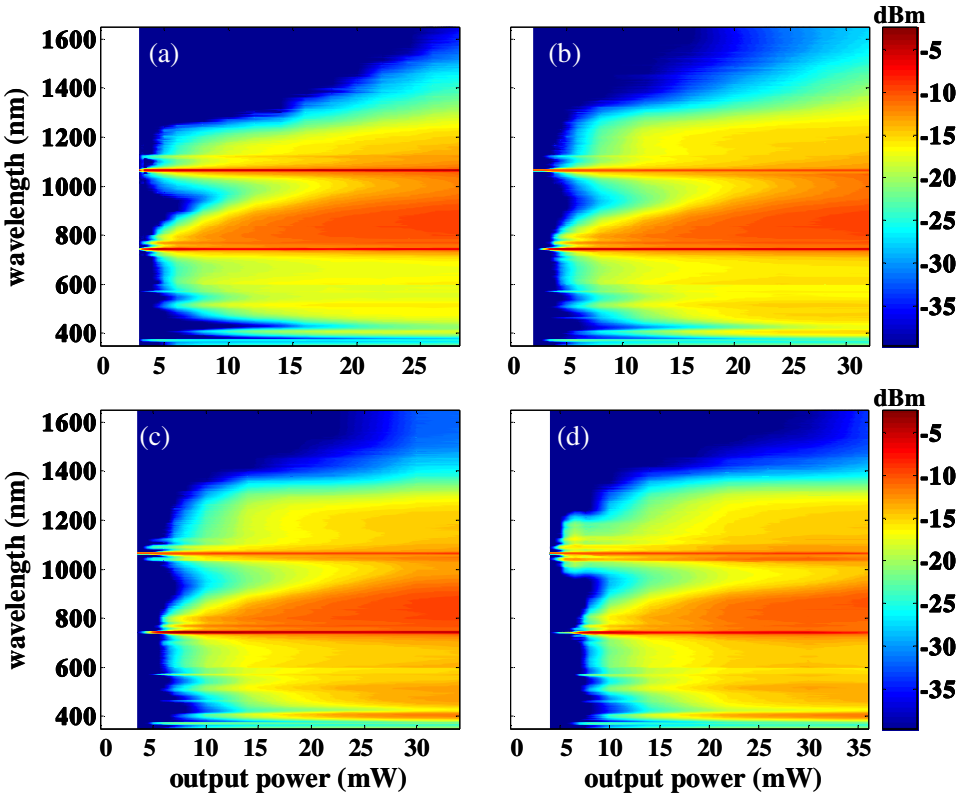

Fig. 3. Output power spectra (point Z of Fig. 1) for (a) 7 m, (b) 5 m, (c) 3 m, (d) 2 m PCF-A + inflated and tapered section (device-A). False-colour intensity scales in dBm/5nm are the same for all plots.

The spectrum from the optimum pigtail length of 3 m is given in Fig. 4 (blue traces). The spectrum after 3 m of un-modified fibre is shown in Fig. 4(a), which demonstrates the spectrum incident on the inflated and tapered section at point Y in Fig. 1. The final output spectrum with 30 mW of average output power at point Z of Fig. 1 is shown in Fig. 4(b). It is obvious that SC generation taking place in the device fills almost the whole visible region and the gap between 742 nm and 1064 nm as well. In principle, this process is very similar to that reported in Ref. [4]. The difference is the shorter pump wavelength, shorter fibre ZDW, lower pump power and shorter length of fibre. It is the high nonlinearity resulting from the much smaller core size that overcomes the lower pump power and shorter fibre length and delivers good performance in visible SC generation. Raman Scattering will also act on 742 nm and 1064 nm pump wavelengths in the inflated and tapered section, which makes additional contribution to the gap filling between the two peaks and the long wavelength extension to 1350 nm.

#70590 - $15.00 USD Received 3 May 2006; revised 9 June 2006; accepted 9 June 2006

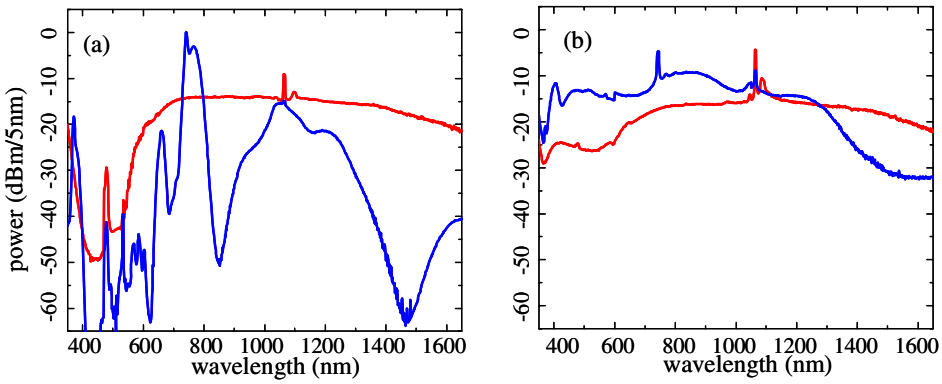

Fig. 4. Spectra from (a) 3 m bare PCF-A (blue) and B (red), equivalent to point Y on Fig. 1, with average output power 37 mW, (b) device-A(blue) and device-B(red), point Z on Fig. 1, with average output power 30 mW. Note that peaks in the region 350-550 nm in (a) are artefacts of the spectrometer used.

In comparison with Ref. [8], our device yields an intense peak at 742 nm instead of a continuum in the first stage, which means much more pump power could be provided to the second stage to enhance the visible continuum generation. With a single FWM process, the maximum conversion to the signal wavelength is governed by the partition of the energy of two pump photons at 1064 nm into a signal photon at 742 nm and an idler photon at 1880 nm. This gives a limit on the efficiency of conversion to 742 nm of 72 % (we achieve 35 % conversion in practice, half of this quantum limit). When the first stage is continuum generation, the pump light is spread out over a broad spectral range. Neglecting Raman contributions, half of the total energy will be at wavelengths shorter than the initial pump. Even if we assume that the energy of this short-wavelength portion is evenly distributed between 700 nm and 1064 nm, only about 30 % will lie in the useful range, 700-800 nm, for the second stage of continuum generation. This is just 15 % of the total pump power.

To illustrate the difference between a continuum and a FWM peak in the first stage, we made a very similar device to device-A with 3 m length of pigtail in another PCF, (PCF-B, hole-to-hole pitch and core diameter similar to PCF-A, but with slightly larger holes, ZDW at 1040 nm) and an identical inflated section, forming device-B. A 3 m length of PCF-B can generate a continuum spanning from 600 to beyond 1700 nm when pumped by the 1064 nm microchip laser. After interacting with the inflated section, the continuum extends to the visible region, but the power level is much lower than that of the device in PCF-A (device-A) because of lower pump power at 700-800 nm. The spectra for 3 m length of bare PCF-B and PCF-B + inflated section (device-B) are plotted in Fig. 4(red traces), which have the same average power level as PCF-A and device-A (Fig. 4, blue traces). From the spectra, we can see that device-B converted more power to long wavelengths (1300-1600 nm) than device-A, and device-A gives much more brightness in the visible. In order to see the continuum evolution clearly, we also plot the output power spectrum of device-B and put it together with that of device-A in Fig. 5. Not only does Fig. 5(b) indicate much lower power level in the visible range and higher power level in the infrared region, but also it shows the rapid extension of the spectrum of device-B into the visible as soon as the continuum extends to wavelengths close to the ZDW of the inflated section. The contrast with Fig. 5(a) is striking, with the direct FWM from 1064 nm to 742 nm occurring efficiently at low power and providing high pump intensity for the visible SC generation. It should be noted that the performance of devices with SC first then ZDW~700 nm (like device-B) can be improved by increasing the pump power, or the length of the second stage as in Ref. [8] where meter-length fibres are used. The efficiency of our technique is shown by the excellent performance of device-A, with a short length and at low power.

#70590 - $15.00 USD Received 3 May 2006; revised 9 June 2006; accepted 9 June 2006

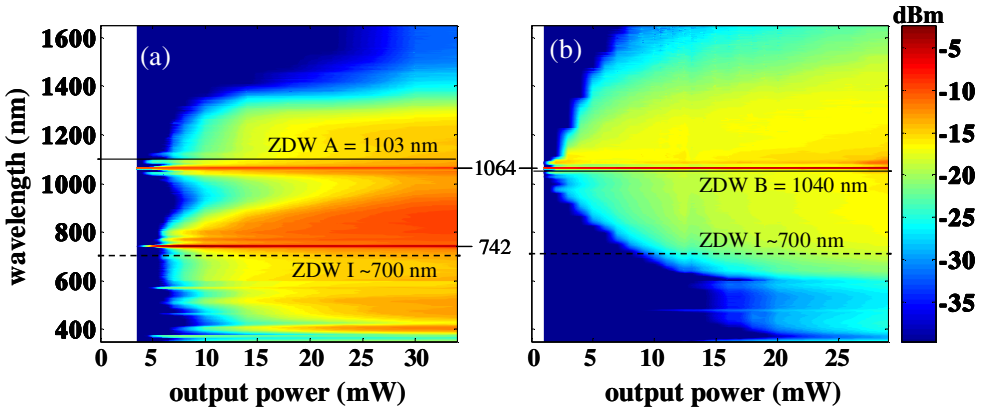

Fig. 5. Output power spectra for $l = 3$ m for (a) device-A, (b) device-B. False-colour intensity scales in dBm/5nm are the same for both plots. Black solid lines are the ZDW of initial fibres (ZDW A, ZDW B) and black dashed lines are the ZDW of inflated sections (ZDW I).

3. Conclusion

In conclusion, we have demonstrated a compact system which can give a bright single-mode visible light source (~ -20 dBm/nm) with a compact and low-cost microchip laser and a single fibre device. The device is convenient to fabricate and both of the ends are 5 μm core PCFs which are compatible with conventional fibre optical components and offer good coupling efficiency in practical applications. Enhanced visible continuum brightness will widen potential applications in biomedical imaging and visible-based microscopy and spectroscopy systems.

Acknowledgments

WJW is a Royal Society University Research Fellow. AW is on leave from National Institute of Telecommunications, Warsaw, Poland.

#70590 - $15.00 USD Received 3 May 2006; revised 9 June 2006; accepted 9 June 2006

J. Opt. A: Pure Appl. Opt. **9** (2007) 1095–1099 doi:10.1088/1464-4258/9/11/021

Enhanced four-wave mixing and parametric oscillation in photonic crystal fibre

K Cook, C Xiong and W J Wadsworth

Center for Photonics and Photonic Materials, Department of Physics, University of Bath, Bath BA2 7AY, UK

E-mail: K.Cook@bath.ac.uk

Received 18 June 2007, accepted for publication 3 October 2007
Published 31 October 2007
Online at stacks.iop.org/JOptA/9/1095

Abstract
We demonstrate efficient four-wave mixing in photonic crystal fibres with nanosecond, 1047 nm pump pulses. The incorporation of a ring cavity configuration allows a parametric oscillator to be formed, generating up to 31 mW of average power at 790 nm with a conversion efficiency of 15%.

Keywords: four-wave mixing, photonic crystal fibres

1. Introduction

In recent years photonic crystal fibres (PCFs) [1, 2] have proven efficient for the nonlinear frequency conversion of light [3–5]. The small nonlinearity of pure silica is enhanced by fibre waveguiding over long lengths, with phasematching provided by the dispersion of the waveguide. PCFs offer advantages over conventional optical fibres in the range of waveguide dispersion which is possible. Supercontinuum generation and four-wave mixing (FWM) have been observed with PCFs pumped in the near-infrared (600–1200 nm) [5–7] using their unique dispersion properties [8–10]. Applications have been found in frequency metrology [3], optical coherence tomography [4] and ultra-short pulse compression [11].

In this paper we build on our previous result of FWM in endlessly single mode PCFs [2] with zero dispersion close to 1064 nm, using nanosecond pulse, Q-switched lasers [5]. In this case two photons of the pump source generate two sidebands (a signal and idler) which are separated equally in frequency by $\Delta\omega$ from the pump, and must be phasematched along the fibre length for optimum efficiency. In general, phasematching and efficient parametric gain can be achieved for pump wavelengths in the vicinity of the zero dispersion wavelength (ZDW), which for conventional step-index fibres is restricted to no lower than 1270 nm—the shortest achievable ZDW [8]. For example, by operating in the anomalous dispersion regime, the phase mismatch between the frequencies can be balanced by the effects of self-phase modulation (SPM) [12]. PCFs, on the other hand, have dispersion profiles greatly influenced by waveguide dispersion, so the ZDW can be shifted to visible wavelengths simply by making the core diameter smaller and increasing the air filling fraction of the cladding [9]. Furthermore, the effects of higher order dispersion in these fibres allow phasematching in the normal dispersion regime; this may be explained in terms of the usual Taylor expansion of the dispersion coefficients (β_2, β_3, β_4 etc), the phase mismatch may therefore be expressed in terms of the difference in propagation constants as

$$\Delta\beta = \beta_2\Delta\omega^2 + \tfrac{1}{12}\beta_4\Delta\omega^4 \qquad (1)$$

(with odd β terms cancelling). A small normal (positive) value of β_2 may be balanced by a relatively high and negative value of β_4 [10, 13]. FWM in the normal dispersion regime has been investigated extensively in previous work [5] showing that the frequencies of the signal and idler depend critically on the chromatic dispersion of the fibre and the off-set of the pump source from the fibre ZDW. Using sub-nanosecond, microjoule pulses at 1064 nm from a Q-switched microchip laser, this work demonstrated distinct FWM signal peaks from 686 to 975 nm for a range of PCFs with varying ZDWs. Furthermore, it was shown that the threshold for FWM can be significantly reduced if the process is seeded by a CW diode laser operating at the idler wavelength [5]. The process of seeding by means of an external source or by providing feedback is a common method used to enhance nonlinear effects and has been applied previously to FWM in fibers [14–16]. If feedback is provided to enhance FWM then this is the exact definition of an optical parametric oscillator (OPO).

The wide tuneability of such fibre wavelength converters has been demonstrated by tuning the pump wavelength and/or

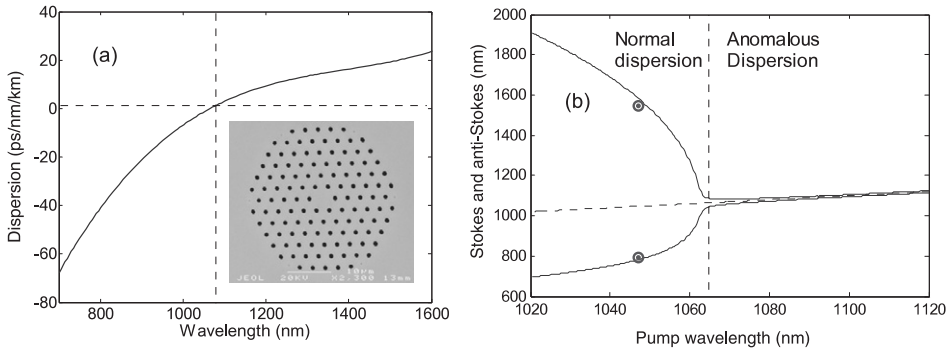

Figure 1. (a) Measured chromatic dispersion curve. Inset: an SEM image of the PCF cross-section. (b) Phasematching diagram calculated from the dispersion curve of (a) (solid curve) and measured FWM peaks (circles).

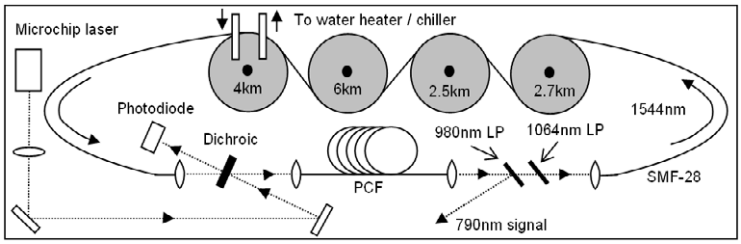

Figure 2. Experimental set-up. Dotted lines denote free-space beam paths.

using PCFs with different dispersion properties [6, 7, 14, 18]. In the work of [14], microstructured fiber is placed in a Fabry–Perot cavity and is synchronously pumped by femtosecond pulses from a Ti:sapphire oscillator; this led to amplified signal wavelengths from 590 to 710 nm. In other work various pump sources such as erbium-doped fibre amplifiers and ytterbium fibre lasers have been used to demonstrate this effect in the spectral region around 1500 nm in a range of fibre types, again incorporating feedback to form an OPO [17–20]. As well as ring cavity set-ups, various other configurations have been used to provide feedback such as Fabry–Perot cavities and Sagnac interferometers [17, 21].

All of this previous work has either used mode-locked femtoscond/picosecond sources to synchronously pump the OPO or, in the experiments of [17], operated with a continuous wave pump. Synchronous pumping necessitates the matching of the OPO cavity length with that of the mode-locked pump source. In this paper we consider nanosecond pulses from a Q-switched source. This is different from both the CW and femtosecond pumped OPOs demonstrated previously. The physical length of the pulse is shorter than the fibre used, so we cannot obtain many round trips of the fibre within the pump pulse as one can for long-pulse and CW lasers. We must instead use a cavity in which the round trip time is linked to the repetition rate of the pump laser. This is conceptually similar to a femtosecond synchronously pumped OPO, except that the repetition rate here is determined by an electronic trigger and each pump pulse is independent of the previous pulse, unlike a modelocked laser where each output pulse is derived from a circulating pulse inside the laser and so maintains a pulse-to-pulse coherence. The Q-switched pulse length is much longer (which avoids the rapid walk-off between the signal and pump that occurs when using pulses of picosecond duration or less), and the repetition rate is much lower (necessitating a cavity many kilometres in length). The following experiments also use relatively compact and low-cost Q-switched laser technology which generates 15 ns pulses with a comparatively low repetition rate of several kHz and much lower peak powers than the kW powers used in mode-locked lasers. To provide the feedback, we incorporate a step-index fibre delay loop at the output of a PCF sample, this enables a conversion efficiency of around 15% and a signal power at 790 nm of up to 31 mW.

2. Experimental set-up

For these experiments lengths of up to 10 m of endlessly single-mode PCF were used [2], with a pitch (Λ) of 2.97 μm and a hole diameter to pitch ratio (d/Λ) of 0.39 which corresponds to a core diameter of approximately 5 μm. A scanning electron microscope image of the fibre is shown inset in figure 1(a); it can be seen that the fibre core is symmetrical in shape, therefore we do not expect any effects from 'accidental' birefringence. In order to understand the dispersion properties of the fibre, the group index of the fibre was measured using a low-coherence interferometer [22] with a supercontinuum source. The dispersion curve derived from the measured data is plotted in figure 1(a) revealing a ZDW of 1065 nm. Above and below the ZDW, the fibre is found to exhibit anomalous and normal dispersion, respectively. Figure 1(b) shows the calculated phasematching curve [6] at low pump power, which for a pump wavelength of 1047 nm is seen to be in excellent agreement with the measured FWM peaks. Figure 2 shows the experimental configuration. A Nd:YLF microchip laser was used as a pump source; this was actively Q-switched by an acousto-optic modulator thus ensuring a stabilized repetition

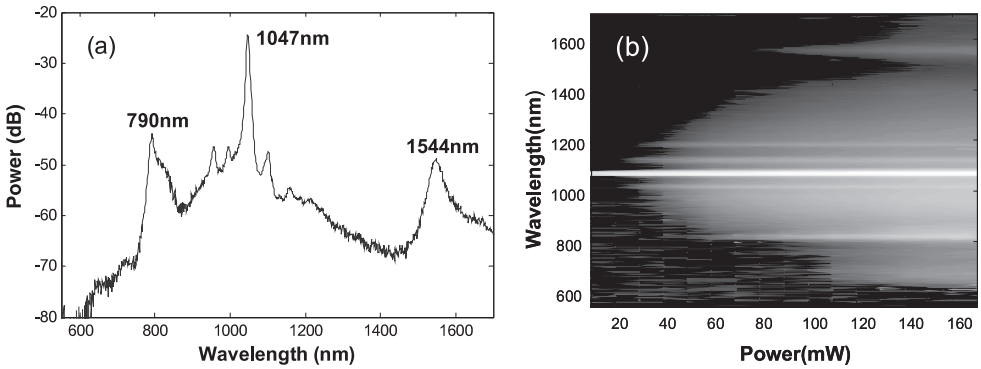

Figure 3. (a) Output spectrum for 6.5 m of PCF at 178 mW output power. (b) Evolution of output spectra with output power for 6.5 m of PCF.

rate. The laser provided pulses of 15 ns duration, centred at 1047 nm and with an average power of 250 mW at 20 kHz. The separation between pulses could be varied in 20 ns steps, corresponding to a repetition rate of 13–20 kHz. The pump source was coupled into the PCF after reflection from a dichroic mirror, which is highly reflective at 1047 nm. The overall input coupling loss was approximately 1 dB. The output of the PCF, now spectrally consisting of two FWM mixing peaks at 790 nm (signal) and 1544 nm (idler), was collimated before passing through two long-pass filters. The first filter was highly transmissive above 980 nm whilst highly reflective at lower wavelengths, thus allowing the signal to be extracted from the cavity. The band edge of the second filter was at 1064 nm, and therefore transmitted the idler whilst reflecting the residual 1047 nm pump. The combined loss of the filter pair was measured to be 0.5 dB at 1540 nm.

To provide feedback and complete the ring cavity, the idler was then coupled into standard single-mode fibre (*Corning* SMF-28e) before being re-injected into the PCF via the input dichroic. The length of the feedback loop was approximately 15.2 km and consisted of four spools of fibre with various lengths spliced together. Assuming a refractive index value of 1.5, the optical path length was 22.8 km, corresponding to the pulse separation at the laser repetition rate of 13.1 kHz. The alignment of the feedback was performed by using a 1540 nm laser diode fibre coupled counter-clockwise into the loop by intersecting the splice between the 2.7 and 2.5 km spools. This method also allowed the total loop loss at 1540 nm to be measured, which was found to be 12.9 dB.

This feedback was temporally overlapped with the succeeding pump pulse in order to seed (induce) FWM in the PCF and achieve parametric amplification. Accurate control over the feedback timing was therefore critical. Coarse control was achieved by varying the pump pulse separation in 20 ns steps. Shorter increments were not possible as the Q-switch drive electronics only allowed switching at a fixed phase of the 54 MHz acoustic wave. The trigger pulse was synchronized with the acoustic drive frequency, and the laser pulse period was stable to much less than 1 ns, and selectable in $1/54$ MHz $=$ 20 ns steps. Fine control of the feedback timing to within less than 1 ns was realized by varying the temperature (and therefore the refractive index) of the final 4 km section of the delay loop. An InGaAs photodiode was used to monitor the idler-pump overlap by recording the partial reflection of the idler from dichroic 1 or the partial transmission of the pump (using bandpass filters to select the required wavelength). All spectral measurements were obtained using an optical spectrum analyser (Ando AO-6315B) with a spectral resolution of 5 nm. All power measurements used a thermal power meter with a flat spectral response.

3. Results

3.1. Single-pass FWM spectra

Initial experiments were performed without the connection of the feedback loop in order to understand the effects of a single pass of the PCF by the 1047 nm pump. A 6.5 m sample was chosen, and the spectrum was recorded by placing the OSA fibre patch cord between the collimating lens of the PCF and the 980 nm long-pass filter. The incident pump power was increased from 14 mW to a maximum of 230 mW (measured after the input dichroic) and was coupled into and through the PCF with an efficiency of approximately 72%. Figure 3(a) shows the spectrum at maximum input power, corresponding to a total output power of 178 mW contained in the whole spectrum. Figure 3(b) shows the evolution of the output spectrum with power. The spectra exhibit two distinct FWM peaks at 790 nm (signal) and 1544 nm (idler) occurring at a threshold of around 60 mW of total output power. It can be seen that both the signal and idler wavelengths have significant spectral widths of 10 nm and 33 nm, respectively. This broad bandwidth relative to the calculated gain bandwidth may be attributed to the finite bandwidth of the pump and the steepness of the phasematching curve (figure 1(b)). The positions of the FWM peaks depend critically on the off-set of the pump wavelength from the ZDW, so any small bandwidth of the pump will yield a much larger FWM bandwidth. Other spectral features include the first Raman Stokes line at 1100 nm, this is a characteristic of all silica-based fibres and occurs at a frequency shift of 13 THz from the pump. The presence and prominence of the anti-Stokes Raman peak at 1000 nm may be explained by considering that the fibre is pumped close to the ZDW; a signature of this is coupling between the Raman and FWM processes.

From [23], a simple expression for the single-pass parametric gain, in the special case of perfect phasematching, may be written as

$$G_s = \tfrac{1}{4}\exp(2\gamma P_p L) \qquad (2)$$

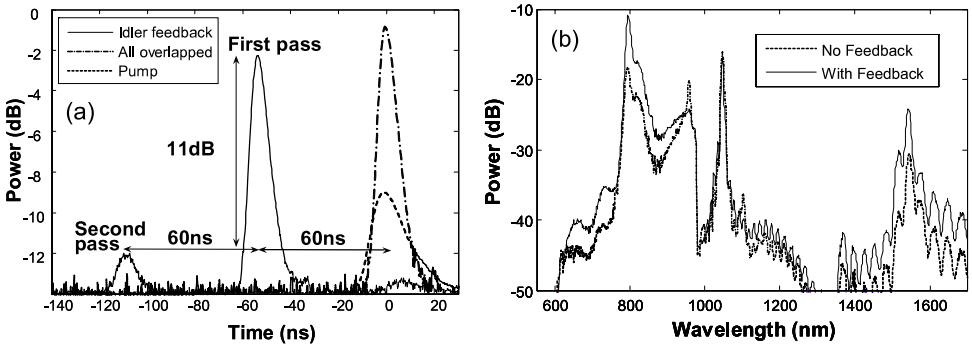

Figure 4. (a) Photodiode traces showing the delay between the pump pulse (dotted curve) and idler first and second pass pulses (solid curve); the semi-dashed curve shows the pulse profile when the overlap is optimized. (b) Extracted spectrum with and without the connection of the feedback loop for 6.5 m of PCF.

where P_p is the power of the pump pulse and L is the fibre length. In dB units, this becomes

$$G_s = 10 \log \left[\tfrac{1}{4} \exp(2\gamma P_p L) \right]. \quad (3)$$

This equation may be used in order to calculate the threshold power required for parametric oscillation; this is the point at which G_s is equal to the roundtrip loss which is measured to be 12.9 dB. For a $\gamma = 6$ km^{-1} W^{-1} [12] and a fibre length of 6.5 m, this leads to a threshold peak power of 55 W which corresponds to an average power of 15 mW; this value is much less than the typical total output power of around 178 mW and indicates that parametric oscillation is certainly possible with our experimental set-up.

3.2. FWM and parametric gain with feedback

In order to complete the ring cavity and provide the feedback necessary for parametric oscillation, the idler was coupled into the SMF-28e fibre and delivered to the beginning of the loop where it was re-injected into the PCF. The 15.2 km length of SMF-28e corresponded only approximately to the pulse separation of 76 μs, therefore the idler was not initially overlapped with the following pump pulse. The separation was reduced to within 20 ns by varying slightly the repetition rate of the laser; fine tuning the overlap to within ± 1 ns was achieved by changing the temperature of the final section of the delay loop. Figure 4(a) shows the various photodiode traces recorded for the idler and pump pulses using a 1540 nm bandpass filter. It shows the idler pulse (solid curve) for the case when the arrival time at the beginning of the loop is 60 ns later than the pump pulse; with this separation it is possible to clearly observe a second pass of the complete ring cavity at a further 60 ns from the pump. By comparing the relative first and second pass powers, it is also possible to deduce the loss incurred by the feedback after one complete round trip; this is measured to be around 11 dB—in fair agreement with the 12.9 dB deduced from the alignment process. Figure 4(a) also shows the case when the overlap is optimized (semi-dashed curve) and the separation of the first pass, second pass and pump is within ± 1 ns and therefore appears as one pulse.

The effects of the feedback on the FWM signal can now be investigated by monitoring the reflection from the 980 nm long-pass filter with the OSA. Figure 4(b) shows the extracted spectrum with and without the idler feedback; the spectra are recorded for a total maximum output power of around 178 mW. The region of interest lies around the signal peak at 790 nm, where an enhancement of around 8 dB can clearly be seen when the feedback is connected. Above the 980 nm band edge of the filter, the spectrum exhibits an oscillatory structure (as expected from a thin-film filter) and contains some of the partially reflected idler which experiences a similar enhancement of 8 dB.

The power of the signal peak was measured to be approximately 12 mW and increased to 25 mW when feedback was introduced. Experiments with a 10 m length of PCF generated signal powers as high as 31 mW; with an input pump power of 230 mW, this corresponds to a total conversion efficiency of 15%. Defined as the ratio of signal power to PCF output power, the internal conversion efficiency is 19%. The stability of the average signal power was less than $\pm 1\%$ and the time-overlap was optimized with an accuracy of ± 1 ns for all the experiments in order to achieve the maximum extracted signal power. The dependence of signal power on the output power was investigated and the relationship is shown in figure 5(a). At powers lower than 100 mW the signal power became unstable and an accurate measurement was not possible. There is a clear increase in slope efficiency with feedback (gradient of the solid line) although the threshold power is largely unchanged at 85 mW.

The dependence of signal power on PCF length was also investigated by cutting back the fibre in 0.5–1 m stages and monitoring the signal power with and without feedback each time. The fibre was cut back from the output end to avoid disturbing the critical co-coupling of the pump and idler into the beginning of the fibre; also the idler-pump temporal overlap was re-optimized after each cut-back. The results are shown in figure 5(a) and indicate that, even for short lengths, the inclusion of feedback greatly affects the signal power.

Power-scaling the signal with longer fibre lengths will eventually be limited by fibre losses, the coherence length of the pump source and ultimately by pump depletion. However, further power improvements may be possible by reducing the round-trip loss experienced by the idler, currently 13 dB (SMF-28e loss 3 dB, dichroic mirrors 2 dB (input) and 0.5 dB (output), free-space coupling losses 3–4 dB). The greatest improvement is to be gained in the input dichroic and the free-space coupling efficiency, which together may help to increase the efficiency of the ring cavity and produce higher signal powers.

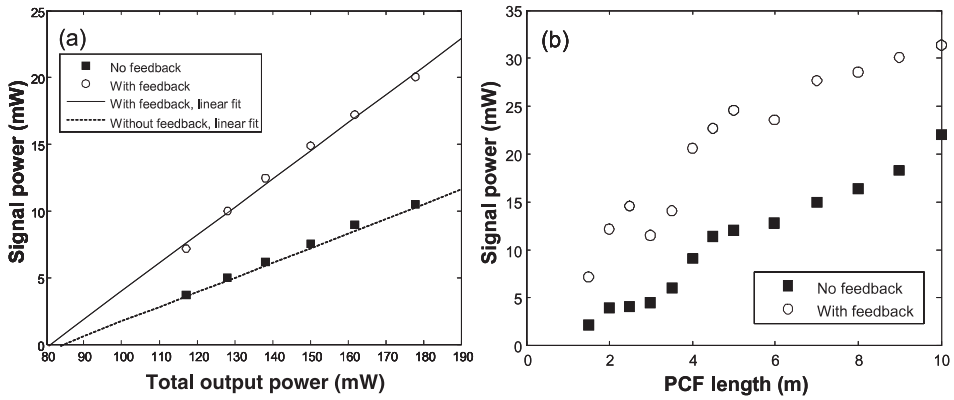

Figure 5. (a) Dependence of signal power on output power for 5.5 m of PCF. (b) Signal powers for increasing PCF length.

4. Conclusion

We have demonstrated efficient phasematched FWM in PCF by exploiting the relatively large degree to which their dispersion properties can now be engineered. Inclusion of feedback allows an OPO to be formed, helping to seed the FWM process and generate extracted signal powers of up to 31 mW, corresponding to a total efficiency of 15%. The ability to accurately design and fabricate PCFs with slightly differing dispersion properties means that we can now envisage a tuneable OPO device in which various PCFs, and therefore various FWM signals, may be selected. The potential of such a device, based on a low-cost compact Q-switched source, has far-reaching applications in areas such as two-photon fluorescence, frequency conversion and all-optical amplification.

References

[1] Knight J C, Broeng J, Birks T A and Russell P St J 1998 *Science* **282** 147/6
[2] Birks T A, Knight J C and Russell P St J 1997 *Opt. Lett.* **22** 961
[3] Udem Th, Holzwarth R and Hänsch T W 2002 *Nature* **416** 233
[4] Wang Y, Zhao Y, Nelson J S, Chen Z and Windeler R S 2003 *Opt. Lett.* **28** 182
[5] Wadsworth W J, Joly N, Knight J C, Birks T A, Biancalana F and Russell P St J 2004 *Opt. Express* **12** 299
[6] Chen A Y H, Wong G K L, Murdoch S G, Leonhardt R, Harvey J D, Knight J C, Wadsworth W J and Russell P St J 2005 *Opt. Lett.* **30** 762
[7] Chow K K, Shu C, Lin C and Bjarklev A 2005 *IEEE Photon. Technol. Lett.* **17** 624
[8] Mogilevtsev D, Birks T A and Russell P St J 1998 *Opt. Lett.* **23** 1662
[9] Knight J C, Arriaga J, Birks T A, Ortigosa-Blanch A, Wadsworth W J and Russell P St J 2000 *IEEE Photon. Technol. Lett.* **12** 807
[10] Reeves W H, Skyrabin D V, Biancalana F, Knight J C, Russell P St J, Omenetto F G, Efimov A and Taylor A J 2003 *Nature* **424** 511
[11] McConnell G and Riis E 2004 *Appl. Phys.* B **78** 557
[12] Agrawal G P 2001 *Nonlinear Fiber Optics* 3rd edn (San Diego, CA: Academic)
[13] Lin C, Reed W A, Pearson A D and Shang A-T 1981 *Opt. Lett.* **6** 493
[14] Sharping J E, Foster M A, Gaeta A L, Lasri J, Lyngnes O and Vogel K 2007 *Opt. Express* **15** 1474
[15] Harvey J D, Leonhardt R, Coen S, Wong G K L, Knight J C, Wadsworth W J and Russell P St J 2003 *Opt. Lett.* **28** 2225
[16] Sharping J E, Fiorentino M, Kumar P and Windeler 2002 *Opt. Lett.* **27** 1675
[17] Marhic M E, Wong K K Y, Kazovsky L G and Tsai T E 2002 *Opt. Lett.* **27** 1439
[18] Li Y, Qian L, Lu D and Fan D 2006 *Opt. Commun.* **267** 491
[19] Deng Y, Lin Q, Lu F, Agrawal G P and Knox W 2005 *Opt. Lett.* **30** 1234
[20] Wong G K L, Murdoch S G, Leonhardt R and Harvey J D 2007 *Opt. Express* **15** 2947
[21] Serkland D K and Kumar P 1999 *Opt. Lett.* **24** 92
[22] Tateda M, Shibata N and Seikai S 1981 *IEEE J. Quantum Electron.* **QE–17** 404
[23] Hansryd J, Andrekson P A, Westlund M, Lie J and Hedekvist P 2002 *IEEE. Sel. Top. Quantum Electron.* **8** 506

Polarized supercontinuum in birefringent photonic crystal fibre pumped at 1064 nm and application to tuneable visible/UV generation

C. Xiong and W. J. Wadsworth

Centre for Photonics and Photonic Materials, Department of Physics, University of Bath, BATH, BA2 7AY, UK
w.j.wadsworth@bath.ac.uk

Abstract: We generate a flat, polarized and single mode supercontinuum (SC) spanning 450-1750 nm in a highly birefringent photonic crystal fibre (PCF) pumped by a 1064 nm microchip laser. More than 99% of the total power is kept in a single linear polarization. The measured power coupling penalty due to the elliptical core is less than 6% (0.25 dB). As one of its applications, we demonstrate tuneable visible/UV generation in the nonlinear crystal BIBO pumped by this polarized SC source. A tuneable range of 400-525 nm is obtained by critical phase matching in BIBO. We also show the results of visible/UV generation in BIBO pumped by the signal wavelength of polarized four-wave mixing (FWM) in PCF.

OCIS codes: (190.4370) Nonlinear optics; (060.2380) Fibre Optic Sources and Detectors; (060.2420) Fibres, polarization-maintaining.

References and links

1. W. J. Wadsworth, N. Joly, J. C. Knight, T. A. Birks, F. Biancalana and P. St. J. Russell, "Supercontinuum and four-wave mixing with Q-switched pulses in endlessly single-mode photonic crystal fibres," Opt. Express **12**, 299-309 (2004).
2. J. C. Travers, S. V. Popov, and J. R. Taylor, "Extended blue supercontinuum generation in cascaded holey fibres," Opt. Lett. **30**, 3132-3134 (2005).
3. A. Kudlinski, A. K. George, J. C. Knight, J. C. Travers, A. B. Rulkov, S. V. Popov, and J. R. Taylor "Zero-dispersion wavelength decreasing photonic crystal fibres for ultraviolet-extended supercontinuum generation," Opt. Express **14**, 5715-5722, (2006).
4. C. Xiong, A. Witkowska, S. G. Leon-Saval, T. A. Birks and W. J. Wadsworth, "Enhanced visible continuum generation from a microchip 1064 nm laser," Opt. Express **14**, 6188-6193, (2006).
5. M. Lehtonen, G. Genty, H. Ludvigsen, and M. Kaivola, "Supercontinuum generation in a highly birefringent microstructured fibre," Appl. Phys. Lett. **82**, 2197-2199 (2003).
6. Z. Zhu and T. Brown, "Polarization properties of supercontinuum spectra generated in birefringent photonic crystal fibres," J. Opt. Soc. Am. B **21**, 249-257 (2004).
7. Z. Zhu and T. Brown, "Experimental studies of polarization properties of supercontinua generated in a birefringent photonic crystal fibre," Opt. Express **12**, 791-796 (2004).
8. A. Ortigosa-Blanch, J. C. Knight, W. J. Wadsworth, J. Arriaga, B. J. Mangan, T. A. Birks, and P. St. J. Russell, "Highly birefringent photonic crystal fibres," Opt. Lett. **25**, 1325-1327 (2000).
9. K. Suzuki, H. Kubota, S. Kawanishi, M. Tanaka and M. Fujita, "Optical properties of a low-loss polarization-maintaining photonic crystal fibre," Opt. Express **9**, 676-680 (2001).
10. H. Hellwig, J. Liebertz, and L. Bohaty, "Exceptional large nonlinear optical coefficients in the monoclinic bismuth borate BiB_3O_6 (BIBO)," Solid State Commun. **109**, 249-251 (1999).
11. H. Hellwig, J. Liebertz, and L. Bohaty, "Linear optical properties of the monoclinic bismuth borate BiB_3O_6," J. Appl. Phys. **88**, 240-244 (2000).
12. C. Du, Z. Wang, J. Liu, X. Xu, B. Teng, K. Fu, J. Wang, Y. Liu, and Z. Shao, "Efficient intracavity second-harmonic generation at 1.06 μm in a BiB_3O_6 (BIBO) crystal," Appl. Phys. B **73**, 215 (2001).
13. Z. Wang, B. Teng, K. Fu, X. Xu, R. Song, C. Du, H. Jiang, J. Wang, and Z. Shao, "Efficient second harmonic generation of pulsed laser radiation in BiB_3O_6 (BIBO) crystal with different phase matching directions," Opt. Commun. **202**, 217 (2002).
14. C. Du, B. Teng, Z. Wang, J. Liu, X. Xu, G. Xu, K. Fu, J. Wang, Y. Liu, and Z. Shao, "Actively Q-switched intracavity second-harmonic generation of 1.06 μm in BiB_3O_6 crystal," Opt. Laser Technol. **34**, 343 (2002).
15. C. Czeranowsky, E. Heumann, and G. Huber, "All-solid-state continuous-wave frequency-doubled Nd:YAG BiBO laser with 2.8-W output power at 473 nm," Opt. Lett. **28**, 432 (2003).

#91141 - $15.00 USD Received 21 Dec 2007; revised 29 Jan 2008; accepted 30 Jan 2008; published 6 Feb 2008

16. M. Ghotbi and M. Ebrahim-Zadeh, A. Majchrowski and E. Michalski, and I. V. Kityk, "High-average-power femtosecond pulse generation in the blue using BiB_3O_6," Opt. Lett. **29**, 2530-2532 (2004).
17. M. Ghotbi and M. Ebrahim-Zadeh, "Optical second harmonic generation properties of BiB_3O_6," Opt. Express **12**, 6002-6019, (2004).
18. M. Ghotbi and M. Ebrahim-Zadeh, "990 mW average power, 52% efficient, high-repetition-rate picosecond-pulse generation in the blue with BiB_3O_6," Opt. Lett. **30**, 3395-3397 (2005).
19. C. Du, S. Ruan, and Y. Yu, "High-power intracavity second-harmonic generation of 1.34 μm in BiB_3O_6 crystal," Opt. Express **13**, 8591-8595, (2005).
20. M. Thorhauge, J. L. Mortensen, P. Tidemand-Lichtenberg and P. Buchhave, "Tuneable intra-cavity SHG of CW Ti:Sapphire lasers around 785 nm and 810 nm in BiBO-crystals," Opt. Express **14**, 2283-2288 (2006).
21. M. Ghotbi, A. Esteban-Martin, and M. Ebrahim-Zadeh, "BiB_3O_6 femtosecond optical parametric oscillator," Opt. Lett. **31**, 3128-3130, (2006).
22. Z. Sun, M. Ghotbi, and M. Ebrahim-Zadeh, "Widely tuneable picosecond optical parametric generation and amplification in BiB_3O_6," Opt. Express **15**, 4139-4148, (2007).
23. C. Xiong, S. G. Leon-Saval, F. Couny, and W. J. Wadsworth, "Residual pump peak removal for ultra-flattened supercontinuum generation by Photonic Crystal Fibres," CLEO/QELS and Photonic Applications Systems Technologies 2006 Technical Digest (Optical Society of America, Washington, DC, 2006), paper CWO4. http://www.opticsinfobase.org/abstract.cfm?URI=CLEO-2006-CWO4
24. A. V. Smith, D. J. Armstrong, and W. J. Alford, "Increased acceptance bandwidths in optical frequency conversion by use of multiple walk-off-compensating nonlinear crystals," J. Opt. Soc. Am. B **15**, 122-141 (1998).
25. R. J. Gehr, M. W. Kimmel, and A. V. Smith, "Simultaneous spatial and temporal walk-off compensation in frequency-doubling femtosecond pulses in β-BaB_2O_4," Opt. Lett. **23**, 1298-1300 (1998).

1. Introduction

Supercontinuum (SC) generation in photonic crystal fibres (PCFs) has been investigated extensively, including using compact picosecond fibre lasers or nanosecond microchip lasers at 1064 nm [1-4]. Recently much attention has been paid to extending the spectrum to short wavelengths by the use of either multiple spliced PCFs with sequentially decreasing zero-dispersion wavelengths (ZDWs) [2], a single piece of ZDW decreasing PCF [3] or an inflated and tapered monolithic PCF device [4]. The continuum generated is generally unpolarized, as the fibre core is large (5 μm) and circular, whereas many applications require polarized SC output from a birefringent fibre. This is readily achieved for PCFs pumped at around 800 nm, where the small cores required to achieve the necessary dispersion at the pump wavelength acquire large birefringence for very little ellipticity [5-7]. For operation at 1064 nm birefringence can be introduced through the application of stress rods whilst maintaining a circular mode. However, stress is not stable at high temperature and may be annealed out. Here we present a highly birefringent PCF based on simple form birefringence [8, 9] introduced to the endlessly single mode (ESM) PCF fabrication technique [1]. Birefringence is simply introduced during fibre drawing process and offers very flexible control. A potential disadvantage of using form birefringence is that the mode is slightly elliptical which causes loss when coupling to circular core fibres or circular laser beams, however we show that this loss is small.

One of the potential applications of this polarized SC source is tuneable visible or UV generation by nonlinear frequency upconversion in nonlinear crystals. BIBO [10, 11] is an attractive nonlinear material for frequency conversion in the visible and UV as it combines the advantages of both high UV transparency and enhanced nonlinearity: the optical transmission of BIBO extends from 2500 nm in the infrared down to 280 nm in the UV. As a biaxial crystal, it offers versatile phase matching properties. Since the introduction of BIBO, a number of frequency conversion experiments have been performed, including second-harmonic generation (SHG) of continuous-wave (CW) radiation at 1.06 μm [12], single-pass SHG of a pulsed laser at 1.06 μm [13], Q-switched SHG at 1.06 μm [14], frequency doubling of a CW Nd:YAG laser [15], tuneable single-pass SHG of a mode-locked Ti:sapphire laser [16-18], CW or Q-switched intra-cavity SHG at 1.34 μm [19], tuneable intra-cavity SHG of a CW Ti:sapphire laser [20], and optical parametric oscillators (OPOs)[21, 22]. All of these experiments directly used a high power laser as the pump source. To achieve tuneability, a complex tuneable laser system such as Ti:sapphire laser is normally needed [16-18, 20, 22]. The presence of a polarized SC source makes compact tuneable visible/UV generation

#91141 - $15.00 USD Received 21 Dec 2007; revised 29 Jan 2008; accepted 30 Jan 2008; published 6 Feb 2008

possible. Unlike the single pump wavelength source in previous frequency conversion experiments, the pump source here is a continuum source, so sum frequency mixing (SFM) becomes possible and the large residual peak at the SC pump wavelength may enhance the process.

2. Polarized continuum generation

We fabricated the birefringent PCFs using a solid core PCF preform with uniform air hole diameters. During the fabrication process, we used differential pressure to enlarge two specific holes alongside the core to induce birefringence. Figure 1 gives the scanning electron microscope (SEM) images of fibre A at different scales. The measured d_2/d_1 ratio is 1.7, hole to hole pitch $\Lambda = 3.09$ μm and hole-pitch ratio $d_1/\Lambda = 0.45$. The two big holes make the core area slightly elliptical: the long axis to short axis length ratio is 1.25. It is the asymmetry that induces the birefringence. Unfortunately asymmetry of the core can also reduce the coupling efficiency to the circular pump laser mode or to other circular fibres. To check this we measured the butt-coupling efficiency between this fibre and a standard symmetrical PCF. The measured power penalty at 1550 nm was less than 6% (0.25 dB). The fibre attenuation was measured to be about 10 dB/km at 1064 nm by the cut-back technique. The calculated polarization beat length at 1064 nm for these fibre parameters is 8.6 mm.

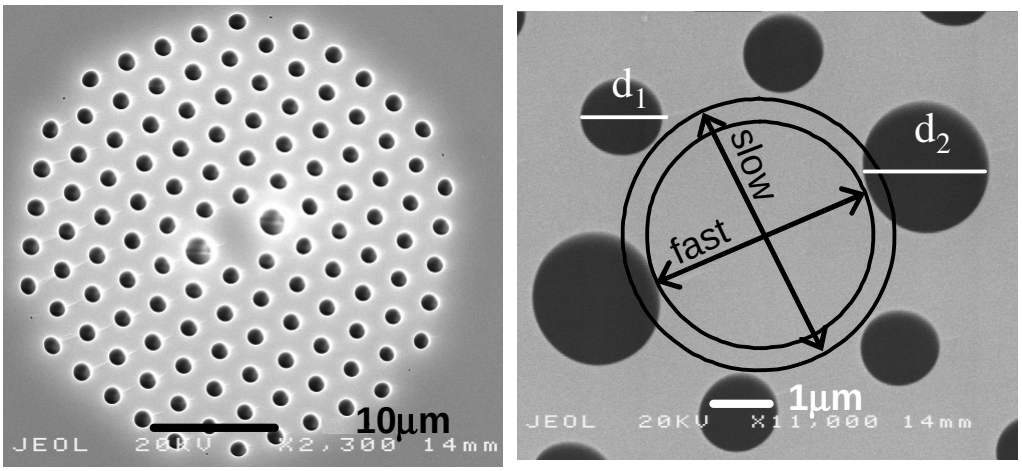

Fig. 1. SEM images of fibre A at different scales.

In the SC experiment, the pump laser was a Nd:YAG Q-switched microchip laser (*Teem Photonics*, model NP-10820) running at a wavelength of $\lambda = 1064$ nm and emitting 0.6 ns (FWHM) pulses with 15 kW peak power at a repetition rate of 7.2 kHz. A polarizer was used to purify the input polarization and a rotating zero-order half-wave plate was put between the polarizer and the fibre input end to adjust the input polarization. A ×40 anti-reflection coated aspheric singlet lens was used to optimize the coupling. The input coupling efficiency was as high as 60%.

Figure 2(a) shows the SC spectrum with an average power of 30 mW from a 6 m length of fibre A when the input polarization was along the slow axis of the fibre. It can be seen that the short wavelength edge is as short as 450 nm and the spectrum is flat over the whole bandwidth from 450 to 1750 nm except for the residual pump peak. We note that this has a shorter wavelength edge in the blue than Ref. [1], although not as short as for some recent structures [3, 4]. We also checked the effect of input polarization on SC generation. Figure 2(b) shows the spectra for different input polarizations with the same pump power. The spectra are similar except that the spectrum extends to shorter wavelengths when the input polarization is along the fast axis. We believe this small difference is because of the slightly different dispersion properties of the two polarization modes.

#91141 - $15.00 USD Received 21 Dec 2007; revised 29 Jan 2008; accepted 30 Jan 2008; published 6 Feb 2008

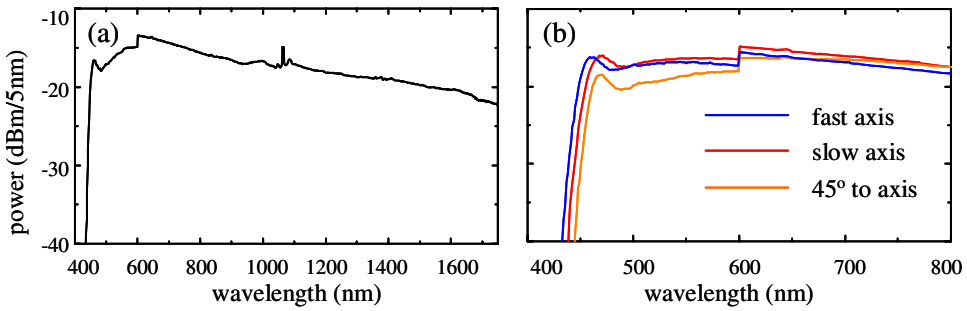

Fig. 2. (a). The spectrum with an average power of 30 mW from a 6 m length of fibre A when the input polarization was along the slow axis. (b) Effect of input polarization on supercontinuum generation. The step at 600 nm is an artefact of the spectrometer used. The resolution of the spectrometer was 5 nm.

In this study, the most important parameter is the polarization property of the continuum source. We checked the polarization of the output light by a broadband birefringent crystal polarizer. We define the polarization extinction ratio (PER) as the power ratio P_s/P_f or P_f/P_s, where P_s and P_f are the measured power when the output polarizer's axis is set along the slow and fast axes of the fibre respectively. The output PER was $P_s/P_f = 110$ and $P_f/P_s = 40$ when the input polarization was along the slow and fast axes (99% and 97.5% single polarization). This is much higher than the PER (less than 2) of a SC produced by a PCF without birefringence and means the output light is well linearly polarized for all the spectral components. The difference between the slow and fast axes derives from the intensity-induced nonlinear birefringence [6, 7]. When the input polarization is along the slow axis, the nonlinear birefringence enhances the linear birefringence; on the contrary, when the input polarization is along the fast axis, the nonlinear birefringence can result in the total cancellation of linear birefringence.

3. SFM and SHG in BIBO

As an application of the polarized SC source we have demonstrated visible/UV output using SFM and SHG in a second-order nonlinear crystal. For a particular nonlinear crystal and pump power, the main factors limiting the conversion efficiency are the acceptance angle and acceptance bandwidth of the crystal and the effective nonlinear interaction length. Both acceptance angle and bandwidth are determined by the crystal length and the effective nonlinear interaction length is determined by the crystal length and the Rayleigh length of the pump beam. Either a longer crystal and less focused pump beam or shorter crystal and tighter focused pump beam may give optimum efficiency. However, in many applications, the generated beam needs to be coupled back into fibres, which requires good beam quality. A beam which is too tightly focused will yield a big divergence angle which will make both measurement and collection difficult. We therefore prefer a relatively long crystal and weakly focused pump beam. Here we chose a 5 mm long BIBO crystal. In order to make full use of the crystal, the optimum Rayleigh length of the focused beam is 2.5 mm, which corresponds to a 20 μm beam waist diameter at a wavelength of ~1 μm. Thus we should choose a ×4 lens or lens combination to focus the beam coming from the 5 μm core diameter fibre. In practice, we tried with different lenses or lens combinations with various magnifications and ×4 lens combination showed the best performance.

3.1 Nonlinear conversion of continuum

The experimental configuration for nonlinear conversion is shown in Fig. 3(a). The continuum source setup was the same as the polarized SC generation setup, except that we used a shorter piece of fibre (0.6 m) because here we need maximum power in the wavelength range of 750-1000 nm rather than maximum bandwidth. We set the pump polarization along the slow

#91141 - $15.00 USD Received 21 Dec 2007; revised 29 Jan 2008; accepted 30 Jan 2008; published 6 Feb 2008

axis of fibre because of the higher output PER. The spectrum taken at point O in Fig. 3(a) is plotted in Fig. 3(b). By use of the continuum source, we can realize a tuneable visible/UV source by just simply rotating the crystal to the critical phase matching angle. To take the advantage of the high nonlinearity of BIBO, the most interesting plane for nonlinear optical interactions is yz (ϕ=90°), which offers the highest effective nonlinearity, with a maximum effective nonlinear coefficient d_{eff} ~ 3.4 pm/V. Type I (e + e → o) phase matching is available for SFM and SHG in this plane for angles 90° < θ < 180° [11, 16]. The crystal was cut for type I phase matching in the yz plane at internal angle close to θ = 155° at normal incidence, and the facets were anti-reflection coated for 850 nm and 425 nm. All experiments were performed at room temperature. We were able to achieve wavelength tuning from 400 to 525 nm, limited by the crystal aperture at larger angles.

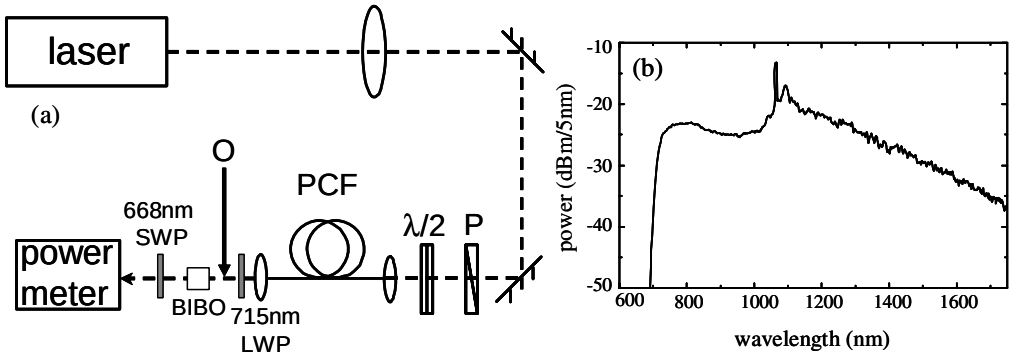

Fig. 3. (a). Setup for SFM and SHG experiment. P, polarizer; λ/2, half-wave plate; 715 nm LWP, long wave pass filter, cut-off wavelength 715 nm; 668 nm SWP, short wave pass filter, cut-off wavelength 668 nm (b) The output spectrum measured at point O in (a) from a 0.6 m length of fibre A, collected using a multimode collection fibre. The resolution of the spectrometer was 5 nm.

In order to determine the nonlinear processes involved we measured the powers for some specific wavelengths in the continuum generated from a 0.6 m length of fibre A using 10 nm bandwidth interference band pass filters (about 45%-50% transmission). The measured powers are shown in table 1 together with the measured powers for corresponding upconverted wavelengths. We notice that the powers at fundamental wavelengths from 800 nm to 950 nm are quite similar, but the powers at upconverted wavelengths differ by a large amount. Moreover, the power at 475 nm is 120 μW which would correspond to 40% SHG conversion efficiency from 950 nm (taking the filter transmission efficiency at 950 nm into account). This would be a remarkable efficiency for such a low pump power. To understand this, we plot the spectra for two typical wavelengths, 425 nm and 475 nm in Fig. 4(a) and calculate the SFM tuning phase matching curves [type I, Fig. 4(b)] by using Sellmeier equations [11]. From Fig. 4(b) we can see that by changing the crystal orientation 475 nm output can be generated by many different SFM processes as well as by SHG of 950 nm. In particular at an angle of about 162.1° (vertical red line), SFM 1064 nm + 860 nm → 475 nm will occur. This will be an efficient process as the residual pump intensity at 1064 nm is very strong and the 860 nm component is included in the continuum, and can explain the high output power at 475 nm. We have previously measured the residual pump in a similar continuum (but 15 m of fibre) to be around 10% of the total output power [23]. Whilst this is a small fraction of the total power, it is concentrated in a narrow spectral range and is far stronger than any of the infrared powers measured in table 1. If we therefore propose that the crystal is placed at 162.1°, we should see strong 475 nm output, but Fig. 4(b) also shows that we should see other blue/visible wavelengths generated from other SFM/SHG processes at this angle: a wavelength slightly longer than 475 nm will be produced by SHG of a wavelength longer than 950 nm; many wavelengths shorter than

#91141 - $15.00 USD Received 21 Dec 2007; revised 29 Jan 2008; accepted 30 Jan 2008; published 6 Feb 2008

475 nm will be produced by SFM of one photon with a wavelength longer than 1064 nm and one shorter than 860 nm. As the input is a continuum spectrum all these processes will occur and we observe a spectrum with a peak at 475 nm, but a broad tail to shorter wavelengths [Fig. 4(a)]. There is a short wavelength limit to the tail as we can see from Fig. 4(b) that to generate 450 nm at an angle of 162.1° requires pump wavelengths less than 710 nm, which are not available in the continuum after the 715 nm long-pass filter. This type of spectrum is observed when generating visible wavelengths from 500 nm to 450 nm.

Table 1. Comparison of powers between the upconverted wavelengths from BIBO and the short wavelengths in the broad continuum source.

Powers for specific wavelengths in the continuum generated from a 0.6 m length of fibre A and corresponding upconverted wavelengths generated from BIBO						
λ(nm)	800	850	900	950	1000	1050
P(μW)	136	144	140	140	218	460
$\lambda/2$(nm)	400	425	450	475	500	525
P(μW)	12	27	66	120	166	190
Powers for short wavelengths in the continuum generated from a 6 m length of fibre A						
λ(nm)	400	450	488	500	530	550
P(μW)	0	11	20	24	40	45

Compared with the spectrum at 475 nm, the spectrum at 425 nm is symmetrical [Fig. 4(a)]. We can see from the phase matching curve [Fig. 4(b)] that at 156.5° (vertical orange line), SFM 1064 nm + 710 nm → 425 nm can take place. This will be weaker than the SFM process considered above generating 475 nm using 1064 nm, as the intensity at 710 nm in the continuum is low. There is now no tail to shorter wavelengths as that would require wavelengths shorter than 710 nm for SFM.

To generate 400 nm there is no SFM possible using the residual pump at 1064 nm, so this must be achieved by SHG of the 800 nm component of the continuum, with consequently very low observed output power.

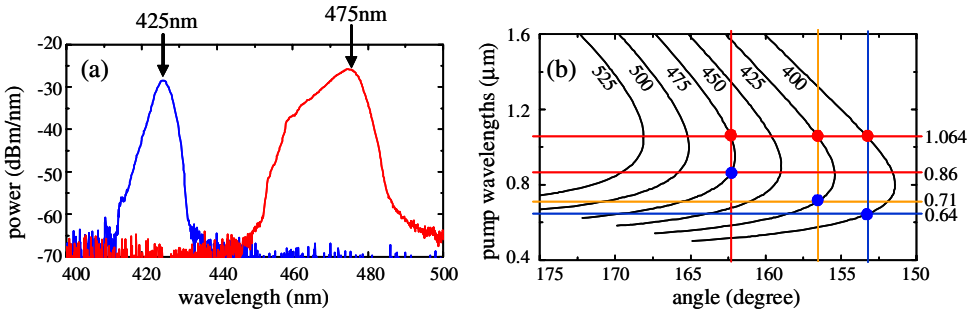

Fig. 4. (a). Spectra at 425 nm and 475 nm generated in BIBO pumped by the continuum source from a 0.6 m length of fibre A. The resolution of the spectrometer was 1 nm. (b) SFM tuning phase matching curves in the yz plane of BIBO for different output wavelengths (marked beside each curve).

From this discussion we can see that the nonlinear process contributing to frequency upconversion here is mainly SFM rather than SHG. Since the pump power is not very high the generated components have very low power, but the powers are still higher compared with what can be generated directly from SC (table 1). Also the use of continuum source brings some new features such as compact, convenient tuning. With the development of high power picosecond fibre lasers, there is a clear possibility for generating more power in the blue/UV.

#91141 - $15.00 USD Received 21 Dec 2007; revised 29 Jan 2008; accepted 30 Jan 2008; published 6 Feb 2008

3.2 Nonlinear conversion of discrete FWM wavelengths

As we discussed above, the visible/UV generation based on a continuum source is tuneable but the power is low. Another way to get a pump source for frequency upconversion is to fabricate a different PCF yielding distinct FWM peaks instead of a broad continuum [1]. Here the fibre we were using is labelled as fibre B. Fibre B was made in the same way as fibre A, except that the pressure applied in the holes was slightly different so that $d_1/\Lambda = 0.29$, $\Lambda = 2.95$ μm and $d_2/d_1 = 1.8$. The pump source, at 1064 nm, is now in the normal dispersion regime of fibre B, so a FWM process will take place [1], in this case generating a signal wave at 834 nm and an idler at 1478 nm.

The conversion from the pump to the signal at 834 nm can be very efficient, leading to sufficient power at 834 nm to allow Raman conversion from this wavelength as it propagates further down the fibre. We chose an optimum fibre length of 1.2 m in order to balance the FWM efficiency and Raman effect. Like fibre A, fibre B is a highly birefringent fibre. The PER was 245 and 60 when the pump polarization was set along the slow and fast axes respectively, which corresponds to 99.6% and 98.4% of power kept in a single polarization. Again for efficient nonlinear upconversion, we set the pump polarization along the slow axis. The FWM spectrum is illustrated in Fig. 5(a). A signal at 834 nm and an idler at 1478 nm are generated. The power at 834 nm was measured to be 14 mW, which is 37% of the total output power 38 mW. We used the ×4 lens combination to focus the beam into 5 mm BIBO and rotated the crystal for phase matching. We got bright visible output at two different angles. The spectra are plotted in Fig. 5(b). The power measurements showed that the powers at 417 nm and 467 nm were 0.53 mW and 0.76 mW respectively. 417 nm comes from SHG of 834 nm and 467 nm comes from SFM between 834 nm and 1064 nm. The SHG efficiency is about 3.8%, which is comparable with previous results at similar pump power level [16]. Also the spectra are symmetric because there is no additional contribution from other wavelengths. For the existing fibre and pump laser, the FWM peak is fixed. But for different fibres with slightly different dispersion properties, the FWM peaks are various. From this point of view, the SHG will be tuneable by use of different fibres in the first stage. We have fabricated PCFs with FWM peaks at around 700 nm, which means the short wavelength can be tuned to as short as 350 nm in this way. The operation is more complex, but the system is still compact and we get much higher power output than the continuum case.

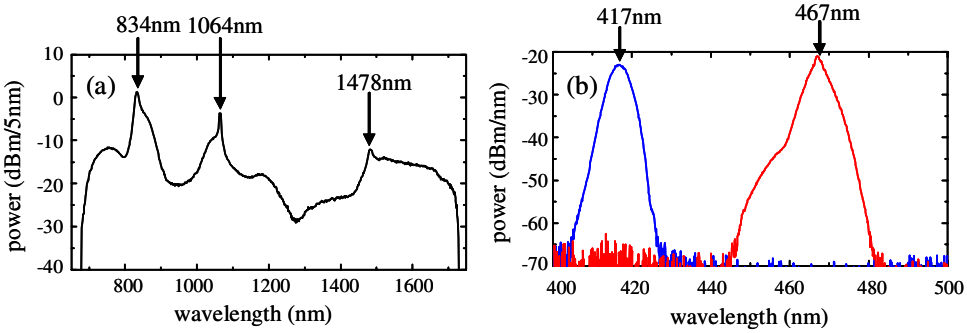

Fig. 5. (a). FWM spectrum from a 1.2 m length of fibre B with an average power of 38 mW. The resolution of the spectrometer was 5 nm. (b) SHG and SFM spectra in BIBO pumped by the FWM output from a 1.2 m length of fibre B. The resolution of the spectrometer was 1 nm.

According to Figs. 4(a) and 5(b), the short wavelengths are generated with no pedestal, down to the level of -35 to -45 dB. This is very useful in some applications such as fluorescence microscopy, where generated fluorescence has longer wavelength but is very weak. The clean spectrum with high extinction ratio makes it easier to distinguish the fluorescence from any background at the same wavelength emitted by the pump. This source is therefore potentially more useful than simply a filtered continuum as a tuneable pump for such applications.

#91141 - $15.00 USD Received 21 Dec 2007; revised 29 Jan 2008; accepted 30 Jan 2008; published 6 Feb 2008

For many applications, it is necessary to couple the generated short wavelength light to a single mode fibre. We therefore measured the coupling efficiency of the free space beam to a piece of ESM PCF. A power of 66 μW at 417 nm was coupled into a 3 m length of ESM PCF. The efficiency was 12.5%, which is not high because the beam is not round due to the spatial walk-off between the fundamental beam and SHG beam in the crystal [24, 25]. If a walk-off compensation technique using multiple crystals [24, 25] could be applied in this experiment, both the upconversion efficiency and the free space-fibre coupling efficiency would be enhanced.

4. Conclusion

In conclusion, we demonstrate a simple way to fabricate highly birefringent PCFs. Using this kind of birefringent PCF, we made a compact continuum source with more than 99% of power in a single linear polarization, whilst the modal asymmetry is sufficiently low that it yields less than 6% (0.25 dB) measured power coupling penalty with symmetrical PCF. The continuum source is flat over the entire bandwidth from 450 nm to 1750 nm.

By use of SC and FWM processes in the birefringent PCFs, we realized tuneable visible/UV generation by critically phase matched SFM and SHG in BIBO. The tuning range was from 400 nm to 525 nm. Further improvements including the use of high power picosecond fibre laser and walk-off compensation technique, are proposed to enhance this compact and convenient tuneable visible/UV source.

Acknowledgment

C. Xiong is supported by ORS scheme. W.J. Wadsworth is a Royal Society University Research Fellow. This project is partially supported by the EPSRC (Grant No. EP/D058074/1).

#91141 - $15.00 USD Received 21 Dec 2007; revised 29 Jan 2008; accepted 30 Jan 2008; published 6 Feb 2008